universität wien

DISSERTATION / DOCTORAL THESIS

Titel der Dissertation /Title of the Doctoral Thesis

How clusters grow to particles: Particle size distribution and growth rate measurements with a DMA-train

verfasst von / submitted by

Dominik Stolzenburg, MSc

angestrebter akademischer Grad / in partial fulfilment of the requirements for the degree of

Doktor der Naturwissenschaften (Dr. rer. nat.)

Wien, 2018 / Vienna, 2018

Studienkennzahl lt. Studienblatt / degree programme code as it appears on the student record sheet:	A 796 605 411
Dissertationsgebiet lt. Studienblatt / field of study as it appears on the student record sheet:	Physik
Betreut von / Supervisor:	Ass.-Prof. Dr. Paul Winkler

Abstract

New particle formation by gas-to-particle conversion is observed all over the globe. It is a major contributor to cloud condensation nuclei concentrations and therefore impacts global climate, as the lifetime and albedo of clouds are affected by the availability of cloud droplet seeds. For a newly formed cluster containing only a few molecules, it is crucial that the initial growth by further vapor addition is fast enough to prevent losses to larger background aerosol. Recent studies have shown that not only sulfuric acid, but also organic molecules of biogenic and anthropogenic origin can contribute to initial particle growth. However, it is still under debate, how the different condensing vapors interact with each other and how external conditions like temperature influence the role of organics. Moreover, complete mass balance between observed gas-phase compounds and particle phase growth has yet to be demonstrated for any organic system.

In this thesis, a new instrument, the DMA-train, for particle size distribution measurements in the cluster-particle transition regime below 10 nm is presented. It uses existing particle sizing technology in a new parallel approach to overcome the problem of low measurable concentrations of ultrafine particles and it therefore can investigate the dynamics of initial growth. Moreover, this allows for the development of a new analysis method, providing size- and time-resolved insights into the aerosol dynamics. The analysis method is applied to a chamber experiment, where new particle formation from the ozonolysis products of two biogenic volatile organic compounds is compared, revealing that particle growth rates below 10 nm show strong variations. A clear curvature effect is identified in two additional studies, using the CLOUD experiment at CERN. It is shown that some highly oxygenated molecules from the ozonolysis of the monoterpene α-pinene are already able to condense onto the smallest molecular clusters. However, only with increasing particle size and a reduced Kelvin-barrier, more and more less oxygenated products can contribute, increasing the particle growth rate. This is further enhanced in the presence of isoprene, where the oxidation chemistry of α-pinene is altered leading to less products with extremely low volatility, suppressing initial but not later growth. On the other hand, it is found that organics do play a decisive role over a wide range of temperatures. The volatility of all oxidation products is strongly reduced at cold temperatures counterbalancing the slower chemical reaction rates. Moreover, mass balance between sensitive gas-phase measurements and precision particle growth rates is demonstrated in an aerosol growth model.

In summary, this thesis shows that the DMA-train can help resolving some long debated topics: It indicates why particle growth rates in the atmosphere accelerate with increasing size, why new particle formation is rarely observed in isoprene-rich environments like the Amazon and that organics are still important for new particle formation at high altitudes, e.g. in the outflow regions of deep convective clouds.

Zusammenfassung

Neupartikelbildung durch Phasenübergange von Spurengasen zu flüssigen oder festen Partikeln in der Atmosphäre ist ein globales Phänomen und der größte Beitrag zur Anzahlkonzentration von Wolkenkondensationskeimen. Dieser Effekt beeinflusst folglich das globale Klima, da die Lebensdauer und Albedo von Wolken durch die zur Verfügung stehende Menge von Kondensationskeimen bestimmt werden. Die neu entstandenen molekularen Cluster müssen schnell genug anwachsen, um nicht an vorhandene größere Aerosolpartikel verloren zu gehen. Aktuelle Studien zeigen, dass nicht nur Schwefelsäure sondern auch organische Substanzen mit biogenem oder anthropogenem Ursprung zu diesem frühen Wachstum beitragen. Es ist jedoch nicht geklärt, wie die verschiedenen kondensierenden Moleküle miteinander interagieren und wie externe Größen, wie Temperatur, diese Prozesse beeinflussen. Darüber hinaus ist es noch für kein organisches System gelungen, das beobachteten Wachstum quantitativ mit den gemessenen Konzentrationen von Gasphase-Molekülen in Übereinstimmung zu bringen.
In dieser Doktorarbeit wird die Entwicklung eines neuen Messinstruments zur Bestimmung von Partikel Größenverteilungen im Bereich von weniger als 10 nm vorgestellt. Dabei wird bereits existierende Technologie in einem neuen parallelen Ansatz angewandt und damit eine erhöhte Sensitivität für geringe Partikelkonzentrationen erreicht. Dieser sogenannte DMA-train liefert neue Einblicke in die Aerosoldynamik von ultrafeinen Partikeln und führt zur Entwicklung einer neuen Analysemethode, die größen- und zeitaufgelöste Aerosolwachstumsraten simultan bestimmen kann. Damit wird bei der Ozonolyse von zwei biogenen volatilen organischen Substanzen gezeigt, dass insbesondere das Aerosolwachstum unterhalb von 10 nm Größenabhängigkeiten aufweist. In zwei weiteren Studien, beide durchgeführt am CERN CLOUD Experiment, wird ein eindeutiger Effekt durch die gekrümmte Oberfläche der Partikel bestätigt: Es wird gezeigt, dass hochoxidierte Moleküle aus der Ozonolyse des Monoterpens α-Pinen bereits zum Kondensationswachstum molekularer Cluster beitragen. Jedoch nur mit zunehmender Größe und abnehmender Kelvin-Barriere können auch weniger oxidierte Produkte aufkondensieren, was die Wachstumsrate erhöht. Dieser Effekt wird in der Gegenwart von Isopren noch zusätzlich verstärkt: Die Oxidations-Chemie von α-Pinen verändert sich und es entstehen weniger Moleküle mit extrem niedrigem Sättigungsdampfdruck, die für das erste Wachstum entscheidend sind. Darüber hinaus wird gezeigt, dass organisches Aerosolwachstum über den weiten Temperaturbereich der Troposphäre von entscheidender Bedeutung sein kann. In diesem Zusammenhang kann auch erstmals eine ausgeglichene Massenbilanz zwischen Wachstumsmessungen und beobachteten Gasphasen-Konzentrationen gezogen werden.
Zusammenfassend demonstriert diese Arbeit, dass der DMA-train einige entscheidende Fragen beantworten kann: Es wird gezeigt, warum in der Atmosphäre meist geringere Wachstumsraten für kleinere Partikel beobachtet werden, warum es kaum Neupartikelbildung in Regionen mit hohen Isopren Emission gibt und dass organische Moleküle auch bei sehr kalten Temperaturen der oberen Troposphäre eine wichtige Rolle spielen.

Contents

Chapter 1

Introduction

Almost everybody already encountered the possible differences in visibility between a clean day after rainfall and a blurry day after a period of stable weather conditions with few winds. The visibility from a hillside close to a large urban area can easily range between the order of just hundreds of meters up to tens of kilometres.

This effect is caused by aerosols, solid or liquid particles suspended in air or any other gas. They affect human life in various different ways and contexts and have an impact on a wide range of physical scales. They are used in nanotechnology within medical and industrial applications and allow for the synthesis of new materials (Swihart, 2003; Buesser and Pratsinis, 2012). Aerosols affect human health by penetrating the respiratory system (Shiraiwa et al., 2017), even down to the smallest aerosol particle sizes (Pedata et al., 2015). Moreover, aerosol air pollution is thought to be a major contributor to premature death on a global scale (Lelieveld et al., 2015).

As already outlined, aerosols are a crucial part of our atmospheric system and fog, dust, smoke and haze affect visibility and are the reason for nice red colored sunsets. But, maybe most importantly, atmospheric aerosols also influence the global climate in multiple ways and are an important key parameter in climate change patterns (Boucher et al., 2013). The Intergovernmental Panel on Climate Change identified atmospheric aerosols as one of the highest uncertainties for climate change predictions (IPCC, 2013).

The effect of aerosols on the global climate are due to their manifold influence on the earth's radiative balance. Aerosol particles directly scatter incoming solar radiation back to space and hence prevent it from reaching the earth's surface and heating it. On the other hand, they can as well directly absorb the radiation causing a warming effect of some atmospheric layers. Both effects are usually classified together as the direct aerosol effect. In contrast to this, aerosol particles also influence the formation and properties of clouds as they act as seeds for the nucleation of every cloud droplet. Thereby they can affect the albedo (Twomey et al., 1984) and the lifetime of clouds (Albrecht, 1989). These effects are usually referred to as the aerosol indirect effect.

Figure **??** (IPCC, 2013) summarizes the anthropogenic influence on the earth's radiative balance in terms of the quantity radiative forcing, which gives the difference in the global net energy flux onto the earth's surface compared to the year 1750 in units of $\mathrm{W\,m^{-2}}$. While the main drivers of climate change, the greenhouse gases CO_2, CH_4 and N_2O are well identified and the significance of these effects are precisely quantified, not even the sign of the net total aerosol effect is yet determined. The uncertainty range of the aerosol indirect effect is the largest, as the differences in global cloud cover and cloud albedo to the pre-industrial

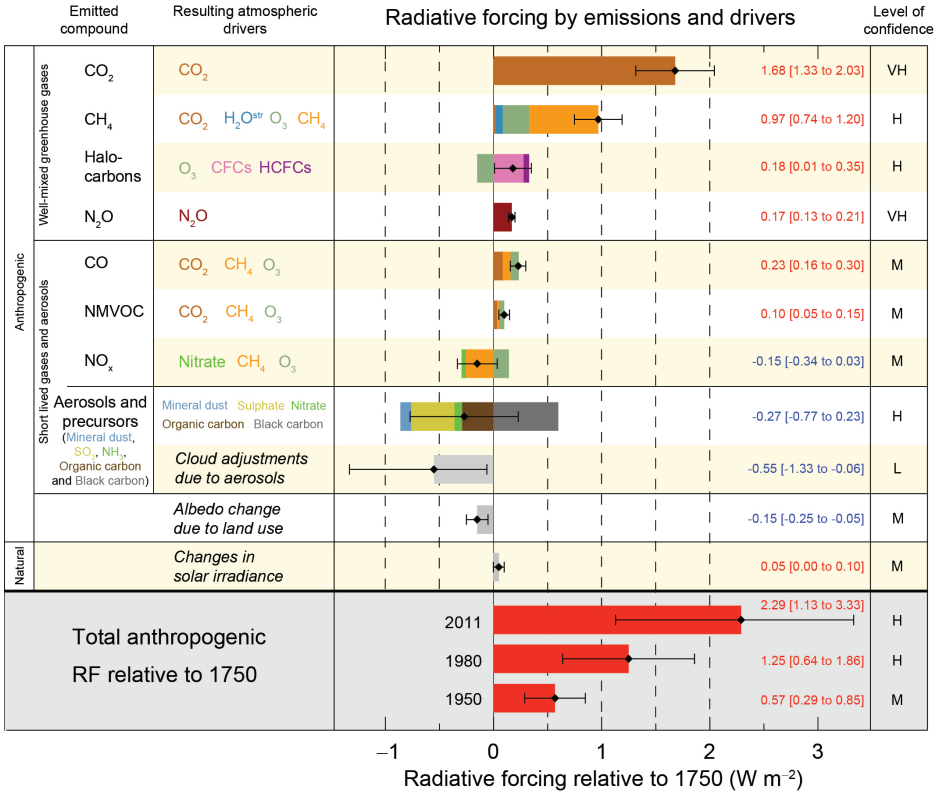

Figure 1: Radiative forcing difference between 2011 and 1750 for the main drivers of climate change are shown together with the aggregated uncertainties. Effect given per emitted compound, while a single atmospheric driver may have several emitted precursors. Figure taken from IPCC (2013).

age cannot be quantified by climate archives, like e.g. CO_2 concentrations. Only a detailed physical understanding of cloud and aerosol formation processes can improve our knowledge and climate change predictions. As formation of cloud droplet seeds and their activation are both multi-phase processes, precise experimental methods covering both, gas- and particle phase are mandatory.

In the last two decades, the high uncertainties of climate models with respect to the indirect aerosol effect have pushed the scientific community towards more in depth investigations, resulting in the development of new experimental approaches and new analysis methods. Therefore, this thesis can be seen as another step to improve the scientific community's understanding of the indirect aerosol effect. This is achieved by the development of a new instrumental approach, the DMA-train, and a new analysis method suited for the precision data acquired by the new experimental technique, discussed in Chapter 2 and 3, respectively. These new developments help to quantify the complex interaction processes between gas and particle phase for nanometre-sized aerosol under precisely controlled laboratory conditions with the CERN CLOUD experiment (Kirkby et al., 2011; Duplissy et al., 2016). Results from

two measurement campaigns with this unique experimental setup are presented in Chapter 4 and 5, focusing on the importance of organic molecules in initial nanoparticle formation. To contextualize the research presented in this thesis and to identify the main research questions, the basics of aerosol formation, aerosol sizing techniques and analysis methods are presented in the following introduction, while the main research achievements of this thesis are discussed all together in Chapter 6.

1.1 New particle formation

The aerosol indirect effect is linked to global cloud condensation nuclei (CCN) concentrations. Atmospheric aerosol particles can act as seeds for cloud droplets if they are large enough. In the case of soluble particles, the Köhler theory describes the activation of seed particles by water (Köhler, 1936). This process, depending on the composition of the aerosol particle, only occurs at particle sizes between 50-100 nm in diameter for typical atmospheric water vapor supersaturations (Seinfeld and Pandis, 2006).

Estimates of the global budget of CCNs are challenging as aerosols are dynamic multi-phase systems with complex interactions between the gas and the particle phase. The largest source of CCN is new particle formation (NPF) by gas-to-particle conversion (Gordon et al., 2017), identified to be a global phenomenon (Kulmala et al., 2004c). In this process, specific vapor molecules nucleate to form small molecular clusters (in the size range of 1 nm), which can then subsequently grow to CCN sizes by condensation of additional molecules. In the atmosphere NPF is usually observed on a regional scale in the atmospheric boundary-layer around mid-day by the appearance of a new particle population at sizes of a few nanometres, eventually growing up to larger particle diameters during the afternoon (Mäkelä et al., 1997). This might point towards important roles of photochemistry and temperature. However, the phenomenon of NPF is not only limited to this typical scenario but also found in many different other settings (McMurry et al., 1981; Lee et al., 2008; Bianchi et al., 2016; Rose et al., 2018).

Such a typical NPF event is shown in Figure **??**, recorded by a Differential Mobility Particle Sizer at a measurement station in Schwechat, Austria. It shows the evolution of the particle size distribution, with the mobility equivalent particle diameter on the y-axis, the time on the x-axis and the color code representing the corresponding particle number concentration of the measurement size-intervals.

The dynamics of the NPF event critically influence the characteristics of the particle size distribution. As already pointed out, NPF is only of climatic relevance if the freshly formed particles can even grow to sizes where they can act as CCN. In competition with growth is the removal of particles from the growing population by coagulation due to collisions and subsequent adherence to pre-existing background aerosol. Key physical parameters which describe NPF are the nucleation rate J in $[\text{particles}\,\text{s}^{-1}\,\text{cm}^{-3}]$ and the growth rate $\text{GR}(d_p)$

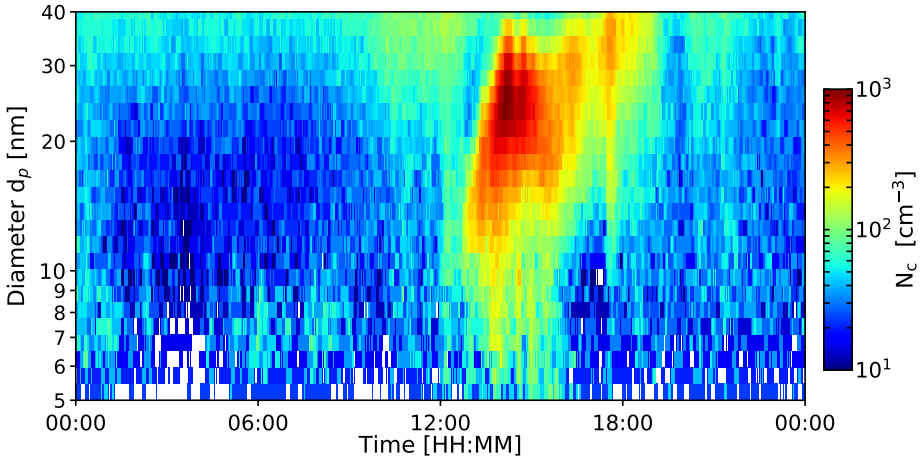

Figure 2: New particle formation event recorded on May 14th 2016 in Schwechat, Austria. Abscissa shows the time of the day, ordinate the electrical mobility equivalent particle diameter as measured with a DMPS system. Red colors indicate high concentrations and blue low concentrations. Around mid-day a new particle population appears at the smallest sizes growing towards larger sizes in the afternoon, a typical characteristic of a new particle formation event.

of the freshly formed particles in [$\mathrm{nm\,h^{-1}}$]. Kerminen and Kulmala (2002) and Lehtinen et al. (2007) connected the formation rate of new particles of a certain diameter d_p with the nucleation rate at the critical cluster size $J(d_{\mathrm{crit}})$ via the assumed constant growth rate GR and the coagulation sink CoagS to a pre-existing particle population:

$$J(d_p) = J(d_{\mathrm{crit}}) \cdot \exp\left(-\gamma \cdot d_{\mathrm{crit}} \cdot \frac{\mathrm{CoagS}(d_{\mathrm{crit}})}{\mathrm{GR}}\right) \tag{1}$$

where $\gamma = \frac{1}{m+1}\left[\left(\frac{d_p}{d_{\mathrm{crit}}}\right)^{m+1} - 1\right]$ is a pre-factor connected to the coagulation sink by the parameter m, which can be inferred from particle size-distribution measurements. Obviously, there is a steep exponential dependence on the growth rate, i.e. only if particles grow fast enough, they are able to reach sizes where they can act as CCN. It is therefore extremely important to identify the processes responsible for particle growth and this especially in the size-range below 10 nm. In that range, the loss mechanism due to coagulation is most important due to the high diffusivity and hence collision rates of sub-10 nm particles.

One of the major substances responsible for aerosol nucleation in the atmosphere is thought to be sulfuric acid (H_2SO_4) (Sipilä et al., 2010; Kulmala et al., 2013), which is produced in the atmosphere by oxidation of SO_2 by the hydroxyl radical (OH•). As the production of OH• is a photochemical process involving the photo-dissociation of ozone, it could explain the dominant occurrence of NPF during mid-day. However, precise laboratory measurements concluded that sulfuric acid alone cannot reproduce the observed atmospheric nucleation rates (Kirkby et al., 2011). Therefore it is assumed to be a process involving several nucleating

species, such as ammonia or amines (Almeida et al., 2013; Kürten et al., 2014), depending very much on the location and specific atmospheric conditions. Moreover, particle growth caused by sulfuric acid and corresponding bases like ammonia or amines proceeds not fast enough to explain the global importance of NPF at atmospheric sulfuric acid concentrations.

A large contribution to atmospheric NPF and subsequent growth might therefore come from organic compounds resulting from the oxidation of volatile organic compounds (VOCs) (Riipinen et al., 2012; Donahue et al., 2013). In urban environments huge quantities of aromatic VOCs are emitted in combustion processes, especially by vehicles (Friedrich and Obermeier, 1999; Warneke et al., 2007). However, at least equally important are VOC emissions by plants (Guenther et al., 1995). The most important atmospheric biogenic VOCs are isoprene (C_5H_8) and monoterpenes ($C_{10}H_{16}$), where the most abundant one is α-pinene. VOCs get oxidized by atmospheric oxidants such as O_3, OH•, and NO_x. Primary oxidation can be followed by a subsequent auto-oxidation process, which might transform VOCs into highly oxygenated molecules (HOMs), some of which possess extremely low vapor pressures (Ehn et al., 2014). Two recent laboratory studies showed that they can nucleate and efficiently grow particles from cluster sizes onward (Kirkby et al., 2016; Tröstl et al., 2016) and some field studies support their influence on atmospheric NPF (Bianchi et al., 2016; Rose et al., 2018). To which extent organics play a decisive role in global aerosol formation is still under debate. The budget of CCN could be highly sensitive to parameters such as abundance of different organic compounds, background aerosol contamination, relative humidity and temperature.

The scientific goal of this thesis is the improvement of our understanding of initial nanoparticle growth, where molecular clusters become more stable particles. In that range, condensation might be very sensitive to particle curvature, as the equilibrium vapor pressure over a curved surface p_{vap} is increased compared to the saturation vapor pressure p_{sat} flat liquid-gas interface, described by the Kelvin relation (e.g. Seinfeld and Pandis, 2006):

$$\frac{p_{\mathrm{vap}}}{p_{\mathrm{sat}}} = \exp\left(\frac{4\sigma M}{R\rho T d_p}\right), \tag{2}$$

where σ and ρ are the macroscopic surface tension and density of the condensing vapor, R is the ideal gas constant and T represents the temperature. As a consequence higher condensing vapor concentrations are needed in order to achieve supersaturation over a curved surface of a small particle with diameter d_p. Due to this so called Kelvin-barrier, it is possible that some compounds can only condense from a certain size onward, where lower vapor supersaturation is required, because the curvature effect becomes smaller. Therefore, there could be a transition between nucleation and subsequent growth where different vapors are nucleating and actually growing the particles. Are both sulphuric acid and organics crucial for initial nanoparticle growth (Kulmala et al., 2013)? And what is the role of different organics? Tröstl et al. (2016) speculated that increased initial growth rates due to HOMs

in the sub-10 nm range can eventually lead to significant differences in the global budget of CCN. If especially biogenic emissions would impact this process, a large part of the global CCN budget would be independent of anthropogenic emissions, pointing towards a reduced anthropogenic radiative forcing by the indirect aerosol effect (Gordon et al., 2016).

To approach these questions, there is a strong need for improved instrumentation of aerosol size-distribution measurements in the sub-10 nm range, where initial molecular clusters start growing towards larger particle sizes. This will be further outlined in the next section.

1.2 Particle sizing in the cluster-particle transition regime

1.2.1 Sub-10 nm aerosol dynamics

Initial aerosol growth processes are strongly influenced by aerosol dynamics (Li and McMurry, 2018), which alter the particle size-distribution $n(d_p, t)$. At high number concentration coagulation of particles within the growing nucleation mode might mimic condensation growth, but will reduce the actual number of particles reaching CCN sizes. Additionally, dilution, losses to background aerosol particles and losses to external surfaces might reduce particle concentrations evolving from NPF. The latter might be very important for chamber experiments, where aerosol formation is studied under precisely controlled laboratory conditions. In theory, all these effects can be described by the continuous aerosol general dynamics equation as given by Seinfeld and Pandis (2006) for the number volume-distribution $n(v, t)$:

$$\begin{aligned}\frac{\partial n(v,t)}{\partial t} =& \frac{1}{2}\int_0^v K(v-q,q)n(v-q,t)n(q,t)\,\mathrm{d}q - n(v,t)\int_0^\infty K(q,v)n(q,t)\,\mathrm{d}q \\ &- \frac{\partial}{\partial v}[I(v)n(v,t)] + S(v) - R(v)n(v,t)\end{aligned} \tag{3}$$

The first two terms on the right-hand-side describe the impact of coagulation on the particle size-distribution, with a positive contribution of smaller particles coagulating to form a particle of volume v, and a negative contribution for particles of volume v coagulating to form larger particles. The next term gives the particle current to a certain volume v due to condensation and is therefore called the growth term with the volume growth rate $I(v)$. $S(v)$ and $R(v)$ are source and removal terms for the aerosol size distribution and can for example describe formation of particles by nucleation and losses to chamber walls or due to dilution.

Apparently, knowledge of the particle volume-distribution $n(v, t)$, or equivalently the particle size-distribution $n(d_p, t)$, is the key for the quantification of these processes. For particles smaller than the wavelength of visible radiation, optical methods for particle size distribution measurements cannot be deployed any longer as the scattering cross section becomes negligible.

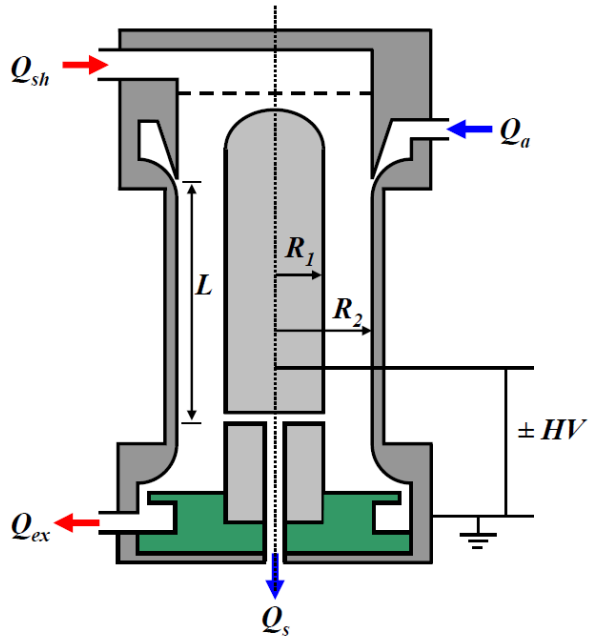

Figure 3: Schmatic drawing of a Vienna-type Differential Mobility Analyzer (DMA). It uses a cylindrical design of the capacitor. A high voltage (HV) can be supplied to the central electrode. The aerosol flow Q_a is introduced by a single inlet but is radially distributed around the sheath flow. It enters the classifying region by a sharp slit and is laminarily combined with the inlet sheath flow Q_{sh}. Through an exit slit at the central electrode, the size-classified aerosol can exit the device, while the excess sheath flow Q_{ex} is cleaned from particles and usually recirculated (so called closed-loop arrangement). Figure taken from Steiner (2011).

1.2.2 Electrical mobility particle sizing

For measurements in the few nanometre size range, electrical mobility spectrometry is widely used. It relies on the electrical mobility Z, which describes the proportionality between the drift velocity $\vec{v}$ of a charged particle in the direction an electrical field $\vec{E}$, i.e. $\vec{v} = Z \cdot \vec{E}$. Particle drift in air is related to the mechanical mobility B and the Stokes drag force $\vec{F}_d$ which depends on the particle size via $\vec{F}_d = -3\pi\eta d_p\vec{v}/C(d_p)$, where η is the dynamic air viscosity and $C(d_p)$ is the Cunningham slip correction which accounts for the transition regime where the particle size becomes comparable to the mean free path of the carrier gas molecules (e.g. Seinfeld and Pandis, 2006). The most commonly used device for electrical mobility classification is the differential mobility analyzer (DMA), which goes back to the pioneering work of Knutson and Whitby (1975). It uses a (most common cylindrical) capacitor in order to separate aerosol particles according to their electrical mobility by laminarily sheathing the aerosol flow with particle-free air inside the geometry of the DMA. A high voltage applied to the central electrode attracts the charged aerosol particles and passes them through the sheath air stream. A schematic drawing of a cylindrical DMA is presented in Fig. **??**.

Variation of the high voltage allows particles with different electrical mobility to pass through

the device. In case of singly charged particles, which is the dominant equilibrium charging state of sub-10 nm aerosol, this coincides with the change of the size of the particles. Subsequent detection of the size-classified aerosol allows for the retrieval of the particle size distribution. Commonly, two different approaches are applied, as the voltage can either be varied stepwise (Reischl, 1991) or continuously ramped (Wang and Flagan, 1990). However, even with a fast-scanning device the time-resolution remains limited to roughly 1 min (Tröstl et al., 2015).

Moreover, these methods face serious limitations for reliable size-distribution measurements at atmospheric particle concentrations below 10 nm. This is due to multiple reasons: First, the diffusion coefficient $D(d_p)$ for aerosol particles is a function of size and strongly increases with decreasing particle diameter. Therefore, smaller particles not only diffuse rapidly onto pre-existing aerosol particles in the case of NPF, but also during every measurement procedure. They impact and get lost on walls of the sampling lines or the analyzing instruments even under laminar sampling flow conditions (Gormley and Kennedy, 1948). Second, nanoparticle sizing according to the electrical mobility relies on charged aerosol particles. Through the effect of cosmic rays and the decay of radioactive radon, charged ions exist in ambient air. However, the distribution of charged aerosol particles depends on ambient conditions. For the retrieval of particle size distributions of neutral and charged particles, a stable charging state of the aerosol particles needs to be maintained during the measurement process. This is usually achieved by using aerosol neutralizers, bringing the sampled particles in contact with a stable bipolar ion atmosphere (e.g. Kallinger and Szymanski, 2015). The charging efficiency of aerosol particles in such devices, however, strongly drops as particle size decreases (Fuchs, 1963). Third, detection of the smallest aerosol particles at low concentrations is extremely challenging. The widely used condensation particle counters (CPCs) detect particles at the single-count level by activating them through heterogeneous nucleation in a supersaturated working vapor. They subsequently grow up to an optically-detectable size. However, such devices always have a lower cutoff in size, i.e. they cannot detect aerosol particles below a certain size (e.g. Stolzenburg and McMurry, 1991). This is again because the energy barrier for heterogeneous nucleation of the working vapor on the sample particles gets larger with decreasing size and thus higher supersaturation is required for activation (Winkler et al., 2008).

1.2.3 The DMA-train concept

Electrical mobility spectrometry at typical atmospheric particle concentrations is challenging in the sub-10 nm size-range and needs to be optimized for the quantification of the processes responsible for molecular clusters to grow towards larger particle sizes.

Diffusional losses of small aerosol particles can be minimized by using short sampling lines and high sampling flow rates. The reduction in DMA size-resolution due to diffusion (Stolzenburg,

1988; Stolzenburg and McMurry, 2008) can be avoided by the usage of high sheath-flow rates (Steiner et al., 2010). However, it requires innovative DMA design in order to reduce diffusional losses inside the device (Brunelli et al., 2009; Jiang et al., 2011a; Franchin et al., 2016). Moreover, the functional size-range of CPCs has been extended down to 1 nm in the last decades by CPC design improvements (Stolzenburg and McMurry, 1991; Vanhanen et al., 2011; Pinterich et al., 2016) and the usage of different working fluids (Iida et al., 2009; Vanhanen et al., 2011; Jiang et al., 2011b; Wimmer et al., 2013).
In this thesis, some of these novel developments have been combined with the idea of a parallel usage of several DMAs all set to different voltages and hence sizes (Flagan et al., 1991; Winkler et al., 2013). This avoids the scanning or stepping procedures of classical electrical mobility spectrometers and thus achieves a higher time-resolution. Moreover, the sensitivity to small particle number concentrations is increased as the different sizes are measured continuously, which leads to higher counting statistics. This concept will be called DMA-train. Chapter 2 shows the development of a new integral instrument following this principle by using six DMAs in parallel and providing all the necessary infrastructure within a mobile instrument rack. Reduction of sampling line losses through a common inlet and the usage of novel DMAs well suited for the sub-10 nm range (Jiang et al., 2011a) leads to higher detectable number concentrations for the size-classified aerosol particles downstream of the DMA. The DMAs are combined with six state-of-the-art ultrafine CPCs (Stolzenburg and McMurry, 1991), two of them even boosted by the usage of two particle size magnifiers (PSMs) (Vanhanen et al., 2011) upstream of the particle counting CPCs. These mixing-type devices are based on diethylene glycol as working fluid and achieve high activation efficiencies of particles smaller than 2 nm. In Chapter 2 the characterizations of the used six Grimm S-DMA, the different CPC types and the total system sampling losses are presented, giving a comprehensive picture of the required correction for the retrieval of size-distribution data. Moreover, it is shown that the DMA-train can catch the evolution of the size-distribution of a highly dynamic aerosol with a reasonable time-resolution of roughly $\sim$10 s. The instrument is operated during α-pinene ozonolysis experiments at the CERN CLOUD experiment (Kirkby et al., 2011; Duplissy et al., 2016) and within Chapter 2 it is demonstrated that particle growth rates at typical atmospheric nucleation rates and hence typical atmospheric number concentrations within the nucleation mode can be inferred with high precision.

1.2.4 Particle growth rate measurement methods

Typically particle growth rates are inferred from particle size-distribution data. The most widely used methods try to follow significant patterns of the size-distribution such as the time of first signal appearance in every channel (Lehtipalo et al., 2014), the time where the maximum concentration in every channel is reached (Kulmala et al., 2012) or they identify local maxima of the size-distribution (Paasonen et al., 2018) or the median diameter (Kulmala

et al., 2012) and track their evolution with time. For chamber experiments, most recent studies made use of the appearance time method (Lehtipalo et al., 2016; Tröstl et al., 2016; Svensmark et al., 2017). Similar for all of these methods, they can only infer an apparent particle growth rate of the observed particle population within the growing mode of the size-distribution. This growth rate however, might not correspond to the growth rate of a single aerosol particle, which is only growing by the condensation of molecules. And, maybe even more importantly, they cannot disentangle possible size- and time-dependencies of the observed growth rates. This has for example lead to the ambiguity of observed increasing particle growth rates during new particle formation (Kulmala et al., 2004a,b, 2013): Is this increase due to an increasing abundance of condensing vapor molecules during the particle growth period or is it an intrinsic property of the condensation process, because the Kelvin-barrier for condensation onto larger particles is lower and thus more species present in the atmosphere are able to drive the growth?

Several authors have therefore proposed to make use of the general dynamic equation in order to infer the particle growth term $I(v)$ directly from size-distribution measurements (Lehtinen et al., 2004; Verheggen and Mozurkewich, 2006; Kuang et al., 2012). This would give the possibility of simultaneously measuring the size- and time dependence of particle growth rates during a new particle formation event. All processes described in Eq. 3 are altering the particle size-distribution. With the knowledge of coagulation efficiencies, dilution processes and loss mechanisms, the general dynamics equation can be solved for the unknown $I(v)$. However, the analysis methods presented so far all require fitting to the observed data and are challenging to apply to atmospheric data in the sub-10 nm size range, which often suffers from low counting statistics.

The improved data quality obtained by the DMA-train technique is therefore directly useful to improve these kind of approaches. Chapter 3 introduces two new analysis methods based on the general dynamics equation for the analysis of particle size-distribution measurements and the retrieval of particle growth rates, which can be directly linked to the condensation growth term $I(v)$. Both methods are designed such that no fitting procedures are required. They take an input particle size distribution measurement and simulate all relevant aerosol dynamics processes expect for condensation growth until the next size-distribution measurement is available.

The first method, called INSIDE, solves the size-integrated general dynamics equation for different lower size-thresholds d_{min}. This is done by evaluating the magnitude of coagulation, loss and dilution processes from the simulated size distribution with respect to the input experimental distribution. With the number of evaluated fixed lower size limits d_{min} being arbitrary, the INSIDE-method provides size-resolved particle growth rates for every measurement time-interval. The second method, called TREND, follows regions within the particle size distribution containing the same fraction of particles. It compares the median diameter of

these regions in the subsequently measured experimental and the simulated distributions and assigns a growth rate due to this shift. In Chapter 3 both methods are tested with simulated particle size distributions and reproduce the model growth rates.

They are then applied to experimental data measured via the DMA-train principle in a chamber experiment performed at the National Center of Atmospheric Research (NCAR) in Boulder, Colorado, USA (e.g Fry et al., 2014). The two investigated organic aerosol systems of Chapter 3, α-pinene and β-caryophyllene ozonolysis show high variations of growth rates in the sub-10 nm range in both the size- and time-dimension. They clearly indicate an acceleration of growth rates in the few nanometre range, showing that indeed a multi-component Kelvin-effect for the condensation of organic molecules (Donahue et al., 2011; Winkler et al., 2012; Tröstl et al., 2016) might be responsible for the widespread atmospheric observations of accelerating growth rates with size (Kulmala et al., 2013). The comparison of the organic systems show very different dynamics: The β-caryophyllene system is extremely fast but leads to a self-quenching effect due to the fast build-up of a high particle sink. Apparently, the characteristics of initial nanoparticle growth in the cluster-particle transition regime are highly sensitive to the condensing organic substances.

1.3 The role of low-volatility organics in initial aerosol growth

Organic compounds constitute a large fraction of 20-90 % of the atmospheric aerosol mass in the submicrometer range, depending on location and time of the year (Jimenez et al., 2009). Since the 1960s there is evidence that organics contribute to urban smog (Leighton, 1961) and to the observed blue haze in forested regions (Went, 1960). In the atmosphere and in dedicated smog chamber studies several authors could show that organics of anthropogenic and biogenic origin form secondary organic aerosol by gas-to-particle conversion; a detailed review can be found in Hallquist et al. (2009). While the important contribution of organic compounds to the mass of larger aerosol particles is certainly validated, an open question is, if organics already contribute to the very early steps of aerosol formation, i.e. to nucleation and initial growth in the atmosphere (Riipinen et al., 2012; Donahue et al., 2013). Organic molecules in the atmosphere show huge varieties (Goldstein and Galbally, 2007) and while many organic compounds partition between gas- and aerosol phase (Donahue et al., 2006), recent studies have drawn the focus on low-volatility organics with a high degree of oxygenation. They are formed through primary oxidation by atmospheric oxidants followed by an auto-oxidation process (Ehn et al., 2014; Rissanen et al., 2014). Their contribution to NPF is suggested by several chamber studies: Metzger et al. (2010) and Riccobono et al. (2014) showed that oxygenated organics of anthropogenic and biogenic origin can enhance nucleation rates. Kirkby et al. (2016) demonstrated that HOMs formed by the oxidation of the biogenic monoterpene α-pinene can nucleate on their own, while Tröstl et al. (2016) proofed that they

participate in initial growth.

However, it is unclear how well the findings for some representative molecules can be linked to observations in the atmosphere. Moreover, organic oxidation chemistry is extremely complex: Reaction pathways and the corresponding rate constants are hardly understood and measured. Therefore, external conditions like temperature might influence critically organic aerosol formation (Praske et al., 2018). Additionally, different oxidation mechanisms and possible interference of different organic compounds could lead to a different behaviour. Smog chamber studies showed an effect of NO_x on secondary organic aerosol formation (Presto et al., 2005; Ng et al., 2007) and Wildt et al. (2014) even observed that NO_x suppresses NPF of biogenic organics. Moreover, field and laboratory studies suggest that as well the presence of isoprene suppresses new particle formation (Kiendler-Scharr et al., 2009; Yu et al., 2014; Lee et al., 2016). However, for both cases the chemical mechanisms causing this reduction are unclear. In addition, it is not resolved, if the suppression mainly affects the nucleating vapors or if NPF is suppressed because of lower particle growth rates. Especially the effects impacting this cluster-particle transition regime are of central interest within the scope of this thesis.

The precision particle growth rate measurements obtained by the newly developed DMA-train are used to investigate the effects of isoprene (Chaper 4) and temperature (Chapter 5) on the production of low-volatility organics and hence their subsequent impact on initial particle growth. For both studies the approach of controlled laboratory conditions for the study of aerosol formation from α-pinene ozonolysis is used within the CLOUD experiment. In the set of the presented experiments, the complexity of the atmospheric simulations is increased compared to Kirkby et al. (2016) and Tröstl et al. (2016) by adding isoprene and varying the temperature. The unique setup of the CLOUD chamber achieves extremely high purities with respect to contaminant organics and sulfuric acid (Schnitzhofer et al., 2014; Frege et al., 2018) and provides a comprehensive array of instruments studying gas- and particle phase during aerosol formation.

Chapter 4 shows that the addition of isoprene does affect the oxidation chemistry of α-pinene and therefore leads to reduced particle nucleation and initial growth rates. This effect is caused by the reduced production of highly oxygenated dimers containing 19-20 carbon atoms, due to the interference of isoprene. The ozonolysis of α-pinene usually leads to the formation of peroxy-radicals (RO_2), which are able to increase their oxygen content by hydrogen shifts and subsequent auto-oxidation (Ehn et al., 2014). Only radical termination reactions, either unimolecular, or via HO_2 or via other RO_2 radicals, do interfere with this process and the latter is a source of highly oxygenated dimers with 19-20 carbon atoms. In the presence of isoprene, the $(RO_2)(RO_2)$ termination processes include reactions with RO_2 radicals from isoprene oxidation, leading to dimers with only 14-15 carbon atoms and less dimers with 19-20 carbon atoms. However, only the formed pure α-pinene dimers are sufficiently large to

have extremely low vapor pressures (Tröstl et al., 2016; Kurtén et al., 2016). The presence of isoprene therefore affects nucleation and initial growth, but not the growth processes of larger particles (>5 nm), because the dimers having 14-15 carbon atoms will contribute to condensation at larger sizes due to the reduced Kelvin-barrier. Chapter 4 therefore clearly supports the findings of a significant curvature effect, as soon as organics participate in condensation growth. Moreover, the direct impact of isoprene on initial growth can for example explain the absence of NPF in isoprene-rich environments such as the Amazon (Martin et al., 2010). For initial growth processes, it is therefore extremely important to account for the possible wide variety of different saturation vapor pressures of organic molecules produced in oxidation processes.

This is further underlined in Chapter 5, where the simpler system of pure α-pinene ozonolysis is investigated at different temperatures. It is demonstrated that the organics play a decisive role in initial growth over a wide range of tropospheric temperatures, because, independent of temperature, growth proceeds at similar speed if the α-pinene ozonolysis reaction rate is held constant. Again, this is linked to the saturation vapor pressure of the large variety of oxidation products. At warm temperatures, the increasing reaction rates of the auto-oxidation process (Praske et al., 2018), lead to a higher abundance of highly oxygenated molecules, with extremely low saturation vapor pressures even at elevated temperatures. At low temperatures the product concentrations of these molecules decrease, but already less oxygenated compounds can condense from the smallest sizes onward. This is again because of the strong exponential decrease of their saturation vapor pressure. Moreover, Chapter 5 demonstrates for the first time for an organic aerosol system mass balance between the compounds measured in the gas phase and accordingly predicted modeled aerosol growth with the observed growth rates. With a comparison to the precisely measured growth rates of the DMA-train a Kelvin-diameter is inferred, directly pointing towards the size-range where the Kelvin-barrier for condensing organics drops and their influence on growth becomes dominant. The following chapters will therefore demonstrate how a newly developed instrument for particle size distribution measurements offers a new perspective on the decisive size-range below 10 nm where the Kelvin effect clearly influences the ability of different atmospheric vapors to contribute to growth and hence NPF.

1.4 References

Albrecht, B.: Aerosols, Cloud Microphysics, and Fractional Cloudiness, Science, 245, 1227–1230, doi:10.1126/science.245.4923.1227, http://science.sciencemag.org/content/245/4923/1227, 1989.

Almeida, J., Schobesberger, S., Kürten, A., Ortega, I. K., Kupiainen-Määttä, O., Praplan, A. P., Adamov, A., Amorim, A., Bianchi, F., Breitenlechner, M., David, A., Dommen, J., Donahue, N. M., Downard, A., Dunne, E., Duplissy, J., Ehrhart, S., Flagan, R., Franchin, A., Guida, R., Hakala, J., Hansel, A., Heinritzi, M., Henschel, H., Jokinen, T., Junninen, H., Kajos, M., Kangasluoma, J., Keskinen, H., Kupc, A., Kurtén, T., Kvashin, A. N., Laaksonen, A., Lehtipalo, K., Leiminger, M., Leppä, J., Loukonen, V., Makhmutov, V., Mathot, S., McGrath, M., Nieminen, T., Olenius, T., Onnela, A., Petäjä, T., Riccobono, F., Riipinen, I., Rissanen, M., Rondo, L., Ruuskanen, T., Santos, F., Sarnela, N., Schallhart, S., Schnitzhofer, R., Seinfeld, J., Simon, M., Sipilä, M., Stozhkov, Y., Stratmann, F., Tomé, A., Tröstl, J., Tsagkogeorgas, G., Vaattovaara, P., Viisanen, Y., Virtanen, A., Vrtala, A., Wagner, P., Weingartner, E., Wex, H., Williamson, C.and Wimmer, D., Ye, P., Yli-Juuti, T., Carslaw, K., Kulmala, M., Curtius, J., Baltensperger, U., Worsnop, D. R., Vehkamäki, H., and Kirkby, J.: Molecular understanding of sulphuric acid–amine particle nucleation in the atmosphere, Nature, 502, 2013.

Bianchi, F., Tröstl, J., Junninen, H., Frege, C., Henne, S., Hoyle, C. R., Molteni, U., Herrmann, E., Adamov, A., Bukowiecki, N., Chen, X., Duplissy, J., Gysel, M., Hutterli, M., Kangasluoma, J., Kontkanen, J., Kürten, A., Manninen, H. E., Münch, S., Peräkylä, O., Petäjä, T., Rondo, L., Williamson, C., Weingartner, E., Curtius, J., Worsnop, D. R., Kulmala, M., Dommen, J., and Baltensperger, U.: New particle formation in the free troposphere: A question of chemistry and timing, Science, 352, 1109–1112, doi:10.1126/science.aad5456, http://science.sciencemag.org/content/352/6289/1109, 2016.

Boucher, O., Randall, D., Artaxo, P., Bretherton, C., Feingold, G., Forster, P., Kerminen, V.-M., Kondo, Y., Liao, H., Lohmann, U., Rasch, P., Satheesh, S., Sherwood, S., Stevens, B., and Zhang, X.: Clouds and Aerosols, in: Climate Change 2013: The Physical Science Basis. Contribution of Working Group I to the Fifth Assessment Report of the Intergovernmental Panel on Climate Change, edited by Stocker, T., Qin, D., Plattner, G.-K., Tignor, M., Allen, S., Boschung, J., Nauels, A., Xia, Y., Bex, V., and Midgle, P., Cambridge University Press, Cambridge, United Kingdom and New York, NY, USA, 2013.

Brunelli, N. A., Flagan, R. C., and Giapis, K. P.: Radial Differential Mobility Analyzer for One Nanometer Particle Classification, Aerosol Sci. Tech., 43, 53–59, doi:10.1080/02786820802464302, http://dx.doi.org/10.1080/02786820802464302, 2009.

Buesser, B. and Pratsinis, S. E.: Design of Nanomaterial Synthesis by Aerosol Processes, Annu. Rev. Chem. Biomol., 3, 103–127, doi:10.1146/annurev-chembioeng-062011-080930, https://doi.org/10.1146/annurev-chembioeng-062011-080930, pMID: 22468598, 2012.

Donahue, N. M., Robinson, A. L., Stanier, C. O., and Pandis, S. N.: Coupled Partitioning, Dilution, and Chemical Aging of Semivolatile Organics, Environ. Sci. Technol., 40, 2635–2643, doi:10.1021/es052297c, http://dx.doi.org/10.1021/es052297c, 2006.

Donahue, N. M., Epstein, S. A., Pandis, S. N., and Robinson, A. L.: A two-dimensional volatility basis set: 1. organic-aerosol mixing thermodynamics, Atmos. Chem. Phys., 11, 3303–3318, doi:10.5194/acp-11-3303-2011, http://www.atmos-chem-phys.net/11/3303/2011/, 2011.

Donahue, N. M., Ortega, I. K., Chuang, W., Riipinen, I., Riccobono, F., Schobesberger, S., Dommen, J., Baltensperger, U., Kulmala, M., Worsnop, D. R., and Vehkamaki, H.: How do organic vapors contribute to new-particle formation?, Faraday Discuss., 165, 91–104, doi:10.1039/C3FD00046J, http://dx.doi.org/10.1039/C3FD00046J, 2013.

Duplissy, J., Merikanto, J., Franchin, A., Tsagkogeorgas, G., Kangasluoma, J., Wimmer, D., Vuollekoski, H., Schobesberger, S., Lehtipalo, K., Flagan, R. C., Brus, D., Donahue, N. M., Vehkamäki, H., Almeida, J., Amorim, A., Barmet, P., Bianchi, F., Breitenlechner, M., Dunne, E. M., Guida, R., Henschel, H., Junninen, H., Kirkby, J., Kürten, A., Kupc, A., Määttänen, A., Makhmutov, V., Mathot, S., Nieminen, T., Onnela, A., Praplan, A. P., Riccobono, F., Rondo, L., Steiner, G., Tome, A., Walther, H., Baltensperger, U., Carslaw, K. S., Dommen, J., Hansel, A., Petäjä, T., Sipilä, M., Stratmann, F., Vrtala, A., Wagner, P. E., Worsnop, D. R., Curtius, J., and Kulmala, M.: Effect of ions on sulfuric acid-water binary particle formation: 2. Experimental data and comparison with QC-normalized classical nucleation theory, J. Geophys. Res.-Atmos., 121, 1752–1775, doi:10.1002/2015JD023539, http://dx.doi.org/10.1002/2015JD023539, 2016.

Ehn, M., Thornton, J. A., Kleist, E., Sipila, M., Junninen, H., Pullinen, I., Springer, M., Rubach, F., Tillmann, R., Lee, B., Lopez-Hilfiker, F., Andres, S., Acir, I.-H., Rissanen, M., Jokinen, T., Schobesberger, S., Kangasluoma, J., Kontkanen, J., Nieminen, T., Kurten, T., Nielsen, L. B., Jorgensen, S., Kjaergaard, H. G., Canagaratna, M., Maso, M. D., Berndt, T., Petaja, T., Wahner, A., Kerminen, V.-M., Kulmala, M., Worsnop, D. R., Wildt, J., and Mentel, T. F.: A large source of low-volatility secondary organic aerosol, Nature, 506, 476–479, doi:10.1038/nature13032, http://dx.doi.org/10.1038/nature13032, 2014.

Flagan, R. C., Wang, S. C., Yin, F., Seinfeld, J. H., Reischl, G., Winklmayr, W., and Karch, R.: Electrical mobility measurements of fine-particle formation during chamber studies of atmospheric photochemical reactions, Environ. Sci. Technol., 25, 883–890, doi:10.1021/es00017a009, http://pubs.acs.org/doi/pdf/10.1021/es00017a009, 1991.

Franchin, A., Downard, A., Kangasluoma, J., Nieminen, T., Lehtipalo, K., Steiner, G., Manninen, H. E., Petäjä, T., Flagan, R. C., and Kulmala, M.: A new high-transmission inlet for the Caltech nano-RDMA for size distribution measurements of sub-3 nm ions at ambient concentrations, Atmos. Meas. Tech., 9, 2709–2720, doi:10.5194/amt-9-2709-2016, https://www.atmos-meas-tech.net/9/2709/2016/, 2016.

Frege, C., Ortega, I. K., Rissanen, M. P., Praplan, A. P., Steiner, G., Heinritzi, M., Ahonen, L., Amorim, A., Bernhammer, A.-K., Bianchi, F., Brilke, S., Breitenlechner, M., Dada, L., Dias, A., Duplissy, J., Ehrhart, S., El-Haddad, I., Fischer, L., Fuchs, C., Garmash, O., Gonin, M., Hansel, A., Hoyle, C. R., Jokinen, T., Junninen, H., Kirkby, J., Kürten, A., Lehtipalo, K., Leiminger, M., Mauldin, R. L., Molteni, U., Nichman, L., Petäjä, T., Sarnela, N., Schobesberger, S., Simon, M., Sipilä, M., Stolzenburg, D., Tomé, A., Vogel, A. L., Wagner, A. C., Wagner, R., Xiao, M., Yan, C., Ye, P., Curtius, J., Donahue, N. M., Flagan, R. C., Kulmala, M., Worsnop, D. R., Winkler, P. M., Dommen, J., and

Baltensperger, U.: Influence of temperature on the molecular composition of ions and charged clusters during pure biogenic nucleation, Atmos. Chem. Phys., 18, 65–79, doi:10.5194/acp-18-65-2018, https://www.atmos-chem-phys.net/18/65/2018/, 2018.

Friedrich, R. and Obermeier, A.: Anthropogenic Emissions of Volatile Organic Compounds, in: Reactive Hydrocarbons in the Atmosphere, edited by Hewitt, C. N., pp. 1 – 39, Academic Press, San Diego, doi:https://doi.org/10.1016/B978-012346240-4/50002-3, https://www.sciencedirect.com/science/article/pii/B9780123462404500023, 1999.

Fry, J. L., Draper, D. C., Barsanti, K. C., Smith, J. N., Ortega, J., Winkler, P. M., Lawler, M. J., Brown, S. S., Edwards, P. M., Cohen, R. C., and Lee, L.: Secondary Organic Aerosol Formation and Organic Nitrate Yield from NO3 Oxidation of Biogenic Hydrocarbons, Environ. Sci. Technol., 48, 11 944–11 953, doi:10.1021/es502204x, http://dx.doi.org/10.1021/es502204x, 2014.

Fuchs, N. A.: On the stationary charge distribution on aerosol particles in a bipolar ionic atmosphere, Geofisica pura e applicata, 56, 185–193, doi:10.1007/BF01993343, http://dx.doi.org/10.1007/BF01993343, 1963.

Goldstein, A. H. and Galbally, I. E.: Known and Unexplored Organic Constituents in the Earth's Atmosphere, Environ. Sci. Technol., 41, 1514–1521, doi:10.1021/es072476p, https://doi.org/10.1021/es072476p, 2007.

Gordon, H., Sengupta, K., Rap, A., Duplissy, J., Frege, C., Williamson, C., Heinritzi, M., Simon, M., Yan, C., Almeida, J., Tröstl, J., Nieminen, T., Ortega, I. K., Wagner, R., Dunne, E. M., Adamov, A., Amorim, A., Bernhammer, A.-K., Bianchi, F., Breitenlechner, M., Brilke, S., Chen, X., Craven, J. S., Dias, A., Ehrhart, S., Fischer, L., Flagan, R. C., Franchin, A., Fuchs, C., Guida, R., Hakala, J., Hoyle, C. R., Jokinen, T., Junninen, H., Kangasluoma, J., Kim, J., Kirkby, J., Krapf, M., Kürten, A., Laaksonen, A., Lehtipalo, K., Makhmutov, V., Mathot, S., Molteni, U., Monks, S. A., Onnela, A., Peräkylä, O., Piel, F., Petäjä, T., Praplan, A. P., Pringle, K. J., Richards, N. A. D., Rissanen, M. P., Rondo, L., Sarnela, N., Schobesberger, S., Scott, C. E., Seinfeld, J. H., Sharma, S., Sipilä, M., Steiner, G., Stozhkov, Y., Stratmann, F., Tomé, A., Virtanen, A., Vogel, A. L., Wagner, A. C., Wagner, P. E., Weingartner, E., Wimmer, D., Winkler, P. M., Ye, P., Zhang, X., Hansel, A., Dommen, J., Donahue, N. M., Worsnop, D. R., Baltensperger, U., Kulmala, M., Curtius, J., and Carslaw, K. S.: Reduced anthropogenic aerosol radiative forcing caused by biogenic new particle formation, P. Nat. Acad. Sci. USA, 113, 12 053–12 058, doi:10.1073/pnas.1602360113, http://www.pnas.org/content/113/43/12053.abstract, 2016.

Gordon, H., Kirkby, J., Baltensperger, U., Bianchi, F., Breitenlechner, M., Curtius, J., Dias, A., Dommen, J., Donahue, N. M., Dunne, E. M., Duplissy, J., Ehrhart, S., Flagan, R. C., Frege, C., Fuchs, C., Hansel, A., Hoyle, C. R., Kulmala, M., Kürten, A., Lehtipalo, K., Makhmutov, V., Molteni, U., Rissanen, M. P., Stozkhov, Y., Tröstl, J., Tsagkogeorgas, G., Wagner, R., Williamson, C., Wimmer, D., Winkler, P. M., Yan, C., and Carslaw, K. S.: Causes and importance of new particle formation in the present-day and preindustrial atmospheres, J. Geophys. Res.-Atmos., 122, doi:10.1002/2017JD026844, http://dx.doi.org/10.1002/2017JD026844, 2017JD026844, 2017.

Gormley, P. G. and Kennedy, M.: Diffusion from a Stream Flowing through a Cylindrical Tube, P. Roy. Irish Acad. A, 52, 163–169, 1948.

Guenther, A., Hewitt, C. N., Erickson, D., Fall, R., Geron, C., Graedel, T., Harley, P., Klinger, L., Lerdau, M., Mckay, W. A., Pierce, T., Scholes, B., Steinbrecher, R., Tallamraju, R., Taylor, J., and Zimmerman, P.: A global model of natural volatile organic compound emissions, J. Geophys. Res.-Atmos., 100, 8873–8892, doi:10.1029/94JD02950, http://dx.doi.org/10.1029/94JD02950, 1995.

Hallquist, M., Wenger, J. C., Baltensperger, U., Rudich, Y., Simpson, D., Claeys, M., Dommen, J., Donahue, N. M., George, C., Goldstein, A. H., Hamilton, J. F., Herrmann, H., Hoffmann, T., Iinuma, Y., Jang, M., Jenkin, M. E., Jimenez, J. L., Kiendler-Scharr, A., Maenhaut, W., McFiggans, G., Mentel, T. F., Monod, A., Prévôt, A. S. H., Seinfeld, J. H., Surratt, J. D., Szmigielski, R., and Wildt, J.: The formation, properties and impact of secondary organic aerosol: current and emerging issues, Atmos. Chem. Phys., 9, 5155–5236, doi:10.5194/acp-9-5155-2009, https://www.atmos-chem-phys.net/9/5155/2009/, 2009.

Iida, K., Stolzenburg, M. R., and McMurry, P. H.: Effect of Working Fluid on Sub-2 nm Particle Detection with a Laminar Flow Ultrafine Condensation Particle Counter, Aerosol Sci. Tech., 43, 81–96, doi:10.1080/02786820802488194, http://dx.doi.org/10.1080/02786820802488194, 2009.

IPCC: Climate Change 2013: The Physical Science Basis. Contribution of Working Group I to the Fifth Assessment Report of the Intergovernmental Panel on Climate Change, Cambridge University Press, Cambridge, United Kingdom and New York, NY, USA, 2013.

Jiang, J., Attoui, M., Heim, M., Brunelli, N. A., McMurry, P. H., Kasper, G., Flagan, R. C., Giapis, K., and Mouret, G.: Transfer Functions and Penetrations of Five Differential Mobility Analyzers for Sub-2 nm Particle Classification, Aerosol Sci. Tech., 45, 480–492, doi:10.1080/02786826.2010.546819, http://www.tandfonline.com/doi/abs/10.1080/02786826.2010.546819, 2011a.

Jiang, J., Chen, M., Kuang, C., Attoui, M., and McMurry, P. H.: Electrical Mobility Spectrometer Using a Diethylene Glycol Condensation Particle Counter for Measurement of Aerosol Size Distributions Down to 1 nm, Aerosol Sci. Tech., 45, 510–521, doi:10.1080/02786826.2010.547538, http://www.tandfonline.com/doi/abs/10.1080/02786826.2010.547538, 2011b.

Jimenez, J. L., Canagaratna, M. R., Donahue, N. M., Prevot, A. S. H., Zhang, Q., Kroll, J. H., DeCarlo, P. F., Allan, J. D., Coe, H., Ng, N. L., Aiken, A. C., Docherty, K. S., Ulbrich, I. M., Grieshop, A. P., Robinson, A. L., Duplissy, J., Smith, J. D., Wilson, K. R., Lanz, V. A., Hueglin, C., Sun, Y. L., Tian, J., Laaksonen, A., Raatikainen, T., Rautiainen, J., Vaattovaara, P., Ehn, M., Kulmala, M., Tomlinson, J. M., Collins, D. R., Cubison, M. J., Dunlea, J., Huffman, J. A., Onasch, T. B., Alfarra, M. R., Williams, P. I., Bower, K., Kondo, Y., Schneider, J., Drewnick, F., Borrmann, S., Weimer, S., Demerjian, K., Salcedo, D., Cottrell, L., Griffin, R., Takami, A., Miyoshi, T., Hatakeyama, S., Shimono, A., Sun, J. Y., Zhang, Y. M., Dzepina, K., Kimmel, J. R., Sueper, D., Jayne, J. T., Herndon, S. C., Trimborn, A. M., Williams, L. R., Wood, E. C., Middlebrook, A. M., Kolb, C. E., Baltensperger, U., and Worsnop, D. R.: Evolution of Organic Aerosols in the Atmosphere, Science, 326, 1525–1529, doi:10.1126/science.1180353, http://science.sciencemag.org/content/326/5959/1525, 2009.

Kallinger, P. and Szymanski, W.: Experimental determination of the steady-state charging probabilities and particle size conservation in non-radioactive and radioactive bipolar aerosol chargers in the size range of 5-40 nm, J. Nanopart. Res., 17, 171, doi: 10.1007/s11051-015-2981-x, http://dx.doi.org/10.1007/s11051-015-2981-x, 2015.

Kerminen, V.-M. and Kulmala, M.: Analytical formulae connecting the "real" and the "apparent" nucleation rate and the nuclei number concentration for atmospheric nucleation events, J. Aerosol Sci., 33, 609 – 622, doi:10.1016/S0021-8502(01)00194-X, http://www.sciencedirect.com/science/article/pii/S002185020100194X, 2002.

Köhler, H.: The nucleus in and the growth of hygroscopic droplets, Trans. Faraday Soc., 32, 1152–1161, doi:10.1039/TF9363201152, http://dx.doi.org/10.1039/TF9363201152, 1936.

Kiendler-Scharr, A., Wildt, J., Maso, M. D., Hohaus, T., Kleist, E., Mentel, T. F., Tillmann, R., Uerlings, R., Schurr, U., and Wahner, A.: New particle formation in forests inhibited by isoprene emissions, Nature, 461, 381, doi:10.1038/nature08292, http://dx.doi.org/10.1038/nature08292, 2009.

Kirkby, J., Curtius, J., Almeida, J., Dunne, E., Duplissy, J., Ehrhart, S., Franchin, A., Gagné, S., Ickes, L., Kürten, A., Kupc, A., Metzger, A., Riccobono, F., Rondo, L., Schobesberger, S., Tsagkogeorgas, G., Wimmer, D., Amorim, A., Bianchi, F., Breitenlechner, M., David, A., Dommen, J., Downard, A., Ehn, M., Flagan, R. C., Haider, S., Hansel, A., Hauser, D., Jud, W., Junninen, H., Kreissl, F., Kvashin, A., Laaksonen, A., Lehtipalo, K., Lima, J., Lovejoy, E. R., Makhmutov, V., Mathot, S., Mikkilä, J., Minginette, P., Mogo, S., Nieminen, T., Onnela, A., Pereira, P., Petäjä, T., Schnitzhofer, R., Seinfeld, J. H., Sipilä, M., Stozhkov, Y., Stratmann, F., Tomé, A., Vanhanen, J., Viisanen, Y., Vrtala, A., Wagner, P. E., Walther, H., Weingartner, E., Wex, H., Winkler, P. M., Carslaw, K. S., Worsnop, D. R., Baltensperger, U., and Kulmala, M.: Role of sulphuric acid, ammonia and galactic cosmic rays in atmospheric aerosol nucleation, Nature, 476, 429–433, doi: 10.1038/nature10343, http://dx.doi.org/10.1038/nature10343, 2011.

Kirkby, J., Duplissy, J., Sengupta, K., Frege, C., Gordon, H., Williamson, C., Heinritzi, M., Simon, M., Yan, C., Almeida, J., Tröstl, J., Nieminen, T., Ortega, I. K., Wagner, R., Adamov, A., Amorim, A., Bernhammer, A.-K., Bianchi, F., Breitenlechner, M., Brilke, S., Chen, X., Craven, J., Dias, A., Ehrhart, S., Flagan, R. C., Franchin, A., Fuchs, C., Guida, R., Hakala, J., Hoyle, C. R., Jokinen, T., Junninen, H., Kangasluoma, J., Kim, J., Krapf, M., Kürten, A., Laaksonen, A., Lehtipalo, K., Makhmutov, V., Mathot, S., Molteni, U., Onnela, A., Peräkylä, O., Piel, F., Petäjä, T., Praplan, A. P., Pringle, K., Rap, A., Richards, N. A. D., Riipinen, I., Rissanen, M. P., Rondo, L., Sarnela, N., Schobesberger, S., Scott, C. E., Seinfeld, J. H., Sipilä, M., Steiner, G., Stozhkov, Y., Stratmann, F., Tomé, A., Virtanen, A., Vogel, A. L., Wagner, A. C., Wagner, P. E., Weingartner, E., Wimmer, D., Winkler, P. M., Ye, P., Zhang, X., Hansel, A., Dommen, J., Donahue, N. M., Worsnop, D. R., Baltensperger, U., Kulmala, M., Carslaw, K. S., and Curtius, J.: Ion-induced nucleation of pure biogenic particles, Nature, 533, 521–526, doi:10.1038/nature17953, http://dx.doi.org/10.1038/nature17953, 2016.

Knutson, E. O. and Whitby, K. T.: Aerosol classification by electric mobility: apparatus,

theory, and applications, J. Aerosol Sci., 6, 443–451, doi:10.1016/0021-8502(75)90060-9, http://www.sciencedirect.com/science/article/pii/0021850275900609, 1975.

Kürten, A., Jokinen, T., Simon, M., Sipilä, M., Sarnela, N., Junninen, H., Adamov, A., Almeida, J., Amorim, A., Bianchi, F., Breitenlechner, M., Dommen, J., Donahue, N. M., Duplissy, J., Ehrhart, S., Flagan, R. C., Franchin, A., Hakala, J., Hansel, A., Heinritzi, M., Hutterli, M., Kangasluoma, J., Kirkby, J., Laaksonen, A., Lehtipalo, K., Leiminger, M., Makhmutov, V., Mathot, S., Onnela, A., Petäjä, T., Praplan, A. P., Riccobono, F., Rissanen, M. P., Rondo, L., Schobesberger, S., Seinfeld, J. H., Steiner, G., Tomé, A., Tröstl, J., Winkler, P. M., Williamson, C., Wimmer, D., Ye, P., Baltensperger, U., Carslaw, K. S., Kulmala, M., Worsnop, D. R., and Curtius, J.: Neutral molecular cluster formation of sulfuric acid–dimethylamine observed in real time under atmospheric conditions, P. Nat. Acad. Sci. USA, 111, 15 019–15 024, doi:10.1073/pnas.1404853111, http://www.pnas.org/content/111/42/15019.abstract, 2014.

Kuang, C., Chen, M., Zhao, J., Smith, J., McMurry, P. H., and Wang, J.: Size and time-resolved growth rate measurements of 1 to 5 nm freshly formed atmospheric nuclei, Atmos. Chem. Phys., 12, 3573–3589, doi:10.5194/acp-12-3573-2012, http://www.atmos-chem-phys.net/12/3573/2012/, 2012.

Kulmala, M., Kerminen, V.-M., Anttila, T., Laaksonen, A., and O'Dowd, C. D.: Organic aerosol formation via sulphate cluster activation, J. Geophys. Res.-Atmos., 109, doi:10.1029/2003JD003961, http://dx.doi.org/10.1029/2003JD003961, d04205, 2004a.

Kulmala, M., Laakso, L., Lehtinen, K. E. J., Riipinen, I., Dal Maso, M., Anttila, T., Kerminen, V.-M., Hõrrak, U., Vana, M., and Tammet, H.: Initial steps of aerosol growth, Atmos. Chem. Phys., 4, 2553–2560, doi:10.5194/acp-4-2553-2004, https://www.atmos-chem-phys.net/4/2553/2004/, 2004b.

Kulmala, M., Vehkamäki, H., Petäjä, T., Dal Maso, M., Lauri, A., Kerminen, V.-M., Birmili, W., and McMurry, P. H.: Formation and growth rates of ultrafine atmospheric particles: a review of observations, J. Aerosol Sci., 35, 143–176, doi:10.1016/j.jaerosci.2003.10.003, http://www.sciencedirect.com/science/article/pii/S0021850203004373, 2004c.

Kulmala, M., Petäjä, T., Nieminen, T., Sipilä, M., Manninen, H. E., Lehtipalo, K., Dal Maso, M., Aalto, P. P., Junninen, H., Paasonen, P., Riipinen, I., Lehtinen, K. E. J., Laaksonen, A., and Kerminen, V.-M.: Measurement of the nucleation of atmospheric aerosol particles, Nat. Protoc., 7, 1651–1667, doi:10.1038/nprot.2012.091, http://dx.doi.org/10.1038/nprot.2012.091, 2012.

Kulmala, M., Kontkanen, J., Junninen, H., Lehtipalo, K., Manninen, H. E., Nieminen, T., Petäjä, T., Sipilä, M., M., Schobesberger, S., Rantala, P., Franchin, A., Jokinen, T., Järvinen, E., Äijälä, M., Kangasluoma, J., Hakala, J., Aalto, P. P., Paasonen, P., Mikkilä, J., Vanhanen, J., Aalto, J., Hakola, H., Makkonen, U., Ruuskanen, T., Mauldin, R. L., Duplissy, J., Vehkamäki, H., Bäck, J., Kortelainen, A., Riipinen, I., Kurtén, T., Johnston, M. V., Smith, J. N., Ehn, M., Mentel, T. F., Lehtinen, K. E. J., Laaksonen, A., Kerminen, V.-M., and Worsnop, D. R.: Direct Observations of Atmospheric Aerosol Nucleation, Science, 339, 943–946, doi:10.1126/science.1227385, http://science.sciencemag.org/content/339/6122/943, 2013.

Kurtén, T., Tiusanen, K., Roldin, P., Rissanen, M., Luy, J.-N., Boy, M., Ehn, M., and Donahue, N.: Alpha-Pinene Autoxidation Products May Not Have Extremely Low Saturation Vapor Pressures Despite High O:C Ratios, J. Phys. Chem. A, 120, 2569–2582, doi:10.1021/acs.jpca.6b02196, http://dx.doi.org/10.1021/acs.jpca.6b02196, pMID: 27049168, 2016.

Lee, S.-H., Young, L.-H., Benson, D. R., Suni, T., Kulmala, M., Junninen, H., Campos, T. L., Rogers, D. C., and Jensen, J.: Observations of nighttime new particle formation in the troposphere, J. Geophys. Res.-Atmos., 113, doi:10.1029/2007JD009351, https://agupubs.onlinelibrary.wiley.com/doi/abs/10.1029/2007JD009351, 2008.

Lee, S.-H., Uin, J., Guenther, A. B., Gouw, J. A., Yu, F., Nadykto, A. B., Herb, J., Ng, N. L., Koss, A., Brune, W. H., Baumann, K., Kanawade, V. P., Keutsch, F. N., Nenes, A., Olsen, K., Goldstein, A., and Ouyang, Q.: Isoprene suppression of new particle formation: Potential mechanisms and implications, J. Geophys. Res.-Atmos., 121, 14,621–14,635, doi:10.1002/2016JD024844, https://agupubs.onlinelibrary.wiley.com/doi/abs/10.1002/2016JD024844, 2016.

Lehtinen, K. E., Maso, M. D., Kulmala, M., and Kerminen, V.-M.: Estimating nucleation rates from apparent particle formation rates and vice versa: Revised formulation of the Kerminen–Kulmala equation, J. Aerosol Sci., 38, 988 – 994, doi:http://dx.doi.org/10.1016/j.jaerosci.2007.06.009, http://www.sciencedirect.com/science/article/pii/S0021850207001024, 2007.

Lehtinen, K. E. J., Rannik, U., Petäjä, T., Kulmala, M., and Hari, P.: Nucleation rate and vapor concentration estimations using a least squares aerosol dynamics method, J. Geophys. Res.-Atmos., 109, doi:10.1029/2004JD004893, http://dx.doi.org/10.1029/2004JD004893, 2004.

Lehtipalo, K., Leppä, J., Kontkanen, J., Kangasluoma, J., Franchin, A., Wimmer, D., Schobesberger, S., Junninen, H., Petäjä, T., Sipilä, M., Mikkilä, J., Vanhanen, J., Worsnop, D. R., and Kulmala, M.: Methods for determining particle size distribution and growth rates between 1 and 3 nm using the Particle Size Magnifier, Boreal Environ. Res., 19, 215–236, 2014.

Lehtipalo, K., Rondo, L., Kontkanen, J., Schobesberger, S., Jokinen, T., Sarnela, N., Kürten, A., Ehrhart, S., Franchin, A., Nieminen, T., Riccobono, F., Sipilä, M., Yli-Juuti, T., Duplissy, J., Adamov, A., Ahlm, L., Almeida, J., Amorim, A., Bianchi, F., Breitenlechner, M., Dommen, J., Downard, A. J., Dunne, E. M., Flagan, R. C., Guida, R., Hakala, J., Hansel, A., Jud, W., Kangasluoma, J., Kerminen, V.-M., Keskinen, H., Kim, J., Kirkby, J., Kupc, A., Kupiainen-Määttä, O., Laaksonen, A., Lawler, M. J., Leiminger, M., Mathot, S., Olenius, T., Ortega, I. K., Onnela, A., Petäjä, T., Praplan, A., Rissanen, M. P., Ruuskanen, T., Santos, F. D., Schallhart, S., Schnitzhofer, R., Simon, M., Smith, J. N., Tröstl, J., Tsagkogeorgas, G., Tomé, A., Vaattovaara, P., Vehkamäki, H., Vrtala, A. E., Wagner, P. E., Williamson, C., Wimmer, D., Winkler, P. M., Virtanen, A., Donahue, N. M., Carslaw, K. S., Baltensperger, U., Riipinen, I., Curtius, J., Worsnop, D. R., and Kulmala, M.: The effect of acid–base clustering and ions on the growth of atmospheric nano-particles, Nat. Commun., 7, 11 594, doi:10.1038/ncomms11594, http://dx.doi.org/10.1038/ncomms11594, 2016.

Leighton, P.: Photochemistry of Air Pollution, Academic Press, New York, 1961.

Lelieveld, J., Evans, J. S., Fnais, M., Giannadaki, D., and Pozzer, A.: The contribution of outdoor air pollution sources to premature mortality on a global scale, Nature, 525, 367, doi:10.1038/nature15371, http://dx.doi.org/10.1038/nature15371, 2015.

Li, C. and McMurry, P. H.: Errors in Nanoparticle Growth Rates Inferred from Measurements in Chemically Reacting Aerosol Systems, Atmos. Chem. Phys. Discuss., 2018, 1–21, doi:10.5194/acp-2018-260, https://www.atmos-chem-phys-discuss.net/acp-2018-260/, 2018.

Martin, S. T., Andreae, M. O., Artax, P., Baumgardner, D., Chen, Q., Goldstein, A. H., Guenther, A., Heald, C. L., Mayol-Bracero, O. L., McMurry, P. H., Pauliquevis, T., Pöschl, U., Prather, K. A., Roberts, G. C., Saleska, S. R., Silva, D. M. A., Spracklen, D. V., Swietlicki, E., and Trebs, I.: Sources and properties of Amazonian aerosol particles, Rev. Geophys., 48, doi:10.1029/2008RG000280, https://agupubs.onlinelibrary.wiley.com/doi/abs/10.1029/2008RG000280, 2010.

McMurry, P., Rader, D., and Stith, J.: Studies of aerosol formation in power plant plumes— I. Growth laws for secondary aerosols in power plant plumes: Implications for chemical conversion mechanisms, Atmos. Environ., 15, 2315 – 2327, doi:https://doi.org/10.1016/0004-6981(81)90262-6, http://www.sciencedirect.com/science/article/pii/0004698181902626, plumes and Visibility Measurements and Model Components, 1981.

Metzger, A., Verheggen, B., Dommen, J., Duplissy, J., Prevot, A. S. H., Weingartner, E., Riipinen, I., Kulmala, M., Spracklen, D. V., Carslaw, K. S., and Baltensperger, U.: Evidence for the role of organics in aerosol particle formation under atmospheric conditions, P. Nat. Acad. Sci. USA, 107, 6646–6651, doi:10.1073/pnas.0911330107, http://www.pnas.org/content/107/15/6646, 2010.

Mäkelä, J. M., Aalto, P., Jokinen, V., Pohja, T., Nissinen, A., Palmroth, S., Markkanen, T., Seitsonen, K., Lihavainen, H., and Kulmala, M.: Observations of ultrafine aerosol particle formation and growth in boreal forest, Geophys. Res. Lett., 24, 1219–1222, doi:10.1029/97GL00920, https://agupubs.onlinelibrary.wiley.com/doi/abs/10.1029/97GL00920, 1997.

Ng, N. L., Chhabra, P. S., Chan, A. W. H., Surratt, J. D., Kroll, J. H., Kwan, A. J., McCabe, D. C., Wennberg, P. O., Sorooshian, A., Murphy, S. M., Dalleska, N. F., Flagan, R. C., and Seinfeld, J. H.: Effect of NO_x level on secondary organic aerosol (SOA) formation from the photooxidation of terpenes, Atmos. Chem. Phys., 7, 5159–5174, doi:10.5194/acp-7-5159-2007, https://www.atmos-chem-phys.net/7/5159/2007/, 2007.

Paasonen, P., Peltola, M., Kontkanen, J., Junninen, H., Kerminen, V.-M., and Kulmala, M.: Comprehensive analysis of particle growth rates from nucleation mode to cloud condensation nuclei in Boreal forest, Atmos. Chem. Phys. Discuss., 2018, 1–28, doi:10.5194/acp-2018-169, https://www.atmos-chem-phys-discuss.net/acp-2018-169/, 2018.

Pedata, P., Stoeger, T., Zimmermann, R., Peters, A., Oberdörster, G., and D'Anna, A.: "Are we forgetting the smallest, sub 10 nm combustion generated particles?",

Part. Fibre Toxicol., 12, 34, doi:10.1186/s12989-015-0107-3, https://doi.org/10.1186/s12989-015-0107-3, 2015.

Pinterich, T., Vrtala, A., Kaltak, M., Kangasluoma, J., Lehtipalo, K., Petäjä, T., Winkler, P. M., Kulmala, M., and Wagner, P. E.: The versatile size analyzing nuclei counter (vSANC), Aerosol Sci.Tech., 50, 947–958, doi:10.1080/02786826.2016.1210783, http://dx.doi.org/10.1080/02786826.2016.1210783, 2016.

Praske, E., Otkjær, R. V., Crounse, J. D., Hethcox, J. C., Stoltz, B. M., Kjaergaard, H. G., and Wennberg, P. O.: Atmospheric autoxidation is increasingly important in urban and suburban North America, P. Nat. Acad. Sci. USA, 115, 64–69, doi:10.1073/pnas.1715540115, http://www.pnas.org/content/115/1/64, 2018.

Presto, A. A., Huff Hartz, K. E., and Donahue, N. M.: Secondary Organic Aerosol Production from Terpene Ozonolysis. 2. Effect of NOx Concentration, Environ. Sci. Technol., 39, 7046–7054, doi:10.1021/es050400s, https://doi.org/10.1021/es050400s, pMID: 16201628, 2005.

Reischl, G.: Measurement of Ambient Aerosols by the Differential Mobility Analyzer Method: Concepts and Realization Criteria for the Size Range Between 2 and 500 nm, Aerosol Sci. Tech., 14, 5–24, doi:10.1080/02786829108959467, http://dx.doi.org/10.1080/02786829108959467, 1991.

Riccobono, F., Schobesberger, S., Scott, C. E., Dommen, J., Ortega, I. K., Rondo, L., Almeida, J., Amorim, A., Bianchi, F., Breitenlechner, M., David, A., Downard, A., Dunne, E. M., Duplissy, J., Ehrhart, S., Flagan, R. C., Franchin, A., Hansel, A., Junninen, H., Kajos, M., Keskinen, H., Kupc, A., Kürten, A., Kvashin, A. N., Laaksonen, A., Lehtipalo, K., Makhmutov, V., Mathot, S., Nieminen, T., Onnela, A., Petäjä, T., Praplan, A. P., Santos, F. D., Schallhart, S., Seinfeld, J. H., Sipilä, M., Spracklen, D. V., Stozhkov, Y., Stratmann, F., Tomé, A., Tsagkogeorgas, G., Vaattovaara, P., Viisanen, Y., Vrtala, A., Wagner, P. E., Weingartner, E., Wex, H., Wimmer, D., Carslaw, K. S., Curtius, J., Donahue, N. M., Kirkby, J., Kulmala, M., Worsnop, D. R., and Baltensperger, U.: Oxidation Products of Biogenic Emissions Contribute to Nucleation of Atmospheric Particles, Science, 344, 717–721, doi:10.1126/science.1243527, http://science.sciencemag.org/content/344/6185/717, 2014.

Riipinen, I., Yli-Juuti, T., Pierce, J. R., Petäjä, T., Worsnop, D. R., Kulmala, M., and Donahue, N. M.: The contribution of organics to atmospheric nanoparticle growth, Nat. Geosci., 5, 453–458, doi:10.1038/ngeo1499, http://dx.doi.org/10.1038/ngeo1499, 2012.

Rissanen, M. P., Kurtén, T., Sipilä, M., Thornton, J. A., Kangasluoma, J., Sarnela, N., Junninen, H., Jørgensen, S., Schallhart, S., Kajos, M. K., Taipale, R., Springer, M., Mentel, T. F., Ruuskanen, T., Petäjä, T., Worsnop, D. R., Kjaergaard, H. G., and Ehn, M.: The Formation of Highly Oxidized Multifunctional Products in the Ozonolysis of Cyclohexene, J. Am. Chem. Soc., 136, 15 596–15 606, doi:10.1021/ja507146s, https://doi.org/10.1021/ja507146s, pMID: 25283472, 2014.

Rose, C., Zha, Q., Dada, L., Yan, C., Lehtipalo, K., Junninen, H., Mazon, S. B., Jokinen, T., Sarnela, N., Sipilä, M., Petäjä, T., Kerminen, V.-M., Bianchi, F., and Kulmala, M.: Observations of biogenic ion-induced cluster formation in the atmosphere, Science Advances, 4,

doi:10.1126/sciadv.aar5218, http://advances.sciencemag.org/content/4/4/eaar5218, 2018.

Schnitzhofer, R., Metzger, A., Breitenlechner, M., Jud, W., Heinritzi, M., De Menezes, L.-P., Duplissy, J., Guida, R., Haider, S., Kirkby, J., Mathot, S., Minginette, P., Onnela, A., Walther, H., Wasem, A., Hansel, A., and the CLOUD Team: Characterisation of organic contaminants in the CLOUD chamber at CERN, Atmos. Meas. Tech., 7, 2159–2168, doi:10.5194/amt-7-2159-2014, http://www.atmos-meas-tech.net/7/2159/2014/, 2014.

Seinfeld, J. and Pandis, S.: Atmospheric Chemistry and Physics: From Air Pollution to Climate Change, 2nd edition, Wiley, second edition edn., 2006.

Shiraiwa, M., Ueda, K., Pozzer, A., Lammel, G., Kampf, C. J., Fushimi, A., Enami, S., Arangio, A. M., Fröhlich-Nowoisky, J., Fujitani, Y., Furuyama, A., Lakey, P. S. J., Lelieveld, J., Lucas, K., Morino, Y., Pöschl, U., Takahama, S., Takami, A., Tong, H., Weber, B., Yoshino, A., and Sato, K.: Aerosol Health Effects from Molecular to Global Scales, Environ. Sci. Technol., 51, 13 545–13 567, doi:10.1021/acs.est.7b04417, https://doi.org/10.1021/acs.est.7b04417, pMID: 29111690, 2017.

Sipilä, M., Berndt, T., Petäjä, T., Brus, D., Vanhanen, J., Stratmann, F., Patokoski, J., Mauldin, R. L., Hyvärinen, A.-P., Lihavainen, H., and Kulmala, M.: The Role of Sulfuric Acid in Atmospheric Nucleation, Science, 327, 1243–1246, doi:10.1126/science.1180315, http://science.sciencemag.org/content/327/5970/1243, 2010.

Steiner, G.: High Resolution Mobility Spectrometry Of Molecular Ions and Their Effect On The Charging Probabilities Of Airborne Particles Under Bipolar Diffusion Charging Conditions, phdthesis, University of Vienna, http://ubdata.univie.ac.at/AC08824686, 2011.

Steiner, G., Attoui, M., Wimmer, D., and Reischl, G. P.: A Medium Flow, High-Resolution Vienna DMA Running in Recirculating Mode, Aerosol Sci. Tech., 44, 308–315, doi:10.1080/02786821003636763, http://dx.doi.org/10.1080/02786821003636763, 2010.

Stolzenburg, M. R.: An Ultrafine Aerosol Size Distribution System, Ph.D. thesis, University of Minnesota, 1988.

Stolzenburg, M. R. and McMurry, P. H.: An Ultrafine Aerosol Condensation Nucleus Counter, Aerosol Sci. Tech., 14, 48–65, doi:10.1080/02786829108959470, http://dx.doi.org/10.1080/02786829108959470, 1991.

Stolzenburg, M. R. and McMurry, P. H.: Equations Governing Single and Tandem DMA Configurations and a New Lognormal Approximation to the Transfer Function, Aerosol Sci. Tech., 42, 421–432, doi:10.1080/02786820802157823, http://dx.doi.org/10.1080/02786820802157823, 2008.

Svensmark, H., Enghoff, M., Shaviv, N., and Svensmark, J.: Increased ionization supports growth of aerosols into cloud condensation nuclei, Nat. Commun., 8, 2199, doi:10.1038/s41467-017-02082-2, https://doi.org/10.1038/s41467-017-02082-2, 2017.

Swihart, M. T.: Vapor-phase synthesis of nanoparticles, Curr. Opin. Colloid. In., 8, 127 – 133, doi:https://doi.org/10.1016/S1359-0294(03)00007-4, http://www.sciencedirect.com/science/article/pii/S1359029403000074, 2003.

Tröstl, J., Tritscher, T., Bischof, O. F., Horn, H.-G., Krinke, T., Baltensperger, U., and Gysel, M.: Fast and precise measurement in the sub-20 nm size range using a Scanning Mobility Particle Sizer, J. Aerosol Sci., 87, 75–87, doi:10.1016/j.jaerosci.2015.04.001, http://www.sciencedirect.com/science/article/pii/S0021850215000543, 2015.

Tröstl, J., Chuang, W. K., Gordon, H., Heinritzi, M., Yan, C., Molteni, U., Ahlm, L., Frege, C., Bianchi, F., Wagner, R., Simon, M., Lehtipalo, K., Williamson, C., Craven, J. S., Duplissy, J., Adamov, A., Almeida, J., Bernhammer, A.-K., Breitenlechner, M., Brilke, S., Dias, A., Ehrhart, S., Flagan, R. C., Franchin, A., Fuchs, C., Guida, R., Gysel, M., Hansel, A., Hoyle, C. R., Jokinen, T., Junninen, H., Kangasluoma, J., Keskinen, H., Kim, J., Krapf, M., Kürten, A., Laaksonen, A., Lawler, M., Leiminger, M., Mathot, S., Möhler, O., Nieminen, T., Onnela, A., Petäjä, T., Piel, F. M., Miettinen, P., Rissanen, M. P., Rondo, L., Sarnela, N., Schobesberger, S., Sengupta, K., Sipilä, M., Smith, J. N., Steiner, G., Tomè, A., Virtanen, A., Wagner, A. C., Weingartner, E., Wimmer, D., Winkler, P. M., Ye, P., Carslaw, K. S., Curtius, J., Dommen, J., Kirkby, J., Kulmala, M., Riipinen, I., Worsnop, D. R., Donahue, N. M., and Baltensperger, U.: The role of low-volatility organic compounds in initial particle growth in the atmosphere, Nature, 533, 527–531, doi:10.1038/nature18271, http://dx.doi.org/10.1038/nature18271, 2016.

Twomey, S. A., Piepgrass, M., and Wolfe, T. L.: An assessment of the impact of pollution on global cloud albedo, Tellus B, 36, 356–366, doi:10.3402/tellusb.v36i5.14916, http://dx.doi.org/10.3402/tellusb.v36i5.14916, 1984.

Vanhanen, J., Mikkilä, J., Lehtipalo, K., Sipilä, M., Manninen, H. E., Siivola, E., Petäjä, T., and Kulmala, M.: Particle Size Magnifier for Nano-CN Detection, Aerosol Sci. Tech., 45, 533–542, doi:10.1080/02786826.2010.547889, http://www.tandfonline.com/doi/abs/10.1080/02786826.2010.547889, 2011.

Verheggen, B. and Mozurkewich, M.: An inverse modeling procedure to determine particle growth and nucleation rates from measured aerosol size distributions, Atmos. Chem. Phys., 6, 2927–2942, doi:10.5194/acp-6-2927-2006, http://www.atmos-chem-phys.net/6/2927/2006/, 2006.

Wang, S. and Flagan, R.: Scanning Electrical Mobility Spectrometer, Aerosol Sci. Tech., 13, 230–240, doi:10.1080/02786829008959441, http://dx.doi.org/10.1080/02786829008959441, 1990.

Warneke, C., McKeen, S. A., de Gouw, J. A., Goldan, P. D., Kuster, W. C., Holloway, J. S., Williams, E. J., Lerner, B. M., Parrish, D. D., Trainer, M., Fehsenfeld, F. C., Kato, S., Atlas, E. L., Baker, A., and Blake, D. R.: Determination of urban volatile organic compound emission ratios and comparison with an emissions database, J. Geophys. Res.-Atmos., 112, doi:10.1029/2006JD007930, https://agupubs.onlinelibrary.wiley.com/doi/abs/10.1029/2006JD007930, 2007.

Went, F.: Blue Hazes in the Atmosphere, Nature, 187, 641, http://dx.doi.org/10.1038/187641a0, 1960.

Wildt, J., Mentel, T. F., Kiendler-Scharr, A., Hoffmann, T., Andres, S., Ehn, M., Kleist, E., Müsgen, P., Rohrer, F., Rudich, Y., Springer, M., Tillmann, R., and Wahner, A.: Suppression of new particle formation from monoterpene oxidation by NO_x, Atmos. Chem. Phys.,

14, 2789–2804, doi:10.5194/acp-14-2789-2014, https://www.atmos-chem-phys.net/14/2789/2014/, 2014.

Wimmer, D., Lehtipalo, K., Franchin, A., Kangasluoma, J., Kreissl, F., Kürten, A., Kupc, A., Metzger, A., Mikkilä, J., Petäjä, T., Riccobono, F., Vanhanen, J., Kulmala, M., and Curtius, J.: Performance of diethylene glycol-based particle counters in the sub-3 nm size range, Atmos. Meas. Tech., 6, 1793–1804, doi:10.5194/amt-6-1793-2013, http://www.atmos-meas-tech.net/6/1793/2013/, 2013.

Winkler, P. M., Steiner, G., Vrtala, A., Vehkamäki, H., Noppel, M., Lehtinen, K. E. J., Reischl, G. P., Wagner, P. E., and Kulmala, M.: Heterogeneous Nucleation Experiments Bridging the Scale from Molecular Ion Clusters to Nanoparticles, Science, 319, 1374–1377, doi:10.1126/science.1149034, http://science.sciencemag.org/content/319/5868/1374, 2008.

Winkler, P. M., Ortega, J., Karl, T., Cappellin, L., Friedli, H. R., Barsanti, K., McMurry, P. H., and Smith, J. N.: Identification of the biogenic compounds responsible for size-dependent nanoparticle growth, Geophys. Res. Lett., 39, doi:10.1029/2012GL053253, http://dx.doi.org/10.1029/2012GL053253, l20815, 2012.

Winkler, P. M., Ortega, J., Karl, T., McMurry, P. H., and Smith, J. N.: A fast-scanning DMA train for precision quantification of early nanoparticle growth, AIP Conference Proceedings, 1527, 165–168, doi:10.1063/1.4803229, http://aip.scitation.org/doi/abs/10.1063/1.4803229, 2013.

Yu, H., Ortega, J., Smith, J. N., Guenther, A. B., Kanawade, V. P., You, Y., Liu, Y., Hosman, K., Karl, T., Seco, R., Geron, C., Pallardy, S. G., Gu, L., Mikkilä, J., and Lee, S.-H.: New Particle Formation and Growth in an Isoprene-Dominated Ozark Forest: From Sub-5 nm to CCN-Active Sizes, Aerosol Sci. Technol., 48, 1285–1298, doi:10.1080/02786826.2014.984801, https://doi.org/10.1080/02786826.2014.984801, 2014.

Chapter 2

A DMA-train for precision measurement of sub-10 nm aerosol dynamics

This chapter was published by D.Stolzenburg, G.Steiner and P.M.Winkler in *Atmospheric Measurement Techniques*, 2017, 10, 1639-1651

Abstract. Measurements of aerosol dynamics in the sub-10 nm size range are crucially important for quantifying the impact of new particle formation onto the global budget of cloud condensation nuclei. Here we present the development and characterization of a differential mobility analyzer train (DMA-train), operating six DMAs in parallel for high-time-resolution particle-size-distribution measurements below 10 nm. The DMAs are operated at six different but fixed voltages and hence sizes, together with six state-of-the-art condensation particle counters (CPCs). Two Airmodus A10 particle size magnifiers (PSM) are used for channels below 2.5 nm while sizes above 2.5 nm are detected by TSI 3776 butanol-based or TSI 3788 water-based CPCs. We report the transfer functions and characteristics of six identical Grimm S-DMAs as well as the calibration of a butanol-based TSI model 3776 CPC, a water-based TSI model 3788 CPC and an Airmodus A10 PSM. We find cutoff diameters similar to those reported in the literature. The performance of the DMA-train is tested with a rapidly changing aerosol of a tungsten oxide particle generator during warmup. Additionally we report a measurement of new particle formation taken during a nucleation event in the CLOUD chamber experiment at CERN. We find that the DMA-train is able to bridge the gap between currently well-established measurement techniques in the cluster–particle transition regime, providing high time resolution and accurate size information of neutral and charged particles even at atmospheric particle concentrations.

2.1 Introduction

Atmospheric aerosols still constitute the largest uncertainties in climate models through their ambiguous effects on the climate system (Carslaw et al., 2013). In addition to the direct effects of scattering and absorption on incoming solar radiation, higher aerosol number concentrations can increase the albedo of clouds (Ramanathan et al., 2001) and their lifetime (Albrecht, 1989), leading to significant indirect radiative forcing.

New particle formation from gaseous precursor vapors is frequently observed in the atmosphere (Kulmala et al., 2004). Model simulations show that up to 50 % of the global budget of cloud condensation nuclei (CCN) might originate from new particle formation (Spracklen et al., 2008; Merikanto et al., 2009). However, these numbers strongly depend on the dynamics of the newly formed aerosol (Weber et al., 1997). Nucleation occurring at the critical cluster size between 1 and 2 nm is often followed by growth (Venzac et al., 2008; Riccobono et al., 2012) up to sizes of around 50–100 nm, where the particles can act as CCN (Lihavainen et al., 2003; Kerminen et al., 2005; Kuang et al., 2009). In competition with the growth by condensation is the probability of the newly formed particles to coagulate with bigger pre-existing aerosol. The driving mechanisms responsible for the aerosol growth are hence of big interest in current research (Ehn et al., 2014; Tröstl et al., 2016) but still require detailed studies of aerosol dynamics especially in the crucial sub-10 nm size range where coagulation losses are the highest.

Electrical mobility analysis is widely used in order to infer aerosol size information (e.g., Flagan, 1998). To this end differential mobility analyzers (DMAs) are commonly used (Knutson and Whitby, 1975). Recent improvements of DMAs made accurate particle sizing down to cluster sizes around 1 nm possible (Brunelli et al., 2009; Steiner et al., 2010; Jiang et al., 2011a; Fernández de la Mora and Kozlowski, 2013). Size-distribution information is then obtained by applying either a stepwise varying (Winklmayr et al., 1991) or continuously ramped voltage (Wang and Flagan, 1990) to a DMA and measuring the downstream aerosol concentration.

In a great number of applications condensation particle counters (CPCs) are used for aerosol detection at single particle counting level. The generation of the supersaturated vapor as well as the used working fluid itself varies for different CPC types. All of them, either expansion type with various working fluids (Winkler et al., 2008; Pinterich et al., 2016), mixing type with diethylene glycol (DEG) (Vanhanen et al., 2011) or the most common laminar-flow type with butanol (Stolzenburg and McMurry, 1991), water (Hering et al., 2005; Kupc et al., 2013) or DEG (Wimmer et al., 2013), have reached particle detection at sizes as low as $\sim$1–2 nm, i.e., close to the critical cluster size.

Particle-size-distribution measurements in the sub-10 nm range done by combining a DMA with a state-of-the-art CPC are reported for example by Jiang et al. (2011b) and Kuang et al. (2012a). Another approach was used by Lehtipalo et al. (2014) with a particle size magnifier (PSM) operated in scanning mode. There, the instrument's lower size-detection

cutoff is varied in order to infer size-distribution information of sub-3 nm particles based on pre-(post-)calibration with the electrical mobility technique.

Wang and Flagan (1990) already pointed out the need for sufficient time resolution, which depends on the actual aerosol system under investigation. In atmospheric and especially in chamber studies, particle growth rates between 10 and 100 $\mathrm{nm\,h^{-1}}$ can be observed and hence it might be favorable to achieve scan times as low as 10 s, e.g., in order to resolve the rise of the particle concentration in distinct size channels for precision quantification of nanoparticle growth rates (e.g., Dal Maso et al., 2002; Svenningsson et al., 2008). However, while several fast mobility scanning techniques are capable of measuring size distributions with a time resolution in the order of seconds (Wang et al., 2002; Olfert et al., 2008; Tröstl et al., 2015), the scanning cutoff method is still limited in that respect.

In contrast, poor counting statistics oftentimes prevents quantitative analysis of nanoparticle dynamics due to high diffusional sampling losses and low particle charging probabilities for sub-10 nm particles (Wiedensohler, 1988). Therefore a (fast) scanning over different sizes with a DMA is usually not suitable to exploit the full counting statistics at one size. The scanning cutoff technique, however, does not rely on particle charging and not directly on mobility analysis. But it needs very careful and broad calibration measurements, as the cutoff strongly depends on the (unknown) aerosol chemical composition (Kangasluoma et al., 2014). Accordingly, the sizing information might have high systematic uncertainties.

Here we present the development of a newly designed DMA-train setup featuring six DMAs operated in parallel at six distinct but fixed voltages in combination with six state-of-the-art CPCs to obtain fast and precise size-distribution measurements. The idea was first brought forward by Flagan et al. (1991), who showed that especially rapidly changing aerosol can be tracked with this method. This approach has been used recently to study nanoparticle formation in the NCAR aerosol chamber (Winkler et al., 2013). We now refined it for the application in the cluster–particle transition regime in the sub-10 nm range.

2.2 The DMA-train setup

The DMA-train was planned and constructed as a fixed mounted setup providing all necessary power supplies, flow pumps and controls, including a unified data acquisition system. Furthermore, the inlets to all six channels are kept identical in length and shape to assure equal flow patterns. Figure 1 shows the main design features. In order to keep the instrument as compact as possible a symmetrical two-layer design was chosen, with two identical layers consisting of three DMAs. The inlet is located in between the layers with a common flow for all channels at a flow rate of 11 liter per minute ($\mathrm{l\,min^{-1}}$) maintained by the sample flow of the six CPCs used. In order to reduce diffusional sampling losses, core sampling provides an additional $9\,\mathrm{l\,min^{-1}}$ make-up flow in the main sampling line controlled by a critical orifice.

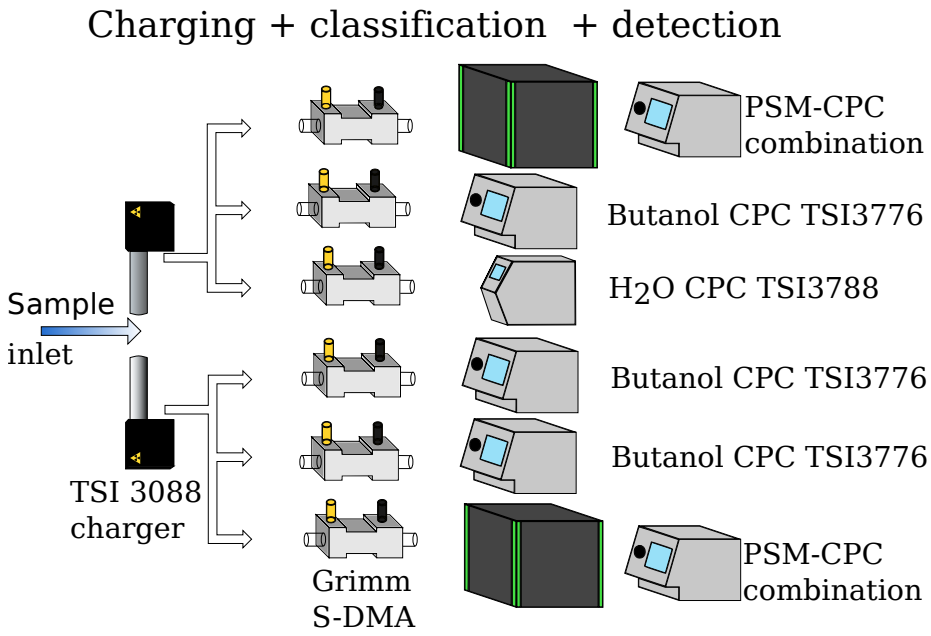

Figure 1: Scheme of the DMA-train setup. The design follows a classical SMPS design in each channel. After bringing the aerosol to a well-defined charging state, it is split and classified in six identical Grimm S-DMAs and subsequently detected in condensation particle counters. For optimal detection of sub-2.5 nm particles a combination of a Airmodus A10 particle size magnifier (PSM) with a butanol-based TSI 3776 CPC is used. Particles equal or larger than 2.5 nm are detected by either TSI model 3776 or TSI model 3788 CPCs to allow for maximum flexibility with respect to particle activation properties. The whole setup measures $80 \times 135 \times 140$ cm, excluding the flow supply unit.

The flow is then split up at a 0.5 inch union T into two transport flows for the two layers with 5.5 l min^{-1} each. The subsequent design follows the classical approach of a differential/scanning mobility particle sizer (DMPS/SMPS) (Wang and Flagan, 1990). Each stream is passing through a soft X-ray bipolar Advanced Aerosol Neutralizer (AAN) model 3088 from TSI Inc. Kallinger and Szymanski (2015) found that the AAN reproduces well the predicted charging probability for negative particles predicted by Wiedensohler (1988) for flow rates up to 5 l min^{-1} and down to sizes as small as 5 nm. Moreover, Kallinger et al. (2012) reported that the size distribution of the negative aerosol charger ions does not exceed mobility diameters of 1.6 nm for flow rates even as high as 16 l min^{-1}. This basically sets the lower sizing limit of the DMA-train.

After the aerosol has reached a defined charging state at the exit of the AAN, the flow is split up three-fold in a custom-built three-way flow splitter. Thereby the DMAs receive two 1.5 and one 2.5 l min^{-1} streams on each layer of the DMA-train, respectively. The tubing between flow splitting and the DMA entrance is kept as short as possible.

Afterwards the aerosol is classified in six stainless steel Grimm S-DMAs, which follow the "Vienna-type" design (Reischl, 1991). Some characterization results can be found in Jiang

et al. (2011a). The closed-loop sheath-air flow of the DMAs is regulated by temperature controlled critical orifices connected to a single high throughput vacuum pump offering eight separate pumping chambers. The critical orifices of six pumping chambers provide a flow of $15\,\mathrm{l\,min^{-1}}$ while two closed loop circuits can be connected to two additional pumping chambers with $10\,\mathrm{l\,min^{-1}}$ critical orifices. Accordingly, we can operate four DMAs at a sheath flow rate of $15\,\mathrm{l\,min^{-1}}$ and two DMAs at $25\,\mathrm{l\,min^{-1}}$. The common flow unit designed by Grimm Aerosol Technik GmbH & Co. KG is furthermore equipped with sensors for temperature, pressure and relative humidity for the simultaneous monitoring of all eight pumping circuits. The sheath air is dried by six 2.26 l volume silica-gel dryers and filtered in active charcoal filters from chemical impurities and in HEPA filters from remaining aerosol particles. The six identical HV modules from Grimm Aerosol are able to provide positive voltages up to +6 kV to the central electrode of the S-DMA.

Afterwards the classification the detection is performed with six modern CPCs. Three channels are equipped with a TSI 3776 butanol-based ultrafine CPC with a cutoff diameter as low as $\sim 2.5\,\mathrm{nm}$ (Stolzenburg and McMurry, 1991; Hermann et al., 2007). For one channel a TSI 3788 water-based ultrafine CPC is used (Kupc et al., 2013). The last two channels are operated with a combination of an Airmodus A10 PSM together with a TSI 3776 butanol CPC for the activation of sub-2 nm aerosol (Vanhanen et al., 2011). An additional hyco-membrane pump provides the necessary operating vacuum for the Airmodus PSMs. The usage of particle counters with different working fluids introduces a possible feature to the DMA-train: sampling aerosol of the same size in two or three channels with different CPC types can therefore provide information on aerosol composition (Kulmala et al., 2007), as the activation efficiencies of the CPCs depend on the chemical composition of the seed particle (Kangasluoma et al., 2014).

The particle counters are directly connected to the Grimm S-DMA outlet, such that further transport losses are minimized. As the PSMs require a higher sample flow of $2.5\,\mathrm{l\,min^{-1}}$, the two DMAs upstream are operated at a sheath-air flow rate of $25\,\mathrm{l\,min^{-1}}$ to keep the DMA resolution similar to the channels with only $1.5\,\mathrm{l\,min^{-1}}$ sample flow and $15\,\mathrm{l\,min^{-1}}$ sheath flow.

The complete setup is controlled by a National Instruments LabView (Version 2014F) data acquisition software. It provides the control of the HV modules, the readout of the CPCs and important sheath-air parameters, such that stable operating conditions of all devices can be verified during operation.

2.3 Laboratory characterization

2.3.1 DMA calibration

All six DMAs used in the DMA-train are of identical type and purchased as Grimm S-DMAs from Grimm Aerosol Technik GmbH & Co. KG. To test their performance we used a high-resolution DMA (UDMA) operated at sheath-air flow rates of $\sim 450\,\mathrm{l\,min^{-1}}$, in detail described by Steiner et al. (2010).

For the calibration setup the UDMA classified nanoparticles from either a tungsten oxide generator or an electrospray source to create well-defined mobility standards. The calibration setup is shown in Figure 2 and follows the classical tandem-DMA configuration, which is described in detail for example by Stolzenburg and McMurry (2008). A brief description of the procedure is given in Sect. 2.3.1.

Calibration of the UDMA

Due to the high sheath flow rates in the UDMA, which are not measurable during operation, a calibration of the voltage–mobility relation is necessary. This was done by using clusters of positively electrosprayed tetraheptylammonium bromide (THABr) (Ude and Fernández de la Mora, 2005). The spectrum recorded by a Faraday cup electrometer (FCE) downstream of the UDMA shows clear peaks at electrical mobilities of 0.97, 0.65 and $0.53\,\mathrm{cm\,V^{-2}\,s^{-1}}$, each associated with clusters of the form $\mathrm{A}^+\,(\mathrm{AB})_n$ of the electrosprayed salt.

A fit to the well-identified monomer allows to calibrate the voltage–mobility relation of the

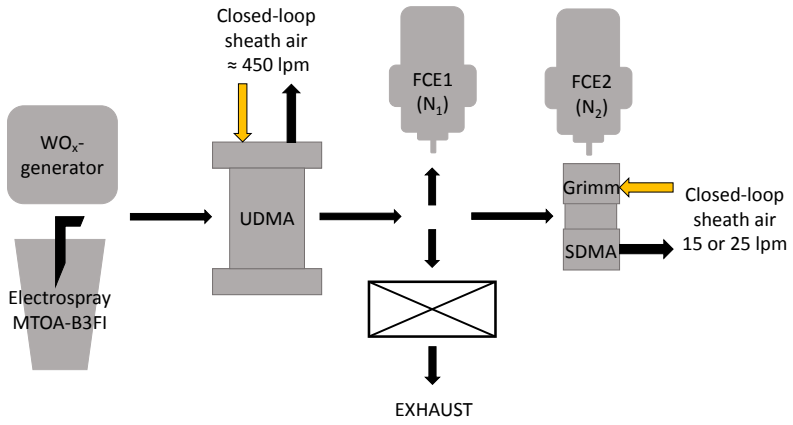

Figure 2: Calibration setup for the retrieval of the Grimm S-DMA transfer function and the gauging of the voltage–mobility relation. After aerosol generation particles are classified in a high-resolution DMA (UDMA) and then led into the Grimm S-DMA. Two Faraday cup electrometers (FCEs) are measuring the concentration upstream and downstream of the Grimm S-DMA.

UDMA shown in Equation (**??**) (Stolzenburg and McMurry, 2008),

$$Z = \frac{1}{V} \cdot \frac{\ln\left(R_i/R_o\right) \cdot Q_{\mathrm{sh}}}{2 \cdot \pi \cdot L}, \tag{1}$$

by identifying the peak voltage of the monomer with a lognormal fit and then calculating the corresponding sheath-air flow rate Q_{sh}. All other parameters of Equation (**??**), the outer and inner electrode radii R_o and R_i as well as the length of the classification region L are geometric factors which correspond to the construction values.

Calibration of the voltage–mobility relation for six Grimm S-DMAs

In order to calibrate the Grimm S-DMA voltage–mobility relation a tungsten oxide nanoparticle generator from Grimm Aerosol was connected to the UDMA. The calibration of the UDMA done with the positively charged THABr monomer is assumed to be valid as long as the flow conditions are not changed. Tungsten oxide particles of mean diameters 2.0, 2.5, 3.0, 4.0 and 5.0 nm were classified. The Grimm S-DMA was connected downstream of the UDMA as was the reference FCE (FCE1) measuring the concentration N_1 immediately after the UDMA. As shown in Figure 2 a second electrometer (FCE2) measured the concentration N_2 downstream of the Grimm S-DMA while the DMA voltage was scanned in logarithmic equidistant intervals. For each classified particle size, a reference measurement was performed with the Grimm S-DMA removed and the FCE2 directly connected to the UDMA, thereby correcting the relative concentration ratio N_2/N_1 for nonidealities in flow splitting, possible different diffusional losses or electrometer offsets. A least-squares lognormal fit is used again for identifying the peak voltage. The fitted mean voltages for all selected mobilities and DMAs are plotted in Figure 3.

To extend the calibration size range below 2 nm, a negative mobility standard from the ionic liquid methyltrioctylammonium bis(trifluoromethylsulfonyl)imide (short MTOA-B3FI) was used due to the positive high voltages applied to the Grimm S-DMAs. A typical recorded spectrum downstream of the UDMA while electrospraying MTOA-B3FI is illustrated in Figure 4. The peaks of the MTOA-B3FI monomer (A^-) and dimer ($A^-(AB)_1$) are well separated at mobilities of 1.80 and 0.77 $\mathrm{cm\,V^{-2}\,s^{-1}}$, respectively. These mobilities correspond to mobility diameters of 1.06 nm for the monomer and 1.62 nm for the dimer. The trimer ($A^-(AB)_2$) and the tetramer ($A^-(AB)_3$) can be identified in Figure 4 as well. However, they were not used for calibration measurements as they overlap with the background from multiply charged bigger clusters.

In a second set of experiments the same procedure as for the size-classified tungsten oxide particles was repeated with the UDMA classifying monomer or dimer of the MTOA-B3FI and therefore providing a calibration measurement using a strictly monodisperse aerosol. The peak mobilities retrieved from the lognormal fit are added to Figure 3. For all calibration runs, the

sheath-air flow rate Q_{sh} is measured with a Gilian Gilibrator-2 low-pressure drop bubble flow meter from Sensidyne, LP. For the individual sheath-air circuits of the flow unit the sheath-air flow rate is very stable over time due to the temperature control of the critical orifices. Therefore, the classification length L is used as the free parameter of the least-squares fit to the data in Figure 3, according to the inverse of Equation (**??**). For the other parameters, the design values of $R_i = 0.013$ and $R_o = 0.020\,\mathrm{m}$ are used.
The results summarized in Table 1 are all slightly higher than the specified classification length by the manufacturer of 13 nm but are still in reasonable agreement. Moreover, all six DMAs seem to be identical within the uncertainties of the measurements.

Retrieval of the transfer function of the Grimm S-DMA

Additionally, the well-defined mobility of the classified MTOA-B3FI monomer and dimer allows us to infer information about the DMA transfer function and its penetration characteristics. According to Jiang et al. (2011a), the response downstream of the test DMA can be written as

$$\frac{N_2}{N_1} = \eta_{\mathrm{dma}}\left(d_{\mathrm{p}}\right) \cdot \Omega\left(V, Z\left(d_{\mathrm{p}}\right)\right), \tag{2}$$

because only the monodisperse MTOA monomer or dimer particles were sent into the Grimm S-DMAs.

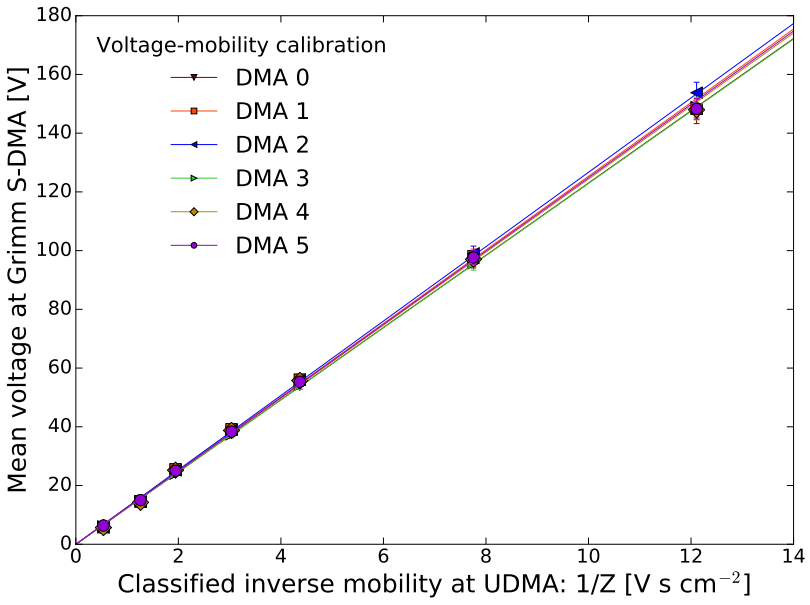

Figure 3: Calibration of the voltage–mobility relation for all six Grimm S-DMAs used. The mean voltage of least-squares fits to the relative FCE response downstream of the six Grimm S-DMAs is plotted against the classified inverse mobility of the UDMA. The linear least-squares fit has only one free parameter: the effective classification length of the Grimm S-DMAs.

DMA serial number	L (mm)	Classified mobility standard	f_σ (−)	η_{pene} (−)	$\mathrm{L}_{\mathrm{pene}}$ (m)
0	(13.5 ± 0.2)	MTOA-B3FI monomer	(1.22 ± 0.03)	(0.049 ± 0.001)	(1.59 ± 0.14)
		MTOA-B3FI dimer	(1.18 ± 0.01)	(0.178 ± 0.001)	
1	(13.3 ± 0.2)	MTOA-B3FI monomer	(1.12 ± 0.01)	(0.041 ± 0.001)	(1.73 ± 0.14)
		MTOA-B3FI dimer	(1.14 ± 0.01)	(0.158 ± 0.017)	
2	(13.1 ± 0.2)	MTOA-B3FI monomer	(1.15 ± 0.03)	(0.037 ± 0.003)	(1.79 ± 0.14)
		MTOA-B3FI dimer	(1.11 ± 0.02)	(0.150 ± 0.004)	
3	(13.5 ± 0.2)	MTOA-B3FI monomer	(1.05 ± 0.01)	(0.038 ± 0.003)	(1.59 ± 0.07)
		MTOA-B3FI dimer	(1.02 ± 0.01)	(0.182 ± 0.005)	
4	(13.4 ± 0.2)	MTOA-B3FI monomer	(1.20 ± 0.02)	(0.053 ± 0.002)	(1.45 ± 0.09)
		MTOA-B3FI dimer	(1.09 ± 0.02)	(0.205 ± 0.032)	
5	(13.3 ± 0.2)	MTOA-B3FI monomer	(1.01 ± 0.02)	(0.049 ± 0.002)	(1.50 ± 0.09)
		MTOA-B3FI dimer	(1.04 ± 0.01)	(0.195 ± 0.014)	

Table 1: Voltage–mobility calibration and transfer function characteristics of all Grimm S-DMAs used. L is the calibrated classification length of the DMA, f_σ accounts for additional transfer function broadening and L_{pene} represents an effective diffusional length for inlet and outlet losses of the DMA.

Here N_2 and N_1 correspond to the FCE concentration readings downstream and upstream of the test DMA, η_{dma} represents a loss parameter for losses in the inlet and outlet regions of the Grimm S-DMAs and $\Omega\left(V, Z\left(d_{\mathrm{p}}\right)\right)$ is the DMA transfer function. The notation we use here and details about DMA transfer functions can be found in Stolzenburg and McMurry (2008). In general the transfer function yields the fraction of particles with mobility Z passing the DMA operated at a fixed voltage V. However, in the setup presented in Figure 2 the DMA voltage was not fixed to one value and monodisperse particles of different mobilities were sent into the DMA. In the measurements presented here, the size of the particles was fixed with the UDMA and the voltage of the tested DMA was scanned. Hence, the measured response cannot be directly projected back into the transfer function as the transfer function of the DMA becomes a function of the DMA voltage due to the significant diffusional broadening below 2 nm (Stolzenburg, 1988; Jiang et al., 2011a).

The transfer function properties are therefore retrieved by a least-squares fit of Equation (1) to the measured ratio N_2/N_1 by assuming Stolzenburg's diffusive transfer function (Stolzenburg and McMurry, 2008), including a voltage dependence of the transfer function width $\sigma_{\mathrm{theo}}\left(V\right)$. As suggested by Jiang et al. (2011a), two fit parameters are used: the penetration loss parameter η_{dma}, which just reduces the transfer function height due to losses in the inlet and outlet region of the DMA, and an additional broadening parameter for the transfer function f_σ. This is a multiplicative factor to the theoretical width σ_{theo}, which accounts for instrument nonidealities like electrode misalignment and distortions of the flow pattern.

A representative measurement of the MTOA-B3FI monomer and dimer is shown in Figure 5 and the results for all DMAs are reported in Table 1. Generally we find an additional broadening, f_σ, between 1.01 and 1.22 for all DMAs and both mobility standards. The measure-

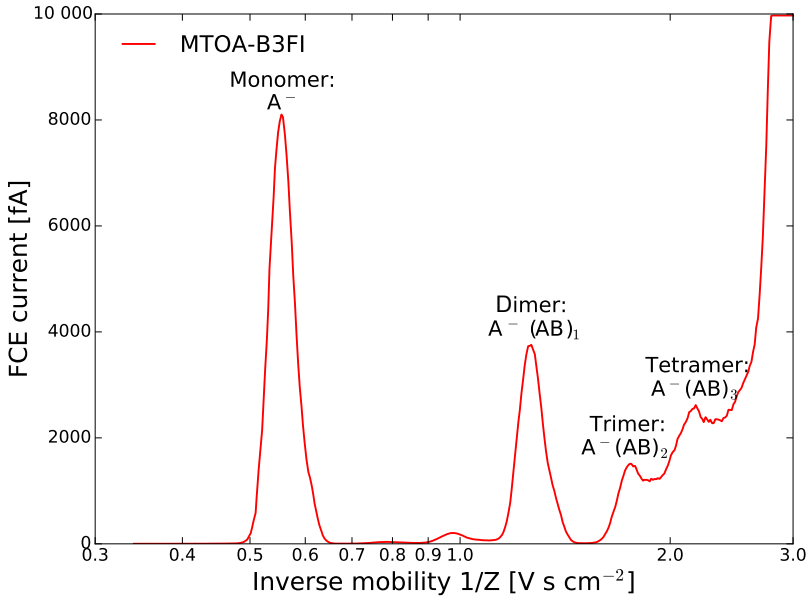

Figure 4: Typical MTOA-B3FI spectrum as recorded by a FCE downstream of the UDMA. The peaks of the monomer and dimer are clearly visible and well separated. The trimer and tetramer can be identified as well but are overlapped by a background of multiply charged larger clusters.

ments of the dimer and monomer for the individual DMAs are very consistent for all DMAs, confirming the deviation from the Stolzenburg theory. Moreover, it supports the results of the voltage–mobility calibration: all six DMAs perform similarly but differ slightly from the manufacturer values.

The penetrated fractions η_{dma} of the inlet and outlet regions of the Grimm S-DMA derived from the monomer and dimer measurement can be described by considering them as diffusional losses. As suggested by various authors (Reineking and Porstendörfer, 1986; Karlsson and Martinsson, 2003; Jiang et al., 2011a), the modified Gormley and Kennedy equation (Gormley and Kennedy, 1948; Cheng, 2011),

$$\begin{aligned} \eta_{\mathrm{pene}}(d_{\mathrm{p}}) &= 0.819e^{-3.66\mu} + 0.0975e^{-22.3\mu} \\ &\quad + 0.0325e^{-57.0\mu} + 0.0154e^{-107.6\mu} \\ &\quad \text{for } \mu > 0.02 \\ \eta_{\mathrm{pene}}(d_{\mathrm{p}}) &= 1.0 - 2.56\mu^{2/3} + 1.2\mu + 0.1767\mu^{4/3} \\ &\quad \text{for } \mu \leq 0.02, \end{aligned} \tag{3}$$

reproduces well the diameter dependence of such losses with $\mu = \frac{D\,L_{\mathrm{tube}}\pi}{Q}$ and D the particle diffusivity, Q the volume flow and L_{tube} the length of the tube (all in SI units).

As the flow through the entrance and exit region of the DMA Q_{ae} is known, it is appropriate to

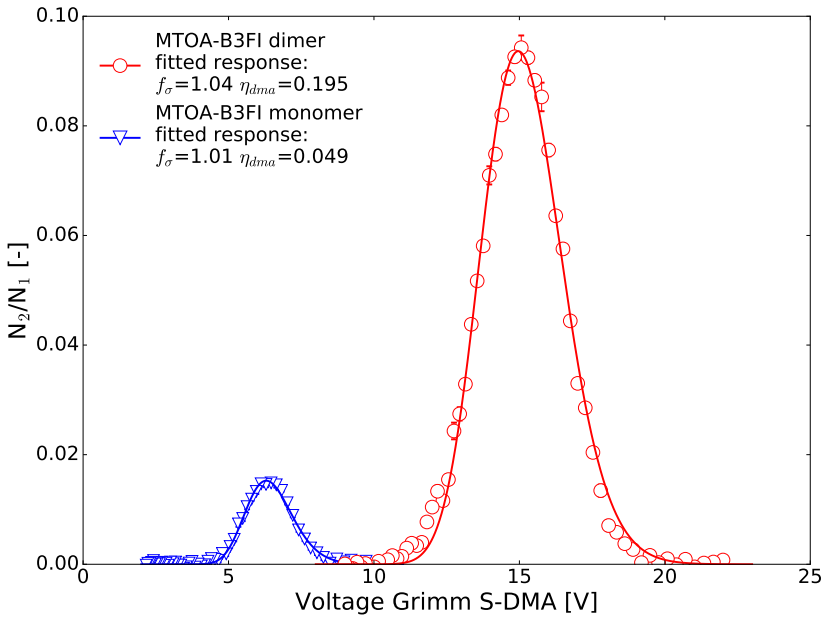

Figure 5: Voltage scan of a Grimm S-DMA while the UDMA is classifying either MTOA-B3FI monomer or dimer. The measurements are fitted by the expected response based on Stolzenburg's diffusive transfer function and two additional free parameters: a penetration efficiency η_{dma} and an additional width parameter f_σ. Reported results correspond to DMA serial number 5.

report an effective diffusional length L_{pene}. It can be used in Equation (2) in order to extrapolate the DMA penetration to different sizes by setting $\eta_{\mathrm{dma}} = \eta_{\mathrm{pene}}\,(Q = Q_{\mathrm{ae}}, L_{\mathrm{tube}} = L_{\mathrm{pene}})$; i.e., the DMA losses are represented by diffusional losses through a straight tube.
As summarized in Table 1, we find effective penetration lengths close to 1.6 m for all DMAs. The very good transmission characteristics of the Grimm S-DMA are underlined by the fact that the highly diffusive MTOA-B3FI monomer can still be detected downstream of the DMA and the transmission of the MTOA-B3FI dimer (1.62 nm) is even as high as 8–10 %.
The measurements of the transfer function therefore confirm that the Grimm S-DMA is well suited even for measurements in the sub-2 nm regime, where resolution and transmission normally drop significantly.

2.3.2 Characterization of the CPCs

The performance of the three different types of CPCs used in the DMA-train was tested with the calibration setup shown in Figure 6. Silver nanoparticles were generated in a tube furnace and then sent into one of the six calibrated Grimm S-DMAs for size classification. The DMA was operated at 1.5 l min^{-1} aerosol flow, controlled by the throughput of the silver furnace and at 15 l min^{-1} sheath-air flow. An additional make-up flow was supplied after the DMA exit to account for the flow rates of the detectors. The total flow was then split up at a four-way flow splitter similar to TSI model 3708 with two exits closed.

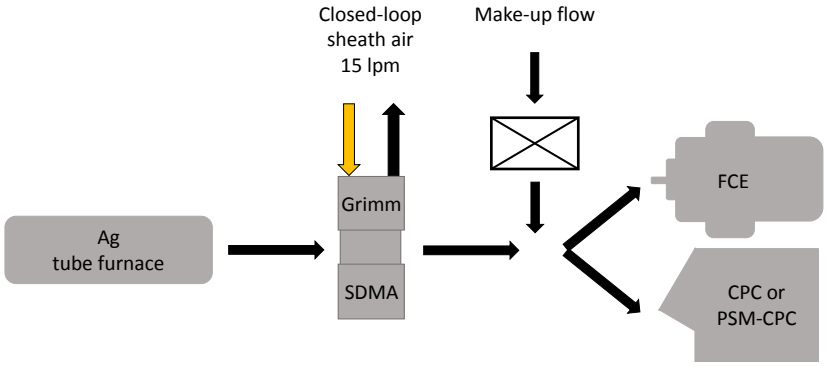

Figure 6: Calibration setup for the determination of the counting efficiency curve of the three types of condensation particle counters used. Silver aerosol particles are generated in a tube furnace and classified in one of the Grimm S-DMAs. Afterwards the flow is split into the CPC under investigation and a reference FCE.

The counting efficiency is calculated as the ratio of the measured concentrations of the particle counter under investigation and the reference FCE. The results of three typical efficiency measurements are shown in Figure **??**. In order to represent the functional form of the activation curve best, we use the Gompertz function (Gompertz, 1825; Winsor, 1932),

$$\eta_{\mathrm{cpc}}\left(d_{\mathrm{p}}\right) = A \cdot e^{\left(-e^{\left(-k\cdot\left(d_{\mathrm{p}}-d_{\mathrm{p0}}\right)\right)}\right)}, \tag{4}$$

and fit it within a least-squares routine to the observed data. Free parameters are the plateau height A, d_{p0} and k.

From the fit a $d_{\mathrm{p50}} \simeq \frac{0.3665}{k} + d_{\mathrm{p0}}$ cutoff diameter is inferred, where the counting efficiency reaches 50 % of the plateau height A. The temperature settings we used are reported in Table 2 together with the determined cutoff diameters. We find that the DEG-based PSM together with the TSI 3776 for detection achieve the lowest cutoff, well below 2 nm. Rather moderate temperature settings with a $\Delta T = 75\,^{\circ}\mathrm{C}$ between saturator and growth tube and the usage of different test aerosol compared to the manufacturer explain why the PSM does not reach the instrument's cutoff specifications as low as 1 nm. However, these settings allow for an operation with very low background from homogeneous nucleation occurring inside the PSM, guaranteeing a high signal-to-noise ratio and still sufficient activation above 1.7 nm.

The two TSI particle counters, types 3776 and 3788, reach the cutoff values specified by the manufacturer. In contrast to the PSM, where the turbulent mixing prevents the activation of all particles (Vanhanen et al., 2011), the two counters clearly reach 100 % counting efficiency above $\sim$4 nm (see Figure **??**). Thus the parameter A of Equation (**??**) is set to 1 in the reported fits. The water-based TSI 3788 CPC shows the higher d_{p50} cutoff due to the unfavorable conditions for nucleation of water on silver. Much better activation properties for the water-based 3788 are reported when sampling sodium chloride particles (Kangasluoma et al.,

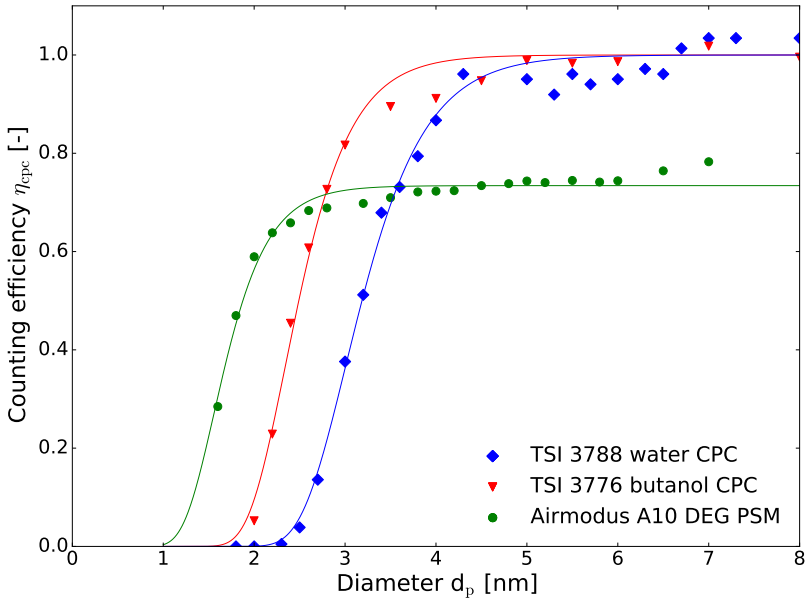

Figure 7: Characterization of the counting efficiency with silver nanoparticles for the three types of condensation particle counters used. Green represents the DEG-based Airmodus PSM A10, red the butanol-based TSI 3776 and blue the water-based TSI 3788.

2014).

CPC type	Settings	d_{p50} (nm)
TSI 3776	$T_{sat} = 39\,°C$, $T_{con} = 10\,°C$	(2.5 ± 0.1)
TSI 3788	$T_{con} = 15\,°C$, $T_{gt} = 75\,°C$	(3.2 ± 0.1)
Airmodus A 10	$T_{sat} = 80\,°C$, $T_{gt} = 5\,°C$, $T_{in} = 40\,°C$	(1.7 ± 0.2)

Table 2: Results of the cutoff diameter measurements with Ag seed particles for the three types of used particle counters and the corresponding settings for the measurements. For the TSI instruments we used the standard manufacturer settings.

The composition dependence of the d_{p50} cutoff values of the various CPCs should be kept in mind, when investigating undefined aerosol. In this first approach we can, however, already verify that the particle counters we used operate as specified by the manufacturers. Moreover, most channels in the DMA-train can be set such that the classified particle diameter lies in the plateau region, well above the cutoff. Thus, inferred particle number concentrations should not depend too much on the pattern of the size-dependent counting efficiency curves. For sub-2.5 nm channels, as well as for the potential feature of comparing activation properties of the examined aerosol with different counters, more detailed calibration measurements would be beneficial because in these cases the classified diameters will be close to the cutoff values.

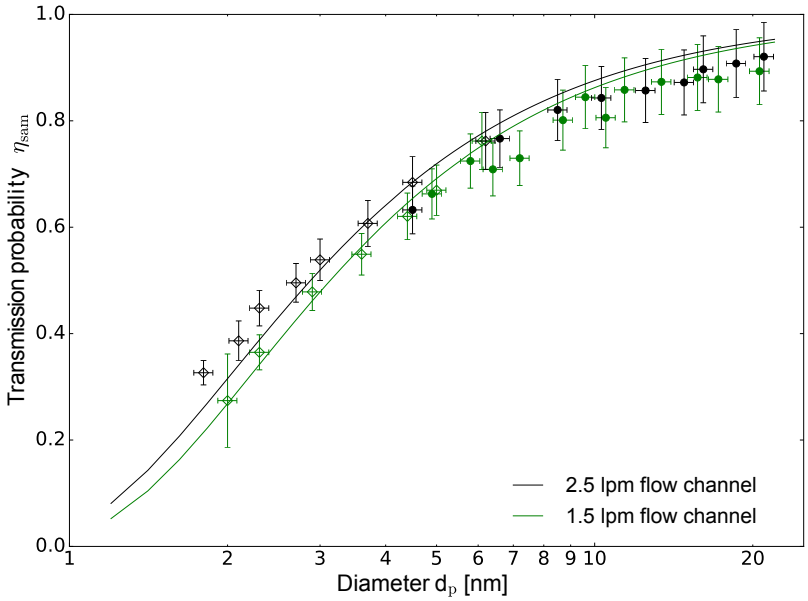

Figure 8: Transmission calibration of the DMA-train. The green points show a measurement for the channels operated with a $1.5\,\mathrm{L\,min^{-1}}$ final sample flow (the CPC channels) and the black points for the channels with a $2.5\,\mathrm{l\,min^{-1}}$ final sample flow (the PSM channels). Open symbols are measured with tungsten oxide aerosol particles and filled symbols are measured with silver aerosol particles. The solid lines represent a threefold Gormley and Kennedy equation fit with two free parameters.

2.3.3 Instrument transmission

With the DMA-train fully set up, a calibration of the instrument's sampling efficiency was done. Nanoparticles were produced either in the silver tube furnace ($>5\,\mathrm{nm}$) or in the tungsten oxide particle generator ($<5\,\mathrm{nm}$) and subsequently classified with one of the Grimm S-DMAs removed from the rack. The aerosol flow from the generators was diluted in order to achieve the $20\,\mathrm{l\,min^{-1}}$ sample flow required by the DMA-train. Directly at the main inlet of the DMA-train, an additional core-sampling probe was used for measuring the inlet concentration with an FCE. With all instruments in operation inside the DMA-train a second FCE was installed at the position of the removed DMA used for aerosol size classification and hence measuring the concentration occurring at the DMA inlet in standard operation. In order to account for FCE measurement offsets, a cross-calibration of the two FCEs was done over the full possible FCE-current measurement range. The concentration ratios of the two FCEs corrected for the offset are shown in Figure **??**.

We present two different types of transmission measurements, in order to account for the different sample flow rates. As expected, the channels with a higher sample flow rate of $2.5\,\mathrm{l\,min^{-1}}$ achieve a higher transmission compared to the channels with a $1.5\,\mathrm{l\,min^{-1}}$ sample flow rate, which can be seen in Figure **??**. Among channels with the same volume flow rates no significant differences were found.

Final sample flow	L_{eff1} (m)	L_{eff2} (m)
$2.5\,\text{l}\,\text{min}^{-1}$	(1.6 ± 0.1)	(0.75 ± 0.04)
$1.5\,\text{l}\,\text{min}^{-1}$	(1.6 ± 0.1)	(0.88 ± 0.04)

Table 3: Results of the transmission calibration of the DMA-train. The two free fit parameters for the threefold Gormley and Kennedy Equation (**??**) are reported for the two sample flow rates.

The functional dependence of the sampling losses is fitted with a threefold Gormley and Kennedy equation. This accounts for the fact that the flow within the sampling procedure is reduced in two steps. After the $20\,\text{l}\,\text{min}^{-1}$ main sample flow, the chargers are passed with a flow of $5.5\,\text{l}\,\text{min}^{-1}$, followed by the final sampling flow after the three-fold flow splitter. The fitted function is reported in Equation (**??**):

$$\begin{aligned}\eta_{\text{sam}} = \eta_{\text{pene}} &\left(Q = 20\,\text{L}\,\text{min}^{-1},\, L = 0.85\,\text{m}\right) \\ &\cdot \eta_{\text{pene}} \left(Q = 5.5\,\text{L}\,\text{min}^{-1},\, L = L_{\text{eff1}}\right) \\ &\cdot \eta_{\text{pene}} \left(Q = 1.5/2.5\,\text{L}\,\text{min}^{-1}, L = L_{\text{eff2}}\right).\end{aligned} \tag{5}$$

As the main sampling line upstream of the core-sampling probe is just a straight tube of 0.85 m length, this part of the fitting function is fixed. When the long sampling probe is not used, it can just be neglected. The fit is therefore left with two free parameters, L_{eff1} and L_{eff2}, summarized in Table 3.

2.4 Size-distribution measurements

The fully characterized DMA-train can be used to infer size-distribution information of sub-10 nm aerosol. For data inversion it is preferable to combine the DMA-train data with other instruments covering the size range above 10 nm. This reduces possible systematic errors from multiply charged bigger particles.

Raw data are inverted according to the procedure of Stolzenburg and McMurry (2008). We use

$$\left.\frac{\text{d}N}{\text{d}\ln d_{\text{p}}}\right|_{d_{\text{p}}^*} = \frac{N \cdot a^*}{\beta \cdot f_{\text{c}}(d_{\text{p}}^*) \cdot \eta_{\text{sam}}(d_{\text{p}}^*) \cdot \eta_{\text{cpc}}(d_{\text{p}}^*) \cdot \eta_{\text{dma}}(d_{\text{p}}^*)}, \tag{6}$$

assuming symmetrical flow conditions at the DMAs (Jiang et al., 2011b). Here N represents the raw counts of the particle counter used in the DMA-train channel (PSM channels are corrected for their internal instrument dilution) operated at classifying diameter d_{p}^*. β is the ratio of aerosol to sheath flow used in the DMAs, f_{c} corresponds to the Fuchs charging efficiency according to Wiedensohler's approximation (Wiedensohler, 1988) and $a^* = (-\text{d}\ln Z/\text{d}\ln d_{\text{p}})|_{d_{\text{p}}^*}$. The different diameter-dependent efficiencies η are already explained in detail in the previous

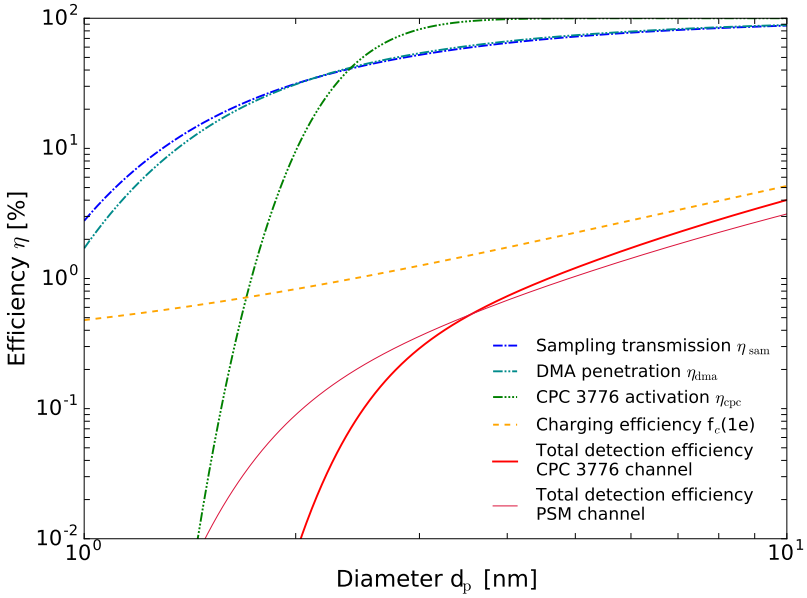

Figure 9: Efficiency in % of the several individual contributions and the total value are plotted against the set diameter at the corresponding DMA. This is similar for all three channels using a TSI 3776 CPC as particle counter downstream of the DMA. For the two channels using a Airmodus A10 PSM, the total efficiency is shown as well.

section and summarized in Figure **??**. It shows the individual contributions and the total detection efficiency of the instrument for a channel with a TSI 3776 butanol CPC. For comparison the total detection efficiency of a channel using an Airmodus A10 PSM is illustrated as well.

If the channels of the DMA-train are then set to different diameters, an approximation of the measured aerosol size distribution can be obtained by linearly interpolating between the six channels. It should be kept in mind that if the spacing between the different size channels gets bigger, local structures of the size distribution cannot be resolved any longer. However, for a wide range of measurement applications the inferred size-distribution information will be precise enough to infer the aerosol dynamics in the range below 10 nm. This is demonstrated in the following with two example measurements.

2.4.1 Fast-changing aerosol of a tungsten oxide generator at warmup

In order to test the performance of the DMA-train with an aerosol which undergoes very rapid changes, we connected the tungsten oxide generator directly to the inlet of the DMA-train. For comparison, a standard DMPS system (Winklmayr et al., 1991) was connected to the core-sampling probe at the entrance of the DMA-train. The DMPS system uses a FCE as particle detector, which sampled the aerosol at a flow rate of $2.9\,\mathrm{l\,min^{-1}}$. The tungsten oxide generator was then switched on and we followed the evolution of the size distribution with

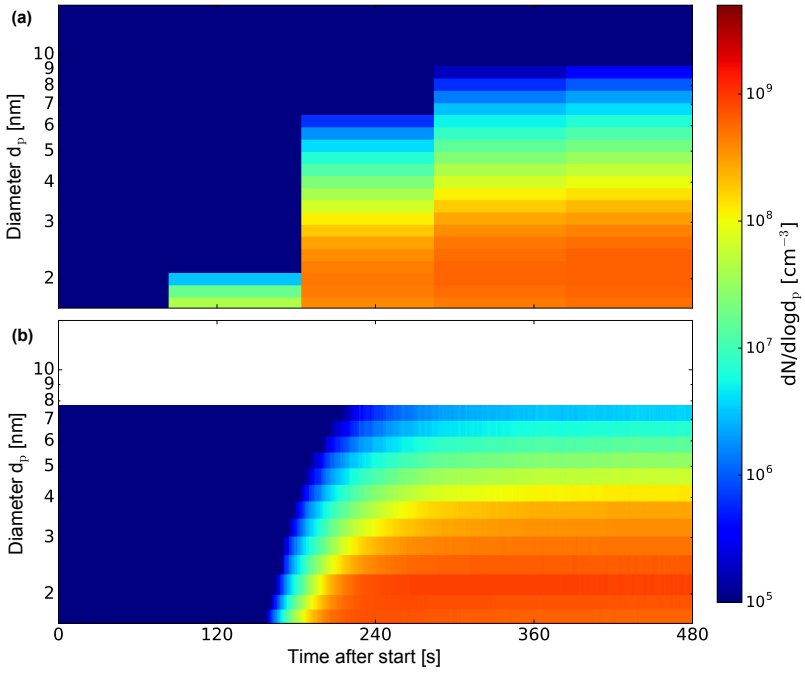

Figure 10: Evolution of the size distribution measured by a conventional DMPS **(a)** and the DMA-train **(b)** of a tungsten oxide generator during warmup. The generator is switched on a time 0. The DMA-train uses its maximum resolution of 1 s while the DMPS bins are placed between start and stop of the scanning cycle.

both systems in parallel, which is shown in Figure 7.

The DMPS system only achieves five scanning cycles during the 8 min of warmup, although its particle scanning range is already reduced from standard operation mode. As the DMPS scanning cycle starts at the highest voltages, i.e., at the biggest particle sizes, it already detects the first small particles at the end of the second scanning cycle. In Figure 7, however, the scanning information is binned into the time window between start and end of the scan. During the third scan the generator almost achieved its full performance.

The DMA-train, in contrast, produces concentration signals in 1 s time intervals, but the actual time resolution will vary among the different size channels. Based on transmission time and CPC response times specified by the manufacturers a conservative estimate of the overall time resolution is on the order of 5 s. Still the resolution is high enough to provide detailed information about the warmup between 1.7 and 7.26 nm with the DMAs are set to 1.7, 2.14, 2.82, 3.63, 5.18 and 7.26 nm. It can be clearly seen that as the tungsten oxide coil warms up, first particles of smaller diameter are produced and then, subsequently, the size distribution reaches bigger sizes. The same trend can be observed with the DMPS system, but much less details, e.g., the precise onset of particles at a certain size, can be resolved. The absolute concentrations, however, agree reasonably well within a factor of 2.

2.4.2 DMA-train operated at the CLOUD experiment

The DMA-train was operated at the CLOUD experiment during a technical run, where instruments could be tested intensively. CLOUD is described in detail elsewhere (Kirkby et al., 2011; Duplissy et al., 2016) and recently published detailed results about pure biogenic nucleation (Kirkby et al., 2016) and subsequent growth (Tröstl et al., 2016).
Figure **??** shows the time evolution of the different size channels of the DMA-train during a typical nucleation event from pure α-pinene ozonolysis in the CLOUD chamber. After establishing stable gas concentrations, switching off the electrical field cage inside the chamber at time 0 starts ion-induced nucleation (Kirkby et al., 2016). The subsequent growth of the particles could be tracked by the DMA-train. The signal consecutively appears at the different particle size bins, clearly showing the growth of the particles from smaller to bigger sizes. In Figure **??**, in total nine different sizes are covered as some DMAs are automatically set to higher voltages and thus bigger particles, as soon as a steady-state concentration is reached in the smaller size channels. This opens an opportunity for covering wider size ranges with the DMA-train during particle growth events and allows for the determination of size-dependent growth rates by relating the signal appearance times to their classified diameters (e.g, Tröstl et al., 2016). In this model case of growth driven by organic vapors, the signal rises from 0 to its plateau value in one channel within 5 min. This clearly points out the need for sufficient time resolution in order to precisely capture the particle rise and hence improve growth rate evaluation.
However, CLOUD is typically operated close to atmospheric conditions, and particle number concentrations are low. Hence, the expected signal, especially below 2.5 nm, is only in the range of a few counts per minute. As there is no scanning cycle involved, data are acquired constantly at each size, allowing for averaging over longer time periods in order to even identify very low counts. This can be seen in Figure **??**, where a 2 min average was applied to the larger size channels, but a 5 min average to the 1.7 and 2.0 nm channels in order to account for the lower count rates at smaller sizes. Although sampling losses are highest and charging and activation efficiencies are lowest below 2 nm, respectively, the DMA-train is still sensitive to the low count rates and can therefore resolve even that early growth, which was not possible by a fast-scanning nano-SMPS (Tröstl et al., 2015), connected to the chamber at the same time.
In this context it should be noted that for such low concentrations the DMA-train signal relies on a stable and negligible background. Especially the temperature settings of the PSMs need to be chosen carefully to allow detection of sub-2 nm particles while avoiding homogeneous nucleation at the same time. It is another important feature of the DMA-train that the background can easily be tested at any point in time by setting the DMA voltages to 0 V and measuring particle-free sheath air. For the settings used in this study we determined the background to be less than 1 count per minute.

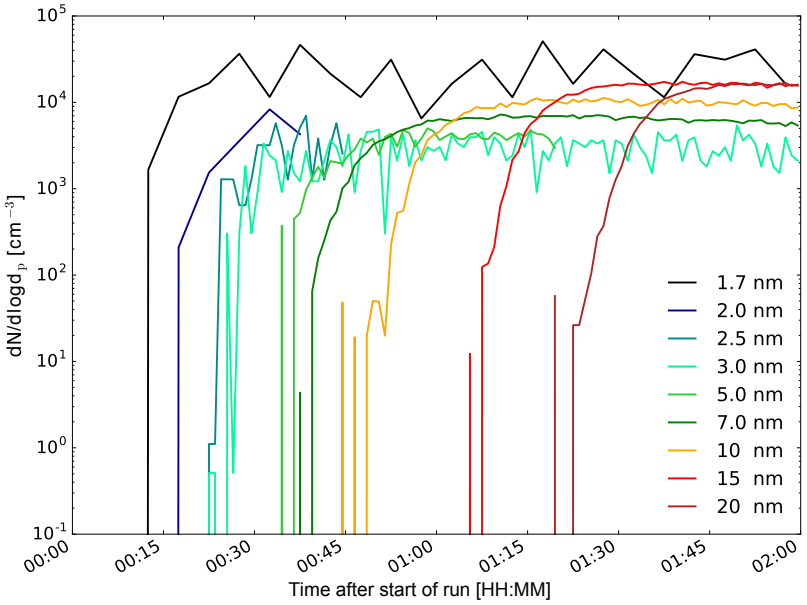

Figure 11: Time evolution of the signal in the different DMA-train channels during an α-pinene ozonolysis event in the CLOUD chamber. In order to cover a wider size range, some DMAs are switched to bigger sizes as soon as a steady state is reached. The clear subsequent appearance of the signal in the different channels verifies the size calibration and allows for the determination of particle growth rates.

2.5 Conclusions

The DMA-train concept has been presented and its performance was demonstrated by calibration experiments of DMAs, CPCs and sampling losses. These measurements showed that our particle counters operate as specified by the manufacturers. The usage of different CPC types might allow estimates of the chemical composition of the sampled aerosol at different sizes due to the different activation probabilities of the counters with respect to the seed particle composition. All six Grimm S-DMAs reach accurate size classification with a transmission as high as 8–10 % at diameters as low as 1.6 nm. The sampling losses are minimized as much as possible by using a compact setup, which only needs short sampling tubes and provides high flow rates during the sampling procedure.

Fast-changing aerosol can be measured with a time resolution on the order of seconds. A measurement of a tungsten oxide generator during warmup and a comparison to a DMPS system measuring in parallel showed the advantageous use of the DMA-train when analyzing fast-changing aerosol. Furthermore the comparison could also verify the absolute concentrations inferred from the DMA-train.

The DMA-train is fully mobile and therefore adjusted for measurements at atmospheric conditions as demonstrated during an intensive measurement campaign at the CLOUD experiment. Measuring at several fixed sizes in parallel offers the possibility of using the full

counting statistics at the distinct sizes. At low concentrations and small sizes an averaging of the signal allows us to increase the sensitivity significantly compared to other state-of-the-art instruments which infer size-distribution information through scanning procedures.
Thus, the DMA-train allows us to bridge the gap between measurements in the cluster size range obtained by mass-spectrometry or scanning PSMs and results from conventional SMPS systems above 10 nm. Furthermore it provides a high time resolution to observe very fast aerosol growth, especially in the critical sub-10 nm range, where diffusional losses are very high and the survival of freshly nucleated particles is crucial for growing them to atmospherically relevant sizes.
If combined with other measurement devices such as conventional SMPS systems, the full particle size range can be measured, beginning at cluster sizes as low as 1.6 nm, which is the lower size limit for the DMA-train due to the charger ions. This might allow us to perform detailed comparisons to aerosol growth models (Rao and McMurry, 1989) or apply inverse modeling procedures in order to obtain precise size- and time-dependent growth rates (Verheggen and Mozurkewich, 2006; Kuang et al., 2012b). Thus the DMA-train opens a new field for the analysis of aerosol growth processes.

Author Contributions

D. S. and P. M. W. designed the setup, **D. S.** and G. S. performed the calibration experiments, **D. S.** performed the size-distribution measurements, **D. S.**, G. S. and P. M. W. were involved in the scientific interpretation and discussion, and **D. S.**, G. S. and P. M. W. wrote the manuscript.

Acknowledgements

We thank Andrea Ojdanic for her help with the CPC characterizations and Iris Brodacz for her support in operating the UDMA. We gratefully acknowledge the CLOUD experiment for providing us the opportunity for instrument testing. This work was supported by the European Research Council under the European Community's Seventh Framework Programme (FP7/2007/2013)/ERC grant agreement no. 616075 and the Austrian Science Fund, FWF, project number P27295-N20.

2.6 References

Albrecht, B.: Aerosols, Cloud Microphysics, and Fractional Cloudiness, Science, 245, 1227–1230, doi:10.1126/science.245.4923.1227, http://science.sciencemag.org/content/245/4923/1227, 1989.

Brunelli, N. A., Flagan, R. C., and Giapis, K. P.: Radial Differential Mobility Analyzer for One Nanometer Particle Classification, Aerosol Sci. Tech., 43, 53–59, doi:10.1080/02786820802464302, http://dx.doi.org/10.1080/02786820802464302, 2009.

Carslaw, K. S., Lee, L. A., Reddington, C. L., Pringle, K. J.and Rap, A., Forster, P. M., Mann, G. W., Spracklen, D. V., Woodhouse, M., Regayre, L. A., and Pierce, J. R.: Large contribution of natural aerosols to uncertainty in indirect forcing, Nature, 503, 67–71, doi:10.1038/nature12674, http://dx.doi.org/10.1038/nature12674, 2013.

Cheng, Y.-S.: Instruments and Samplers Based on Diffusional Separation, in: Aerosol Measurement: Principles, Techniques, and Applications, pp. 365–379, John Wiley and Sons, Inc., doi:10.1002/9781118001684.ch16, http://dx.doi.org/10.1002/9781118001684.ch16, 2011.

Dal Maso, M., Kulmala, M., Lehtinen, K. E. J., Mäkelä, J. M., Aalto, P., and O'Dowd, C. D.: Condensation and coagulation sinks and formation of nucleation mode particles in coastal and boreal forest boundary layers, J. Geophys. Res.-Atmos., 107, PAR 2–1–PAR 2–10, doi:10.1029/2001JD001053, http://dx.doi.org/10.1029/2001JD001053, 2002.

Duplissy, J., Merikanto, J., Franchin, A., Tsagkogeorgas, G., Kangasluoma, J., Wimmer, D., Vuollekoski, H., Schobesberger, S., Lehtipalo, K., Flagan, R. C., Brus, D., Donahue, N. M., Vehkamäki, H., Almeida, J., Amorim, A., Barmet, P., Bianchi, F., Breitenlechner, M., Dunne, E. M., Guida, R., Henschel, H., Junninen, H., Kirkby, J., Kürten, A., Kupc, A., Määttänen, A., Makhmutov, V., Mathot, S., Nieminen, T., Onnela, A., Praplan, A. P., Riccobono, F., Rondo, L., Steiner, G., Tome, A., Walther, H., Baltensperger, U., Carslaw, K. S., Dommen, J., Hansel, A., Petäjä, T., Sipilä, M., Stratmann, F., Vrtala, A., Wagner, P. E., Worsnop, D. R., Curtius, J., and Kulmala, M.: Effect of ions on sulfuric acid-water binary particle formation: 2. Experimental data and comparison with QC-normalized classical nucleation theory, J. Geophys. Res.-Atmos., 121, 1752–1775, doi:10.1002/2015JD023539, http://dx.doi.org/10.1002/2015JD023539, 2016.

Ehn, M., Thornton, J. A., Kleist, E., Sipila, M., Junninen, H., Pullinen, I., Springer, M., Rubach, F., Tillmann, R., Lee, B., Lopez-Hilfiker, F., Andres, S., Acir, I.-H., Rissanen, M., Jokinen, T., Schobesberger, S., Kangasluoma, J., Kontkanen, J., Nieminen, T., Kurten, T., Nielsen, L. B., Jorgensen, S., Kjaergaard, H. G., Canagaratna, M., Maso, M. D., Berndt, T., Petaja, T., Wahner, A., Kerminen, V.-M., Kulmala, M., Worsnop, D. R., Wildt, J., and Mentel, T. F.: A large source of low-volatility secondary organic aerosol, Nature, 506, 476–479, doi:10.1038/nature13032, http://dx.doi.org/10.1038/nature13032, 2014.

Fernández de la Mora, J. and Kozlowski, J.: Hand-held differential mobility analyzers of high resolution for 1–30 nm particles: Design and fabrication considerations, J. Aerosol Sci., 57, 45 – 53, doi:10.1016/j.jaerosci.2012.10.009, http://www.sciencedirect.com/science/article/pii/S0021850212001772, 2013.

Flagan, R. C.: History of Electrical Aerosol Measurements, Aerosol Sci. Tech., 28, 301–380, doi:10.1080/02786829808965530, http://dx.doi.org/10.1080/02786829808965530, 1998.

Flagan, R. C., Wang, S. C., Yin, F., Seinfeld, J. H., Reischl, G., Winklmayr, W., and Karch, R.: Electrical mobility measurements of fine-particle formation during chamber studies of atmospheric photochemical reactions, Environ. Sci. Technol., 25, 883–890, doi:10.1021/es00017a009, http://pubs.acs.org/doi/pdf/10.1021/es00017a009, 1991.

Gompertz, B.: On the Nature of the Function Expressive of the Law of Human Mortality, and on a New Mode of Determining the Value of Life Contingencies, Philos. T. R. Soc. Lond., 115, 513–583, 1825.

Gormley, P. G. and Kennedy, M.: Diffusion from a Stream Flowing through a Cylindrical Tube, P. Roy. Irish Acad. A, 52, 163–169, 1948.

Hering, S. V., Stolzenburg, M. R., Quant, F. R., Oberreit, D. R., and Keady, P. B.: A Laminar-Flow, Water-Based Condensation Particle Counter (WCPC), Aerosol Sci. Tech., 39, 659–672, doi:10.1080/02786820500182123, http://dx.doi.org/10.1080/02786820500182123, 2005.

Hermann, M., Wehner, B., Bischof, O., Han, H.-S., Krinke, T., Liu, W., Zerrath, A., and Wiedensohler, A.: Particle counting efficiencies of new TSI condensation particle counters, J. Aerosol Sci., 38, 674 – 682, doi:10.1016/j.jaerosci.2007.05.001, http://www.sciencedirect.com/science/article/pii/S0021850207000705, 2007.

Jiang, J., Attoui, M., Heim, M., Brunelli, N. A., McMurry, P. H., Kasper, G., Flagan, R. C., Giapis, K., and Mouret, G.: Transfer Functions and Penetrations of Five Differential Mobility Analyzers for Sub-2 nm Particle Classification, Aerosol Sci. Tech., 45, 480–492, doi:10.1080/02786826.2010.546819, http://www.tandfonline.com/doi/abs/10.1080/02786826.2010.546819, 2011a.

Jiang, J., Chen, M., Kuang, C., Attoui, M., and McMurry, P. H.: Electrical Mobility Spectrometer Using a Diethylene Glycol Condensation Particle Counter for Measurement of Aerosol Size Distributions Down to 1 nm, Aerosol Sci. Tech., 45, 510–521, doi:10.1080/02786826.2010.547538, http://www.tandfonline.com/doi/abs/10.1080/02786826.2010.547538, 2011b.

Kallinger, P. and Szymanski, W.: Experimental determination of the steady-state charging probabilities and particle size conservation in non-radioactive and radioactive bipolar aerosol chargers in the size range of 5-40 nm, J. Nanopart. Res., 17, 171, doi:10.1007/s11051-015-2981-x, http://dx.doi.org/10.1007/s11051-015-2981-x, 2015.

Kallinger, P., Steiner, G., and Szymanski, W. W.: Characterization of four different bipolar charging devices for nanoparticle charge conditioning, J. Nanopart. Res., 14, 944, doi:10.1007/s11051-012-0944-z, http://dx.doi.org/10.1007/s11051-012-0944-z, 2012.

Kangasluoma, J., Kuang, C., Wimmer, D., Rissanen, M. P., Lehtipalo, K., Ehn, M., Worsnop, D. R., Wang, J., Kulmala, M., and Petäjä, T.: Sub-3 nm particle size and composition dependent response of a nano-CPC battery, Atmos. Meas. Tech., 7, 689–700, doi:10.5194/amt-7-689-2014, http://www.atmos-meas-tech.net/7/689/2014/, 2014.

Karlsson, M. N. A. and Martinsson, B. G.: Methods to measure and predict the transfer function size dependence of individual DMAs, J. Aerosol Sci., 34, 603 – 625, doi:10.1016/S0021-8502(03)00020-X, http://www.sciencedirect.com/science/article/pii/S002185020300020X, 2003.

Kerminen, V.-M., Lihavainen, H., Komppula, M., Viisanen, Y., and Kulmala, M.: Direct observational evidence linking atmospheric aerosol formation and cloud droplet activation, Geophys. Res. Lett., 32, doi:10.1029/2005GL023130, http://dx.doi.org/10.1029/2005GL023130, l14803, 2005.

Kirkby, J., Curtius, J., Almeida, J., Dunne, E., Duplissy, J., Ehrhart, S., Franchin, A., Gagné, S., Ickes, L., Kürten, A., Kupc, A., Metzger, A., Riccobono, F., Rondo, L., Schobesberger, S., Tsagkogeorgas, G., Wimmer, D., Amorim, A., Bianchi, F., Breitenlechner, M., David, A., Dommen, J., Downard, A., Ehn, M., Flagan, R. C., Haider, S., Hansel, A., Hauser, D., Jud, W., Junninen, H., Kreissl, F., Kvashin, A., Laaksonen, A., Lehtipalo, K., Lima, J., Lovejoy, E. R., Makhmutov, V., Mathot, S., Mikkilä, J., Minginette, P., Mogo, S., Nieminen, T., Onnela, A., Pereira, P., Petäjä, T., Schnitzhofer, R., Seinfeld, J. H., Sipilä, M., Stozhkov, Y., Stratmann, F., Tomé, A., Vanhanen, J., Viisanen, Y., Vrtala, A., Wagner, P. E., Walther, H., Weingartner, E., Wex, H., Winkler, P. M., Carslaw, K. S., Worsnop, D. R., Baltensperger, U., and Kulmala, M.: Role of sulphuric acid, ammonia and galactic cosmic rays in atmospheric aerosol nucleation, Nature, 476, 429–433, doi:10.1038/nature10343, http://dx.doi.org/10.1038/nature10343, 2011.

Kirkby, J., Duplissy, J., Sengupta, K., Frege, C., Gordon, H., Williamson, C., Heinritzi, M., Simon, M., Yan, C., Almeida, J., Tröstl, J., Nieminen, T., Ortega, I. K., Wagner, R., Adamov, A., Amorim, A., Bernhammer, A.-K., Bianchi, F., Breitenlechner, M., Brilke, S., Chen, X., Craven, J., Dias, A., Ehrhart, S., Flagan, R. C., Franchin, A., Fuchs, C., Guida, R., Hakala, J., Hoyle, C. R., Jokinen, T., Junninen, H., Kangasluoma, J., Kim, J., Krapf, M., Kürten, A., Laaksonen, A., Lehtipalo, K., Makhmutov, V., Mathot, S., Molteni, U., Onnela, A., Peräkylä, O., Piel, F., Petäjä, T., Praplan, A. P., Pringle, K., Rap, A., Richards, N. A. D., Riipinen, I., Rissanen, M. P., Rondo, L., Sarnela, N., Schobesberger, S., Scott, C. E., Seinfeld, J. H., Sipilä, M., Steiner, G., Stozhkov, Y., Stratmann, F., Tomé, A., Virtanen, A., Vogel, A. L., Wagner, A. C., Wagner, P. E., Weingartner, E., Wimmer, D., Winkler, P. M., Ye, P., Zhang, X., Hansel, A., Dommen, J., Donahue, N. M., Worsnop, D. R., Baltensperger, U., Kulmala, M., Carslaw, K. S., and Curtius, J.: Ion-induced nucleation of pure biogenic particles, Nature, 533, 521–526, doi:10.1038/nature17953, http://dx.doi.org/10.1038/nature17953, 2016.

Knutson, E. O. and Whitby, K. T.: Aerosol classification by electric mobility: apparatus, theory, and applications, J. Aerosol Sci., 6, 443–451, doi:10.1016/0021-8502(75)90060-9, http://www.sciencedirect.com/science/article/pii/0021850275900609, 1975.

Kuang, C., McMurry, P. H., and McCormick, A. V.: Determination of cloud condensation nuclei production from measured new particle formation events, Geophys. Res. Lett., 36, doi:10.1029/2009GL037584, http://dx.doi.org/10.1029/2009GL037584, l09822, 2009.

Kuang, C., Chen, M., McMurry, P. H., and Wang, J.: Modification of Laminar Flow Ultrafine Condensation Particle Counters for the Enhanced Detection of 1 nm Condensation Nuclei,

Aerosol Sci. Tech., 46, 309–315, doi:10.1080/02786826.2011.626815, http://dx.doi.org/10.1080/02786826.2011.626815, 2012a.

Kuang, C., Chen, M., Zhao, J., Smith, J., McMurry, P. H., and Wang, J.: Size and time-resolved growth rate measurements of 1 to 5 nm freshly formed atmospheric nuclei, Atmos. Chem. Phys., 12, 3573–3589, doi:10.5194/acp-12-3573-2012, http://www.atmos-chem-phys.net/12/3573/2012/, 2012b.

Kulmala, M., Kerminen, V.-M., Anttila, T., Laaksonen, A., and O'Dowd, C. D.: Organic aerosol formation via sulphate cluster activation, J. Geophys. Res.-Atmos., 109, doi:10.1029/2003JD003961, http://dx.doi.org/10.1029/2003JD003961, d04205, 2004.

Kulmala, M., Mordas, G., Petäjä, T., Grönholm, T., Aalto, P. P., Vehkamäki, H., Hienola, A. I., Herrmann, E., Sipilä, M., Riipinen, I., Manninen, H. E., Hämeri, K., Stratmann, F., Bilde, M., Winkler, P. M., Birmili, W., and Wagner, P. E.: The condensation particle counter battery (CPCB): A new tool to investigate the activation properties of nanoparticles, J. Aerosol Sci., 38, 289 – 304, doi:10.1016/j.jaerosci.2006.11.008, http://www.sciencedirect.com/science/article/pii/S0021850206002138, 2007.

Kupc, A., Bischof, O., Tritscher, T., Beeston, M., Krinke, T., and Wagner, P. E.: Laboratory Characterization of a New Nano-Water-Based CPC 3788 and Performance Comparison to an Ultrafine Butanol-Based CPC 3776, Aerosol Sci. Tech., 47, 183–191, doi:10.1080/02786826.2012.738317, http://dx.doi.org/10.1080/02786826.2012.738317, 2013.

Lehtipalo, K., Leppä, J., Kontkanen, J., Kangasluoma, J., Franchin, A., Wimmer, D., Schobesberger, S., Junninen, H., Petäjä, T., Sipilä, M., Mikkilä, J., Vanhanen, J., Worsnop, D. R., and Kulmala, M.: Methods for determining particle size distribution and growth rates between 1 and 3 nm using the Particle Size Magnifier, Boreal Environ. Res., 19, 215–236, 2014.

Lihavainen, H., Kerminen, V.-M., Komppula, M., Hatakka, J., Aaltonen, V., Kulmala, M., and Viisanen, Y.: Production of "potential" cloud condensation nuclei associated with atmospheric new-particle formation in northern Finland, J. of Geophys. Res.-Atmos., 108, doi:10.1029/2003JD003887, http://dx.doi.org/10.1029/2003JD003887, 4782, 2003.

Merikanto, J., Spracklen, D. V., Mann, G. W., Pickering, S. J., and Carslaw, K. S.: Impact of nucleation on global CCN, Atmos. Chem. Phys., 9, 8601–8616, doi:10.5194/acp-9-8601-2009, http://www.atmos-chem-phys.net/9/8601/2009/, 2009.

Olfert, J. S., Kulkarni, P., and Wang, J.: Measuring aerosol size distributions with the fast integrated mobility spectrometer, J. Aerosol Sci., 39, 940 – 956, doi:http://dx.doi.org/10.1016/j.jaerosci.2008.06.005, http://www.sciencedirect.com/science/article/pii/S002185020800116X, 2008.

Pinterich, T., Vrtala, A., Kaltak, M., Kangasluoma, J., Lehtipalo, K., Petäjä, T., Winkler, P. M., Kulmala, M., and Wagner, P. E.: The versatile size analyzing nuclei counter (vSANC), Aerosol Sci.Tech., 50, 947–958, doi:10.1080/02786826.2016.1210783, http://dx.doi.org/10.1080/02786826.2016.1210783, 2016.

Ramanathan, V., Crutzen, P. J., Kiehl, J. T., and Rosenfeld, D.: Aerosols, Climate, and the Hydrological Cycle, Science, 294, 2119–2124, doi:10.1126/science.1064034, http://science.sciencemag.org/content/294/5549/2119, 2001.

Rao, N. and McMurry, P.: Nucleation and Growth of Aerosol in Chemically Reacting Systems: A Theoretical Study of the Near-Collision-Controlled Regime, Aerosol Sci. Tech., 11, 120–132, doi:10.1080/02786828908959305, http://dx.doi.org/10.1080/02786828908959305, 1989.

Reineking, A. and Porstendörfer, J.: Measurements of Particle Loss Functions in a Differential Mobility Analyzer (TSI, Model 3071) for Different Flow Rates, Aerosol Sci. Tech., 5, 483–486, doi:10.1080/02786828608959112, http://dx.doi.org/10.1080/02786828608959112, 1986.

Reischl, G.: Measurement of Ambient Aerosols by the Differential Mobility Analyzer Method: Concepts and Realization Criteria for the Size Range Between 2 and 500 nm, Aerosol Sci. Tech., 14, 5–24, doi:10.1080/02786829108959467, http://dx.doi.org/10.1080/02786829108959467, 1991.

Riccobono, F., Rondo, L., Sipilä, M., Barmet, P., Curtius, J., Dommen, J., Ehn, M., Ehrhart, S., Kulmala, M., Kürten, A., Mikkilä, J., Paasonen, P., Petäjä, T., Weingartner, E., and Baltensperger, U.: Contribution of sulfuric acid and oxidized organic compounds to particle formation and growth, Atmos. Chem. Phys., 12, 9427–9439, doi:10.5194/acp-12-9427-2012, https://www.atmos-chem-phys.net/12/9427/2012/, 2012.

Spracklen, D. V., Carslaw, K. S., Kulmala, M., Kerminen, V.-M., Sihto, S.-L., Riipinen, I., Merikanto, J., Mann, G. W., Chipperfield, M. P., Wiedensohler, A., Birmili, W., and Lihavainen, H.: Contribution of particle formation to global cloud condensation nuclei concentrations, Geophys. Res. Lett., 35, doi:10.1029/2007GL033038, http://dx.doi.org/10.1029/2007GL033038, l06808, 2008.

Steiner, G., Attoui, M., Wimmer, D., and Reischl, G. P.: A Medium Flow, High-Resolution Vienna DMA Running in Recirculating Mode, Aerosol Sci. Tech., 44, 308–315, doi:10.1080/02786821003636763, http://dx.doi.org/10.1080/02786821003636763, 2010.

Stolzenburg, M. R.: An Ultrafine Aerosol Size Distribution System, Ph.D. thesis, University of Minnesota, 1988.

Stolzenburg, M. R. and McMurry, P. H.: An Ultrafine Aerosol Condensation Nucleus Counter, Aerosol Sci. Tech., 14, 48–65, doi:10.1080/02786829108959470, http://dx.doi.org/10.1080/02786829108959470, 1991.

Stolzenburg, M. R. and McMurry, P. H.: Equations Governing Single and Tandem DMA Configurations and a New Lognormal Approximation to the Transfer Function, Aerosol Sci. Tech., 42, 421–432, doi:10.1080/02786820802157823, http://dx.doi.org/10.1080/02786820802157823, 2008.

Svenningsson, B., Arneth, A., Hayward, S., Holst, T., Massling, A., Swietlicki, E., Hirsikko, A., Junninen, H., Riipinen, I., Vana, M., Dal-Maso, M., Hussein, T., and Kulmala, M.:

Aerosol particle formation events and analysis of high growth rates observed above a sub-arctic wetland–forest mosaic, Tellus B, 60, 353–364, doi:10.1111/j.1600-0889.2008.00351.x, http://dx.doi.org/10.1111/j.1600-0889.2008.00351.x, 2008.

Tröstl, J., Tritscher, T., Bischof, O. F., Horn, H.-G., Krinke, T., Baltensperger, U., and Gysel, M.: Fast and precise measurement in the sub-20 nm size range using a Scanning Mobility Particle Sizer, J. Aerosol Sci., 87, 75–87, doi:10.1016/j.jaerosci.2015.04.001, http://www.sciencedirect.com/science/article/pii/S0021850215000543, 2015.

Tröstl, J., Chuang, W. K., Gordon, H., Heinritzi, M., Yan, C., Molteni, U., Ahlm, L., Frege, C., Bianchi, F., Wagner, R., Simon, M., Lehtipalo, K., Williamson, C., Craven, J. S., Duplissy, J., Adamov, A., Almeida, J., Bernhammer, A.-K., Breitenlechner, M., Brilke, S., Dias, A., Ehrhart, S., Flagan, R. C., Franchin, A., Fuchs, C., Guida, R., Gysel, M., Hansel, A., Hoyle, C. R., Jokinen, T., Junninen, H., Kangasluoma, J., Keskinen, H., Kim, J., Krapf, M., Kürten, A., Laaksonen, A., Lawler, M., Leiminger, M., Mathot, S., Möhler, O., Nieminen, T., Onnela, A., Petäjä, T., Piel, F. M., Miettinen, P., Rissanen, M. P., Rondo, L., Sarnela, N., Schobesberger, S., Sengupta, K., Sipilä, M., Smith, J. N., Steiner, G., Tomè, A., Virtanen, A., Wagner, A. C., Weingartner, E., Wimmer, D., Winkler, P. M., Ye, P., Carslaw, K. S., Curtius, J., Dommen, J., Kirkby, J., Kulmala, M., Riipinen, I., Worsnop, D. R., Donahue, N. M., and Baltensperger, U.: The role of low-volatility organic compounds in initial particle growth in the atmosphere, Nature, 533, 527–531, doi:10.1038/nature18271, http://dx.doi.org/10.1038/nature18271, 2016.

Ude, S. and Fernández de la Mora, J.: Molecular monodisperse mobility and mass standards from electrosprays of tetra-alkyl ammonium halides, J. Aerosol Sci., 36, 1224 – 1237, doi:10.1016/j.jaerosci.2005.02.009, http://www.sciencedirect.com/science/article/pii/S0021850205000510, 2005.

Vanhanen, J., Mikkilä, J., Lehtipalo, K., Sipilä, M., Manninen, H. E., Siivola, E., Petäjä, T., and Kulmala, M.: Particle Size Magnifier for Nano-CN Detection, Aerosol Sci. Tech., 45, 533–542, doi:10.1080/02786826.2010.547889, http://www.tandfonline.com/doi/abs/10.1080/02786826.2010.547889, 2011.

Venzac, H., Sellegri, K., Laj, P., Villani, P., Bonasoni, P., Marinoni, A., Cristofanelli, P., Calzolari, F., Fuzzi, S., Decesari, S., Facchini, M.-C., Vuillermoz, E., and Verza, G. P.: High frequency new particle formation in the Himalayas, P. Natl. Acad. Sci. USA, 105, 15 666–15 671, doi:10.1073/pnas.0801355105, http://www.pnas.org/content/105/41/15666.abstract, 2008.

Verheggen, B. and Mozurkewich, M.: An inverse modeling procedure to determine particle growth and nucleation rates from measured aerosol size distributions, Atmos. Chem. Phys., 6, 2927–2942, doi:10.5194/acp-6-2927-2006, http://www.atmos-chem-phys.net/6/2927/2006/, 2006.

Wang, J., Flagan, R. C., and Seinfeld, J. H.: Diffusional losses in particle sampling systems containing bends and elbows, J. Aerosol Sci., 33, 843 – 857, doi:https://doi.org/10.1016/S0021-8502(02)00042-3, http://www.sciencedirect.com/science/article/pii/S0021850202000423, 2002.

Wang, S. and Flagan, R.: Scanning Electrical Mobility Spectrometer, Aerosol Sci. Tech., 13, 230–240, doi:10.1080/02786829008959441, http://dx.doi.org/10.1080/02786829008959441, 1990.

Weber, R. J., Marti, J. J., and McMurry, P. H.: Measurements of new particle formation and ultrafine particle growth rates at a clean continental site, J. Geophys. Res.-Atmos., 102, 4375–4385, doi:10.1029/96JD03656, http://dx.doi.org/10.1029/96JD03656, 1997.

Wiedensohler, A.: An approximation of the bipolar charge distribution for particles in the submicron size range, J. Aerosol Sci., 19, 387 – 389, doi:10.1016/0021-8502(88)90278-9, http://www.sciencedirect.com/science/article/pii/0021850288902789, 1988.

Wimmer, D., Lehtipalo, K., Franchin, A., Kangasluoma, J., Kreissl, F., Kürten, A., Kupc, A., Metzger, A., Mikkilä, J., Petäjä, T., Riccobono, F., Vanhanen, J., Kulmala, M., and Curtius, J.: Performance of diethylene glycol-based particle counters in the sub-3 nm size range, Atmos. Meas. Tech., 6, 1793–1804, doi:10.5194/amt-6-1793-2013, http://www.atmos-meas-tech.net/6/1793/2013/, 2013.

Winkler, P. M., Steiner, G., Vrtala, A., Vehkamäki, H., Noppel, M., Lehtinen, K. E. J., Reischl, G. P., Wagner, P. E., and Kulmala, M.: Heterogeneous Nucleation Experiments Bridging the Scale from Molecular Ion Clusters to Nanoparticles, Science, 319, 1374–1377, doi:10.1126/science.1149034, http://science.sciencemag.org/content/319/5868/1374, 2008.

Winkler, P. M., Ortega, J., Karl, T., McMurry, P. H., and Smith, J. N.: A fast-scanning DMA train for precision quantification of early nanoparticle growth, AIP Conference Proceedings, 1527, 165–168, doi:10.1063/1.4803229, http://aip.scitation.org/doi/abs/10.1063/1.4803229, 2013.

Winklmayr, W., Reischl, G. P., Lindner, A. O., and Berner, A.: A new electromobility spectrometer for the measurement of aerosol size distributions in the size range from 1 to 1000 nm, J. Aerosol Sci., 22, 289 – 296, doi:10.1016/S0021-8502(05)80007-2, http://www.sciencedirect.com/science/article/pii/S0021850205800072, 1991.

Winsor, C.: The Gompertz curve as a growth curve, P. Natl. Acad. Sci. USA, 18, 1–8, http://www.pnas.org/content/18/1/1.short, 1932.

Chapter 3

Resolving nanoparticle growth mechanisms from size- and time-dependent growth rate analysis

This chapter was published by L.Pichelstorfer, D.Stolzenburg, J.Ortega, T.Karl, H.Kokkola, A.Laakso, K.E.J.Lehtinen, J.N.Smith, P.H.McMurry and P.M.Winkler in *Atmospheric Chemistry and Physics*, 2018, 18, 1307-1323

Abstract. Atmospheric new particle formation occurs frequently in the global atmosphere and may play a crucial role in climate by affecting cloud properties. The relevance of newly formed nanoparticles depends largely on the dynamics governing their initial formation and growth to sizes where they become important for cloud microphysics. One key to the proper understanding of nanoparticle effects on climate is therefore hidden in the growth mechanisms. In this study we have developed and successfully tested two independent methods based on the aerosol general dynamics equation, allowing detailed retrieval of time- and size-dependent nanoparticle growth rates. Both methods were used to analyze particle formation from two different biogenic precursor vapors in controlled chamber experiments. Our results suggest that growth rates below 10 nm show much more variation than is currently thought and pin down the decisive size range of growth at around 5 nm where in-depth studies of physical and chemical particle properties are needed.

3.1 Introduction

Aerosol nanoparticle formation from gas-to-particle conversion occurs frequently throughout the global atmosphere (Kulmala et al., 2004). Despite their small sizes these particles might be of climate relevance through the indirect aerosol–cloud effect (Twomey et al., 1984). Modeling results suggest that this secondary aerosol formation mechanism contributes roughly 50 % of particles to the budget of cloud condensation nuclei (Spracklen et al., 2008; Merikanto et al., 2009; Gordon et al., 2017). New particle formation (NPF) has been the subject of numerous studies for several decades. Besides experimental studies under ambient and laboratory conditions, substantial effort has been put into the modeling of aerosol dynamics to address phenomena such as nucleation, condensation/evaporation and coagulation. In order for newly formed particles to eventually become cloud condensation nuclei, particles need to grow sufficiently fast to prevent them from being scavenged by pre-existing particles.

Importantly, the formation rate at a specific diameter $J\,(d_\mathrm{p})$ is highly sensitive to the diameter growth rate $\mathrm{d}d_\mathrm{p}/\mathrm{d}t$. Knowledge of $\mathrm{d}d_\mathrm{p}/\mathrm{d}t$ is needed not only to calculate particle formation rates; it intrinsically contains information on the growth mechanisms (McMurry and Wilson, 1982). The diameter growth rate as a function of particle size and time is therefore key to the understanding of growth mechanisms during gas-to-particle conversion. Several authors have characterized growth rates from the first appearance of various particle sizes over time, which is referred to as the appearance time method (e.g., Kulmala et al., 2013; Lehtipalo et al., 2014; Tröstl et al., 2016). Others showed that a fit of a lognormal distribution to the nucleation mode particles can be used to infer the growth of the population over time (Kulmala et al., 2012). However, these methods cannot fully resolve both the size and time dependencies of the observed growth rates in highly dynamic systems. Therefore, several attempts have been made in the past to derive $\mathrm{d}d_\mathrm{p}/\mathrm{d}t$ by solving the general aerosol dynamics equation (GDE) (Lehtinen et al., 2004; Verheggen and Mozurkewich, 2006; Kuang et al., 2012) using growth rate analysis on the basis of experimental number-size distribution measurements (Heisler and Friedlander, 1977; McMurry et al., 1981; Wang et al., 2006). Those techniques typically require some kind of fitting and additionally might suffer from insufficient data quality, which is usually limited over a certain size range and/or time resolution of the sizing technique being applied. Number-size distribution measurements typically take 1–2 min per scan, and can therefore be too slow to characterize the observed size-resolved growth rates. Hence, determination of $\mathrm{d}d_\mathrm{p}/\mathrm{d}t$ is still a major source of uncertainty in the proper characterization of nanoparticle growth. Here we present a new approach to this problem that compares two different methods based on GDE analysis. The methods are tested and compared to simulated NPF events. Both approaches are then applied to experimental data from particles formed from the ozonolysis of monoterpenes and sesquiterpenes in a 10 m^3 aerosol chamber. State-of-the-art particle sizing instrumentation (Stolzenburg et al., 2017) enables the methods to quantify size- and time-dependent growth rates over the crucial size range between 2

and 50 nm. This thereby helps to improve our understanding of the differences between monoterpenes and sesquiterpenes in new particle formation, which have been emphasized by recent studies (Zhao et al., 2017).

3.2 Description of growth rate determination

Change rates of the number-size distribution are described by the continuous GDE as in Seinfeld and Pandis (2006):

$$\begin{aligned}\frac{\partial n(v,t)}{\partial t} = & \frac{1}{2}\int_0^v K(v-q,q)n(v-q,t)n(q,t)\,\mathrm{d}q \\ & - n(v,t)\int_0^\infty K(q,v)n(q,t)\,\mathrm{d}q - \frac{\partial}{\partial v}[I(v)n(v,t)] \\ & + S(v) - R(v), \end{aligned} \tag{1}$$

where $n(v,t)$ represents the number volume distribution at time t and volume v, $K(v,q)$ is the coagulation kernel, $I(v)$ a particle current across the volume v and $S(v)$ and $R(v)$ are size-dependent source or removal terms, respectively.

In a well-controlled aerosol chamber experiment, the GDE is governed by just a few effects. An aerosol dynamics module accounting for dilution, wall losses and coagulation is used to calculate simulated number-size distributions $n^{\mathrm{sim}}(t_{j+1}, d_{\mathrm{p}})$ (Pichelstorfer and Hofmann, 2015) evolving from measured experimental input number-size distributions $n^{\mathrm{exp}}(t_j, d_{\mathrm{p}})$ between two subsequent time steps t_j and t_{j+1}. With growth as the only unknown in the GDE, comparison between the simulated and the measured number-size distribution $n^{\mathrm{exp}}(t_{j+1}, d_{\mathrm{p}})$ allows for its quantification. Here we focus primarily on two different methods that have been employed to determine size- and time-dependent growth rates from this comparison. A brief description of the software tool used to interpret the experimental data is given below; details can be found in Appendices 3.6.1 and 3.6.2. Potential errors of the analysis methods are discussed in Appendix 3.6.6.

3.2.1 Tracking REgions of the Number-size Distribution: the TREND method

The first method in estimating particle growth rates is based on the assumption that regions r_i between $d_{\mathrm{p},i}$ and $d_{\mathrm{p},i+1}$ (each containing a certain fraction $1/m$ of the total simulated particle number concentration N_∞^{sim}) of the simulated number-size distribution, $n^{\mathrm{sim}}(t_{j+1}, d_{\mathrm{p}})$, can be assigned to regions in the experimental number-size distribution, $n^{\mathrm{exp}}(t_{j+1}, d_{\mathrm{p}})$, (see Fig. **??**). Hence, the method tracks regions of the number-size distribution, and is hereafter called TREND method.

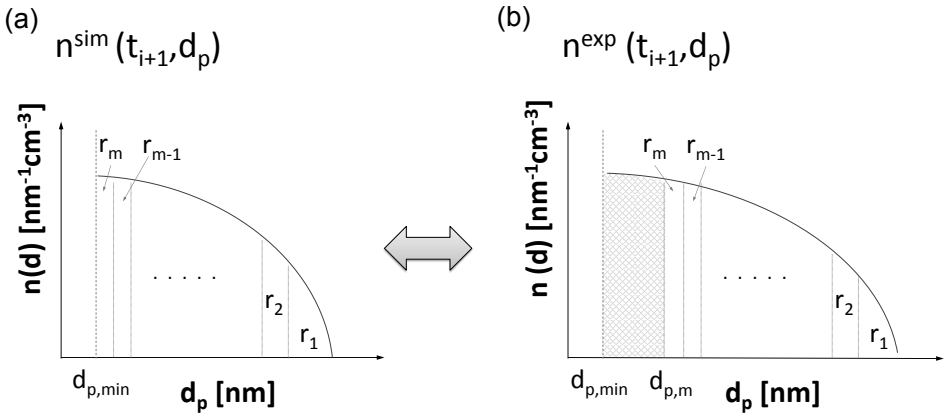

Figure 1: Schematic comparison of defined regions $r_{i=[1,m]}$ of the simulated $n^{\mathrm{sim}}(t_{j+1}, d_{\mathrm{p}})$ **(a)** and experimental $n^{\mathrm{exp}}(t_{j+1}, d_{\mathrm{p}})$ **(b)** number-size distributions allows for the determination of the growth rate. Particle diameter is plotted on the abscissa; particle number-size distribution is plotted on the ordinates of the graphs. The shaded area on the right-hand graph depicts the particles that grew beyond the minimum diameter $d_{\mathrm{p,min}}$ within the last time span $\Delta t = t_{j+1} - t_j$. Particles of size $d_{\mathrm{p,min}}$ at time t_j are of size $d_{\mathrm{p},m}$ at time t_{j+1} (see right-hand graph).

The particle number concentration within each region N_{r} is defined as

$$N_{\mathrm{r}} = \frac{N_{\infty}^{\mathrm{sim}}}{m} \quad \text{with} \quad N_{\infty}^{\mathrm{sim}} = \int_{d_{\mathrm{p,min}}}^{\infty} n^{\mathrm{sim}}(t_{j+1}, d_{\mathrm{p}})\,\mathrm{d}d_{\mathrm{p}}, \tag{2}$$

where m is an integer parameter which determines the number of used regions and $d_{\mathrm{p,min}}$ is the smallest diameter used (e.g., a lower measurement threshold, or the size of a nucleating cluster). Note that the particle number concentration N_{r} is always determined from the simulated number-size distribution n^{sim}. The limits of the regions are related to the number-size distribution by

$$\int_{d_{\mathrm{p,r}_{i+1}}}^{d_{\mathrm{p,r}_i}} n(t_{j+1}, d_{\mathrm{p}})\,\mathrm{d}d_{\mathrm{p}} = N_{\mathrm{r}}. \tag{3}$$

This equation can be solved for the simulated ($n^{\mathrm{sim}}(t_{j+1}, d_{\mathrm{p}})$) and the experimentally determined ($n^{\mathrm{exp}}(t_{j+1}, d_{\mathrm{p}})$) number-size distributions by setting the upper integration limit to the maximum diameter of the distribution $d_{\mathrm{p,r_{imax}}}$ and subsequent numeric integration towards smaller particle sizes until N_{r} is reached. In this way, the next region limit $d_{\mathrm{p,r_{imax-1}}}$ is found and the procedure is repeated until all limits of the m regions are determined. Figure **??** illustrates the principle for determination of the m regions for $n^{\mathrm{sim}}(t_{j+1}, d_{\mathrm{p}})$ and $n^{\mathrm{exp}}(t_{j+1}, d_{\mathrm{p}})$. For each of the regions ($r_{i=[1,m]}$) of the experimental and the simulated number-size distribution, the count median diameter $d_{\mathrm{CMD},i}$ is determined and used to calculate the growth rate

(GR) of a particle with diameter $d^*_{\mathrm{p},i} = \frac{d^{\mathrm{exp}}_{\mathrm{CMD},i} + d^{\mathrm{sim}}_{\mathrm{CMD},i}}{2}$:

$$\mathrm{GR}\left(d^*_{\mathrm{p},i}, (t_{j+1} + t_j)/2\right)) = \frac{d^{\mathrm{exp}}_{\mathrm{CMD},i} - d^{\mathrm{sim}}_{\mathrm{CMD},i}}{t_{j+1} - t_j}. \tag{4}$$

Note that the procedure described above has limitations and benefits, of which the most important are listed below:

1. Growth is decoupled from the other dynamic processes. Thus large relative changes in the limits of the region $d_{\mathrm{p,r}_i}$ may cause errors.

2. Rapid changes in the growth rate require adequate time resolution of the experimental data as the result of the analysis method being a mean growth rate for the respective time interval.

3. Influence of the coagulation process by particles smaller than $d_{\mathrm{p,min}}$ can only be estimated.

4. The present method utilizes integral values to determine the growth rate. Thus local minima and maxima of the measured number-size distribution (e.g., due to low particle concentration) may cancel out. However, this depends on the choice of the width of regions, which can be set for each analysis run.

3.2.2 INterpreting the change rate of the Size-Integrated general Dynamic Equation: the INSIDE method

The second method is based on explicit manipulation of the adapted, size-integrated GDE (see Equation 1), which gives the change in integrated number concentration featuring a diameter larger than d_{eval}:

$$\begin{aligned}\left.\frac{\mathrm{d}N_\infty}{\mathrm{d}t}\right|^{\infty}_{d_{\mathrm{eval}}} = &\left.\frac{\mathrm{d}d_{\mathrm{p}}}{\mathrm{d}t}\right|_{d_{\mathrm{eval}}} \cdot n\left(d_{\mathrm{p}}, t\right)|_{d_{\mathrm{eval}}} + \frac{\mathrm{d}N_{\infty,\mathrm{coag}}}{\mathrm{d}t} \\ &- \int_{d_{\mathrm{eval}}}^{\infty} \beta_{\mathrm{wall}}\left(d_{\mathrm{p}}\right) n\left(d_{\mathrm{p}}, t\right) \mathrm{d}d_{\mathrm{p}} - \beta_{\mathrm{dil}}, N_\infty\end{aligned} \tag{5}$$

where t is time, v is the particle volume, $n(d_{\mathrm{p}}, t)$ is the number-size distribution and d_{eval} the smallest particle diameter considered (not necessarily equal to the minimum measured diameter $d_{\mathrm{p,min}}$). N_∞ depicts the total integrated number concentration, from d_{eval} to ∞. Note that compared to Equation (1), the loss terms have been adopted for a chamber experiment and the particle current $I(d_{\mathrm{p}})$ now represents the particle growth at the evaluation size d_{eval}. The first term on the right-hand side considers particles that grow into the range $[d_{\mathrm{eval}}, \infty]$; the second term considers number-size distribution changes due to coagulation; the third term describes losses at system walls; and the fourth term losses by dilution. Coagulation

and wall losses are approximated by a comparison between the simulated number distribution $n^{\mathrm{sim}}(t_{j+1})$ and the experimental number distribution $n^{\mathrm{exp}}(t_j)$ at two discrete and subsequent points in time and for the considered interval $[d_{\mathrm{eval}},\infty]$:

$$\begin{aligned}\left.\frac{\mathrm{d}N_{\infty}^{\mathrm{sim}}}{\mathrm{d}t}\right|_{d_{\mathrm{eval}}}^{\infty} &= \left.\frac{\mathrm{d}N_{\infty,\mathrm{coag}}}{\mathrm{d}t}\right|_{d_{\mathrm{eval}},\infty} - \int_{d_{\mathrm{eval}}}^{\infty} \beta_{\mathrm{wall}}\left(d_{\mathrm{p}}\right) n\left(d_{\mathrm{p}},t\right) \mathrm{d}d_{\mathrm{p}} - \beta_{\mathrm{dil}} N_{\infty} \\ &\approx \frac{N_{[d_{\mathrm{eval}},\infty]}^{\mathrm{sim}}(t_{j+1}) - N_{[d_{\mathrm{eval}},\infty]}^{\mathrm{exp}}(t_j)}{t_{j+1}-t_j}. \end{aligned} \tag{6}$$

Therefore Equation (**??**) can be rearranged:

$$\left.\frac{\mathrm{d}d_{\mathrm{p}}}{\mathrm{d}t}\right|_{d_{\mathrm{eval}}} = \frac{\left.\frac{\mathrm{d}N_{\infty}}{\mathrm{d}t}\right|_{d_{\mathrm{eval}}}^{\infty} - \left.\frac{\mathrm{d}N_{\infty}^{\mathrm{sim}}}{\mathrm{d}t}\right|_{d_{\mathrm{eval}}}^{\infty}}{n\left(d_{\mathrm{p}},t\right)|_{d_{\mathrm{eval}}}}. \tag{7}$$

The differential of the total change in number concentration is similarly approximated by the difference between the experimental number distribution of two subsequent points in time, i.e.,

$$\left.\frac{\mathrm{d}N_{\infty}}{\mathrm{d}t}\right|_{d_{\mathrm{eval}}}^{\infty} = \frac{N_{[d_{\mathrm{eval}},\infty]}^{\mathrm{exp}}\left(t_{j+1}\right) - N_{[d_{\mathrm{eval}},\infty]}^{\mathrm{exp}}\left(t_j\right)}{t_{j+1}-t_j}. \tag{8}$$

Due to these approximations of the differential expressions in Equation (**??**), the number concentration at the evaluated diameter $n\left(d_{\mathrm{eval}},t\right)$ is expressed as $(n^{\mathrm{exp}}\left(d_{\mathrm{eval}},t_{j+1}\right) + n^{\mathrm{exp}}\left(d_{\mathrm{eval}},t_j\right))/2$. Furthermore the number-size distribution $n\left(d_{\mathrm{p}},t\right)$ is transformed to the measured quantity of $\mathrm{d}N/\mathrm{d}\log d_{\mathrm{p}}\left(d_{\mathrm{p}}\right) = 2.303 \cdot d_{\mathrm{p}} \cdot n(d_{\mathrm{p}},t)$. As a result the diameter growth rate at diameter d_{eval} can then be given by

$$\begin{aligned}\mathrm{GR}\left(d_{\mathrm{eval}},(t_{j+1}+t_j)/2\right) =& \frac{N_{[d_{\mathrm{eval}},\infty]}^{\mathrm{exp}}\left(t_{j+1}\right) - N_{[d_{\mathrm{eval}},\infty]}^{\mathrm{sim}}\left(t_{j+1}\right)}{t_{j+1}-t_j} \\ &\cdot \frac{2.303 \cdot d_{\mathrm{p}}}{\frac{\mathrm{d}N}{d\log d_{\mathrm{p}}}\left(d_{\mathrm{eval}},(t_j+t_{j+1})/2\right)}. \end{aligned} \tag{9}$$

For the INSIDE method the most important limitations and benefits can be summarized as follows:

1. The INSIDE method also features aspects 1 to 3 of the TREND method.

2. It allows for determination of GR at pre-selected diameters while TREND method determines GR and d_{p} based on the number m of regions considered.

3. Fluctuations or scatter in the input number-size distribution may significantly change the result due to the $\frac{\mathrm{d}N(d_{\mathrm{eval}},(t_j+t_{j+1})/2)}{\mathrm{d}\log d_{\mathrm{p}}}$ dependence.

3.3 Testing of the analysis methods

In order to test the analysis methods described above, number size distributions generated by the model SALSA (Sectional Aerosol module for Large Scale Applications; Kokkola et al., 2008) were used. Detailed information about the input parameters for the SALSA model can be found in Appendix 3.6.7. Figure 1 shows the growth rate functions serving as input for the SALSA model and the results of the two analysis methods.

Note that no fitting was done. Both models capture the slope of the input growth rate curve well; however, there are some deviations. Both models show an increasing scatter of the data with increasing particle diameter. This can be explained by the different representations of the number-size distribution within the models. While the SALSA model uses a volume-based moving average representation, the analysis methods consider a distribution of the particles within each size bin. Thus the larger the particles grow the more pronounced the differences between the set growth rate (applied by SALSA) and the analyzed growth rate (determined by INSIDE and TREND) become. Furthermore, some pronounced deviations between measured and determined growth rate occur for the INSIDE method, which are not found for the TREND method. They show up only at the upper end of the number-size distribution where number concentrations are low.

These pronounced deviations are not found in the TREND method which uses integrated number concentration values with respect to dynamic diameters (see Figure **??**) to determine growth rates and hence all regions have fixed counting statistics. Except for this problem,

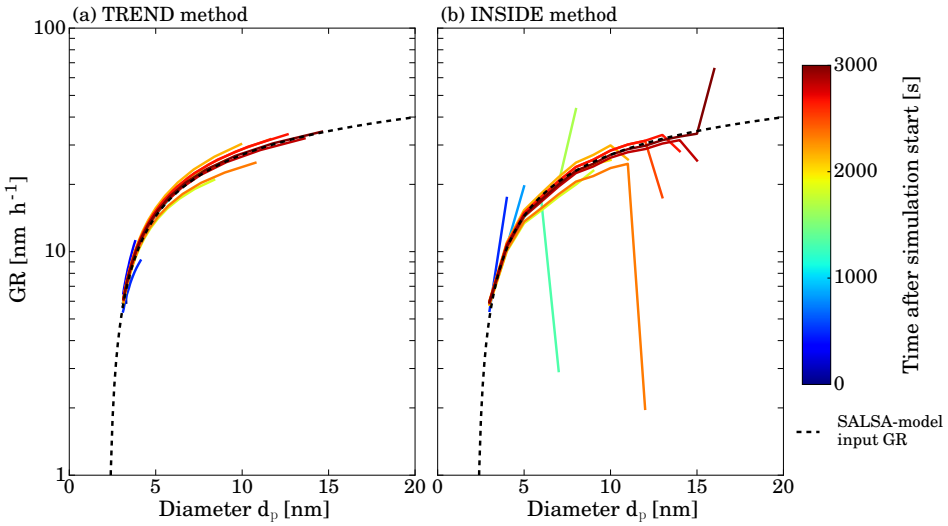

Figure 2: Results of the two GDE-based analysis methods on simulated input size distribution generated by the SALSA model. Panel **(a)** shows the results of the TREND method and panel **(b)** the results of the INSIDE method. The black dashed line represents the time-independent input growth rate function, and the solid lines the results of the two methods as a function of diameter. The color coding of the lines corresponds to the different times.

both methods are able to determine growth curves by analyzing $\frac{\mathrm{d}N}{\mathrm{d}\log d_\mathrm{p}}$ representations of number-size distributions especially for small particle sizes and low particle numbers. Statistical analysis of the deviation between the generated growth rate (SALSA) and results from the INSIDE and TREND method reflect this behavior. Each analyzed growth rate data point is compared to the SALSA input value at the same diameter. The mean relative deviation and the corresponding standard deviation are 1.2 and 5.0 % for the TREND method and 6.5 and 12.7 % for the INSIDE method, respectively. The effect of higher particle concentration and hence larger influence of coagulation has been investigated in similar simulations featuring higher nucleation rates and are discussed in Appendix 3.6.3. It seems that the TREND method works better for analyzing the leading edge of the newly formed particle size distributions, and it in general shows less scatter due to its integral method. On the other hand, the INSIDE method performed very well when analyzing GR at higher particle concentrations; however, it is more sensitive to scatter in the experimental input data which has to be considered when real data is analyzed. Note that statistical errors occurring especially during the measurement of low concentration aerosols may cause deviations between observed and analyzed growth rates.

3.4 Growth rate evaluation from chamber experiments

Both methods described above were used to analyze growth rates from NPF events produced in the aerosol chamber at the National Center for Atmospheric Research (NCAR) in Boulder, CO, USA. Experiments were performed in a 10 m^3 teflon bag which was continuously flushed by zero air at a flow rate of 40 $\mathrm{l\,min}^{-1}$. A biogenic volatile organic compound (VOC; α-pinene or β-caryophyllene) was added to the zero air until steady state concentrations of $\sim$ 4 ppb were obtained. Subsequently, a UV mercury lamp was turned on in one of the zero air lines to increase ozone in the chamber steadily and initiate ozonolysis of the VOC and subsequent NPF. For both experiments steady-state ozone concentrations of $\sim$ 25–30 ppb were reached at the end of the experiment. Additional details of the experimental setup can be found in Winkler et al. (2013). Evolution of the number-size distribution was monitored by a regular scanning mobility particle spectrometer (SMPS) and a prototype differential mobility analyzer train (DMA train). The DMA train uses several DMAs and condensation particle counters (CPCs) in parallel. Each DMA is set to transmit only particles of a specific mobility diameter to monitor the size evolution of individual sizes preferably in the sub-10 nm size range at high time resolution (on the order of seconds). Operation principles from a similar, advanced setup can be found in Stolzenburg et al. (2017).

Figure **??** shows combined size distribution measurements for particles from both VOCs. Details of the data inversion procedure can be found in Appendix 3.6.5. It can be clearly seen that not only the absolute particle yield is higher in the β-caryophyllene system, but

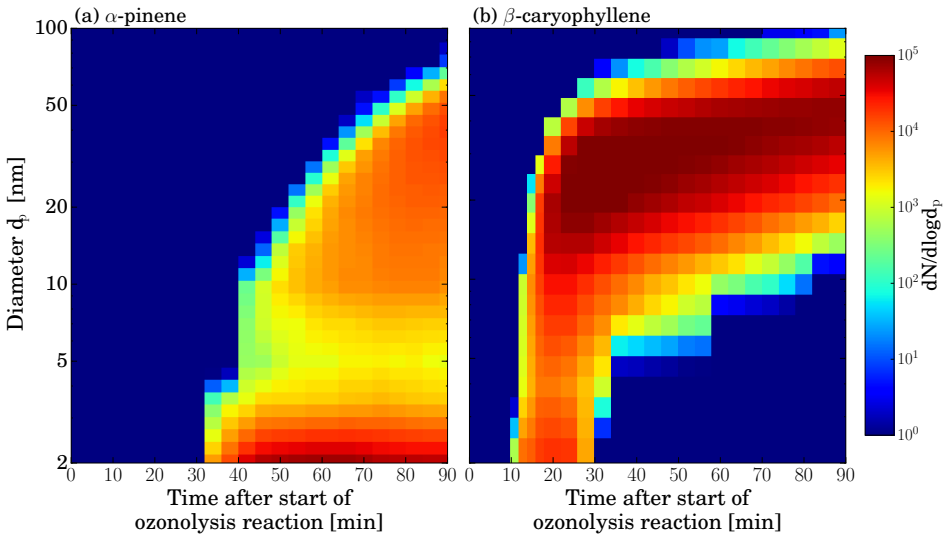

Figure 3: Combined, DMA train and SMPS data, showing size distribution evolution over time for the ozonolysis of two different VOCs. Panel **(a)** shows the α-pinene ozonolysis experiment and panel **(b)** the β-caryophyllene ozonolysis experiment. Transition between DMA train and SMPS measurement is at 14 nm.

also growth proceeds much faster than in the case of α-pinene. While the first appearance of particles is observed after $\sim$10 minute for the sesquiterpene, it takes roughly 3 times as long for the monoterpene. Obviously, there is quite different growth dynamics involved.

These different dynamics can be quantified by analyzing the evolution of the number-size distribution with the two methods described above. In Figure 2 the results for the α-pinene system are shown. Both methods show the same trend and similar absolute growth rate values. As already discussed during the test with simulated size distributions, the results of the TREND method do not cover the full size range at every time step due to the choice of the size interval number m. The INSIDE method on the other hand generally shows more scatter, especially in regions where counting statistics above the evaluation size d_{eval} are poor and therefore those results are greyed out.

This analysis reveals that growth rates above 10 nm have a negligible size dependence. However, a strong size dependence is seen below 10 nm with peak growth rates around 7 nm and strongly decreasing growth rates in the sub-5 nm size range, independent of the measurement time. This can be explained by a multi-component Kelvin effect, where some of the α-pinene reaction products can only participate in growth when particles have grown large enough to overcome the Kelvin barrier, as shown in Tröstl et al. (2016) for the α-pinene system. For the peak at 5 nm we can exclude the contribution of particle coagulation below the measurement size range (Olenius and Riipinen, 2017) as shown in Appendix 3.6.4.

Additionally, the results from the TREND method are compared with growth rate values calculated by the appearance time method in Figure 2c, as this method is used in other chamber studies (Tröstl et al., 2016). The appearance time method shows a similar trend

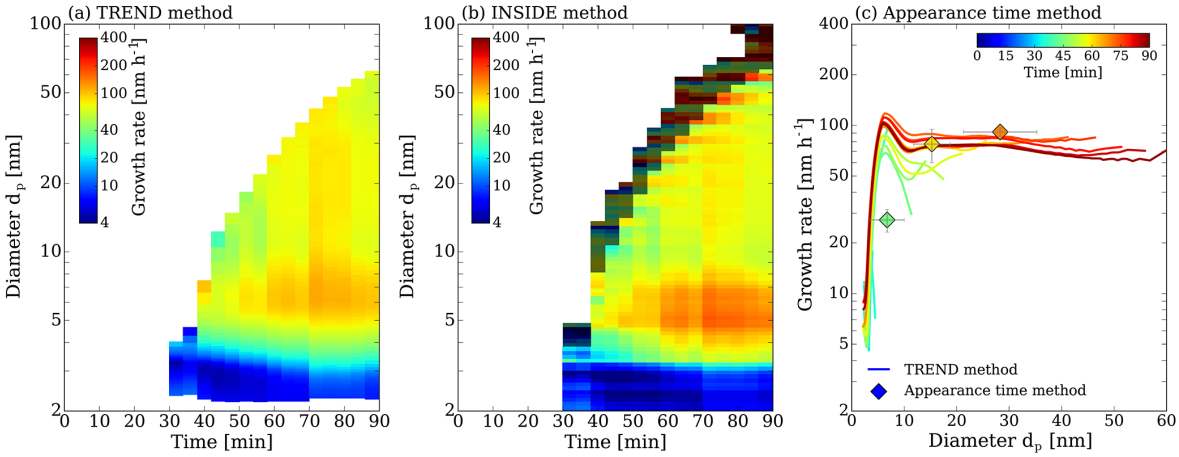

Figure 4: Growth rate analysis of the α-pinene ozonolysis experiment. Panel **(a)** shows the results of the TREND method, while panel **(b)** shows the results of the INSIDE method. The color coding represents the growth rates in nm h^{-1}. For the INSIDE method regions with low counting statistics are greyed out. Panel **(c)** shows a comparison of the growth rate analysis results obtained from the TREND method (continuous lines) with results from the widely used appearance time method (discrete points).

as TREND method for the three possible appearance time measurements. The appearance time method does not reveal the complete time and size dependencies of the growth, and could neither conclude about the observation of a multi-component Kelvin effect nor about the observed higher growth rates at around 5 nm. Moreover the TREND method shows the clear trend of increasing growth rates until a more or less steady state growth is reached. We speculate that this is due to the slow accumulation of condensable low-volatility vapors by the ozonolysis (proceeding at a rate constant of $k_{\alpha\mathrm{p.}\times\mathrm{O_3}}\ (293\,\mathrm{K}) = 9.06\times10^{-17}\,\mathrm{cm^3 molecule^{-1} s^{-1}}$; Atkinson et al., 2006) and subsequent auto-oxidation of α-pinene.

This seems to be completely different in the β-caryophyllene system. The results of the growth rate analysis are presented in Figure 3. The corresponding comparison of the results from the TREND method with the calculated growth rates from the appearance time method and with growth rates inferred by the lognormal distribution method are displayed in Figure 3c and both show good agreement. The lognormal distribution function method was not applied to the α-pinene data set as measured particle size distributions differ strongly from lognormal shape.

High growth rates at the beginning of the observed events are followed by a drop of growth rates in all sizes as the particle growth goes on. This can be explained by the very high oxidation potential and high reaction rates of β-caryophyllene, where the reaction rate constant for ozonolysis ($k_{\beta\mathrm{c.}\times\mathrm{O_3}}\ (298\,\mathrm{K}) = 1.2\times10^{-14}\,\mathrm{cm^3 molecule^{-1} s^{-1}}$ (Richters et al., 2015)) is three orders of magnitude higher than in the case of α-pinene. Condensable vapors are therefore quickly formed and the steady state β-caryophyllene concentration at the beginning of the experiment is depleted by this fast reaction. Together with the fast build up of a large

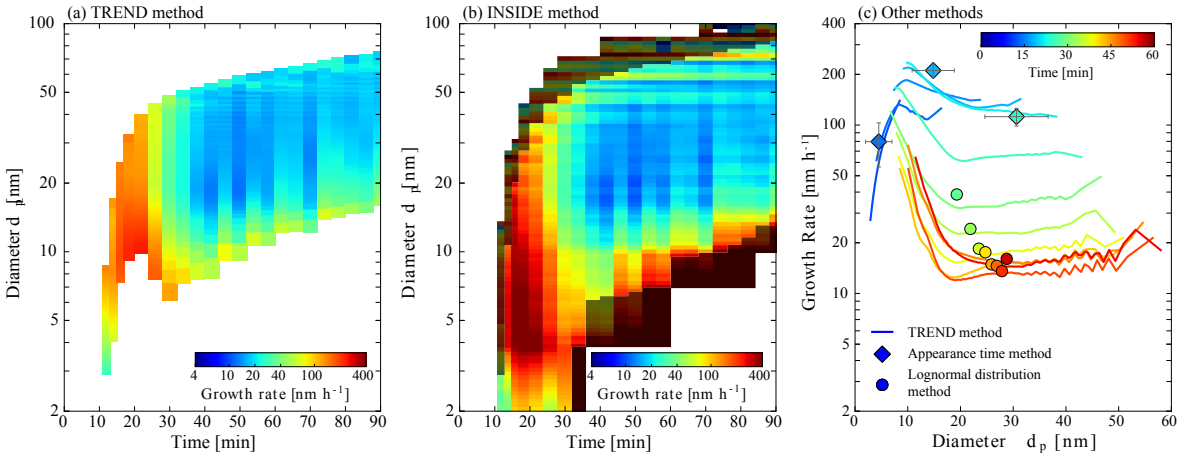

Figure 5: Growth rate analysis of the β-caryophyllene ozonolysis experiment. Panel **(a)** shows the results of the TREND method, while panel **(b)** shows the results of the INSIDE method. The color coding represents the growth rates in nm h^{-1}. For the INSIDE method, regions with low counting statistics are greyed out. Panel **(c)** shows a comparison of the growth rate analysis results obtained from the TREND method (continuous lines) with results from two other methods, namely the appearance time method and the lognormal distribution method (discrete diamonds and circles, respectively).

condensational sink, this shuts off new particle formation and reduces the fast growth rates.

In such a highly dynamic case it becomes evident that time resolution greater than the 240 s from the SMPS scans would yield a better data set for the applied analysis methods. Additionally, when the particles reach larger sizes, the higher total particle number concentration increases the influence of coagulation and might disturb the results derived at small sizes. Moreover, due to the higher particle number concentrations in the growing mode, the inferred size range of the growth rates by the TREND method shrinks. A more detailed discussion of the uncertainties of the two methods can be found in Appendix 3.6.6. In general, the biggest sources of errors are low time resolution of the measurement data and scattering of the experimental data. Further, a source of high potential error is coagulation. For the experimental data presented in this work, the estimated error of the GR determination associated with the analysis tools is typically in the range from 2 to 35 % depending on the analysis method and the experiment.

Despite the challenges in the highly dynamic case of β-caryophyllene ozonolysis, both methods reveal that the size dependence of the growth rates is most significant in the sub-10 nm region, as in the case of α-pinene. Moreover, the INSIDE method still covers the full size range for the analysis of the size dependence. When new particles are formed at the beginning of the experiment it reveals extremely high growth rates of up to 250 nm h^{-1} between 5 and 10 nm. Similar to the case of α-pinene, but somewhat less significant, are the lower growth rates in the sub-3 nm range. The smaller reduction of growth in that size range indicates that the vapors produced from the ozonolysis of β-caryophyllene are less volatile compared to the

products of α-pinene and can therefore participate in growth starting from the smallest sizes and greater. This is predictable because a sesquiterpene with 15 carbon atoms will be less volatile than a monoterpene (e.g., Donahue et al., 2011).

3.5 Conclusions

We presented two methods to determine size- and time-dependent growth rates by analyzing particle size distributions and solving the GDE. The TREND method tracks regions of the number-size distribution. The INSIDE method is based on interpreting the size-integrated GDE, and determines growth rates at certain d_{eval}.

Both methods reliably reproduce input growth rates from simulated size distributions and allow for quantitative comparison. The TREND method generally shows less scatter and less sensitivity to low counting statistics but cannot always cover the full range of particle sizes where growth is actually observed. The INSIDE method is capable of determining growth rates wherever particles are measured. However, determination of growth rates at very low or very high particle concentrations may suffer from considerable errors. This is due to insufficient counting statistics of the measured input data on the one hand, and considerable coagulation effects on the other hand. While coagulation is typically considered in the GDE analysis a precise description of coagulation requires detailed knowledge of the aerosol properties (e.g., inter-particle forces or shape; Chan and Mozurkewich, 2001), which are typically unknown for newly formed particles. Moreover, coagulation will become more important when ambient data with high background aerosol loadings are considered. Theoretically, both methods could directly incorporate a background aerosol as long as it can be separated from the nucleation mode. A more detailed implementation of background aerosol and coagulation effect will be necessary for the application of the methods to ambient data sets.

We applied our methods to experimental size distribution data from chamber studies to derive size- and time-dependent growth rates from ozonolysis of two different biogenic VOC precursors. Both methods agree well with the widely used appearance time method and provide valuable insights on some unexpected details of the growth dynamics in these systems.

For both studied VOC systems, a strong increase in growth rates was found for the smallest diameters until a maximum value was reached at around 7 nm. This finding strongly suggests that (biogenic) growth is governed by a multi-component Kelvin effect which allows for condensation of vapor molecules only if the particles exceed a certain size. This observation is very pronounced in the case of a-pinene and was reported independently from other studies (Winkler et al., 2012; Tröstl et al., 2016). For the β-caryophyllene system, it is less significant, indicating that the majority of β-caryophyllene ozonolysis products are generally less volatile and can participate in growth at particle diameters well below 10 nm. This system

showed highly dynamic behavior and fast changing growth rates over time, as the condensable vapors quickly became depleted in the chamber due to the high reactivity of β-caryophyllene and low-volatility reaction products. Growth rates above 10 nm generally showed only minor size dependence. Regarding the different nanoparticle-forming behavior of monoterpenes and sesquiterpenes, similar findings were recently reported from plant emission studies in a chamber environment (Zhao et al., 2017).

Our analysis underline the critical need to accurately quantify growth dynamics in the sub-10 nm size range. This range is crucially important for the survival probability of newly formed particles and clearly features the biggest changes in growth rates. One of the prerequisites for the successful application of our newly developed methods is having size distribution measurements providing time resolution below 1 min and good counting statistics. We see these requirements fulfilled in latest state-of-the-art instrumentation (Jiang et al., 2011a; Stolzenburg et al., 2017), allowing full exploitation of growth dynamics in the future. We also plan to make the analysis tool kit publicly available in order to allow for wide application and improvement by the scientific community.

Author contributions

P. M. W., J. O., T. K., P. H. M. and J. N. S. performed the experiments; L. P., **D. S.**, P. M. W. and P. H. M. developed the analysis tools; **D. S.** and L. P. analyzed the data; H. K., A. L. and K. E. J. L. provided the simulation input; L. P., **D. S.**, P. H. M., K. E. J. L. and P. M. W. were involved in the scientific interpretation and discussion; and L. P., **D. S.** and P. M. W. wrote the manuscript.

Acknowledgements

This work was supported by the European Research Council under the European Community's Seventh Framework Programme (FP7/2007–2013)/ERC grant agreement no. 616075. Peter H. McMurry's work was supported by U.S. DOE grant DE-SC0011780. James N. Smith acknowledges funding from DOE under grant no. DE-SC0014469. The National Center for Atmospheric Research is supported by the National Science Foundation.

3.6 Appendix

3.6.1 Description of the software tool used to interpret the experimental data

The flowchart contained in Figure **??** outlines the data analysis method. In the first step, number-size distributions measured or generated by means of computer simulation are transformed from $\frac{\mathrm{d}N}{\mathrm{d}\log d_\mathrm{p}}$ representation to bin concentration. This includes an automatic fitting process since the incoming data provides information at given diameters (i.e., no analytical function). The representation of the particle size distribution is similar to the so-called hybrid structure (Chen and Lamb, 1994) and features a fixed size grid containing uniform distributions each having an upper and a lower limit and a number density (i.e., a particle number concentration per diameter interval). Integration of number density from the lower to the upper size limit results in the number concentration within the bin. This structure allows for calculation of coagulation and phase transition without suffering from numerical diffusion. Furthermore, it provides continuous-like number-size distributions which are required to minimize numerical error in the growth rate calculation. A more detailed description can be found elsewhere (Pichelstorfer and Hofmann, 2015).

The input (experimental or simulated) number-size distribution (at time t_j) and wall loss information are used to calculate dynamical changes to the aerosol that occur during the period of time between two measurements. These changes include coagulation, deposition and dilution. Note that the influence of particles smaller than a minimum diameter $d_{\mathrm{p,min}}$ is not considered in this simulation. Details of the aerosol dynamics module can be found in Appendix 3.6.2. The result of the aerosol dynamics simulation is a simulated particle size distribution at time t_{j+1} which is then compared to the measured particle size distribution at time t_{j+1} to determine the growth rate.

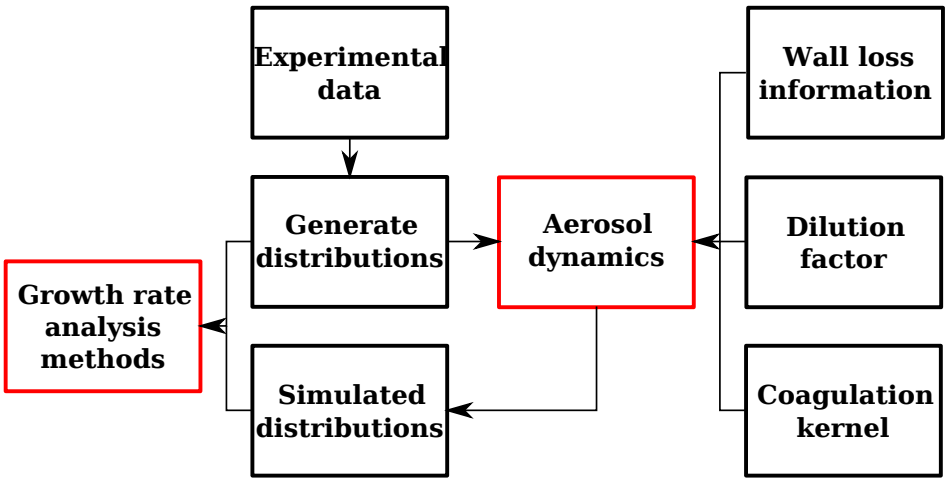

Figure 6: Flow chart describing the principle of the data analysis.

3.6.2 Description of the aerosol dynamics module

Figure 4 outlines the procedure of the aerosol dynamics module. An experimentally determined particle size distribution $n_{\mathrm{exp}}(t_j, d_{\mathrm{p}})$ measured at time t_j enters the integration time loop (ordinary Eulerian forward integration). The aerosol altering processes, namely dilution, coagulation and deposition, are calculated sequentially. A control parameter C is used to ensure that relative changes done to the distribution are below a certain maximum value (e.g., 0.1 % relative change in particle concentration within a time step) to enable quasi-simultaneous calculation of the processes. If the change is larger than this limit, changes during this integration time step are ignored and the integration time step Δt is divided by 2. Otherwise the distribution is updated and system time t_i is increased by Δt. That way integration time steps are optimized in order to save computational time and achieve desired accuracy.

The result of the aerosol dynamics module is a simulated distribution $n_{\mathrm{sim}}(t_{j+1}, d_{\mathrm{p}})$ at time t_{j+1}. This distribution was generated neglecting the influence of nucleation, coagulation of particles smaller than $d_{\mathrm{p,min}}$ and phase transition. Coagulation is described by numerically solving a discrete version of the Smoluchowski equation (Smoluchowski, 1917):

$$\frac{\mathrm{d}n_k}{\mathrm{d}t} = -\sum_{i=1}^{s} \beta_{ik}(..) n_i n_k + \frac{1}{2} \sum_{f(i+j)=f(k)} \beta_{ij}(..) n_i n_j, \tag{10}$$

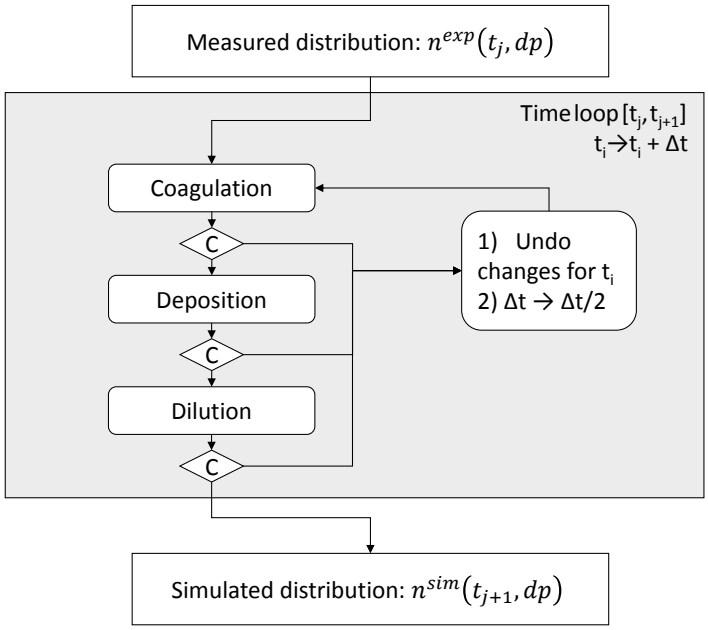

Figure 7: Flow diagram of the aerosol dynamics model calculating the changes to a particle size distribution $n_{\mathrm{exp}}(t_j, d_{\mathrm{p}})$ within the time interval $[t_j, t_{j+1}]$. C stands for control parameter and t stands for time.

where n_k is the number concentration within size bin k, t is time and β_{ik} is the coagulation coefficient describing the probability of two particles of size bin i and k, respectively, to collide with each other. Collisions are assumed to be 100 % effective. Furthermore, the only coagulation mechanism considered is thermal coagulation of neutral (i.e., uncharged) particles. A potential error caused by neglecting additional inter-particle forces is discussed and estimated in Appendix 3.6.6. A more detailed description of the solution can be found elsewhere (Pichelstorfer et al., 2013).
Wall loss of particles is described by

$$\frac{\mathrm{d}n_i}{\mathrm{d}t} = -\beta_{\mathrm{wall},i} \cdot n_i, \tag{11}$$

where $\beta_{\mathrm{wall},i}$ is the size-dependent wall loss coefficient determining the loss of particles of size i per second. In the present work the wall loss rate is obtained from literature for particles larger than 12 nm (Fry et al., 2014). For smaller particles, the loss rate was estimated based on experimental data using a method described by Crump and Seinfeld (1981).
Dilution is described similarly to wall loss. For the description of dilution we assume that the chamber is well mixed (i.e., no concentration gradients, which has been verified in the NCAR chamber using CO_2 tracer experiments). Thus, dilution can be described analogously to wall loss by applying a size-independent loss coefficient, which can be determined from dilution flow and chamber volume.
The result of the simulation is a particle size distribution $n_{\mathrm{sim}}(d_{\mathrm{p}}, t_{j+1})$ which is calculated based on the experimentally determined number-size distribution at time t_i, $n_{\mathrm{exp}}(d_{\mathrm{p}}, t_j)$.

3.6.3 Performance in the case of high particle concentrations

In order to test the models' performance when coagulation must be considered, similar simulations featuring higher nucleation rates ($J = 3000\,\mathrm{particles\,cm^{-3}\,s^{-1}}$) were considered.
Figure 5 depicts analyzed GR and set growth rate, respectively, against particle diameter for two different simulations using TREND method. Results in panel a were calculated neglecting coagulation while for the results shown in panel b, the effect of coagulation was included. Clearly panel b shows better agreement between the theoretical curve and the analysis result for small particle diameters. As particles get larger, the data points start to scatter. This is caused by the different representations of the particle size distributions by the analysis software and SALSA model. However, note that equations used to calculate the coagulation kernel are the same for both models.
We therefore conclude that our methods can handle the effects of coagulation, and the small discrepancies of this test analysis are due to different simulation representations, which will not occur when experimental data sets are used. However, in the cases of low particle growth rates and high coagulation sinks, the effects of coagulation might become more important

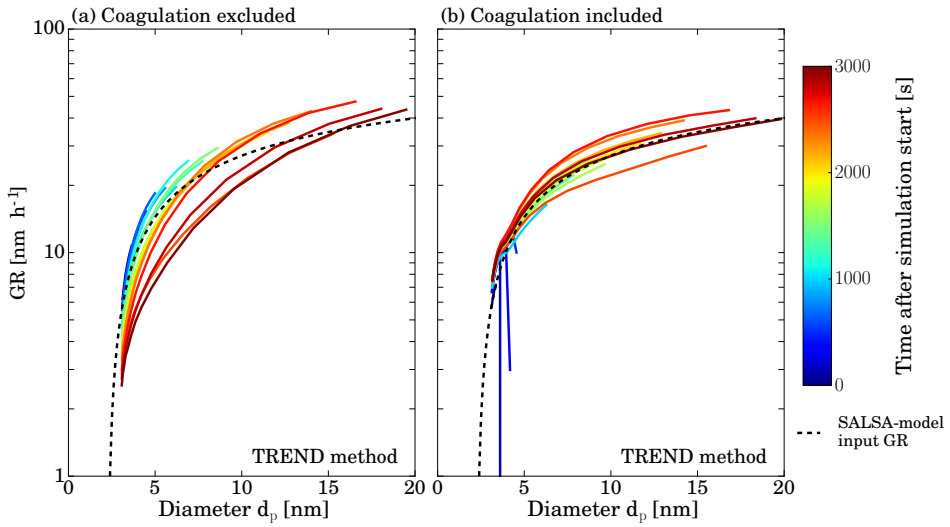

Figure 8: Analyzed (straight lines) and set growth rate (dashed lines) as a function of particle diameter. Panel **(b)** shows results obtained by considering the effect of coagulation while results depicted by panel **(a)** were determined neglecting coagulation.

and a more detailed quantification of coagulation effects might be necessary.

3.6.4 Potential effect of particles below the detection limit on the growth rate

As described in Sect. 3.2.2 both methods of the developed growth rate analysis do not take into account the interaction with particles smaller than the size detected experimentally (i.e., below 3 nm in diameter). This effect is known to cause difficulties in aerosol dynamics simulations (Olenius and Riipinen, 2017). While it is rather unlikely that those small particles affect the deposition of larger particles to the chamber walls significantly, they might cause additional particle growth due to coagulation. Neglecting this contribution might cause an overestimation of the growth rate.

In order to estimate the effect of particle coagulation of sub-detectable sizes on the growth rate, we first generate a particle size distribution based on McMurry (1980). McMurry considers the formation rate of condensable monomers by chemical reaction and their subsequent growth to larger particles by coagulation. In this, dimensionless equations were solved numerically to generate dimensionless number-size distributions. The dimensionless number-size distributions used in this work were determined similarly to this method but using a different model representation of the number-size distribution (McMurry and Li, 2017) and converted to a dimensional representation by using the following parameters (adjusted for oxidation products of α-pinene, according to Kirkby et al., 2016):

- particle density of 0.5 to 2 g cm^{-3};
- monomer volume of 0.2 to 0.8 nm^3 (based on the density and an estimated molecular

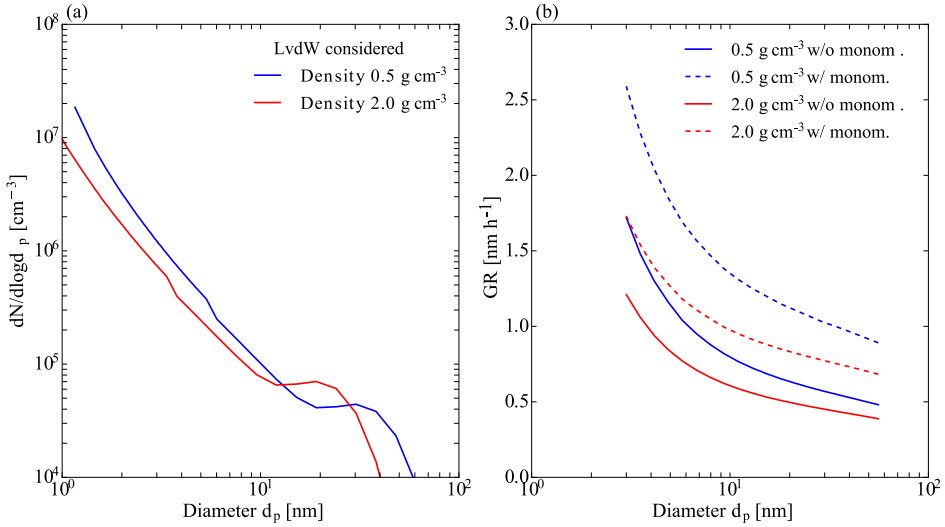

Figure 9: Effects of sub-$d_{\mathrm{p,min}}$ particles. **(a)** Number size distribution derived from dimensionless results calculated for a collision-controlled limit according to McMurry and Li (2017). LvdW stands for London van der Waals forces, which are taken into account in calculating the resulting size distributions. **(b)** GR ($\mathrm{nm\,h^{-1}}$) resulting from collisions with sub-$d_{\mathrm{p,\,min}}$ particles as a function of particle diameter for particle density of 0.5 and 2 $\mathrm{g\,cm^{-3}}$. Further, collisions with monomers are considered (w/monom.) and neglected (w/o monom).

mass of 246 $\mathrm{g\,mol^{-1}}$ for the condensable vapor);

- monomer formation rate of $4.4 \times 10^4\,\mathrm{s^{-1}\,cm^{-3}}$, estimated based on O_3 and α-pinene concentration considering a reaction constant of $k_{\alpha\mathrm{p.}\times O_3}$ (278 K) $\approx 4.0 \times 10^{-17}\,\mathrm{cm^3}$ $\mathrm{molecule^{-1}\ s^{-1}}$ (Atkinson et al., 2006) and highly oxidized molecule (HOM) formation probability of 2.9 % at 278 K for the reaction product (Kirkby et al., 2016).

The resulting number-size distributions are depicted by Figure 6. Obviously, concentrations in the detectable size range (i.e., larger than 3 nm for the given experiments) suggested by the numerical method are much higher than measured ones. This might be caused by the fact that our basic approach to this numerical method neglects wall losses. However, we concluded that the number-size distributions determined may still be used to estimate a maximum contribution of sub-3 nm particles to the growth rate.

The number-size distribution in the diameter range from 0.8 to 3 nm was divided in five logarithmically spaced sections. In the next step the contribution to the growth rate per hour of a particle due to coagulation with particles (constant concentration of 1 particle $\mathrm{cm^{-3}}$) in each of the sections is computed. The coagulation kernels are determined using a formulation for the transition regime (e.g., Hinds, 1999).

Multiplication of this growth rate function by the number-size distribution as determined above results in the growth rate ($\mathrm{nm\,h^{-1}}$) of particles larger than 3 nm due to coagulation (see Figure 6b). For the sake of completeness we also plotted the effect considering monomer addition (i.e., condensational growth). The maximum effect on growth is around 1.7 $\mathrm{nm\,h^{-1}}$

for a particle density of $2\,\mathrm{g\,cm^{-3}}$ and around $1.2\,\mathrm{nm\,h^{-1}}$ for a particle density of $0.5\,\mathrm{g\,cm^{-3}}$. Comparing these numbers to Figs. 2 and 3 in the main text we find a maximum contribution of roughly 10 % for α-pinene experiments and roughly 5 % for β-caryophyllene. For most of the growth rates determined, this coagulation effect is on the order of 1–2 %. Further note that the numerical model proposed by McMurry (1980) is based on a collision-controlled particle formation regime suggesting rather high particle concentrations which, at least in the range above 3 nm, are not found experimentally. Thus the GR shown by Figure 6b can be seen as an estimate on the upper limit of the contribution of sub-3 nm particles to the growth rate.

3.6.5 Data inversion for DMA train and SMPS

For the experimental data obtained at the NCAR biogenic aerosol chamber a combined data inversion procedure for the DMA train and the SMPS measuring the same aerosol source is applied. Both instruments rely on electrical mobility analysis done by differential mobility analyzers (DMAs). While the SMPS operates one DMA in scanning mode, the DMA train operates five DMAs in parallel at fixed voltages and hence particle sizes. Data inversion is based on the procedure of Stolzenburg and McMurry (2008):

$$\left.\frac{\mathrm{d}N}{\mathrm{d}\ln d_\mathrm{p}}\right|_{d_\mathrm{p}^*} = \frac{N \cdot a^*}{\beta \cdot f_\mathrm{c}(d_\mathrm{p}^*) \cdot \eta_\mathrm{sam}(d_\mathrm{p}^*) \cdot \eta_\mathrm{cpc}(d_\mathrm{p}^*) \cdot \eta_\mathrm{dma}(d_\mathrm{p}^*)}\,, \tag{12}$$

where N is the measured raw concentration downstream of the DMA, which is operated to select a centroid diameter d_p^*, β is the ratio of aerosol-to-sheath flow in the DMA, $a^* = (-\mathrm{d}\ln Z/\mathrm{d}\ln d_\mathrm{p})|_{d_\mathrm{p}^*}$, f_c is the charging efficiency for singly charged particles and η_sam describes the total sampling losses, η_cpc the condensation particle counter's activation efficiency and η_dma the inlet and outlet penetration efficiencies of the used DMA.

Note that for both instruments most of the parameters are distinct. Sampling efficiencies are inferred from sampling line lengths, sample flow rates and classified diameters and assumed to follow the diffusional losses according to Gormley and Kennedy (1948), which are different for the SMPS system and the DMA train. CPC activation curves η_cpc depend on the used particle counters, a TSI Inc. model 3760 for the SMPS, and four TSI Inc. model 3025A CPCs and one modified TSI model 3775, which uses diethylene glycol as working fluid (Iida et al., 2009; Jiang et al., 2011b), for the DMA train. DMA penetration efficiencies η_dma differ as well, as the DMA train used five TSI model 3085A nano-DMAs, and the SMPS used one long column DMA, TSI model 3081.

Moreover, Equation (7) only considers singly charged particles. Bipolar charging probabilities below 100 nm are generally dominated by singly charged particles (Fuchs, 1963). Only a doubly charge correction was therefore applied for the SMPS data. With the SMPS data fully corrected, it could be used to calculate the expected doubly charged contribution on the raw DMA train signal by considering the different losses for the DMA train system. We find

that the contribution of doubly charged particles in the DMA train measurement range is completely negligible in the two considered experiments.
In both of the measurements presented above, the SMPS measured down to 10 nm in size and at least one DMA train channel was fully overlapping with the measured size distribution of the SMPS. In the overlapping size channel at 14 nm small deviations ($< 20\,\%$) between the instruments were found. This is most probably due to uncertainties in the input of the inversion procedure, e.g., material dependencies in applied CPC counting efficiencies (Kangasluoma et al., 2014) and deviations from the assumed sampling penetration efficiencies through the usage of bent tubing (Wang et al., 2002). Therefore the SMPS spectra were normalized to fit perfectly in the overlapping region. This procedure might however cause some uncertainties in the presented analysis.
Furthermore, the DMA train does not rely on a scanning procedure and therefore acquires concentration data at the fixed sizes within each second. The SMPS requires 120 s to scan from low voltage to high voltage and another 120 s to reverse. The results from each d_p bin are averaged resulting in a complete size distribution every 240 s. The DMA train data were then averaged over the scanning cycle of the SMPS. This basically provided the necessary counting statistics for the DMA train channels below 10 nm where particle penetration and charging efficiencies are usually very low. For the case of α-pinene two runs under similar conditions (same ozone and α-pinene concentrations) were performed and averaged in order to improve the quality of the measured size distributions.

3.6.6 Errors of the analysis methods

In the following potential errors of the analysis methods TREND and INSIDE are discussed. Note that errors originating from the experiment are not part of this section, which solely describes the error caused by the analysis methods itself. Both analysis methods are not exact as they are derived from quantities that are either averaged (with respect to time and/or particle diameter) or generated by means of numerical simulation.
Further, both methods rely on simulated particle size distributions. In case coagulation is not dominant (as it is the case in the present work) the error due to numerical simulation can be neglected. Other simulation errors may originate from dilution of the aerosol and particle wall losses. Given that these processes are known (i.e., determined experimentally), the simulation result is on the order of 0.1 %.
An additional source of uncertainty is the fact that particle growth cannot be taken into account for the calculation of other dynamic processes since it is determined from the simulated data. This affects coagulation and wall losses. In order to estimate the effect of particle growth on the calculation of wall loss, the change in median diameter determined by the TREND method is considered. For α-pinene we find an average change ($\Delta\ d_\mathrm{p}$) of 34 % with a standard deviation of 14 %. β-caryophyllene shows a change of 46 % with a standard devia-

tion of 25 %. Thus, the software underestimates the particle diameter and, as a consequence, overestimates deposition. To estimate the effect on the growth rate, the simulations are repeated with an altered wall loss mechanism: for the determination of wall loss the particle diameters are increased by $\Delta\ d_\mathrm{p}$. The resulting average change in the GR is less than 2 % for α-pinene and less than 4 % for β-caryophyllene.
Considering inter-particle forces (Chan and Mozurkewich, 2001) enhancing coagulation results in an average error of less than 2 % for both experimental data sets (note that an increase in coagulation coefficient due to inter-particle forces by a factor of 5 was assumed). INSIDE and TREND determine growth rates for a certain time interval Δt which limits the time resolution. To estimate the resulting relative error we consider the growth rate at a certain diameter and at various points in time:

$$\Delta\mathrm{GR}\left(d_\mathrm{p}, t_i\right) = \left[1 - \frac{\mathrm{GR}\left(d_\mathrm{p}, t_{i-1}\right) + \mathrm{GR}\left(d_\mathrm{p}, t_{i+1}\right)}{2 \cdot \mathrm{GR}\left(d_\mathrm{p}, t_i\right)}\right] \cdot \frac{2 \cdot \Delta t}{t_{i+1} - t_{i-1}}. \tag{13}$$

The mean resulting error and corresponding standard deviation are 0.4 and 7.6 %, respectively, for the α-pinene data, and 7.2 and 26.4 % for β-caryophyllene.
The TREND method calculates growth rates for m regions of the number-size distribution. For all input data we varied m from 10 to more than 500 and found that the results are quite stable. The smaller the m, the wider the region and hence the larger the diameter range the GR is attributed to, so the method has a lower size resolution but lowers the statistical uncertainties if one region is defined by several measured particle size distribution intervals. Increasing m above the number of input size distribution channels generally will not increase the performance of the model significantly. In the present work the number-size distribution is typically divided into 100 regions each containing 1/100 of the total particle number concentration. Accordingly, regions have an average width of 2 % and a standard deviation of 5 % for the two experimental data sets considered.
To conclude, for experiments with α-pinene and β-caryophyllene, the main error regarding the growth rate results from the choice of time period between two determinations of the growth rates. Further, the choice of the width of the regions in the TREND method is important. Both quantities can be reduced to limit the errors. However, note that a reduction increases errors due to scattering inputs from the measurement system. The only error which cannot be influenced is the error due to numerical simulation which is typically negligible ($\sim$ 0.1 %) in the case coagulation does not play a dominant role.

3.6.7 Input data for SALSA simulations

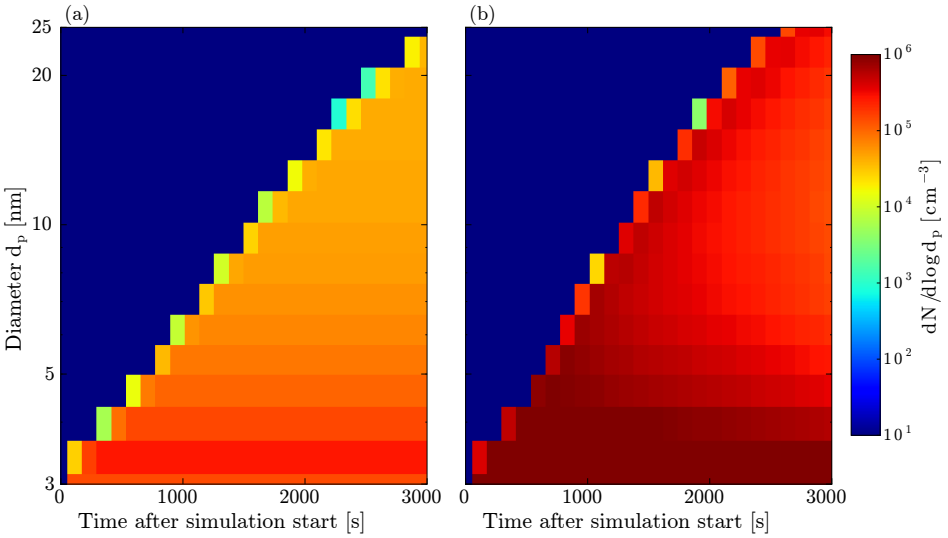

Figure 10: Size distributions generated by the SALSA module and used for the testing of the analysis methods in Sect. 3.3. Panel **(a)** shows the input used for Figure 1, while panel **(b)** shows the input with a higher formation rate used for Figure 5.

Data used for	T (K)	J_3 (cm^{-3} s^{-1})	β_{wall} (s^{-1})	GR (nm h^{-1})	Output
Figure 1	293.15	10	$0.0059 \cdot d_{\mathrm{p}}^{-1.0341}$	$(70-5) \cdot \frac{d_{\mathrm{p}}^{0.01}-1.0110}{1.0471-1.011} + 5$	every 120 s
Figure 5	293.15	3000	$0.0059 \cdot d_{\mathrm{p}}^{-1.0341}$	$(70-5) \cdot \frac{d_{\mathrm{p}}^{0.01}-1.0110}{1.0471-1.011} + 5$	every 120 s

Table 1: Input data used to generate particle size distributions with the SALSA module. J_3 depicts the nucleation rate (i.e., the number concentration of particles being added to the 3 nm sized particles per second).

3.7 References

Atkinson, R., Baulch, D. L., Cox, R. A., Crowley, J. N., Hampson, R. F., Hynes, R. G., Jenkin, M. E., Rossi, M. J., Troe, J., and Subcommittee, I.: Evaluated kinetic and photochemical data for atmospheric chemistry: Volume II - gas phase reactions of organic species, Atmos. Chem. Phys., 6, 3625–4055, doi:10.5194/acp-6-3625-2006, http://www.atmos-chem-phys.net/6/3625/2006/, updated values of the rate constant can be found on the IUPAC website at http://iupac.pole-ether.fr/htdocs/datasheets/pdf/Ox_VOC8_O3_apinene.pdf, 2006.

Chan, T. W. and Mozurkewich, M.: Measurement of the coagulation rate constant for sulfuric acid particles as a function of particle size using tandem differential mobility analysis, J. Aerosol Sci., 32, 321 – 339, doi:http://dx.doi.org/10.1016/S0021-8502(00)00081-1, http://www.sciencedirect.com/science/article/pii/S0021850200000811, 2001.

Chen, J. and Lamb, D.: Simulation of Cloud Microphysical and Chemical Processes Using a Multicomponent Framework. Part I: Description of the Microphysical Model, J. Atmos. Sci., 51, 2613–2630, doi:10.1175/1520-0469(1994)051<2613:SOCMAC>2.0.CO;2, http://dx.doi.org/10.1175/1520-0469(1994)051<2613:SOCMAC>2.0.CO;2, 1994.

Crump, J. G. and Seinfeld, J. H.: Turbulent deposition and gravitational sedimentation of an aerosol in a vessel of arbitrary shape, J. Aerosol Sci., 12, 405 – 415, doi:http://dx.doi.org/10.1016/0021-8502(81)90036-7, www.sciencedirect.com/science/article/pii/0021850281900367, 1981.

Donahue, N. M., Epstein, S. A., Pandis, S. N., and Robinson, A. L.: A two-dimensional volatility basis set: 1. organic-aerosol mixing thermodynamics, Atmos. Chem. Phys., 11, 3303–3318, doi:10.5194/acp-11-3303-2011, http://www.atmos-chem-phys.net/11/3303/2011/, 2011.

Fry, J. L., Draper, D. C., Barsanti, K. C., Smith, J. N., Ortega, J., Winkler, P. M., Lawler, M. J., Brown, S. S., Edwards, P. M., Cohen, R. C., and Lee, L.: Secondary Organic Aerosol Formation and Organic Nitrate Yield from NO3 Oxidation of Biogenic Hydrocarbons, Environ. Sci. Technol., 48, 11 944–11 953, doi:10.1021/es502204x, http://dx.doi.org/10.1021/es502204x, 2014.

Fuchs, N. A.: On the stationary charge distribution on aerosol particles in a bipolar ionic atmosphere, Geofisica pura e applicata, 56, 185–193, doi:10.1007/BF01993343, http://dx.doi.org/10.1007/BF01993343, 1963.

Gordon, H., Kirkby, J., Baltensperger, U., Bianchi, F., Breitenlechner, M., Curtius, J., Dias, A., Dommen, J., Donahue, N. M., Dunne, E. M., Duplissy, J., Ehrhart, S., Flagan, R. C., Frege, C., Fuchs, C., Hansel, A., Hoyle, C. R., Kulmala, M., Kürten, A., Lehtipalo, K., Makhmutov, V., Molteni, U., Rissanen, M. P., Stozkhov, Y., Tröstl, J., Tsagkogeorgas, G., Wagner, R., Williamson, C., Wimmer, D., Winkler, P. M., Yan, C., and Carslaw, K. S.: Causes and importance of new particle formation in the present-day and preindustrial atmospheres, J. Geophys. Res.-Atmos., 122, doi:10.1002/2017JD026844, http://dx.doi.org/10.1002/2017JD026844, 2017JD026844, 2017.

Gormley, P. G. and Kennedy, M.: Diffusion from a Stream Flowing through a Cylindrical Tube, P. Roy. Irish Acad. A, 52, 163–169, 1948.

Heisler, S. and Friedlander, S.: Gas-to-particle conversion in photochemical smog: Aerosol growth laws and mechanisms for organics, Atmos. Environ., 11, 157 – 168, doi:http://dx.doi.org/10.1016/0004-6981(77)90220-7, www.sciencedirect.com/science/article/pii/0004698177902207, 1977.

Hinds, W.: Aerosol technology: properties, behavior, and measurement of airborne particles, New York: Wiley, 1999.

Iida, K., Stolzenburg, M. R., and McMurry, P. H.: Effect of Working Fluid on Sub-2 nm Particle Detection with a Laminar Flow Ultrafine Condensation Particle Counter, Aerosol Sci. Tech., 43, 81–96, doi:10.1080/02786820802488194, http://dx.doi.org/10.1080/02786820802488194, 2009.

Jiang, J., Attoui, M., Heim, M., Brunelli, N. A., McMurry, P. H., Kasper, G., Flagan, R. C., Giapis, K., and Mouret, G.: Transfer Functions and Penetrations of Five Differential Mobility Analyzers for Sub-2 nm Particle Classification, Aerosol Sci. Tech., 45, 480–492, doi:10.1080/02786826.2010.546819, http://www.tandfonline.com/doi/abs/10.1080/02786826.2010.546819, 2011a.

Jiang, J., Chen, M., Kuang, C., Attoui, M., and McMurry, P. H.: Electrical Mobility Spectrometer Using a Diethylene Glycol Condensation Particle Counter for Measurement of Aerosol Size Distributions Down to 1 nm, Aerosol Sci. Tech., 45, 510–521, doi:10.1080/02786826.2010.547538, http://www.tandfonline.com/doi/abs/10.1080/02786826.2010.547538, 2011b.

Kangasluoma, J., Kuang, C., Wimmer, D., Rissanen, M. P., Lehtipalo, K., Ehn, M., Worsnop, D. R., Wang, J., Kulmala, M., and Petäjä, T.: Sub-3 nm particle size and composition dependent response of a nano-CPC battery, Atmos. Meas. Tech., 7, 689–700, doi:10.5194/amt-7-689-2014, http://www.atmos-meas-tech.net/7/689/2014/, 2014.

Kirkby, J., Duplissy, J., Sengupta, K., Frege, C., Gordon, H., Williamson, C., Heinritzi, M., Simon, M., Yan, C., Almeida, J., Tröstl, J., Nieminen, T., Ortega, I. K., Wagner, R., Adamov, A., Amorim, A., Bernhammer, A.-K., Bianchi, F., Breitenlechner, M., Brilke, S., Chen, X., Craven, J., Dias, A., Ehrhart, S., Flagan, R. C., Franchin, A., Fuchs, C., Guida, R., Hakala, J., Hoyle, C. R., Jokinen, T., Junninen, H., Kangasluoma, J., Kim, J., Krapf, M., Kürten, A., Laaksonen, A., Lehtipalo, K., Makhmutov, V., Mathot, S., Molteni, U., Onnela, A., Peräkylä, O., Piel, F., Petäjä, T., Praplan, A. P., Pringle, K., Rap, A., Richards, N. A. D., Riipinen, I., Rissanen, M. P., Rondo, L., Sarnela, N., Schobesberger, S., Scott, C. E., Seinfeld, J. H., Sipilä, M., Steiner, G., Stozhkov, Y., Stratmann, F., Tomé, A., Virtanen, A., Vogel, A. L., Wagner, A. C., Wagner, P. E., Weingartner, E., Wimmer, D., Winkler, P. M., Ye, P., Zhang, X., Hansel, A., Dommen, J., Donahue, N. M., Worsnop, D. R., Baltensperger, U., Kulmala, M., Carslaw, K. S., and Curtius, J.: Ion-induced nucleation of pure biogenic particles, Nature, 533, 521–526, doi:10.1038/nature17953, http://dx.doi.org/10.1038/nature17953, 2016.

Kokkola, H., Korhonen, H., Lehtinen, K. E. J., Makkonen, R., Asmi, A., Järvenoja, S., Anttila, T., Partanen, A.-I., Kulmala, M., Järvinen, H., Laaksonen, A., and Kerminen, V.-M.: SALSA - a Sectional Aerosol module for Large Scale Applications, Atmos. Chem. Phys., 8, 2469–2483, doi:10.5194/acp-8-2469-2008, http://www.atmos-chem-phys.net/8/2469/2008/, 2008.

Kuang, C., Chen, M., Zhao, J., Smith, J., McMurry, P. H., and Wang, J.: Size and time-resolved growth rate measurements of 1 to 5 nm freshly formed atmospheric nuclei, Atmos. Chem. Phys., 12, 3573–3589, doi:10.5194/acp-12-3573-2012, http://www.atmos-chem-phys.net/12/3573/2012/, 2012.

Kulmala, M., Kerminen, V.-M., Anttila, T., Laaksonen, A., and O'Dowd, C. D.: Organic aerosol formation via sulphate cluster activation, J. Geophys. Res.-Atmos., 109, doi:10.1029/2003JD003961, http://dx.doi.org/10.1029/2003JD003961, d04205, 2004.

Kulmala, M., Petäjä, T., Nieminen, T., Sipilä, M., Manninen, H. E., Lehtipalo, K., Dal Maso, M., Aalto, P. P., Junninen, H., Paasonen, P., Riipinen, I., Lehtinen, K. E. J., Laaksonen, A., and Kerminen, V.-M.: Measurement of the nucleation of atmospheric aerosol particles, Nat. Protoc., 7, 1651–1667, doi:10.1038/nprot.2012.091, http://dx.doi.org/10.1038/nprot.2012.091, 2012.

Kulmala, M., Kontkanen, J., Junninen, H., Lehtipalo, K., Manninen, H. E., Nieminen, T., Petäjä, T., Sipilä, M., M., Schobesberger, S., Rantala, P., Franchin, A., Jokinen, T., Järvinen, E., Äijälä, M., Kangasluoma, J., Hakala, J., Aalto, P. P., Paasonen, P., Mikkilä, J., Vanhanen, J., Aalto, J., Hakola, H., Makkonen, U., Ruuskanen, T., Mauldin, R. L., Duplissy, J., Vehkamäki, H., Bäck, J., Kortelainen, A., Riipinen, I., Kurtén, T., Johnston, M. V., Smith, J. N., Ehn, M., Mentel, T. F., Lehtinen, K. E. J., Laaksonen, A., Kerminen, V.-M., and Worsnop, D. R.: Direct Observations of Atmospheric Aerosol Nucleation, Science, 339, 943–946, doi:10.1126/science.1227385, http://science.sciencemag.org/content/339/6122/943, 2013.

Lehtinen, K. E. J., Rannik, U., Petäjä, T., Kulmala, M., and Hari, P.: Nucleation rate and vapor concentration estimations using a least squares aerosol dynamics method, J. Geophys. Res.-Atmos., 109, doi:10.1029/2004JD004893, http://dx.doi.org/10.1029/2004JD004893, 2004.

Lehtipalo, K., Leppä, J., Kontkanen, J., Kangasluoma, J., Franchin, A., Wimmer, D., Schobesberger, S., Junninen, H., Petäjä, T., Sipilä, M., Mikkilä, J., Vanhanen, J., Worsnop, D. R., and Kulmala, M.: Methods for determining particle size distribution and growth rates between 1 and 3 nm using the Particle Size Magnifier, Boreal Environ. Res., 19, 215–236, 2014.

McMurry, P. and Wilson, J.: Growth laws for the formation of secondary ambient aerosols: Implications for chemical conversion mechanisms, Atmos. Environ., 16, 121 – 134, doi:10.1016/0004-6981(82)90319-5, http://www.sciencedirect.com/science/article/pii/0004698182903195, 1982.

McMurry, P., Rader, D., and Stith, J.: Studies of aerosol formation in power plant plumes— I. Growth laws for secondary aerosols in power plant plumes: Implications for chemical conversion mechanisms, Atmos. Environ., 15, 2315 – 2327, doi:https://doi.org/10.1016/0004-6981(81)90262-6, http://www.sciencedirect.com/science/article/pii/0004698181902626, plumes and Visibility Measurements and Model Components, 1981.

McMurry, P. H.: Photochemical aerosol formation from SO2: A theoretical analysis of smog chamber data, J. Colloid Interface Sci., 78, 513 – 527, doi:10.1016/0021-9797(80)90589-5, http://dx.doi.org/10.1016/0021-9797(80)90589-, 1980.

McMurry, P. H. and Li, C.: The dynamic behavior of nucleating aerosols in constant reaction rate systems: Dimensional analysis and generic numerical solutions, Aerosol Sci. Tech., 0, 1–14, doi:10.1080/02786826.2017.1331292, http://dx.doi.org/10.1080/02786826.2017.1331292, 2017.

Merikanto, J., Spracklen, D. V., Mann, G. W., Pickering, S. J., and Carslaw, K. S.: Impact of nucleation on global CCN, Atmos. Chem. Phys., 9, 8601–8616, doi:10.5194/acp-9-8601-2009, http://www.atmos-chem-phys.net/9/8601/2009/, 2009.

Olenius, T. and Riipinen, I.: Molecular-resolution simulations of new particle formation: Evaluation of common assumptions made in describing nucleation in aerosol dynamics models, Aerosol Science and Technology, 51, 397–408, doi:10.1080/02786826.2016.1262530, http://dx.doi.org/10.1080/02786826.2016.1262530, 2017.

Pichelstorfer, L. and Hofmann, W.: Modeling aerosol dynamics of cigarette smoke in a denuder tube, J. Aerosol Sci., 88, 72 – 89, doi:10.1016/j.jaerosci.2015.05.009, http://www.sciencedirect.com/science/article/pii/S0021850215000828, 2015.

Pichelstorfer, L., Winkler-Heil, R., and Hofmann, W.: Lagrangian/Eulerian model of coagulation and deposition of inhaled particles in the human lung, J. Aerosol Sci., 64, 125 – 142, doi:10.1016/j.jaerosci.2013.05.007, http://www.sciencedirect.com/science/article/pii/S0021850213001353, 2013.

Richters, S., Herrmann, H., and Berndt, T.: Gas-phase rate coefficients of the reaction of ozone with four sesquiterpenes at 295 +/- 2 K, Phys. Chem. Chem. Phys., 17, 11 658–11 669, doi:10.1039/C4CP05542J, http://dx.doi.org/10.1039/C4CP05542J, updated values of the rate constant can be found on the IUPAC website at http://iupac.pole-ether.fr/htdocs/datasheets/pdf/Ox_VOC32_O3_bcaryophyllene.pdf, 2015.

Seinfeld, J. and Pandis, S.: Atmospheric Chemistry and Physics: From Air Pollution to Climate Change, 2nd edition, Wiley, second edition edn., 2006.

Smoluchowski, M.: Versuch einer mathematischen Theorie der Koagulationskinetik kolloider Lösungen, Z. Phys. Chem., 92, 129 – 168, doi:https://doi.org/10.1515/zpch-1918-9209, //www.degruyter.com/view/j/zpch.1918.92.issue-1/zpch-1918-9209/zpch-1918-9209.xml, 1917.

Spracklen, D. V., Carslaw, K. S., Kulmala, M., Kerminen, V.-M., Sihto, S.-L., Riipinen, I., Merikanto, J., Mann, G. W., Chipperfield, M. P., Wiedensohler, A., Birmili, W., and Lihavainen, H.: Contribution of particle formation to global cloud condensation nuclei concentrations, Geophys. Res. Lett., 35, doi:10.1029/2007GL033038, http://dx.doi.org/10.1029/2007GL033038, l06808, 2008.

Stolzenburg, D., Steiner, G., and Winkler, P. M.: A DMA-train for precision measurement of sub-10 nm aerosol dynamics, Atmos. Meas. Tech., 10, 1639–1651, doi:10.5194/amt-10-1639-2017, http://www.atmos-meas-tech.net/10/1639/2017/, 2017.

Stolzenburg, M. R. and McMurry, P. H.: Equations Governing Single and Tandem DMA Configurations and a New Lognormal Approximation to the Transfer Function, Aerosol Sci. Tech., 42, 421–432, doi:10.1080/02786820802157823, http://dx.doi.org/10.1080/02786820802157823, 2008.

Tröstl, J., Chuang, W. K., Gordon, H., Heinritzi, M., Yan, C., Molteni, U., Ahlm, L., Frege, C., Bianchi, F., Wagner, R., Simon, M., Lehtipalo, K., Williamson, C., Craven, J. S., Duplissy, J., Adamov, A., Almeida, J., Bernhammer, A.-K., Breitenlechner, M., Brilke, S., Dias, A., Ehrhart, S., Flagan, R. C., Franchin, A., Fuchs, C., Guida, R., Gysel, M., Hansel, A., Hoyle, C. R., Jokinen, T., Junninen, H., Kangasluoma, J., Keskinen, H., Kim, J., Krapf, M., Kürten, A., Laaksonen, A., Lawler, M., Leiminger, M., Mathot, S., Möhler, O., Nieminen, T., Onnela, A., Petäjä, T., Piel, F. M., Miettinen, P., Rissanen, M. P., Rondo, L., Sarnela, N., Schobesberger, S., Sengupta, K., Sipilä, M., Smith, J. N., Steiner, G., Tomè, A., Virtanen, A., Wagner, A. C., Weingartner, E., Wimmer, D., Winkler, P. M., Ye, P., Carslaw, K. S., Curtius, J., Dommen, J., Kirkby, J., Kulmala, M., Riipinen, I., Worsnop, D. R., Donahue, N. M., and Baltensperger, U.: The role of low-volatility organic compounds in initial particle growth in the atmosphere, Nature, 533, 527–531, doi:10.1038/nature18271, http://dx.doi.org/10.1038/nature18271, 2016.

Twomey, S. A., Piepgrass, M., and Wolfe, T. L.: An assessment of the impact of pollution on global cloud albedo, Tellus B, 36, 356–366, doi:10.3402/tellusb.v36i5.14916, http://dx.doi.org/10.3402/tellusb.v36i5.14916, 1984.

Verheggen, B. and Mozurkewich, M.: An inverse modeling procedure to determine particle growth and nucleation rates from measured aerosol size distributions, Atmos. Chem. Phys., 6, 2927–2942, doi:10.5194/acp-6-2927-2006, http://www.atmos-chem-phys.net/6/2927/2006/, 2006.

Wang, J., Flagan, R. C., and Seinfeld, J. H.: Diffusional losses in particle sampling systems containing bends and elbows, J. Aerosol Sci., 33, 843 – 857, doi:https://doi.org/10.1016/S0021-8502(02)00042-3, http://www.sciencedirect.com/science/article/pii/S0021850202000423, 2002.

Wang, J., Collins, D., Covert, D., Elleman, R., Ferrare, R. A., Gasparini, R., Jonsson, H., Ogren, J., Sheridan, P., and Tsay, S.-C.: Temporal variation of aerosol properties at a rural continental site and study of aerosol evolution through growth law analysis, J. Geophys. Res.-Atmos., 111, doi:10.1029/2005JD006704, http://dx.doi.org/10.1029/2005JD006704, d18203, 2006.

Winkler, P. M., Ortega, J., Karl, T., Cappellin, L., Friedli, H. R., Barsanti, K., McMurry, P. H., and Smith, J. N.: Identification of the biogenic compounds responsible for size-dependent nanoparticle growth, Geophys. Res. Lett., 39, doi:10.1029/2012GL053253, http://dx.doi.org/10.1029/2012GL053253, l20815, 2012.

Winkler, P. M., Ortega, J., Karl, T., McMurry, P. H., and Smith, J. N.: A fast-scanning DMA train for precision quantification of early nanoparticle growth, AIP Conference Proceedings, 1527, 165–168, doi:10.1063/1.4803229, http://aip.scitation.org/doi/abs/10.1063/1.4803229, 2013.

Zhao, D. F., Buchholz, A., Tillmann, R., Kleist, E., Wu, C., Rubach, F., Kiendler-Scharr, A., Rudich, Y., Wildt, J., and Mentel, T. F.: Environmental conditions regulate the impact of plants on cloud formation, Nat. Commun., 8, 14 067, doi:10.1038/ncomms14067, `http://dx.doi.org/10.1038/ncomms14067`, 2017.

Chapter 4

Molecular understanding of the suppression of aerosol nucleation by isoprene

This chapter by M.Heinritzi, L.Dada, M.Simon, D.Stolzenburg, A.C.Wagner, L.Fischer and the CLOUD collaboration[1] was submitted on May 7th 2018 and is under review for publication in *Nature*

Abstract. Nucleation of atmospheric aerosols from gaseous precursors produces roughly half of the global cloud condensation nuclei, thus strongly affecting cloud coverage and Earth's radiative balance (Dunne et al., 2016). Recent studies show that highly oxygenated products of monoterpene ($C_{10}H_{16}$) oxidation (Ehn et al., 2014) can nucleate on their own (Kirkby et al., 2016) or with the help of sulfuric acid (Riccobono et al., 2014). Monoterpenes are emitted from trees; however, many plants also emit isoprene (C_5H_8), which has the highest global emissions of all biogenic organic vapors (Guenther et al., 2012). Several field measurements and laboratory studies have shown that isoprene suppresses new-particle-formation, but the cause of this suppression is under debate (Kiendler-Scharr et al., 2009; Kanawade et al., 2011; Kiendler-Scharr et al., 2012; Yu et al., 2014; Lee et al., 2016; Martin et al., 2010). Here we show that isoprene suppresses nucleation of monoterpene oxidation products by altering peroxy-radical (RO_2•) termination reactions and thus inhibiting the formation of highly oxygenated dimers containing 19 to 20 carbon atoms. We observe an increase of dimers with 14 to 15 carbon atoms, which are, however, not efficient nucleators on their own. This suppression decreases when the monoterpene-to-isoprene ratio increases. Additionally, the altered oxidation chemistry reduces early growth in the size range from 1.3 to 3.2 nm by a factor of roughly 2 compared to monoterpene-only conditions, resulting in a lower survival probability for newly formed particles. For larger sizes, we observe no reduction in growth rate. By identifying peroxy-radical termination as the critical mechanism responsible for isoprene suppression of pure biogenic new-particle-formation and initial growth, our findings can explain the hitherto puzzling absence of biogenic new-particle-formation in the Amazon (Martin et al., 2010) and the southeastern United States (Lee et al., 2016).

[1] Full author list: Martin Heinritzi, Lubna Dada, Mario Simon, Dominik Stolzenburg, Andrea C. Wagner, Lukas Fischer, Lauri R. Ahonen, Andrea Baccarini, Paulus S. Bauer, Bernhard Baumgartner, Frederico Bianchi, Sophia Brilke, Dexian Chen, Antonio Dias, Josef Dommen, Henning Finkenzeller, Carla Frege, Claudia Fuchs, Olga Garmash, Hamish Gordon, Imad El Haddad, Xucheng He, Johanna Helm, Victoria Hofbauer, Christopher R. Hoyle, Juha Kangasluoma, Timo Keber, Changhyuk Kim, Andreas Kürten, Katrianne Lehtipalo, Markus Leiminger, Huajun Mai, Vladimir Makhmutov, Serge Mathot, Ugo Molteni, Tuomo Nieminen, Antti Onnela, Eva Partol, Monica Passananti, Tuuka Petäjä, Veronika Pospisilova, Laurianne L. J. Quéléver, Matti P. Rissanen, Mikko Sipilä, Yuri Stozhkov, Christian Tauber, Alexander L. Vogel, Rainer Volkamer, Robert Wagner, Mingyi Wang, Lena Weitz, Daniela Wimmer, Mao Xiao, Penglin Ye, Antonio Amorim, Urs Baltensperger, Armin Hansel, Markku Kulmala, António Tomé, Paul M. Winkler, Douglas R. Worsnop, Neil M. Donahue, Jasper Kirkby, Joachim Curtius

4.1 Letter

Nucleation of aerosol particles is observed in many environments, ranging from boreal forests to urban and coastal areas, from polar to tropical regions and from the boundary layer to the free troposphere (Kulmala et al., 2004). Gaseous sulfuric acid, ammonia (Kirkby et al., 2011), amines (Almeida et al., 2013) and, in coastal regions, iodine (Sipilä et al., 2016), were shown to contribute to nucleation. Additionally, a small fraction of the large pool of organic molecules in the atmosphere, namely highly oxygenated molecules (HOMs), some of which possess extremely low vapor pressures, nucleate together with other precursors as well as on their own (Kirkby et al., 2016; Riccobono et al., 2014; Tröstl et al., 2016). This means nature is nucleating particles on a large scale without pollution, and this may have been especially pervasive in the pre-industrial atmosphere (Gordon et al., 2016). HOMs are formed at molar yields in the single-digit percent range from the oxidation of monoterpenes ($C_{10}H_{16}$) with endocyclic C=C double-bonds (Ehn et al., 2014; Kirkby et al., 2016). Monoterpenes are emitted by a variety of trees in regions ranging from the tropics to northern latitudes, often reaching mixing ratios of tens to hundreds of parts per trillion by volume (p.p.t.) (Guenther et al., 2012; Jardine et al., 2015). Isoprene is a hemiterpene (C_5H_8) emitted by broad-leaf trees and has the highest emissions of any biogenic organic compound, with concentrations reaching several parts per billion by volume (p.p.b.) in the Amazon rainforest and the southeastern United States despite high reactivity (Guenther et al., 2012; Lee et al., 2016; Martin et al., 2010). Numerous studies report suppression of nucleation in isoprene-rich environments, even if sufficient monoterpenes are present (Kiendler-Scharr et al., 2009; Kanawade et al., 2011; Kiendler-Scharr et al., 2012; Yu et al., 2014; Lee et al., 2016). This isoprene suppression effect has been demonstrated in carefully controlled chamber studies (Kiendler-Scharr et al., 2009, 2012) and observed in isoprene-rich ambient locations (Kanawade et al., 2011; Yu et al., 2014; Lee et al., 2016). In addition to observing isoprene suppression, earlier studies have proposed mechanisms to explain it. One possibility is OH• depletion by isoprene, which would reduce the oxidation rate of monoterpenes and thus supersaturation driving nucleation (Kiendler-Scharr et al., 2009, 2012). However, OH• is observed to remain high and undisturbed in isoprene-rich environments due to atmospheric OH• recycling mechanisms triggered by isoprene (Taraborrelli et al., 2012; Martinez et al., 2010; Fuchs et al., 2013). Further, HOM formation from endocyclic monoterpenes is dominated by ozonolysis (Ehn et al., 2014; Kirkby et al., 2016). Another proposed possibility is the deactivation of sulfuric acid cluster growth due to addition of isoprene oxidation products (Lee et al., 2016). However, HOMs can nucleate without sulfuric acid (Kirkby et al., 2016) and suppression of nucleation by isoprene is observed in pristine environments such as the Amazon (Martin et al., 2010).

Isoprene oxidation by OH• triggers complex peroxy-radical chemistry with a variety of products such as hydroxy-hydroperoxides (ISOPOOH), hydroperoxy-aldehydes (HPALD) as well as second-generation low volatility compounds (Teng et al., 2017; Berndt et al., 2016a). Iso-

prene oxidation products with low volatility contribute to secondary organic aerosol formation (Carlton et al., 2009; Krechmer et al., 2015; Claeys et al., 2004). However, the interaction of isoprene and monoterpene oxidation chemistry and the consequent effect on nucleation and growth of new particles remains unclear. One consequence of this is an over-prediction of cloud condensation nuclei (CCN) in the Amazon by models that simulate pure biogenic nucleation, but neglect the role of isoprene in new-particle-formation (Gordon et al., 2016).

Here we show on a molecular level how isoprene affects the chemistry of monoterpene oxidation, thus reducing nucleation rates. We conducted experiments at the CLOUD (Cosmics Leaving OUtdoor Droplets) chamber at CERN (European Center for Nuclear Research) in Geneva, Switzerland. The CLOUD chamber is a 26.1 m^3 stainless steel aerosol reactor with very controlled and clean conditions that span those found in the atmosphere. It is equipped with a suite of state-of-the-art mass spectrometers and particle-counting instruments. We measured isoprene and α-pinene with a newly developed proton transfer reaction mass spectrometer and the resulting HOMs with a nitrate chemical ionization atmospheric pressure interface time-of-flight mass spectrometer (CI-APi-TOF). The forming particles were detected with a suite of particle size magnifiers (PSM) and counters, as well as a newly developed DMA-train (for further details on instrumentation see Methods).

We performed several experiments at +5°C, 38% relative humidity and 40-50 p.p.b. of ozone. We first added α-pinene alone to the chamber at three concentrations representing atmospheric values (roughly 330, 660 and 1200 p.p.t., recreating conditions similar to Kirkby et al. (2016)), then isoprene (around 4 p.p.b.) alone and finally an α-pinene and isoprene mixture under dark and UV-illuminated conditions (see Extended Data Fig. 1 and 2).

Ozone attack to the endocyclic α-pinene C=C double bond leads to the well-described formation of RO_2• radicals via intramolecular H-shift and autoxidation (mainly $C_{10}H_{15}O_{4,6,8,10}$ from now on referred to as $RO_2(\alpha p)$) as well as a wide spectrum of closed-shell monomers (mainly $C_{10}H_{14,16}O_{5,7,9,11}$) and covalently bound dimers (mainly $C_{20}H_{30}O_{8-16}$ and $C_{19}H_{28}O_{7-11}$, see Fig. **??**a) (Ehn et al., 2014; Kirkby et al., 2016; Rissanen et al., 2015). These highly oxygenated molecules (HOMs) nucleate at atmospherically relevant concentrations with the help of ions but without other species (e.g. sulfuric acid or bases) required (Kirkby et al., 2016). Here, we group the HOMs according to carbon atom number and define C_5, C_{10}, C_{15} and C_{20} classes as sum of all HOMs with 2-5, 6-10, 11-15 and 16-20 carbon atoms, respectively. This resembles the basic building block unit of a C_5 isoprenoid skeleton.

An isoprene/ozone mixture in the CLOUD chamber produces $C_5H_9O_{5-9}$ RO_2• radicals (referred to as RO_2(ip)) which terminate to $C_5H_8O_{5-8}$ and $C_5H_{10}O_{5-9}$ monomers and also some $C_{10}H_{18}O_{8-10}$ dimers under UV-illuminated conditions (see Extended Data Fig. 5). The $C_5H_9O_{5-9}$ radicals originate presumably from an OH• addition to isoprene and subsequent autoxidation. Under dark conditions, when the only source of OH• is isoprene ozonolysis at 26 % yield (Malkin et al., 2010), we observe only C_5 monomers. None of these molecules

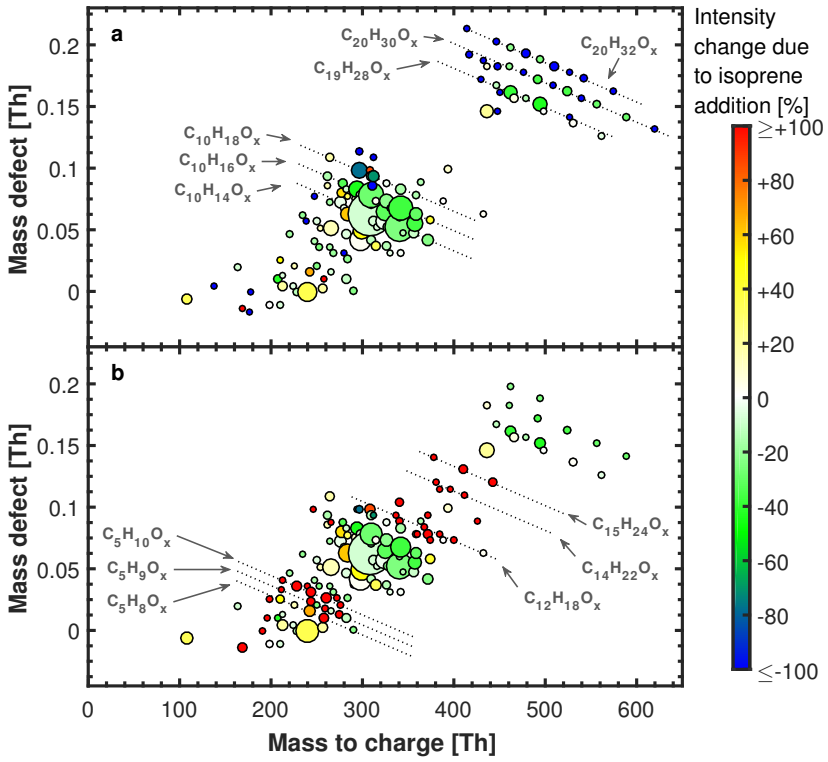

Figure 1: Mass defect plots of neutral HOM molecules measured with nitrate CI-APi-TOF without isoprene (a) and with isoprene added (b). α-pinene levels were 666 and 618 p.p.t., respectively. Ozone levels were 40 and 46 p.p.b., respectively. Isoprene was 3.8 p.p.b. in (b). The area of the marker points is linearly scaled with the intensity of the HOM signals. The lower cut-off was set to $5{\cdot}10^4$ cm^{-3} to exclude noise. Color code shows the relative intensity change for each HOM peak due to isoprene addition, i.e. the percentage intensity change between (a) and (b). The color for each peak is thus the same in (a) and (b). HOM intensity in (a) was scaled up linearly by 7 % to match [α-pinene]·[O_3] levels present in (b) to calculate the intensity change.

are able to nucleate under atmospherically relevant conditions despite having an oxygen to carbon ratio (O:C)≥1.

When isoprene is present together with α-pinene and ozone, the HOM chemistry of α-pinene is altered. We observe the appearance of C_{15} and an increase in C_5 class molecules compared to α-pinene only conditions as well as a decrease in C_{20} and C_{10} class molecules (see Fig. **??** and Extended Data Fig. 3). Without isoprene, $RO_2(\alpha p)$ can terminate with another $RO_2(\alpha p)$, thus forming either one C_{20} dimer or two C_{10} monomers. Monomers can also be formed by termination with HO_2 or unimolecular termination (Rissanen et al., 2015). The presence of RO_2(ip) offers additional termination channels (see Extended Data Fig. 10) and acts as an additional loss term for $RO_2(\alpha p)$. Their reaction is expected to result in C_5 and C_{10} monomers as well as C_{15} dimers. Most importantly, the reduced $RO_2(\alpha p)$ steady state concentrations lead to a reduction of C_{20} class dimers by roughly 40 % compared to their level in the absence of isoprene for all studied α-pinene concentrations (see Extended Data Fig. 3).

We measured the particle formation rate directly at 1.7 nm cut-off diameter with a scanning Particle Size Magnifier (PSM) under neutral (high voltage field cage switched on, see Methods for details) and ion conditions (high voltage field cage switched off, allowing for galactic cosmic ray (gcr) ionization in the chamber), further referred to as J_n and J_{gcr} (see Methods for detail). Fig. **??** shows J_n and J_{gcr} plotted against total HOM concentration (the sum of the C_5, C_{10}, C_{15} and C_{20} classes) for the α-pinene only case and α-pinene + isoprene. For the α-pinene only case we find good agreement with Kirkby et al. (2016). However, the presence of 3.5–4 p.p.b. of isoprene and the consequent change in oxidation chemistry reduces J_{gcr} by a factor of two to four and J_n even more by around one order of magnitude. The suppression is stronger for lower α-pinene concentrations and thus higher values of R (the ratio of isoprene to monoterpene carbon). The larger difference between J_{gcr} and J_n with isoprene present compared to α-pinene only conditions is direct evidence that isoprene oxidation products destabilize the nucleating clusters, thus making cluster stabilization through the presence of charge more efficient. This also confirms that C_{20} class molecules are mainly responsible for pure biogenic nucleation (Frege et al., 2018). C_{15} class molecules, which tend to counteract the losses of the C_{20} class, do not prevent a decrease in J. Earlier studies have already suggested that C_{10} class molecules do not have low enough vapor pressure to qualify as Extremely Low Volatility Organic Compounds (Tröstl et al., 2016; Kurtén et al., 2016) and thus drive nucleation, leaving C_{20} class molecules as the most likely nucleator molecules. Regressing each individual HOM peak with J_{gcr} under both dark and UV conditions also gives the highest coefficient of determination with J for C_{20} class molecules (see Extended Data Fig. 7). Additionally, Extended Data Fig. 8 shows that the coefficient of determination for J vs C_{20} is higher (0.95) than for J vs C_{15}+C_{20} (0.73).

It has been argued that OH• depletion by isoprene is responsible for the absence of nucleation in isoprene-rich environments (Kiendler-Scharr et al., 2009, 2012); however, under atmospheric conditions, isoprene induced OH• recycling can lead to undisturbed high OH• levels, which might not be true in chamber experiments (Taraborrelli et al., 2012; Martinez et al., 2010; Fuchs et al., 2013). In our study we also see an OH• depletion effect due to isoprene addition (see Extended Data Fig. 1 and Methods for detailed discussion). However, if OH• depletion were the reason for suppression of nucleation, an increase of OH• would lead to an increase in the nucleation rate. When we increase OH• levels by switching on UV lights in the presence of isoprene, this reduces $RO_2(\alpha p)$ further, as well as the C_{20} and C_{10} class molecules, while enhancing the C_5 and C_{15} classes (see Extended Data Fig. 1, 4 and 6 as well as Methods for details). Accordingly, J is also reduced slightly instead of being increased. This OH effect can be understood by comparing the reactivity of α-pinene and isoprene towards OH• at our given concentrations. For 330 and 1200 p.p.t. the reactivity of α-pinene towards OH• ($[\alpha p]\cdot k_{\alpha pOH}$) is 20 and 5.5 times lower than the reactivity of 3.5 p.p.b. isoprene towards OH• ($[ip]\cdot k_{ipOH}$), respectively. This implies that any additional OH• will favor the formation of

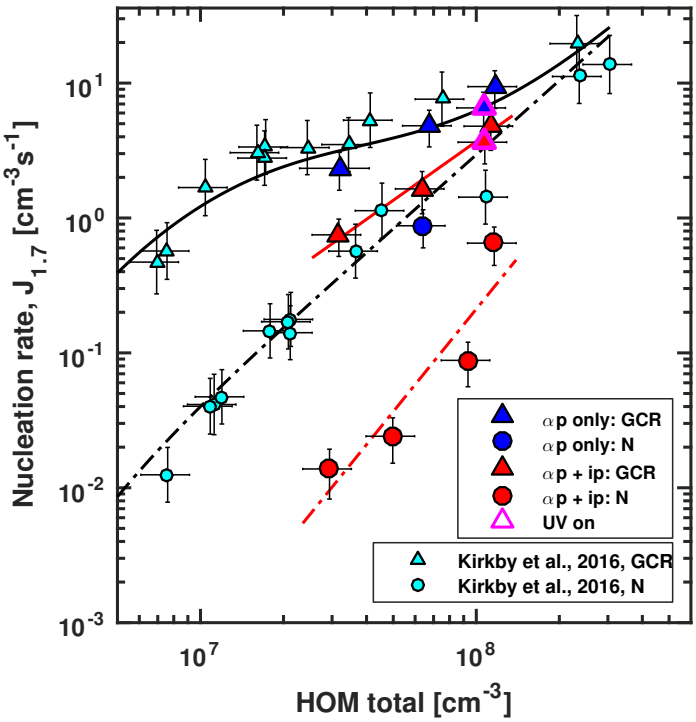

Figure 2: Pure biogenic nucleation rates at 1.7 nm diameter against total HOM concentration with and without isoprene added. HOM total is defined as the sum of C_5, C_{10}, C_{15} and C_{20} carbon classes. Triangles represent J_{gcr} and circles J_n. Light blue points were taken from Kirkby et al. (2016). Dark blue (α-pinene only) and red (isoprene added at 3.5-4 p.p.b.) points were measured in this study. Magenta edges indicate UV-illuminated conditions, black edges represent dark conditions. Black solid and dash/dotted lines are parametrizations of J_{gcr} and J_n from Kirkby et al. (2016). Red solid and dash/dotted lines are power law fits to J_{gcr} and J_n under isoprene presence. Bars indicate 1σ run-to-run uncertainty. The overall systematic scale uncertainty of HOMs of +78 %/-68 % and of J for ±47% is not shown.

additional RO_2(ip) instead of RO_2(αp), thus favoring C_{15} formation over C_{20} formation and consequently reducing nucleation rates. OH• does not enhance nucleation in this chemical system; it suppresses it.

We measured the growth rates of freshly nucleated particles from 1.3 nm onwards with a scanning Particle Size Magnifier and a DMA-train (see Methods for details). The change in HOM chemistry caused by concurrent isoprene oxidation reduces the growth rates of particles in the range of 1.3-1.9 nm and 1.8–3.2 nm roughly by a factor of two (Fig. **??**). This confirms that C_{15} class molecules have a higher vapor pressure than C_{20} class molecules and are thus less efficient than C_{20} class molecules at causing growth of the smallest particles. Likewise, most C_{10} class molecules are too volatile to contribute significantly to the early stages of growth (Tröstl et al., 2016). For the size range from 3.2–8.0 nm and larger, no suppression effect due to isoprene could be measured, indicating that molecules smaller than C_{20} are capable of condensing onto particles at larger sizes. We further find a linear relationship of

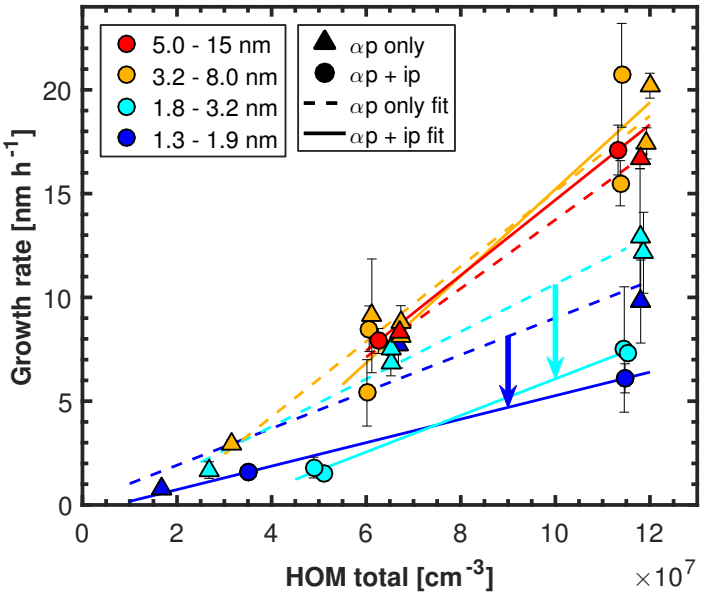

Figure 3: Growth rate of nucleated particles vs total HOM concentration. Triangles represent α-pinene only, circles α-pinene + isoprene conditions. Marker color indicates the size range in which growth rate was measured: dark blue 1.3–1.9 nm (measured by scanning PSM), light blue 1.8–3.2 nm, orange 3.2–8.0 nm (both measured by DMA-train) and red 5.0–15 nm (measured by nanoSMPS). Bars indicate 1σ uncertainties in growth rate estimation. Dashed lines are linear fits to α-pinene only data points; solid lines are linear fits to α-pinene + isoprene conditions, respectively.

growth rate vs C_{20} for 1.3-1.9 and 1.8-3.2 nm, regardless of isoprene presence. For larger sizes the linear relationship is independent of isoprene presence, when plotted against C_{15} + C_{20}, again indicating C_{15} contribution to growth at larger sizes (Extended Data Fig. 9).

Fig. **??** shows the formation rate of particles measured at 1.7, 2.2, 2.5 and 6 nm for gcr conditions and six datasets (low/mid/high α-pinene mixing ratios with and without isoprene). Especially for the lowest α-pinene loading, with the lowest growth rates, we find that the presence of isoprene reduces the survival probability for clusters as they grow to larger sizes. Our measurements agree reasonably well with a theoretical prediction of J vs diameter (see Methods for details). For the highest α-pinene concentrations, a reduction of survival probability due to isoprene addition is barely visible, as the growth rate is relatively high for both cases under the conditions we examined. However, in the atmosphere, condensation sink values of 10^{-2} s^{-1} occur frequently, e.g. in Alabama, USA (Lee et al., 2016). When simulating a condensation sink of $6{\cdot}10^{-3}$ s^{-1}, roughly three times the typical CLOUD wall-loss rate, we find that the survival probability of particles for relatively high α-pinene concentrations (∼1200 p.p.t.) is considerably more reduced when isoprene is present. Our calculation yields a formation rate for 3 nm particles of 0.2 $cm^{-3}\,s^{-1}$ without isoprene and around 0.01 $cm^{-3}\,s^{-1}$ with isoprene for approximately 1200 p.p.t. of α-pinene. As the latter value is barely measurable at atmospheric conditions, our findings can explain the apparent absence of pure biogenic

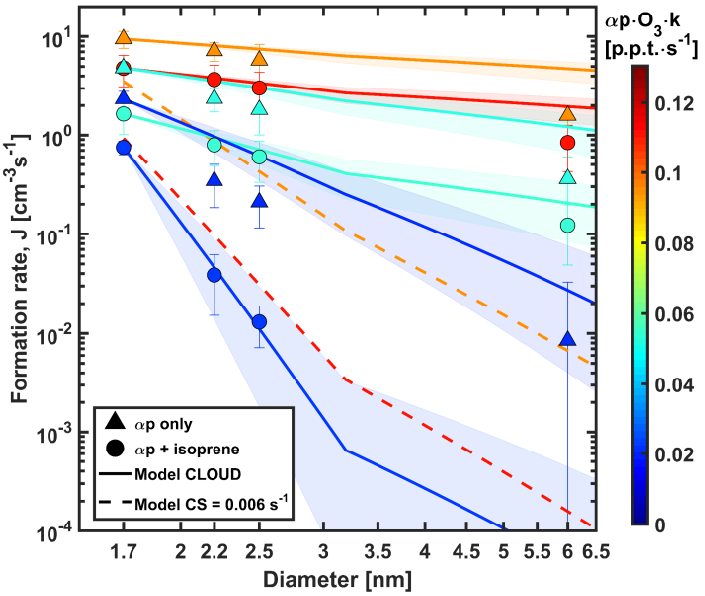

Figure 4: Formation rate (gcr) vs diameter of particles. Triangles represent α-pinene only, circles α-pinene + isoprene conditions. Color code represents [α-pinene]·[O3]·$k_{\alpha pO3}$ and represents low, mid and high α-pinene settings (∼330, ∼660 and ∼1200 p.p.t as well as 40–50 p.p.b. of ozone). Bars indicate 1σ run-to-run uncertainty in J measurement. Solid lines represent parametrizations of J vs diameter using $J_{1.7}$ as starting point as well as growth rates parametrized by using C_{20} and C_{15} + C_{20} concentrations for the size range of 1.7–3.2 nm and 3.2-8.0 nm, respectively (see Methods for details). The shaded areas indicate model predictions with ±30 % change in growth rates. The kink in the modelled lines originates in the discrete change of modeled growth rate when switching from the smaller to the larger size range at 3.2 nm. Dashed red and orange lines show the parametrization for the same [α-pinene]·[O3]·$k_{\alpha pO3}$ levels as the solid red and orange lines, but with an atmospherically often relevant condensation sink of 0.006 s^{-1} instead of the CLOUD wall loss rate of 0.002 s^{-1}, which leads to a reduction of HOMs and thus $J_{1.7}$, as well as reduced growth rates.

nucleation in isoprene-rich environments. Even if monoterpene levels are relatively high, the combined effects of a reduced nucleation rate and lower survival probability due to slower growth rates can inhibit significant new-particle-formation events.

In summary, we find that isoprene interferes with α-pinene HOM chemistry via RO_2• peroxy-radical termination. When isoprene is present, fewer C_{20} class molecules are formed, which directly reduces the nucleation rate by a factor of two to four for atmospherically relevant α-pinene and isoprene concentrations. In the monoterpene-isoprene chemical system, increased OH• does not enhance nucleation, but, on the contrary, reduces it due to C_{20} class reduction. The change in monoterpene HOM chemistry due to isoprene reduces organic growth rates in the 1.3–3.2 nm range by around 50 %, which strongly reduces the probability that the smallest, freshly-nucleated particles will survive scavenging as they grow to larger sizes. For atmospherically relevant conditions, isoprene can thus make the difference between measurable new-particle-formation and its absence even at relatively high monoterpene concentrations

(> 1 p.b.b.). Our findings can thus explain on a molecular level the lack of biogenic new-particle-formation in isoprene-rich environments like the Amazon basin or the southeastern United States.

Author contributions

M. H., L. D., M. Sim., **D. S.**, A. C. W., L. F., L. R. A., F. B., S. B., A. D., J. Du., I. E.-H., H. F., C. Fr., C. Fu., H. G., X. H., J. H., V. H., C. K., T. K., A. K., J. Ka., M. L., K. L., T. M. L., J. L., H. M., U. M., S. M., V. M., B. M., W. N., A. O., T. P., V. P., L. L. J. Q., M. P. R., Y. S., M. Sip., R. V., A. L. V., M. W., L. W., D. W., R. W., M. X., P. Y., C. Y., Q. Z., J. Kir. and A. T. prepared the CLOUD facility and measurement instruments. M. H., L. D., M. Sim., **D. S.**, A. C. W., L. F., L. R. A., F. B., A. B., S. B., P. S. B., B. B., D. C., A. D., J. Du., I. E.-H., H. F., C. Fu., H. G., O. G., X. H., J. H., C. R. H., V. H., C. K., T. K., K. L., J. L., U. M., V. M., B. M., T. N., W. N., M. Pa., L. L. J. Q., M. P. R., C. R., Y. S., C. T., R. V., L. W., D. W., M. X., P. Y., C. Y., Q. Z., J. Kir., A. A. and A. T. collected the data. M. H., L. D., M. Sim., **D. S.**, L. F., H. F., V. H., J. Ka., B. M., T. N., E. P., R. V., M. X. and C. Y. analyzed the data. M. H., L. D., M. Sim., **D. S.**, A. C. W., L. F., J. Do., H. G., A. K., K. L., M. P. R., M. Sip., A. L. V., P. Y., C. Y., N. M. D., J. Kir., U. B., P. M. W., J. Cu., D. R. W., A. H. and M. K. contributed to the scientific discussion. M. H., L. D., M. Sim., **D. S.**, A. C. W., A. K., N. M. D., J. Kir., U. B. and J. Cu. contributed to writing the manuscript.

Acknowledgements

We thank CERN for supporting CLOUD with technical and financial resources, and for providing a particle beam from the CERN Proton Synchrotron. We thank P. Carrie, L.-P. De Menezes, J. Dumollard, K. Ivanova, F. Josa, I. Krasin, R. Kristic, A. Laassiri, O. S. Maksumov, B. Marichy, H. Martinati, S. V. Mizin, R. Sitals, A. Wasem and M. Wilhelmsson for their contributions to the experiment. This research has received funding from the EC Seventh Framework Programme and European Union's Horizon 2020 programme (Marie Curie ITN no. 316662 "CLOUD-TRAIN", MSCA-IF no. 656994 "nano-CAVa", MC-COFUND grant no. 600377, ERC projects no. 692891 "DAMOCLES", no. 638703 "COALA", no. 616075 "NANODYNAMITE", no. 335478 "QAPPA", no. 742206 "ATM-GP", no. 714621 "GASPARCON"), the German Federal Ministry of Education and Research (projects no. 01LK0902A, 01LK1222A 01LK1601A), the Swiss National Science Foundation (projects no. 20020_152907, 200020_172602, 20FI20_159851, 200020_172602, 20FI20_172622), the Academy of Finland (Center of Excellence no. 307331, projects 299574, 296628, 306853, 304013), the Finnish Funding Agency for Technology and Innovation, the Väisälä Foundation, the Nessling Foundation, the Austrian Science Fund (FWF; project

no. J3951-N36), the Austrian research funding association (FFG, project no. 846050), the Portuguese Foundation for Science and Technology (project no. CERN/FP/116387/2010), the Swedish Research Council Formas (project number 2015-749), Vetenskapsrådet (grant 2011-5120), the Presidium of the Russian Academy of Sciences and Russian Foundation for Basic Research (grants 08-02-91006-CERN, 12-02-91522-CERN), the U.S. National Science Foundation (grants AGS1136479, AGS1447056, AGS1439551, CHE1012293, AGS1649147, AGS1602086), the Wallace Research Foundation, the US Department of Energy (grant DE-SC0014469), the NERC GASSP project NE/J024252/1m, the Royal Society (Wolfson Merit Award), United Kingdom Natural Environment Research Council grant NE/K015966/1, Dreyfus Award EP-11-117, the French National Research Agency the Nord-Pas de Calais, European Funds for Regional Economic Development Labex-Cappa grant ANR-11-LABX-0005-01).

4.2 Methods

4.2.1 CLOUD Facility

We conducted our measurements at the CLOUD (Cosmics Leaving OUtdoor Droplets) chamber at CERN (European Center for Nuclear Research), Geneva, Switzerland. The CLOUD chamber is a 26.1 m^3 electro-polished stainless steel tank used to recreate atmospheric condition in the laboratory (for more details on the chamber see (Kirkby et al., 2016, 2011; Duplissy et al., 2016)). Data for this study was taken during the CLOUD 11 campaign in autumn 2016. Various measures are taken to reduce unwanted contaminants. The air in the chamber is mixed from cryogenic nitrogen and oxygen, all lines are made of stainless steel and intense cleaning cycles are performed prior to each campaign. Each cleaning cycle consists of at least 24 h of rinsing the chamber from the inside with ultrapure water, followed by a period of at least 24 h with the chamber at 100°C and high ozone levels (several parts per million by volume). These measures result in very low organic contamination below 150 p.p.t. (Kirkby et al., 2016) in total.

Ultrapure water is used to humidify the air in the chamber. Ozone is produced by a UV ozone generator. Liquid α-pinene (Sigma Aldrich, purity >98 %) is stored in a temperature controlled water bath and evaporated into a dry nitrogen flow and fed into the chamber. Isoprene from a gas bottle (Carbagas AG, purity >99 %) is additionally cleaned by a cryotrap. The cryotrap consists of a 2 m long 1/4 inch stainless steel tube spiral placed in a cryogenic liquid held at 233 K. By using this trap, non-negligible monoterpene-like contaminants in the isoprene gas bottle are effectively frozen out. Isoprene and α-pinene are diluted by separate two stage dilution systems prior to being fed into the chamber. All gases are fed into the chamber from the bottom and are mixed by two magnetically driven fans.

A unique feature of the CLOUD chamber is its controlled ion condition. A high voltage electric field cage (±30 kV) can sweep ions that are constantly produced by naturally occurring galactic cosmic rays out of the chamber in around 1 s. This enables us to study pure neutral nucleation. By switching the field cage off, the formed ions are allowed to stay in the chamber and affect nucleation processes. To artificially enhance ion concentrations, CERN's Proton Synchrotron provides a 3.5 GeV $\pi+$ beam that is diverged to >1 m^2 beam profile and crosses the center region of the chamber.

The CLOUD chamber is equipped with four HgXe UV lamps (LightningCure LC8, Hamamatsu Photonics K.K.) positioned at the top of the chamber and connected via fiber bundles. An additional UV source is provided by a KrF excimer laser (ATLEX-1000, ATL Lasertechnik GmbH) at 248 nm wavelength and also connected to the chamber via fiber bundles to enhance $OH\bullet$ production via photolysis of O_3 further.

4.2.2 Typical Run sequence and conditions

Our experiments were performed at +5 °C and 38 % relative humidity under mostly dark conditions. A typical run sequence can be seen in Extended Data Fig. 1 and 2. First, α-pinene is present with ozone under both neutral and gcr conditions at three different atmospherically relevant concentrations. HOMs are forming as seen by the CI-APi-TOF and new-particle-formation is induced. The purpose of this experiment was also to ensure inter-campaign comparability to Kirkby et al. (2016). In the following run a stable isoprene concentration is established in the chamber and ozone is added shortly afterwards. As ozone and isoprene only react very slowly, effects on HOMs are minor. As UV light in the chamber is switched on, OH• production increases and thus formation of OH• induced isoprene HOMs. However, only the subsequent addition of α-pinene leads to formation of C_{20} class HOMs and thus new-particle-formation. Again, UV effects were studied as well by switching on the Hamamatsu lamp, as well as the KrF-excimer laser.

4.2.3 Gas Phase measurements

Ozone was measured by a calibrated ozone monitor (Thermo Environmental Instruments TEI 49C). Isoprene and α-pinene were measured by the newly developed proton transfer reaction time-of-flight mass spectrometer (PTR3(Breitenlechner et al., 2017)). The instrument was frequently calibrated for both gases and has a limit of detection of 2 p.p.t. for isoprene and α-pinene for 1 s integration time. The accuracy of the instrument for both gases is mainly determined by the uncertainty of the calibration gas standard (5 %) and accuracies of mass flow controllers and is estimated to be 7 %.

The chemical ionization atmospheric pressure interface time-of-flight (CI-APi-TOF) mass spectrometer (Tofwerk AG) measured highly oxygenated organic compounds with a limit of detection of $\sim 5 \cdot 10^4\,\mathrm{cm}^{-3}$. The instrument operates with a nitrate based ion source similar to the design in Eisele and Tanner (1993). However, a corona discharge was used instead of a radioactive source (Kürten et al., 2011). The instrument was calibrated for sulfuric acid (Kürten et al., 2012) and the data corrected for mass dependent transmission efficiency (Heinritzi et al., 2016). HOM quantification was performed as described in Kirkby et al. (2016). The run-to-run uncertainty for HOMs is estimated to be 20 %. Due to technical reasons the CI-APi-TOF could only start measuring at 03 Oct, 10:28 UTC (see Extended Data Fig. 1). As HOMs depend linearly on the product [α-pinene]·[O_3] (Ehn et al., 2014; Kirkby et al., 2016) HOM concentrations measured during the mid α-pinene settings were used and scaled down according to this relation to obtain HOM concentrations for the low α-pinene settings for the appropriate times where J and growth rates were estimated. This also gave a higher uncertainty for this data point (28 %) as indicated in Fig. **??**. The overall uncertainty in HOM quantification consists of contributions from sulfuric acid calibration (+50 %/-33 %), charging efficiency of HOMs in the ion source (25 %), transmission correction

(50 %) and sampling line loss correction (20 %). This results in an overall scale uncertainty for HOMs of +78 %/-68 %. There are however additional uncertainties in our HOM estimation that cannot be readily quantified. On the one hand nitrate ionization of HOMs shows a drop in charging efficiency for HOMs with six or less oxygen atoms (Hyttinen et al., 2017). This leads to an underestimation of these molecules. However, these molecules with comparably low oxygen content are not expected to contribute significantly to nucleation and early growth. Additionally, it was shown that nitrate ionization has a reduced charging efficiency towards HOMs formed by OH• oxidation compared to HOMs formed by ozonolysis (Berndt et al., 2015, 2016b). This could affect also C_{20} class molecules that show OH• dependence, like $C_{20}H_{32}O_7$ (see Extended Data Fig. 1). The real increase of these C_{20} class HOMs due to UV light could be larger than the measured one, thus dampening the overall decrease of C_{20} when UV is switched on. The fact that J decreases when UV is switched on, however, confirms that the total nucleating molecules in the chamber decrease. That effect is thus not strong enough to lead to a real increase instead of a decrease in C_{20} class molecules.

4.2.4 OH estimation and comparison to ambient environments

We estimate OH• levels in our chamber via a steady state approach (see Extended Data Fig. 1). OH• sources taken into account are ozonolysis of α-pinene and isoprene, with yields of 79 % (Tillmann et al., 2010) and 26 % (Malkin et al., 2010; Kroll et al., 1001) respectively, as well as photolysis of ozone with our UV laser. The OH• source strength of the UV laser was characterized with a separate experiment (SO_2 to sulfuric acid conversion) and depends on laser settings, ozone concentration and absolute water vapor concentration. Sink terms taken into account are reactions of OH• with α-pinene and isoprene. Secondary reactions of OH• with further oxidation products of α-pinene or isoprene are not taken into account, as their effect is expected to be minor (e.g. two orders of magnitude smaller than the former sink terms in case of the pinonaldehyde-OH• reaction). OH• recycling in our chamber is expected to be weak, as we do not have NOx in the chamber and most runs are performed under dark conditions. The recycling mechanism due to photolysis of hydroperoxy-aldehydes (HPALDs) (Taraborrelli et al., 2012) can in principal take place during UV runs, however, HPALDs may also decompose on our stainless steel chamber walls without releasing OH• in a process similar to the one described in Bernhammer et al. (2017), thus further reducing recycling efficiency. However, the O_x recycling mechanisms (reaction of O_3 and HO_2 yielding OH•, as well as photolysis of H_2O_2 under UV conditions) might take place in our conditions 43. All gas phase reaction rate constants are preferred values provided by IUPAC (International Union of Pure and Applied Chemistry) and were evaluated at +5°C ($k_{\alpha pO3} = 8.1 \cdot 10^{-17}\,cm^3\,s^{-1}$, $k_{\alpha pOH} = 5.8 \cdot 10^{-11}\,cm^3\,s^{-1}$, $k_{ipO3} = 7.9 \cdot 10^{-18}\,cm^3\,s^{-1}$ and $k_{ipOH} = 1.1 \cdot 10^{-10}\,cm^3\,s^{-1}$).
We calculate OH• levels of around $1 \cdot 10^6\,cm^{-3}$ during dark α-pinene ozonolysis, with roughly a doubling to $2 \cdot 10^6\,cm^{-3}$ when the UV laser is switched on. When isoprene is present

together with α-pinene it foremost acts as a sink for OH• and thus reduces its concentrations. The strength of this depletion depends on the main OH• source strength, i.e., the α-pinene ozonolysis rate. We find OH• levels 5 to 20 times lower when isoprene is present than under α-pinene only conditions. This depletion can also be recognized in the traces of HOMs that originate from OH• oxidation, like $C_{10}H_{18}O_6$ (see Extended Data Fig. 1).

In the atmosphere, OH• levels of $10^6\,cm^{-3}$ and higher are reported even in the presence of isoprene, as several OH• recycling mechanisms take place (Lee et al., 2016; Martinez et al., 2010; Lelieveld et al., 2016). However, given the reduction in C_{20} class molecules when OH• is increased from $2 \cdot 10^5\,cm^{-3}$ to $4 \cdot 10^5\,cm^{-3}$ by switching on UV light, it is a reasonable assumption that, if OH• would be fully replenished to $1 \cdot 10^6\,cm^{-3}$, we would see a further decrease of total C_{20} class molecules and subsequently a reduction in J and early growth rates. This assumption is also valid when the reduced charging efficiency of nitrate ionization towards OH• initiated HOMs is taken into account as outlined above. The decrease of C_{20} class molecules and nucleation rate when OH• is increased is direct evidence that the suppression effect of isoprene on nucleation is not due to depletion of OH•.

4.2.5 Particle Measurements

The total particle number concentration above 2.5 nm is measured by a TSI 3776 condensation particle counter (CPC) using butanol as working fluid. For smaller particles, an Airmodus A10 particle size magnifier (PSM), using diethylene glycol as working fluid, is used (Vanhanen et al., 2011) in combination with an Airmodus A20 CPC. This setup achieves detection of airborne particles down to 1 nm. By varying the supersaturation inside the PSM, particle size distributions between 1 – 3 nm can be inferred (Lehtipalo et al., 2014).

A DMA-train (Stolzenburg et al., 2017) is used to measure the particle size distribution and growth rates between 1.8 – 8.0 nm. It uses a parallel design of six sampling channels each equipped with a differential mobility analyser (DMA) together with an ultrafine condensation particle counter (uCPC). For detection of sub-2.5 nm particles, two of the channels are equipped with either an Airmodus A10 particle size magnifier (PSM) or a TSI 3777 nanoEnhancer as booster stage upstream of the CPC. The channels are operated at fixed sizes to increase time-resolution and counting-statistics leading to higher sensitivities for smaller sizes compared to standard scanning mobility devices.

The size distribution above 5 nm is measured with a TSI Scanning Mobility Particle Sizer (nanoSMPS, Model 3938) using a TSI 3082 nanoDMA and a water-based TSI 3788 CPC for detection of the size-selected particles. For particles larger than 65 nm a custom-built SMPS with a long column DMA was used.

4.2.6 Determination of nucleation rates

The nucleation rate J defines the number of particles formed within a volume per unit of time. It is calculated using the flux of the total concentration of particles growing past a specific diameter (here at 1.7, 2.2, 2.5 and 6 nm). In the following, the method for calculating $J_{1.7}$ is presented, however the calculation for $J_{2.2}$, $J_{2.5}$ and J_6 follows the same procedure unless specified otherwise. The nucleation rate is the sum of the time derivative of the concentration of particles above a certain diameter, as well as correction terms accounting for aerosol losses due to dilution in the chamber, wall losses and coagulation.

$$J_{1.7} = \frac{dN_{\geq 1.7\mathrm{nm}}}{dt} + S_{dil} + S_{wall} + S_{coag} \tag{1}$$

N is the concentration of particles of diameter equal or larger than 1.7 nm. The term S_{dil} describes the size-independent losses of particles due to dilution of the gases in the chamber. The chamber is continuously flushed with a total flow of 230 liters per minute to replenish the sampling flow of the instruments. This results in the dilution factor $k_{dil} = 1.47 \cdot 10^{-4}\,\mathrm{s}^{-1}$ and

$$S_{dil} = N_{\geq 1.7\mathrm{nm}} \cdot k_{dil} \tag{2}$$

The term S_{wall} describes the size-dependent particle losses to the chamber walls and was calculated based on the decay rate of sulfuric acid monomer (of mobility diameter = 0.85 nm (Kulmala et al., 2013)) in the chamber (at temperature = 278 K). The wall loss rate k_{wall} is a function of particle diameter and temperature.

$$S_{wall}(T) = \sum_{d_{p,i=1.7\mathrm{nm}}}^{d_{p,max}} N(d_{p,i}) \cdot k_{wall}(d_{p,i}, T) \tag{3}$$

At 278 K

$$k_{wall}(d_{p,i}) = 1.7 \cdot 10^{-3}\mathrm{nm\ s}^{-1} \cdot \frac{1}{d_{p,i}} \tag{4}$$

The term S_{coag} represents the coagulation losses to the surface of pre-existing aerosol particles in the chamber and was calculated using the full number size distribution present in the chamber (Seinfeld and Pandis, 2006).

$$S_{coag}(d_p = 1.7\mathrm{nm}) = \sum_{d_{p,i}=d_p}^{d_{p,max}} \sum_{d_{p,j}=d_p}^{d_{p,max}} \delta_{i,j} \cdot K(d_{p,i}, d_{p,j}) \cdot N_i \cdot N_j \tag{5}$$

where $K(d_{p,i}, d_{p,j})$ is the coagulation coefficient for particles of the size $d_{p,i}$ and $d_{p,j}$, N_i and N_j are the number concentrations of particles in the size bins $d_{p,i}$ and $d_{p,j}$, and $\delta_{i,j} = 0.5$, if i = j and $\delta_{i,j} = 1$, if $i \neq j$. $d_{p,i}$ is the midpoint diameter for the size bin with index i.

The number size distribution of particles used for the calculation of formation rates were

obtained from the scanning PSM at cut-off diameters 1.7 nm and 2.2 nm for the determination of $J_{1.7}$ and $J_{2.2}$, and from a butanol CPC (model CPC3776, TSI Inc.) of fixed cut-off (2.5 nm) for determining the formation rate of 2.5 nm particles. For determining J_6 the integrated size bins from the nanoSMPS were used. A correction factor of +0.3 nm on the cut-off diameter of the PSM was included to account for the poorer detection efficiency of neutral organic particles compared to calibration with tungsten oxide (Kangasluoma et al., 2014). The concentrations obtained were corrected for sampling line losses. During each run, the value of J was determined after reaching a steady state value. A median value of the formation rate was then obtained. The errors on the reported J rates were obtained by considering an inter-campaign reproducibility error of 30 % as well as a series of run-dependent systematic and statistical uncertainties which include errors on sampling (10 %), dilution (10 %), wall loss (20 %) and coagulation sink (20 %). The resulting overall scale uncertainty for J is 47 %.

4.2.7 Determination of growth rates

Particle growth rates were derived from several instruments individually with the widely used appearance time method (Lehtipalo et al., 2014). For this method the signal rise in a single size channel is fitted with a sigmoidal function during the particle formation event. The fit determines the appearance time t_{app} at which the signal intensity reaches 50 % between a potential background and the final value reached at steady-state nucleation conditions. A linear fit of t_{app} and the corresponding diameters of several size channels yields an average apparent growth rate of the size distribution for a diameter interval. To infer a size-dependence of the measured growth rates, several instruments and size-intervals were used. Growth rates between 1.3 – 1.9 nm were measured with the scanning PSM, the DMA-train size channels were split up into two intervals, one between 1.8 – 3.2 nm and one between 3.2 – 8.0 nm. For size-intervals above 8 nm the size channels of the nanoSMPS were used. Uncertainties in the sigmoidal fit result are promoted to the linear fit of the growth rate providing an estimate of the statistical uncertainties. However, at least a systematic uncertainty of approximately 50 % has to be assumed if apparent growth rates are interpreted as condensational growth values.

4.2.8 Parametrization of J vs diameter

For the parametrization of J vs particle diameter starting from measured $J_{1.7}$ values in **??** the following relation from Kürten et al. (2015) was used:

$$J(d_p) = J(1.7\text{nm}) \cdot \exp\left(-\frac{1}{GR} \cdot \left(C' \cdot \ln\left(\frac{d_p}{1.7}\right) + k_{dil} \cdot (d_p - 1.7\,\text{nm})\right)\right) \quad (6)$$

Here, C' is the product of wall loss rate at a certain diameter and the diameter, GR is the growth rate of particles, d_p is the diameter in nm at which J is to be evaluated and k_{dil} is the

dilution rate of the CLOUD chamber ($1.47{\cdot}10^{-4}\,s^{-1}$). C' was obtained by multiplying the wall loss rate of sulfuric acid monomers in the CLOUD chamber ($2.1 \cdot 10^{-3}\,s^{-1}$) with an estimated diameter of the sulfuric acid monomer (0.85 nm (Kulmala et al., 2013)). As the growth rate could not be determined at the exact same times when the nucleation rates were determined, growth rates were parametrized with respect to HOM concentrations. Extended Data Fig. 9 shows that for the size range from 1.8–3.2 nm, the growth rate is independent of isoprene addition, when plotted against C_{20} class molecules, while for the size range of 3.2–8.0 nm it is independent of isoprene presence when plotted against C_{15} + C_{20}. The linear fits in Extended Data Fig. 9 for the size ranges 1.8–3.2 nm and 3.2–8.0 nm were used to obtain growth rate values at the time of J determination. As we use two discrete growth rate size ranges that originate from our measurements, our model produces a sharp kink at 3.2 nm when reaching the larger size range. For simulating atmospheric conditions with higher losses due to pre-existing aerosol, the wall loss rate of $2.1 \cdot 10^{-3}\,s^{-1}$ was replaced with a condensation sink (CS) of $6 \cdot 10^{-3}\,s^{-1}$, which is well in the range of atmospherically relevant values (Lee et al., 2016). A higher CS means lower HOM concentrations under otherwise similar [α-pinene]·[O_3] levels. HOM levels were thus scaled down by the ratio of k_{wall} to CS. The nucleation rate at 1.7 nm was subsequently scaled down using the power law relation for $J_{1.7}$ vs HOMs in **??** and the related growth rate by again using the fits provided in Extended Data Fig. 9.

4.3 Extended Data

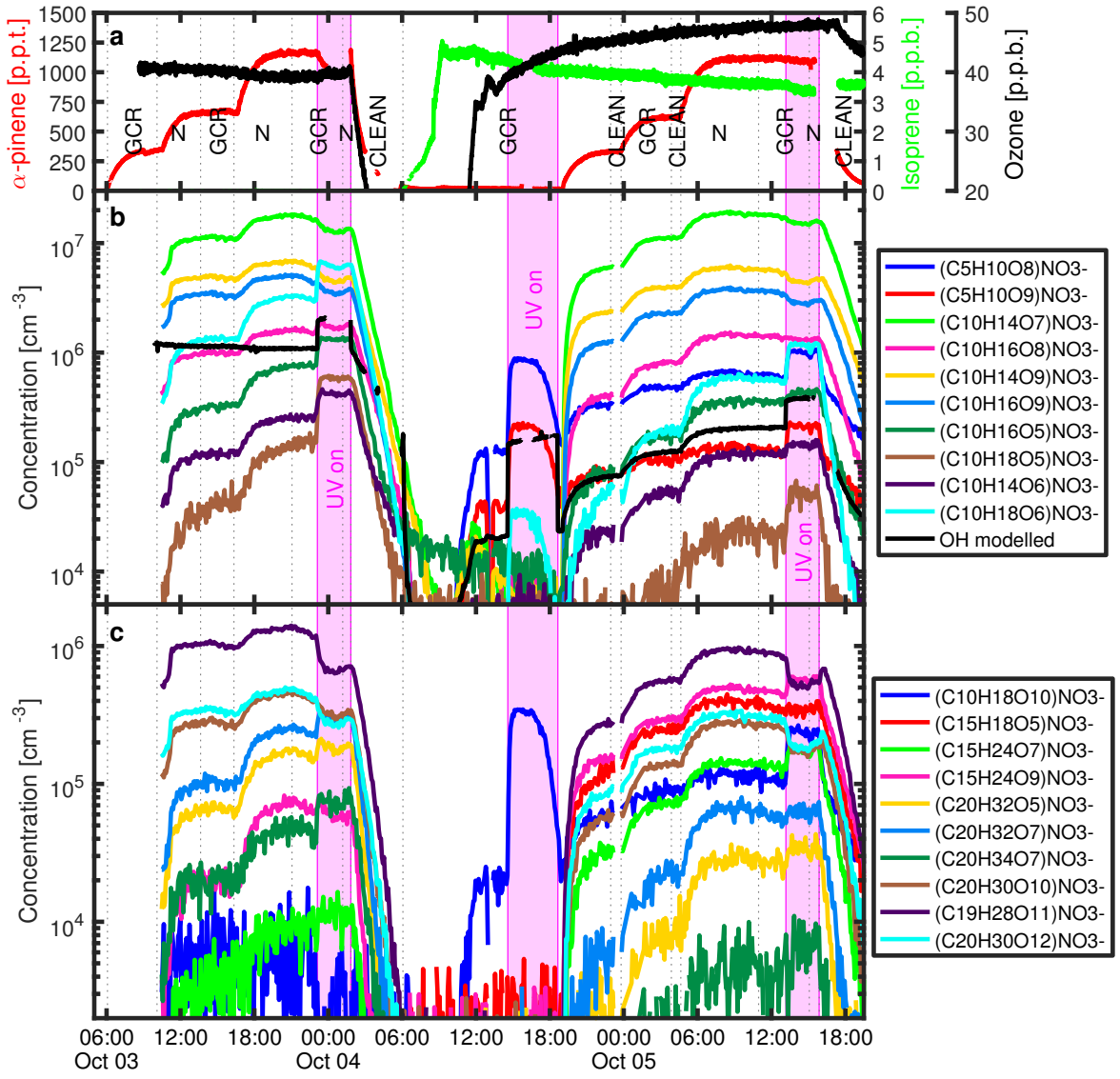

Figure 5: Time series of a nucleation experiment with example HOM traces. (a) shows traces of α-pinene, isoprene and ozone. (b) and (c) show selected time traces of HOM monomers and dimers measured by the CI-APi-TOF, respectively. The temperature in the chamber was +5°C and rel. humidity was 38 %. N, GCR and CLEAN indicate neutral (high voltage cleaning field on), galactic cosmic ray (high voltage cleaning field off) and cleaning (neutral periods to clean the chamber of particles) conditions, respectively. In the first part until 04 Oct, 06:00 UTC, α-pinene was present in the chamber at three different concentrations to study pure biogenic nucleation under both neutral and gcr conditions with an additional UV stage at the end. Afterwards an isoprene/ozone mixture was studied under both dark and UV-illuminated conditions. Note that during the UV stage on 04 Oct the laser intensity deteriorated towards the end of the stage and thus corresponding HOM signals went down as well. At 04 Oct, starting at 18:40 UTC, α-pinene was added at three concentration levels similar to the first part of the experiment.

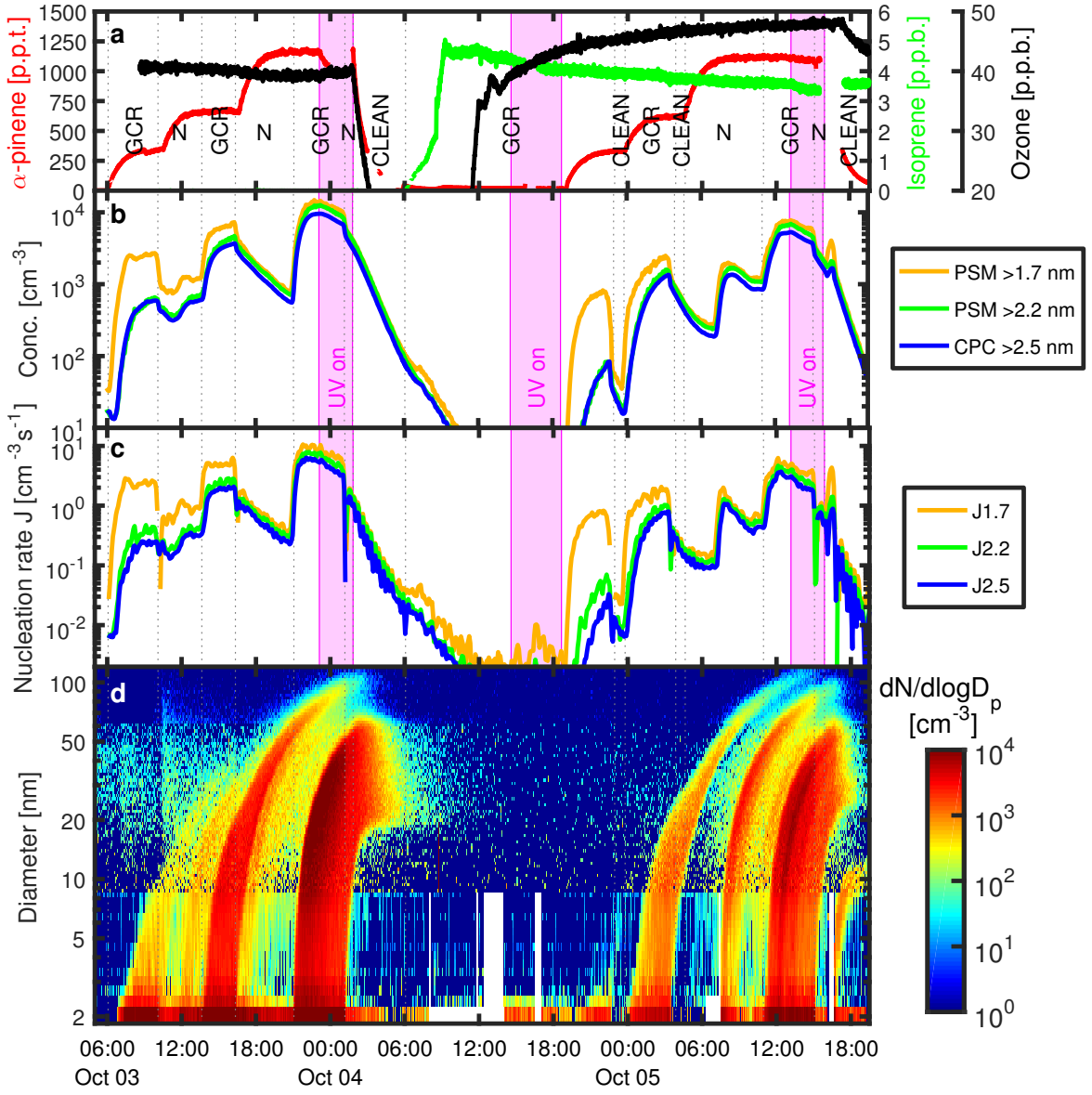

Figure 6: Time series of a nucleation experiment with particle counter data and J rates. The time window shown is the same as in Extended Data Fig. 1 shows traces of α-pinene, isoprene and ozone. N, GCR and CLEAN indicate neutral (high voltage cleaning field on), galactic cosmic ray (high voltage cleaning field off) and cleaning (neutral periods to clean the chamber of particles) conditions, respectively. (b) shows particle concentration above 1.7, 2.2 and 2.5 nm, measured with a scanning PSM (1.7 nm and 2.2 nm) and a butanol-based CPC (2.5 nm). (c) shows the nucleation rate J determined at 1.7, 2.2 and 2.5 nm using the particle concentrations shown in (b). (d) shows a combined size distribution of aerosol particles in the CLOUD chamber. The DMA-train contributed the size range from 1.8 – 8 nm, the nanoSMPS from 8 – 65 nm and the long-SMPS for sizes >65 nm.

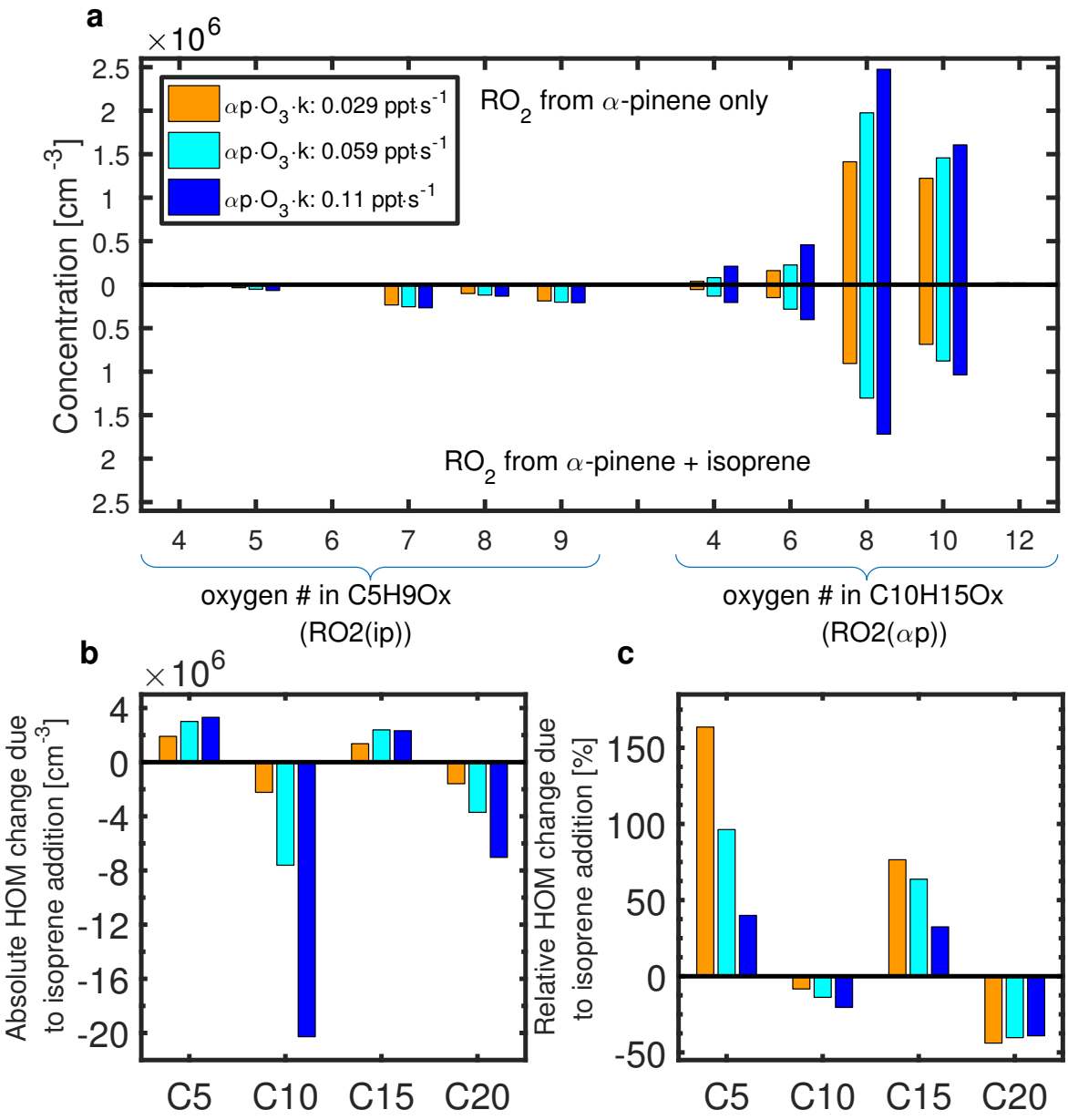

Figure 7: Effects of isoprene addition on RO_2• radical and HOM classes distribution. All data from the α-pinene only runs was slightly scaled up linearly (3, 7 and 16 % for low, mid and high α-pinene levels, respectively) to match the exact same [α-pinene]·[O_3] values as in the α-pinene + isoprene runs. (a) shows the distribution of the most prominent RO_2• radicals originating from isoprene and α-pinene oxidation. (b) shows the absolute and (c) the relative changes of the HOM class distribution due to isoprene addition.

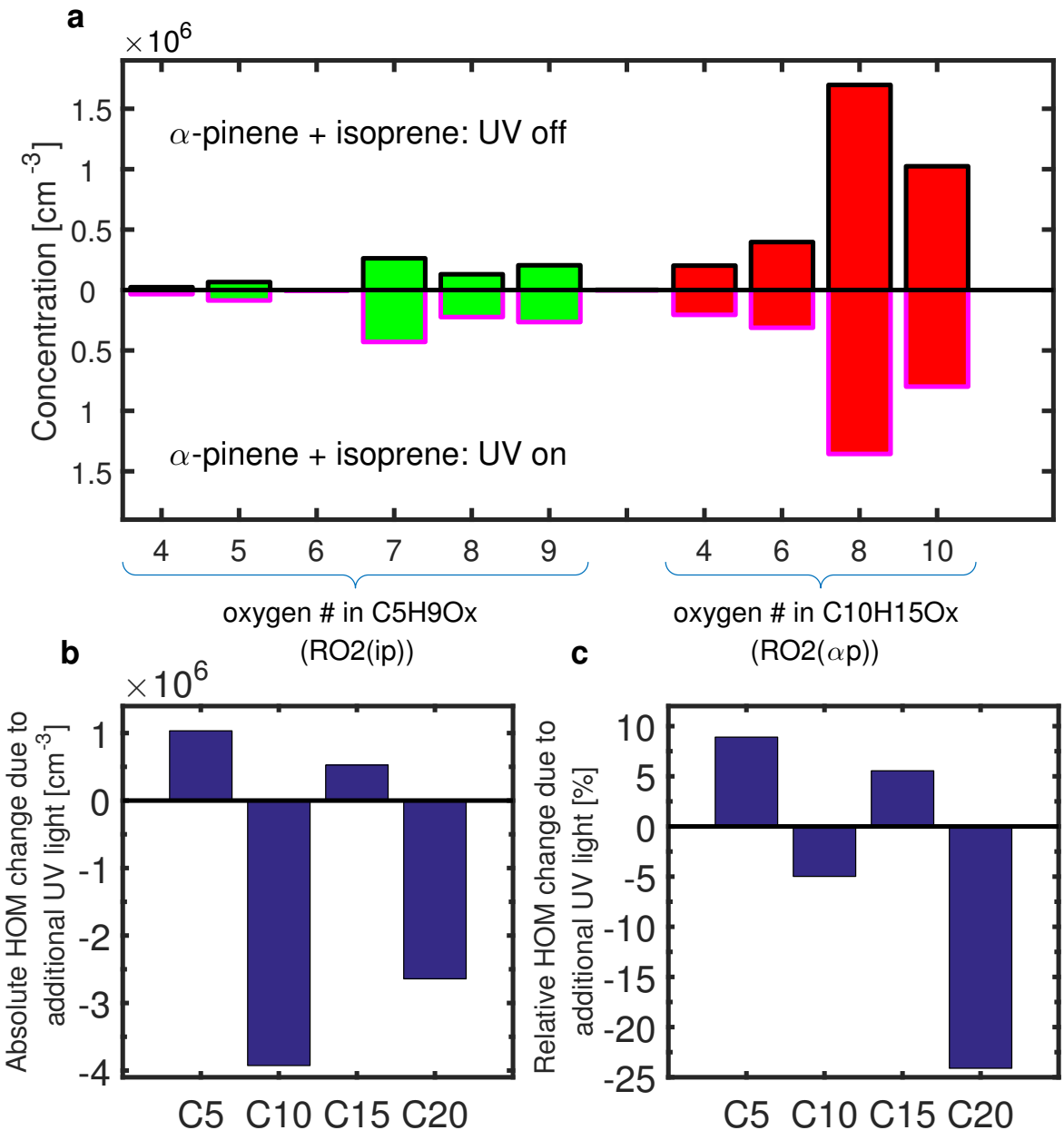

Figure 8: Changes of RO_2• radical and HOM classes distribution due to UV light in an α-pinene, isoprene and ozone mixture. Data from the dark run was slightly scaled down linearly (1.2 %) to match exact same [α-pinene]·[O_3] values as in the UV run. (a) shows the distribution of the most prominent RO_2• radicals originating from isoprene (green) and α-pinene (red) oxidation. (b) shows the absolute and (c) the relative changes of the HOM class distribution due to UV light.

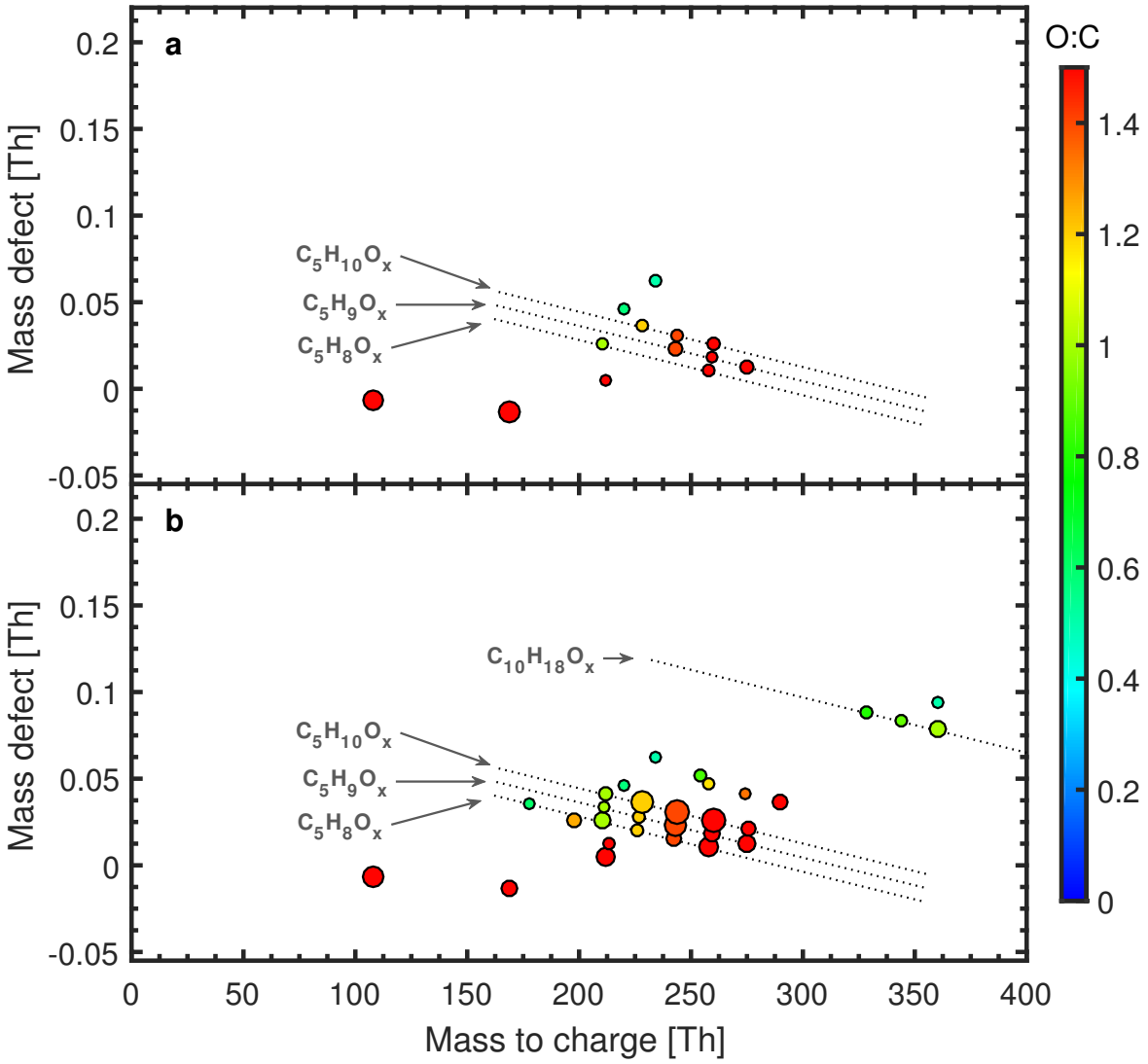

Figure 9: Mass defect plot of HOMs from a mixture of isoprene (4.5 p.p.b.) and ozone (40–50 p.p.b.). (a) dark conditions, (b) UV-illuminated conditions with higher OH• levels. The area of the marker points is linearly scaled to intensity of the HOM signals. The lower cut-off was set to $5 \cdot 10^4\,\mathrm{cm}^{-3}$ to exclude noise. Color code represents oxygen-to-carbon ratio (O:C) of HOMs. UV light strongly enhances OH• and thus HOM production. This even leads to the formation of some C_{10} dimers resulting from the combination of two RO_2(ip).

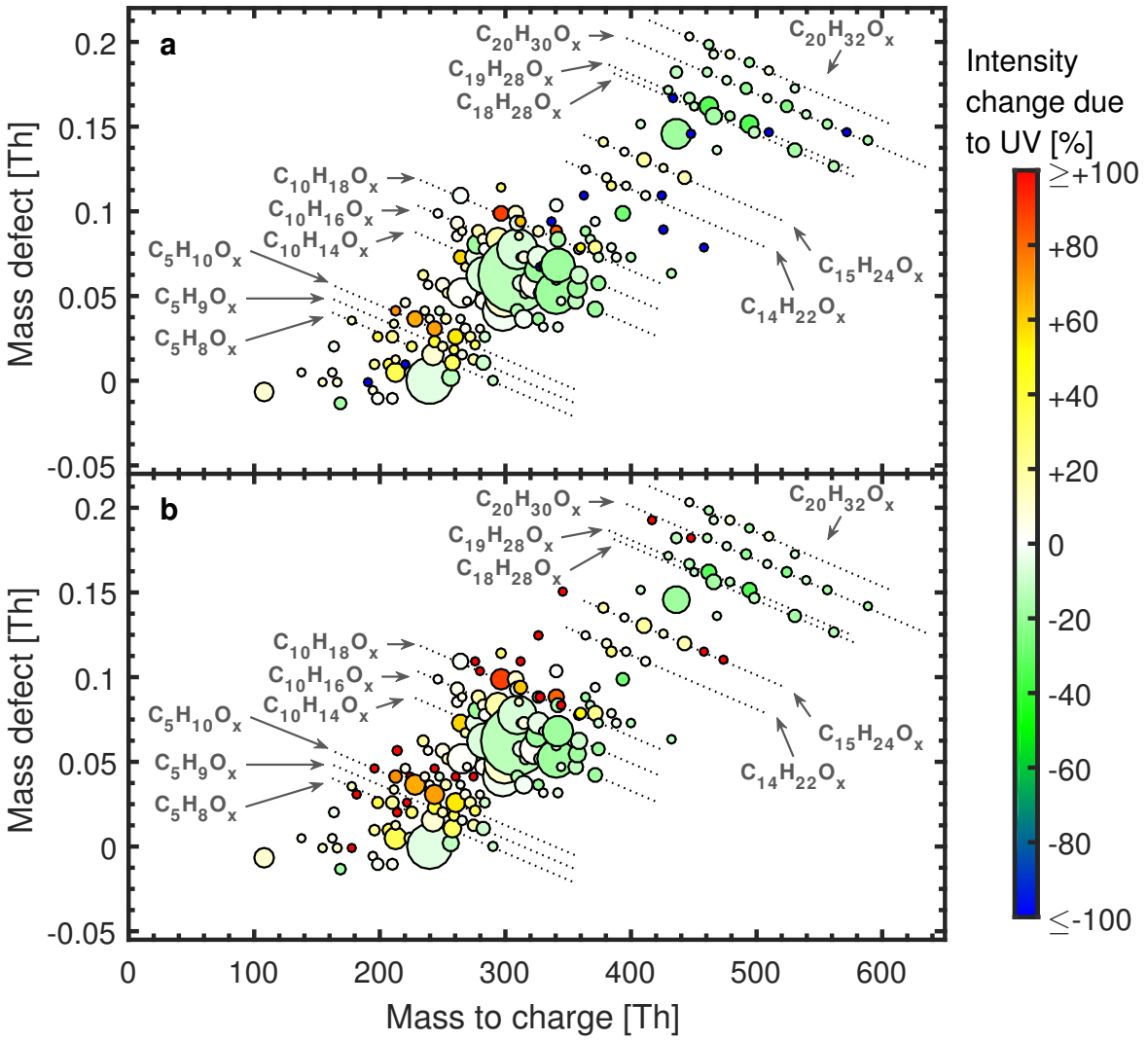

Figure 10: Mass defect plot of HOMs from a mixture of α-pinene, isoprene and ozone under (a) dark and (b) UV-illuminated conditions. α-pinene was 1116 and 1096 p.p.t., isoprene was 3.6 and 3.4 p.p.b. for (a), and (b), respectively. Ozone was 47 p.p.b. for both runs. The area of the marker points is linearly scaled to intensity of the HOM signals. The lower cut-off was set to $5 \cdot 10^4\,\mathrm{cm}^{-3}$ to exclude noise. Color code indicates the change in intensity for each HOM peak when switching from dark to UV light conditions, i.e. the percentage intensity change between (a) and (b). The color for each peak is thus the same in (a) and (b). Data from the dark run was slightly scaled down linearly (1.2 %) to match the same [α-pinene]·[O_3] values as in the UV run for calculating the intensity change.

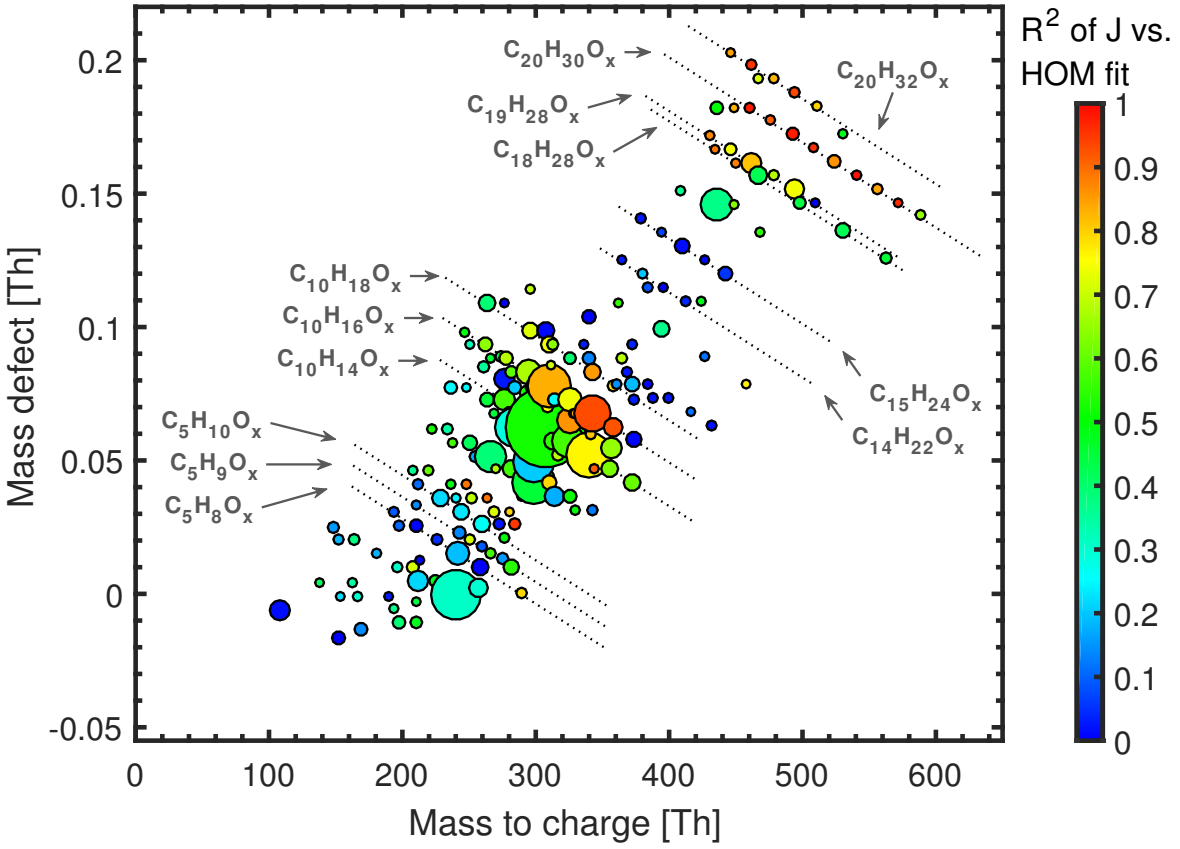

Figure 11: Mass defect plot of HOMs with coefficient of determination of Jgcr vs individual HOM as color code. The data points are taken from a run with 1116 p.p.t. α-pinene, 3.4 p.p.b. isoprene and 47.6 p.p.b. ozone under dark conditions. The area of the marker points is linearly scaled to intensity of the HOM signals. The lower cut-off was set to $5 \cdot 10^4\,\mathrm{cm}^{-3}$ to exclude noise. The color code indicates coefficient of determination (R^2) of a power law fit of J vs every individual HOM peak. The dataset used for the fit contains eight Jgcr data points taken under low/medium/high α-pinene levels with and without isoprene as well as two data points with UV illumination (one α-pinene only and one with α-pinene + isoprene present). High R^2 does not necessarily mean that the corresponding molecules contribute directly to nucleation, but that they are predominantly formed in a chemical setting that favors the production of nucleator molecules.

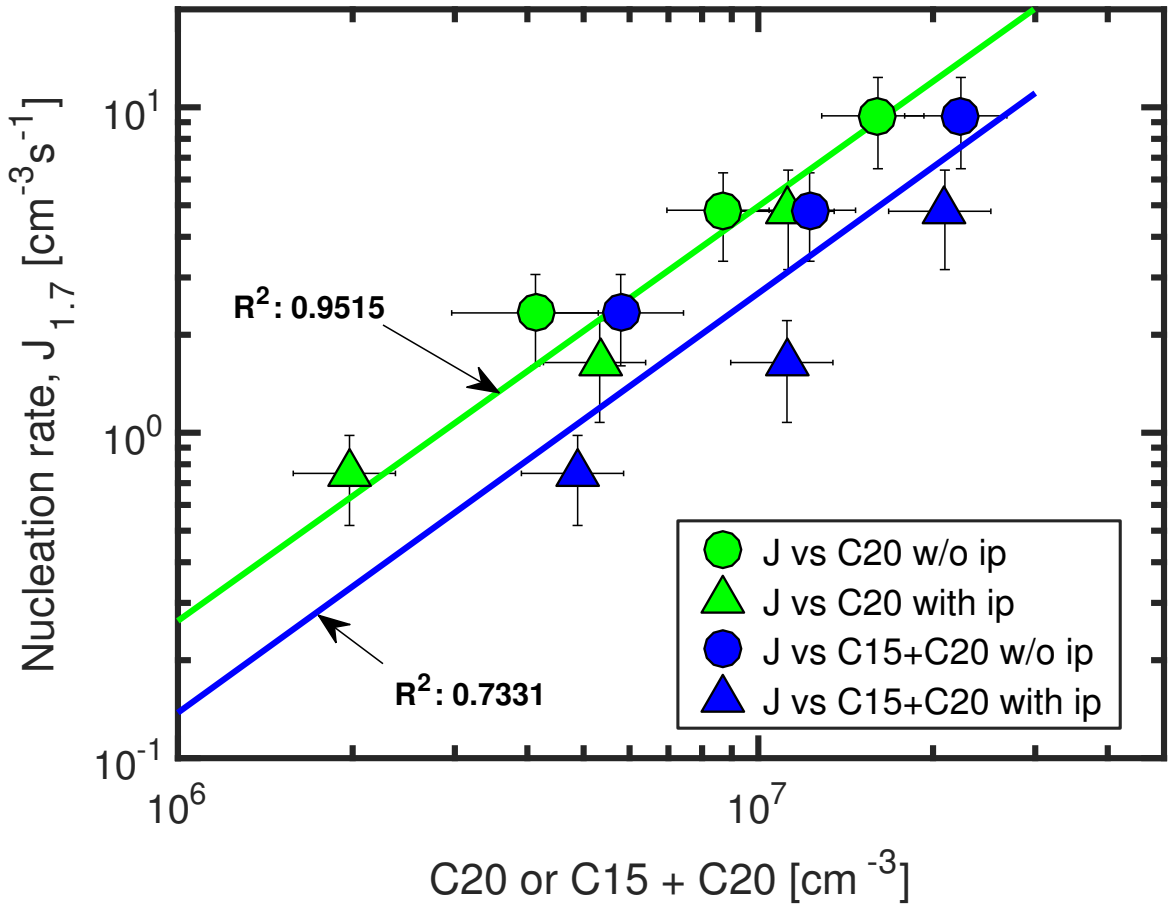

Figure 12: Nucleation rate $J_{1.7}$ with and without isoprene vs C_{20} and C_{15}+C_{20} class molecules. Green and blue marker symbols represent $J_{1.7}$ vs C_{20} and $J_{1.7}$ vs C_{15}+C_{20}, respectively. Circles show data taken without isoprene in the chamber (only α-pinene and ozone present), triangles show data taken with α-pinene and isoprene present at the same time. Bars indicate 1σ run-to-run uncertainty. The overall systematic scale uncertainty of HOMs of +78 %/-68 % and of $J_{1.7}$ for ±47 % is not shown. Green and blue lines are power law fits to $J_{1.7}$ vs C_{20} and $J_{1.7}$ vs C_{15} + C_{20}, respectively.

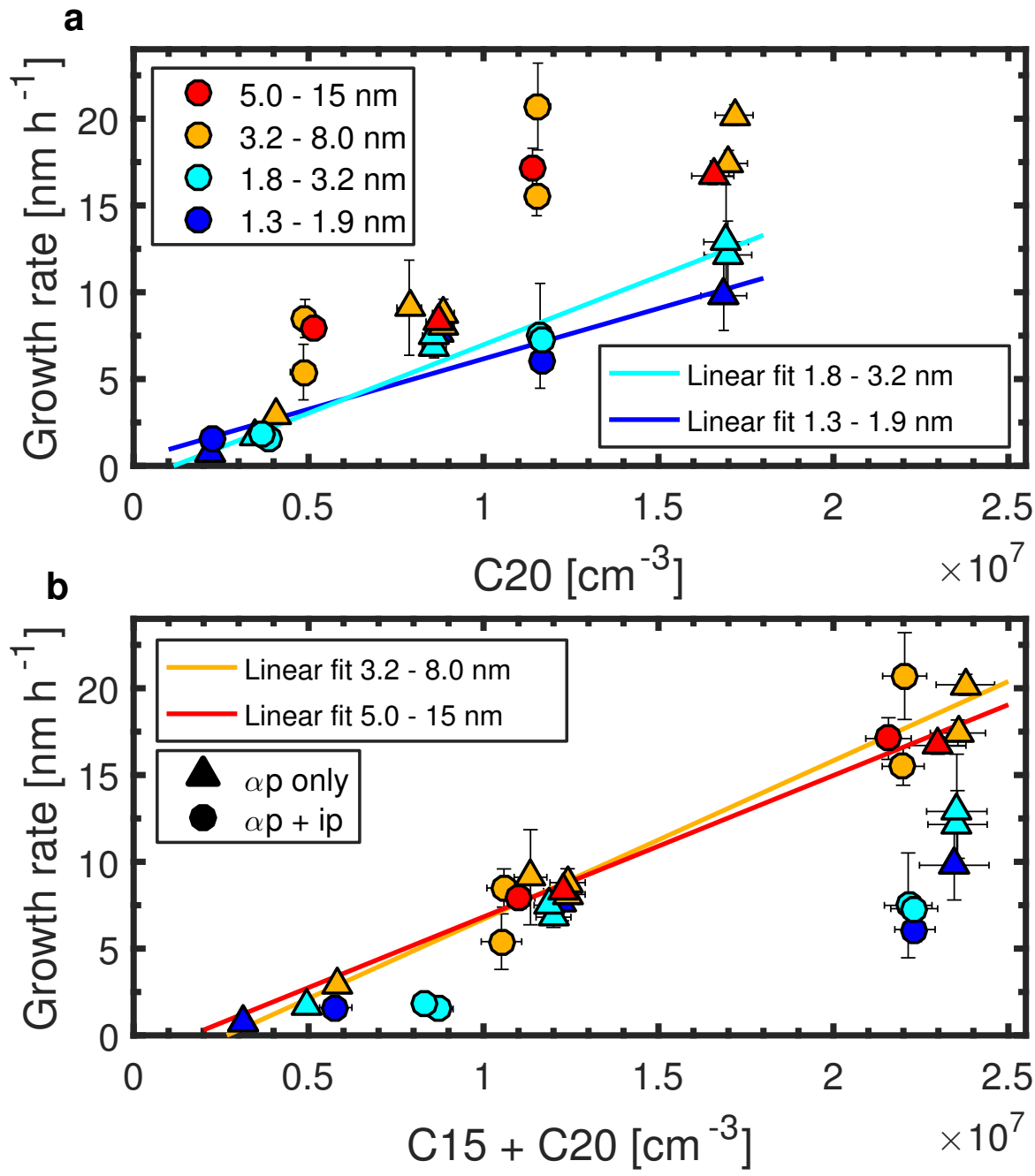

Figure 13: Growth rate vs (a) C_{20} class concentration and (b) C_{15} + C_{20} class concentration. Growth rates were measured by scanning PSM (1.3–1.9 nm, dark blue), DMA-train (1.8–3.2 nm, light blue and 3.2–8.0 nm, orange) and nanoSMPS (5.0–15nm, red). Triangles represent α-pinene only runs, circles represent α-pinene + isoprene runs. The growth rate between 1.8 nm and 3.2 nm can be parametrized by a linear fit when plotted against C_{20} class molecules, for the size range from 3.2–8.0 nm there is a linear relationship for growth rate when plotted against C_{15} + C_{20} class molecules. Both fits were used to parametrize J with respect to diameter as shown in Fig. **??**

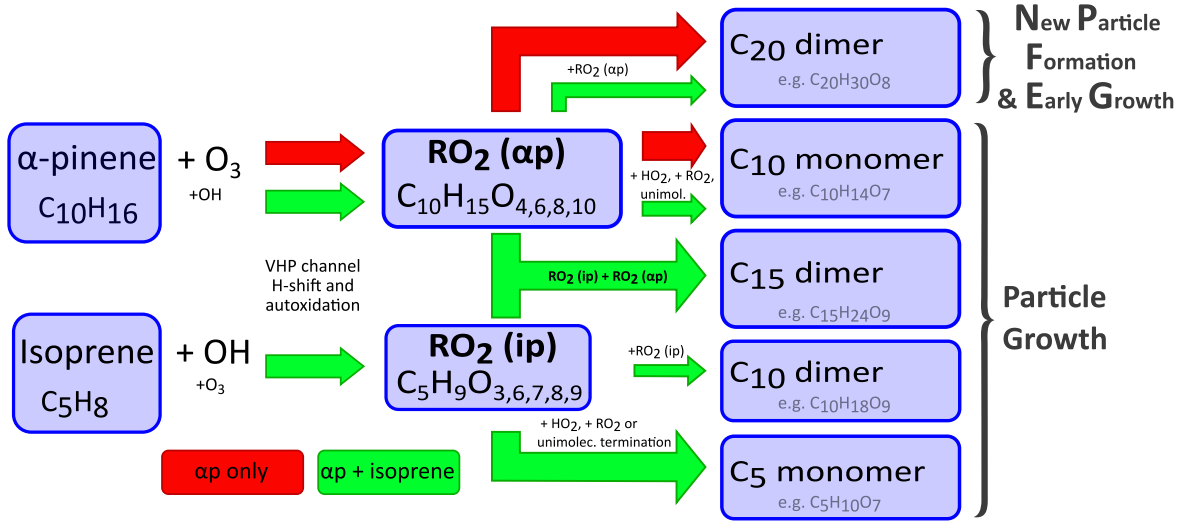

Figure 14: Proposed mechanism for the interference of isoprene in α-pinene oxidation chemistry. The pathway of HOM formation of an α-pinene/ozone mixture alone is indicated by red arrows. When isoprene is present additionally the green arrows indicate the interference of isoprene in α-pinene oxidation chemistry via RO_2• radicals. The oxidation of α-pinene at the conditions used in our experiments (+5°C, 38 % RH) is dominated by ozonolysis. After the initial ozone attack a $C_{10}H_{15}O_4$ peroxy-radical is forming via a vinylhydroperoxyde channel (VHP), which might undergo various intramolecular H-shifts and autoxidation steps (Ehn et al., 2014; Kirkby et al., 2016). Thus the chain of $RO_2(\alpha p)$ mostly consists of $C_{10}H_{15}O_{4,6,8,10}$. These radicals can terminate either via reaction with other RO_2• radicals, via reaction with HO_2 or via unimolecular processes (Rissanen et al., 2015). The resulting closed shell products are then either covalently bound C_{20} class dimers, which are mostly responsible for nucleation or C_{10} class monomers. Possible fragmentation might also lead to some C_5 class molecules being formed even without isoprene present. Isoprene oxidation is dominated by reactions with OH• in the CLOUD chamber, which produce a series of C_5 RO_2• radicals ($C_5H_9O_{3,6,7,8,9}$). These RO_2(ip) radicals can now interfere in the termination of $RO_2(\alpha p)$. The reaction of RO_2(ip) with $RO_2(\alpha p)$ can lead to C_{15} class dimers, C_{10} class monomers or C_5 class monomers. The reaction of RO_2(ip) with another RO_2(ip) can lead to C_{10} class dimers or C_5 class monomers. The presence of RO_2(ip) reduces the steady state concentration of $RO_2(\alpha p)$, as it acts as an additional sink for $RO_2(\alpha p)$. This directly reduces the formation of C_{20} class dimers, as two $RO_2(\alpha p)$ radicals are needed to form one C_{20} class dimer. We link this reduction of C_{20} class dimers to the reduction of the biogenic nucleation rate in the presence of isoprene.

4.4 References

Almeida, J., Schobesberger, S., Kürten, A., Ortega, I. K., Kupiainen-Määttä, O., Praplan, A. P., Adamov, A., Amorim, A., Bianchi, F., Breitenlechner, M., David, A., Dommen, J., Donahue, N. M., Downard, A., Dunne, E., Duplissy, J., Ehrhart, S., Flagan, R., Franchin, A., Guida, R., Hakala, J., Hansel, A., Heinritzi, M., Henschel, H., Jokinen, T., Junninen, H., Kajos, M., Kangasluoma, J., Keskinen, H., Kupc, A., Kurtén, T., Kvashin, A. N., Laaksonen, A., Lehtipalo, K., Leiminger, M., Leppä, J., Loukonen, V., Makhmutov, V., Mathot, S., McGrath, M., Nieminen, T., Olenius, T., Onnela, A., Petäjä, T., Riccobono, F., Riipinen, I., Rissanen, M., Rondo, L., Ruuskanen, T., Santos, F., Sarnela, N., Schallhart, S., Schnitzhofer, R., Seinfeld, J., Simon, M., Sipilä, M., Stozhkov, Y., Stratmann, F., Tomé, A., Tröstl, J., Tsagkogeorgas, G., Vaattovaara, P., Viisanen, Y., Virtanen, A., Vrtala, A., Wagner, P., Weingartner, E., Wex, H., Williamson, C.and Wimmer, D., Ye, P., Yli-Juuti, T., Carslaw, K., Kulmala, M., Curtius, J., Baltensperger, U., Worsnop, D. R., Vehkamäki, H., and Kirkby, J.: Molecular understanding of sulphuric acid–amine particle nucleation in the atmosphere, Nature, 502, 2013.

Berndt, T., Richters, S., Kaethner, R., Voigtländer, J., Stratmann, F., Sipilä, M., Kulmala, M., and Herrmann, H.: Gas-Phase Ozonolysis of Cycloalkenes: Formation of Highly Oxidized RO2 Radicals and Their Reactions with NO, NO2, SO2, and Other RO2 Radicals, J. Phys. Chem. A, 119, 10 336–10 348, doi:10.1021/acs.jpca.5b07295, https://doi.org/10.1021/acs.jpca.5b07295, pMID: 26392132, 2015.

Berndt, T., Herrmann, H., Sipilä, M., and Kulmala, M.: Highly Oxidized Second-Generation Products from the Gas-Phase Reaction of OH Radicals with Isoprene, J. Phys. Chem. A, 120, 10 150–10 159, doi:10.1021/acs.jpca.6b10987, https://doi.org/10.1021/acs.jpca.6b10987, pMID: 27976590, 2016a.

Berndt, T., Richters, S., Jokinen, T., Hyttinen, N., Kurtén, T., Otkjær, R. V., Kjaergaard, H. G., Stratmann, F., Herrmann, H., Sipilä, M., Kulmala, M., and Ehn, M.: Hydroxyl radical-induced formation of highly oxidized organic compounds, Nat. Commun., 7, 13 677, doi:10.1038/ncomms13677, http://dx.doi.org/10.1038/ncomms13677, 2016b.

Bernhammer, A.-K., Breitenlechner, M., Keutsch, F. N., and Hansel, A.: Technical note: Conversion of isoprene hydroxy hydroperoxides (ISOPOOHs) on metal environmental simulation chamber walls, Atmos. Chem. Phys., 17, 4053–4062, doi:10.5194/acp-17-4053-2017, https://www.atmos-chem-phys.net/17/4053/2017/, 2017.

Breitenlechner, M., Fischer, L., Hainer, M., Heinritzi, M., Curtius, J., and Hansel, A.: PTR3: An Instrument for Studying the Lifecycle of Reactive Organic Carbon in the Atmosphere, Anal. Chem., 89, 5824–5831, doi:10.1021/acs.analchem.6b05110, http://dx.doi.org/10.1021/acs.analchem.6b05110, pMID: 28436218, 2017.

Carlton, A. G., Wiedinmyer, C., and Kroll, J. H.: A review of Secondary Organic Aerosol (SOA) formation from isoprene, Atmos. Chem. Phys., 9, 4987–5005, doi:10.5194/acp-9-4987-2009, https://www.atmos-chem-phys.net/9/4987/2009/, 2009.

Claeys, M., Graham, B., Vas, G., Wang, W., Vermeylen, R., Pashynska, V., Cafmeyer, J., Guyon, P., Andreae, M. O., Artaxo, P., and Maenhaut, W.: Formation of Secondary

Organic Aerosols Through Photooxidation of Isoprene, Science, 303, 1173–1176, doi:10.1126/science.1092805, http://science.sciencemag.org/content/303/5661/1173, 2004.

Dunne, E. M., Gordon, H., Kürten, A., Almeida, J., Duplissy, J., Williamson, C., Ortega, I. K., Pringle, K. J., Adamov, A., Baltensperger, U., Barmet, P., Benduhn, F., Bianchi, F., Breitenlechner, M., Clarke, A., Curtius, J., Dommen, J., Donahue, N. M., Ehrhart, S., Flagan, R. C., Franchin, A., Guida, R., Hakala, J., Hansel, A., Heinritzi, M., Jokinen, T., Kangasluoma, J., Kirkby, J., Kulmala, M., Kupc, A., Lawler, M. J., Lehtipalo, K., Makhmutov, V., Mann, G., Mathot, S., Merikanto, J., Miettinen, P., Nenes, A., Onnela, A., Rap, A., Reddington, C. L. S., Riccobono, F., Richards, N. A. D., Rissanen, M. P., Rondo, L., Sarnela, N., Schobesberger, S., Sengupta, K., Simon, M., Sipilä, M., Smith, J. N., Stozkhov, Y., Tomé, A., Tröstl, J., Wagner, P. E., Wimmer, D., Winkler, P. M., Worsnop, D. R., and Carslaw, K. S.: Global atmospheric particle formation from CERN CLOUD measurements, Science, 354, 1119–1124, doi:10.1126/science.aaf2649, http://science.sciencemag.org/content/354/6316/1119, 2016.

Duplissy, J., Merikanto, J., Franchin, A., Tsagkogeorgas, G., Kangasluoma, J., Wimmer, D., Vuollekoski, H., Schobesberger, S., Lehtipalo, K., Flagan, R. C., Brus, D., Donahue, N. M., Vehkamäki, H., Almeida, J., Amorim, A., Barmet, P., Bianchi, F., Breitenlechner, M., Dunne, E. M., Guida, R., Henschel, H., Junninen, H., Kirkby, J., Kürten, A., Kupc, A., Määttänen, A., Makhmutov, V., Mathot, S., Nieminen, T., Onnela, A., Praplan, A. P., Riccobono, F., Rondo, L., Steiner, G., Tome, A., Walther, H., Baltensperger, U., Carslaw, K. S., Dommen, J., Hansel, A., Petäjä, T., Sipilä, M., Stratmann, F., Vrtala, A., Wagner, P. E., Worsnop, D. R., Curtius, J., and Kulmala, M.: Effect of ions on sulfuric acid-water binary particle formation: 2. Experimental data and comparison with QC-normalized classical nucleation theory, J. Geophys. Res.-Atmos., 121, 1752–1775, doi:10.1002/2015JD023539, http://dx.doi.org/10.1002/2015JD023539, 2016.

Ehn, M., Thornton, J. A., Kleist, E., Sipila, M., Junninen, H., Pullinen, I., Springer, M., Rubach, F., Tillmann, R., Lee, B., Lopez-Hilfiker, F., Andres, S., Acir, I.-H., Rissanen, M., Jokinen, T., Schobesberger, S., Kangasluoma, J., Kontkanen, J., Nieminen, T., Kurten, T., Nielsen, L. B., Jorgensen, S., Kjaergaard, H. G., Canagaratna, M., Maso, M. D., Berndt, T., Petaja, T., Wahner, A., Kerminen, V.-M., Kulmala, M., Worsnop, D. R., Wildt, J., and Mentel, T. F.: A large source of low-volatility secondary organic aerosol, Nature, 506, 476–479, doi:10.1038/nature13032, http://dx.doi.org/10.1038/nature13032, 2014.

Eisele, F. and Tanner, D.: Measurement of the gas phase concentration of H2SO4 and methane sulfonic acid and estimates of H2SO4 production and loss in the atmosphere, J. Geophys. Res.-Atmos., 98, 9001–9010, doi:10.1029/93JD00031, https://agupubs.onlinelibrary.wiley.com/doi/abs/10.1029/93JD00031, 1993.

Frege, C., Ortega, I. K., Rissanen, M. P., Praplan, A. P., Steiner, G., Heinritzi, M., Ahonen, L., Amorim, A., Bernhammer, A.-K., Bianchi, F., Brilke, S., Breitenlechner, M., Dada, L., Dias, A., Duplissy, J., Ehrhart, S., El-Haddad, I., Fischer, L., Fuchs, C., Garmash, O., Gonin, M., Hansel, A., Hoyle, C. R., Jokinen, T., Junninen, H., Kirkby, J., Kürten, A., Lehtipalo, K., Leiminger, M., Mauldin, R. L., Molteni, U., Nichman, L., Petäjä, T., Sarnela, N., Schobesberger, S., Simon, M., Sipilä, M., Stolzenburg, D., Tomé, A., Vogel, A. L., Wagner, A. C., Wagner, R., Xiao, M., Yan, C., Ye, P., Curtius, J., Donahue, N. M., Flagan, R. C., Kulmala, M., Worsnop, D. R., Winkler, P. M., Dommen, J., and

Baltensperger, U.: Influence of temperature on the molecular composition of ions and charged clusters during pure biogenic nucleation, Atmos. Chem. Phys., 18, 65–79, doi: 10.5194/acp-18-65-2018, https://www.atmos-chem-phys.net/18/65/2018/, 2018.

Fuchs, H., Hofzumahaus, A., Rohrer, F., Bohn, B., Brauers, T., Dorn, H.-P., Häseler, R., Holland, F., Kaminski, M., Li, X., Lu, K., Nehr, S., Tillmann, R., Wegener, R., and Wahner, A.: Experimental evidence for efficient hydroxyl radical regeneration in isoprene oxidation, Nature Geoscience, 6, 1023, doi:10.1038/ngeo1964, http://dx.doi.org/10.1038/ngeo1964, 2013.

Gordon, H., Sengupta, K., Rap, A., Duplissy, J., Frege, C., Williamson, C., Heinritzi, M., Simon, M., Yan, C., Almeida, J., Tröstl, J., Nieminen, T., Ortega, I. K., Wagner, R., Dunne, E. M., Adamov, A., Amorim, A., Bernhammer, A.-K., Bianchi, F., Breitenlechner, M., Brilke, S., Chen, X., Craven, J. S., Dias, A., Ehrhart, S., Fischer, L., Flagan, R. C., Franchin, A., Fuchs, C., Guida, R., Hakala, J., Hoyle, C. R., Jokinen, T., Junninen, H., Kangasluoma, J., Kim, J., Kirkby, J., Krapf, M., Kürten, A., Laaksonen, A., Lehtipalo, K., Makhmutov, V., Mathot, S., Molteni, U., Monks, S. A., Onnela, A., Peräkylä, O., Piel, F., Petäjä, T., Praplan, A. P., Pringle, K. J., Richards, N. A. D., Rissanen, M. P., Rondo, L., Sarnela, N., Schobesberger, S., Scott, C. E., Seinfeld, J. H., Sharma, S., Sipilä, M., Steiner, G., Stozhkov, Y., Stratmann, F., Tomé, A., Virtanen, A., Vogel, A. L., Wagner, A. C., Wagner, P. E., Weingartner, E., Wimmer, D., Winkler, P. M., Ye, P., Zhang, X., Hansel, A., Dommen, J., Donahue, N. M., Worsnop, D. R., Baltensperger, U., Kulmala, M., Curtius, J., and Carslaw, K. S.: Reduced anthropogenic aerosol radiative forcing caused by biogenic new particle formation, P. Nat. Acad. Sci. USA, 113, 12 053–12 058, doi:10.1073/pnas.1602360113, http://www.pnas.org/content/113/43/12053.abstract, 2016.

Guenther, A. B., Jiang, X., Heald, C. L., Sakulyanontvittaya, T., Duhl, T., Emmons, L. K., and Wang, X.: The Model of Emissions of Gases and Aerosols from Nature version 2.1 (MEGAN2.1): an extended and updated framework for modeling biogenic emissions, Geosci. Model Dev., 5, 1471–1492, doi:10.5194/gmd-5-1471-2012, https://www.geosci-model-dev.net/5/1471/2012/, 2012.

Heinritzi, M., Simon, M., Steiner, G., Wagner, A. C., Kürten, A., Hansel, A., and Curtius, J.: Characterization of the mass-dependent transmission efficiency of a CIMS, Atmos. Meas. Tech., 9, 1449–1460, doi:10.5194/amt-9-1449-2016, https://www.atmos-meas-tech.net/9/1449/2016/, 2016.

Hyttinen, N., Rissanen, M. P., and Kurtén, T.: Computational Comparison of Acetate and Nitrate Chemical Ionization of Highly Oxidized Cyclohexene Ozonolysis Intermediates and Products, J. Phys. Chem. A, 121, 2172–2179, doi:10.1021/acs.jpca.6b12654, https://doi.org/10.1021/acs.jpca.6b12654, pMID: 28234483, 2017.

Jardine, A. B., Jardine, K. J., Fuentes, J. D., Martin, S. T., Martins, G., Durgante, F., Carneiro, V., Higuchi, N., Manzi, A. O., and Chambers, J. Q.: Highly reactive light-dependent monoterpenes in the Amazon, Geophysical Research Letters, 42, 1576–1583, doi:10.1002/2014GL062573, https://agupubs.onlinelibrary.wiley.com/doi/abs/10.1002/2014GL062573, 2015.

Kanawade, V. P., Jobson, B. T., Guenther, A. B., Erupe, M. E., Pressley, S. N., Tripathi, S. N., and Lee, S.-H.: Isoprene suppression of new particle formation in a mixed deciduous

forest, Atmospheric Chemistry and Physics, 11, 6013–6027, doi:10.5194/acp-11-6013-2011, https://www.atmos-chem-phys.net/11/6013/2011/, 2011.

Kangasluoma, J., Kuang, C., Wimmer, D., Rissanen, M. P., Lehtipalo, K., Ehn, M., Worsnop, D. R., Wang, J., Kulmala, M., and Petäjä, T.: Sub-3 nm particle size and composition dependent response of a nano-CPC battery, Atmos. Meas. Tech., 7, 689–700, doi:10.5194/amt-7-689-2014, http://www.atmos-meas-tech.net/7/689/2014/, 2014.

Kiendler-Scharr, A., Wildt, J., Maso, M. D., Hohaus, T., Kleist, E., Mentel, T. F., Tillmann, R., Uerlings, R., Schurr, U., and Wahner, A.: New particle formation in forests inhibited by isoprene emissions, Nature, 461, 381, doi:10.1038/nature08292, http://dx.doi.org/10.1038/nature08292, 2009.

Kiendler-Scharr, A., Andres, S., Bachner, M., Behnke, K., Broch, S., Hofzumahaus, A., Holland, F., Kleist, E., Mentel, T. F., Rubach, F., Springer, M., Steitz, B., Tillmann, R., Wahner, A., Schnitzler, J.-P., and Wildt, J.: Isoprene in poplar emissions: effects on new particle formation and OH concentrations, Atmos. Chem. Phys., 12, 1021–1030, doi:10.5194/acp-12-1021-2012, https://www.atmos-chem-phys.net/12/1021/2012/, 2012.

Kirkby, J., Curtius, J., Almeida, J., Dunne, E., Duplissy, J., Ehrhart, S., Franchin, A., Gagné, S., Ickes, L., Kürten, A., Kupc, A., Metzger, A., Riccobono, F., Rondo, L., Schobesberger, S., Tsagkogeorgas, G., Wimmer, D., Amorim, A., Bianchi, F., Breitenlechner, M., David, A., Dommen, J., Downard, A., Ehn, M., Flagan, R. C., Haider, S., Hansel, A., Hauser, D., Jud, W., Junninen, H., Kreissl, F., Kvashin, A., Laaksonen, A., Lehtipalo, K., Lima, J., Lovejoy, E. R., Makhmutov, V., Mathot, S., Mikkilä, J., Minginette, P., Mogo, S., Nieminen, T., Onnela, A., Pereira, P., Petäjä, T., Schnitzhofer, R., Seinfeld, J. H., Sipilä, M., Stozhkov, Y., Stratmann, F., Tomé, A., Vanhanen, J., Viisanen, Y., Vrtala, A., Wagner, P. E., Walther, H., Weingartner, E., Wex, H., Winkler, P. M., Carslaw, K. S., Worsnop, D. R., Baltensperger, U., and Kulmala, M.: Role of sulphuric acid, ammonia and galactic cosmic rays in atmospheric aerosol nucleation, Nature, 476, 429–433, doi:10.1038/nature10343, http://dx.doi.org/10.1038/nature10343, 2011.

Kirkby, J., Duplissy, J., Sengupta, K., Frege, C., Gordon, H., Williamson, C., Heinritzi, M., Simon, M., Yan, C., Almeida, J., Tröstl, J., Nieminen, T., Ortega, I. K., Wagner, R., Adamov, A., Amorim, A., Bernhammer, A.-K., Bianchi, F., Breitenlechner, M., Brilke, S., Chen, X., Craven, J., Dias, A., Ehrhart, S., Flagan, R. C., Franchin, A., Fuchs, C., Guida, R., Hakala, J., Hoyle, C. R., Jokinen, T., Junninen, H., Kangasluoma, J., Kim, J., Krapf, M., Kürten, A., Laaksonen, A., Lehtipalo, K., Makhmutov, V., Mathot, S., Molteni, U., Onnela, A., Peräkylä, O., Piel, F., Petäjä, T., Praplan, A. P., Pringle, K., Rap, A., Richards, N. A. D., Riipinen, I., Rissanen, M. P., Rondo, L., Sarnela, N., Schobesberger, S., Scott, C. E., Seinfeld, J. H., Sipilä, M., Steiner, G., Stozhkov, Y., Stratmann, F., Tomé, A., Virtanen, A., Vogel, A. L., Wagner, A. C., Wagner, P. E., Weingartner, E., Wimmer, D., Winkler, P. M., Ye, P., Zhang, X., Hansel, A., Dommen, J., Donahue, N. M., Worsnop, D. R., Baltensperger, U., Kulmala, M., Carslaw, K. S., and Curtius, J.: Ion-induced nucleation of pure biogenic particles, Nature, 533, 521–526, doi:10.1038/nature17953, http://dx.doi.org/10.1038/nature17953, 2016.

Krechmer, J. E., Coggon, M. M., Massoli, P., Nguyen, T. B., Crounse, J. D., Hu, W., Day, D. A., Tyndall, G. S., Henze, D. K., Rivera-Rios, J. C., Nowak, J. B., Kimmel, J. R.,

Mauldin, R. L., Stark, H., Jayne, J. T., Sipilä, M., Junninen, H., Clair, J. M. S., Zhang, X., Feiner, P. A., Zhang, L., Miller, D. O., Brune, W. H., Keutsch, F. N., Wennberg, P. O., Seinfeld, J. H., Worsnop, D. R., Jimenez, J. L., and Canagaratna, M. R.: Formation of Low Volatility Organic Compounds and Secondary Organic Aerosol from Isoprene Hydroxyhydroperoxide Low-NO Oxidation, Environ. Sci. Technol., 49, 10 330–10 339, doi:10.1021/acs.est.5b02031, https://doi.org/10.1021/acs.est.5b02031, pMID: 26207427, 2015.

Kroll, J. H., Hanisco, T. F., Donahue, N. M., Demerjian, K. L., and Anderson, J. G.: Accurate, direct measurements of oh yields from gas-phase ozone-alkene reactions using an in situ LIF Instrument, Geophys. Res. Lett., 28, 3863–3866, doi:10.1029/2001GL013406, https://agupubs.onlinelibrary.wiley.com/doi/abs/10.1029/2001GL013406, 1001.

Kürten, A., Rondo, L., Ehrhart, S., and Curtius, J.: Calibration of a Chemical Ionization Mass Spectrometer for the Measurement of Gaseous Sulfuric Acid, J. Phys. Chem. A, 116, 6375–6386, doi:10.1021/jp212123n, https://doi.org/10.1021/jp212123n, pMID: 22364556, 2012.

Kürten, A., Williamson, C., Almeida, J., Kirkby, J., and Curtius, J.: On the derivation of particle nucleation rates from experimental formation rates, Atmos. Chem. Phys., 15, 4063–4075, doi:10.5194/acp-15-4063-2015, https://www.atmos-chem-phys.net/15/4063/2015/, 2015.

Kulmala, M., Kerminen, V.-M., Anttila, T., Laaksonen, A., and O'Dowd, C. D.: Organic aerosol formation via sulphate cluster activation, J. Geophys. Res.-Atmos., 109, doi:10.1029/2003JD003961, http://dx.doi.org/10.1029/2003JD003961, d04205, 2004.

Kulmala, M., Kontkanen, J., Junninen, H., Lehtipalo, K., Manninen, H. E., Nieminen, T., Petäjä, T., Sipilä, M., M., Schobesberger, S., Rantala, P., Franchin, A., Jokinen, T., Järvinen, E., Äijälä, M., Kangasluoma, J., Hakala, J., Aalto, P. P., Paasonen, P., Mikkilä, J., Vanhanen, J., Aalto, J., Hakola, H., Makkonen, U., Ruuskanen, T., Mauldin, R. L., Duplissy, J., Vehkamäki, H., Bäck, J., Kortelainen, A., Riipinen, I., Kurtén, T., Johnston, M. V., Smith, J. N., Ehn, M., Mentel, T. F., Lehtinen, K. E. J., Laaksonen, A., Kerminen, V.-M., and Worsnop, D. R.: Direct Observations of Atmospheric Aerosol Nucleation, Science, 339, 943–946, doi:10.1126/science.1227385, http://science.sciencemag.org/content/339/6122/943, 2013.

Kürten, A., Rondo, L., Ehrhart, S., and Curtius, J.: Performance of a corona ion source for measurement of sulfuric acid by chemical ionization mass spectrometry, Atmos. Meas. Tech., 4, 437–443, doi:10.5194/amt-4-437-2011, https://www.atmos-meas-tech.net/4/437/2011/, 2011.

Kurtén, T., Tiusanen, K., Roldin, P., Rissanen, M., Luy, J.-N., Boy, M., Ehn, M., and Donahue, N.: Alpha-Pinene Autoxidation Products May Not Have Extremely Low Saturation Vapor Pressures Despite High O:C Ratios, J. Phys. Chem. A, 120, 2569–2582, doi:10.1021/acs.jpca.6b02196, http://dx.doi.org/10.1021/acs.jpca.6b02196, pMID: 27049168, 2016.

Lee, S.-H., Uin, J., Guenther, A. B., Gouw, J. A., Yu, F., Nadykto, A. B., Herb, J., Ng, N. L., Koss, A., Brune, W. H., Baumann, K., Kanawade, V. P., Keutsch, F. N., Nenes,

A., Olsen, K., Goldstein, A., and Ouyang, Q.: Isoprene suppression of new particle formation: Potential mechanisms and implications, J. Geophys. Res.-Atmos., 121, 14,621–14,635, doi:10.1002/2016JD024844, https://agupubs.onlinelibrary.wiley.com/doi/abs/10.1002/2016JD024844, 2016.

Lehtipalo, K., Leppä, J., Kontkanen, J., Kangasluoma, J., Franchin, A., Wimmer, D., Schobesberger, S., Junninen, H., Petäjä, T., Sipilä, M., Mikkilä, J., Vanhanen, J., Worsnop, D. R., and Kulmala, M.: Methods for determining particle size distribution and growth rates between 1 and 3 nm using the Particle Size Magnifier, Boreal Environ. Res., 19, 215–236, 2014.

Lelieveld, J., Gromov, S., Pozzer, A., and Taraborrelli, D.: Global tropospheric hydroxyl distribution, budget and reactivity, Atmos. Chem. Phys., 16, 12 477–12 493, doi:10.5194/acp-16-12477-2016, https://www.atmos-chem-phys.net/16/12477/2016/, 2016.

Malkin, T. L., Goddard, A., Heard, D. E., and Seakins, P. W.: Measurements of OH and HO_2 yields from the gas phase ozonolysis of isoprene, Atmos. Chem. Phys., 10, 1441–1459, doi:10.5194/acp-10-1441-2010, https://www.atmos-chem-phys.net/10/1441/2010/, 2010.

Martin, S. T., Andreae, M. O., Artax, P., Baumgardner, D., Chen, Q., Goldstein, A. H., Guenther, A., Heald, C. L., Mayol-Bracero, O. L., McMurry, P. H., Pauliquevis, T., Pöschl, U., Prather, K. A., Roberts, G. C., Saleska, S. R., Silva, D. M. A., Spracklen, D. V., Swietlicki, E., and Trebs, I.: Sources and properties of Amazonian aerosol particles, Rev. Geophys., 48, doi:10.1029/2008RG000280, https://agupubs.onlinelibrary.wiley.com/doi/abs/10.1029/2008RG000280, 2010.

Martinez, M., Harder, H., Kubistin, D., Rudolf, M., Bozem, H., Eerdekens, G., Fischer, H., Klüpfel, T., Gurk, C., Königstedt, R., Parchatka, U., Schiller, C. L., Stickler, A., Williams, J., and Lelieveld, J.: Hydroxyl radicals in the tropical troposphere over the Suriname rainforest: airborne measurements, Atmos. Chem. Phys., 10, 3759–3773, doi:10.5194/acp-10-3759-2010, https://www.atmos-chem-phys.net/10/3759/2010/, 2010.

Riccobono, F., Schobesberger, S., Scott, C. E., Dommen, J., Ortega, I. K., Rondo, L., Almeida, J., Amorim, A., Bianchi, F., Breitenlechner, M., David, A., Downard, A., Dunne, E. M., Duplissy, J., Ehrhart, S., Flagan, R. C., Franchin, A., Hansel, A., Junninen, H., Kajos, M., Keskinen, H., Kupc, A., Kürten, A., Kvashin, A. N., Laaksonen, A., Lehtipalo, K., Makhmutov, V., Mathot, S., Nieminen, T., Onnela, A., Petäjä, T., Praplan, A. P., Santos, F. D., Schallhart, S., Seinfeld, J. H., Sipilä, M., Spracklen, D. V., Stozhkov, Y., Stratmann, F., Tomé, A., Tsagkogeorgas, G., Vaattovaara, P., Viisanen, Y., Vrtala, A., Wagner, P. E., Weingartner, E., Wex, H., Wimmer, D., Carslaw, K. S., Curtius, J., Donahue, N. M., Kirkby, J., Kulmala, M., Worsnop, D. R., and Baltensperger, U.: Oxidation Products of Biogenic Emissions Contribute to Nucleation of Atmospheric Particles, Science, 344, 717–721, doi:10.1126/science.1243527, http://science.sciencemag.org/content/344/6185/717, 2014.

Rissanen, M. P., Kurtén, T., Sipilä, M., Thornton, J. A., Kausiala, O., Garmash, O., Kjaergaard, H. G., Petäjä, T., Worsnop, D. R., Ehn, M., and Kulmala, M.: Effects of Chemical Complexity on the Autoxidation Mechanisms of Endocyclic Alkene Ozonolysis Products: From Methylcyclohexenes toward Understanding alpha-Pinene, J. Phys. Chem.

A, 119, 4633–4650, doi:10.1021/jp510966g, https://doi.org/10.1021/jp510966g, pMID: 25615900, 2015.

Seinfeld, J. and Pandis, S.: Atmospheric Chemistry and Physics: From Air Pollution to Climate Change, 2nd edition, Wiley, second edition edn., 2006.

Sipilä, M., Sarnela, N., Jokinen, T., Henschel, H., Junninen, H., Kontkanen, J., Richters, S., Kangasluoma, J., Franchin, A., Peräkylä, O., Rissanen, M. P., Ehn, M., Vehkamäki, H., Kurten, T., Berndt, T., Petäjä, T., Worsnop, D., Ceburnis, D., Kerminen, V.-M., Kulmala, M., and O'Dowd, C.: Molecular-scale evidence of aerosol particle formation via sequential addition of HIO3, Nature, 537, 532, doi:10.1038/nature19314, http://dx.doi.org/10.1038/nature19314, 2016.

Stolzenburg, D., Steiner, G., and Winkler, P. M.: A DMA-train for precision measurement of sub-10 nm aerosol dynamics, Atmos. Meas. Tech., 10, 1639–1651, doi:10.5194/amt-10-1639-2017, http://www.atmos-meas-tech.net/10/1639/2017/, 2017.

Taraborrelli, D., Lawrence, M. G., Crowley, J. N., Dillon, T. J., Gromov, S., Groß, C. B. M., Vereecken, L., and Lelieveld, J.: Hydroxyl radical buffered by isoprene oxidation over tropical forests, Nat. Geosci., 5, 190, doi:10.1038/ngeo1405, http://dx.doi.org/10.1038/ngeo1405, 2012.

Teng, A. P., Crounse, J. D., and Wennberg, P. O.: Isoprene Peroxy Radical Dynamics, J. Am. Chem. Soc., 139, 5367–5377, doi:10.1021/jacs.6b12838, https://doi.org/10.1021/jacs.6b12838, pMID: 28398047, 2017.

Tillmann, R., Hallquist, M., Jonsson, Å. M., Kiendler-Scharr, A., Saathoff, H., Iinuma, Y., and Mentel, T. F.: Influence of relative humidity and temperature on the production of pinonaldehyde and OH radicals from the ozonolysis of alpha-pinene, Atmos. Chem. Phys., 10, 7057–7072, doi:10.5194/acp-10-7057-2010, https://www.atmos-chem-phys.net/10/7057/2010/, 2010.

Tröstl, J., Chuang, W. K., Gordon, H., Heinritzi, M., Yan, C., Molteni, U., Ahlm, L., Frege, C., Bianchi, F., Wagner, R., Simon, M., Lehtipalo, K., Williamson, C., Craven, J. S., Duplissy, J., Adamov, A., Almeida, J., Bernhammer, A.-K., Breitenlechner, M., Brilke, S., Dias, A., Ehrhart, S., Flagan, R. C., Franchin, A., Fuchs, C., Guida, R., Gysel, M., Hansel, A., Hoyle, C. R., Jokinen, T., Junninen, H., Kangasluoma, J., Keskinen, H., Kim, J., Krapf, M., Kürten, A., Laaksonen, A., Lawler, M., Leiminger, M., Mathot, S., Möhler, O., Nieminen, T., Onnela, A., Petäjä, T., Piel, F. M., Miettinen, P., Rissanen, M. P., Rondo, L., Sarnela, N., Schobesberger, S., Sengupta, K., Sipilä, M., Smith, J. N., Steiner, G., Tomè, A., Virtanen, A., Wagner, A. C., Weingartner, E., Wimmer, D., Winkler, P. M., Ye, P., Carslaw, K. S., Curtius, J., Dommen, J., Kirkby, J., Kulmala, M., Riipinen, I., Worsnop, D. R., Donahue, N. M., and Baltensperger, U.: The role of low-volatility organic compounds in initial particle growth in the atmosphere, Nature, 533, 527–531, doi:10.1038/nature18271, http://dx.doi.org/10.1038/nature18271, 2016.

Vanhanen, J., Mikkilä, J., Lehtipalo, K., Sipilä, M., Manninen, H. E., Siivola, E., Petäjä, T., and Kulmala, M.: Particle Size Magnifier for Nano-CN Detection, Aerosol Sci. Tech., 45, 533–542, doi:10.1080/02786826.2010.547889, http://www.tandfonline.com/doi/abs/10.1080/02786826.2010.547889, 2011.

Yu, H., Ortega, J., Smith, J. N., Guenther, A. B., Kanawade, V. P., You, Y., Liu, Y., Hosman, K., Karl, T., Seco, R., Geron, C., Pallardy, S. G., Gu, L., Mikkilä, J., and Lee, S.-H.: New Particle Formation and Growth in an Isoprene-Dominated Ozark Forest: From Sub-5 nm to CCN-Active Sizes, Aerosol Sci. Technol., 48, 1285–1298, doi:10.1080/02786826.2014.984801, `https://doi.org/10.1080/02786826.2014.984801`, 2014.

Chapter 5

Rapid growth rates of organic aerosol nanoparticles over a wide tropospheric temperature range

This chapter by D.Stolzenburg, L.Fischer, M.Heinritzi, M.Schervish, M.Simon, L.Dada and the CLOUD collaboration[1] was submitted on May 3rd 2018 and is under review for publication in *Proceedings of the National Academy of Sciences*

Abstract. Nucleation and growth of aerosol particles from atmospheric vapors constitutes a major source of global cloud condensation nuclei (CCN). The fraction of newly-formed particles that reaches CCN sizes is highly sensitive to particle growth rates, especially for particle sizes below 10 nm where coagulation losses to larger aerosol particles are greatest. Recent results show that some oxidation products from biogenic volatile organic compounds are major contributors to particle formation and initial growth. However, whether oxidized organics contribute to particle growth over the broad span of tropospheric temperatures remains an open question, and quantitative mass balance for organic growth has yet to be demonstrated at any temperature. Here, in experiments performed under atmospheric conditions in the CERN CLOUD chamber, we show that rapid growth of organic particles occurs over the range from -25°C to +25°C. The lower extent of autoxidation at reduced temperatures is compensated by the decreased volatility of all oxidised states. We could reproduce the measured growth rates using an aerosol growth model based entirely on the experimentally-measured gas-phase spectra of oxidized organic molecules using two complementary mass spectrometers. We show that the growth rates are sensitive to particle curvature and display a clear acceleration as the particles increase in size, corresponding to a Kelvin diameter of 4.8±0.8 nm at 300 K, explaining widespread atmospheric observations that particle growth rates increase in the single-digit-nm size range. Our results demonstrate that organic vapours can contribute to particle growth over a wide range of tropospheric temperatures from molecular cluster sizes onward.

[1] Full author list: Dominik Stolzenburg, Lukas Fischer, Martin Heinritzi, Meredith Schervish, Mario Simon, Lubna Dada, Lauri R. Ahonen, Antonio Amorim, Andrea Baccarini, Paulus S. Bauer, Bernhard Baumgartner, Anton Bergen, Federico Bianchi, Martin Breitenlechner, Sophia Brilke, Stephany Buenrostro Mazon, Dexian Chen, António Dias, Danielle C. Draper, Jonathan Duplissy, Imad El Haddad, Henning Finkenzeller, Carla Frege, Claudia Fuchs, Olga Garmash, Hamish Gordon, Xucheng He, Johanna Helm, Victoria Hofbauer, Christopher R. Hoyle, Changhyuk Kim, Jasper Kirkby, Jenni Kontkanen, Andreas Kürten, Janne Lampilahti, Katrianne Lehtipalo, Markus Leiminger, Huajun Mai, Serge Mathot, Bernhard Mentler, Ugo Molteni, Wei Nie, Tuomo Nieminen, Andrea Ojdanic, Antti Onnela, Monica Passananti, Tuukka Petäjä, Lauriane L. J. Quéléver, Matti P. Rissanen, Nina Sarnela, Simon Schallhart, James N. Smith, Christian Tauber, António Tomé, Alexander L. Vogel, Andrea C. Wagner, Robert Wagner, Mingyi Wang, Lena Weitz, Daniela Wimmer, Mao Xiao, Chao Yan, Penglin Ye, Qiaozhi Zha, Urs Baltensperger, Joachim Curtius, Josef Dommen, Richard C. Flagan, Markku Kulmala, Douglas R. Worsnop, Armin Hansel, Neil M. Donahue, Paul M. Winkler

5.1 Introduction

The global budget of cloud condensation nuclei (CCN) has a significant impact on the Earth's radiative balance, as it affects the albedo and the lifetime of clouds. New particle formation by gas-to-particle conversion is the largest source of CCN Gordon et al. (2017). Especially the early steps of particle growth between 1-10 nm determine the survival chance of freshly formed particles and therefore their climatic relevance (Lehtinen et al., 2007; Pierce and Adams, 2007). The major vapours driving particle growth are sulfuric acid and, maybe more importantly, low volatility organics resulting from the oxidation of volatile organic compounds (VOCs) (Riipinen et al., 2012). Monoterpenes are an important class of atmospheric VOCs with copious emissions from vegetation (Guenther et al., 2012). They are quickly oxidized in the atmosphere and through a subsequent auto-oxidation process rapidly form highly oxygenated molecules (HOMs), which constitute a large source of low-volatility species in the atmosphere (Ehn et al., 2014). Recent studies have shown that HOMs from the ozonolysis of the predominant monoterpene α-pinene are able to form (Kirkby et al., 2016) and efficiently grow particles from cluster sizes onward (Tröstl et al., 2016). Model simulations suggest that they are major contributors to particle formation on a global scale (Gordon et al., 2016). Moreover, the impact of HOMs on initial particle growth might explain the observations of accelerating growth rates between 1-10 nm during particle formation events (Kulmala et al., 2013) by a multi-component Kelvin effect (Donahue et al., 2011b; Tröstl et al., 2016), also known as nano-Köhler theory (Kulmala et al., 2004). This is because HOMs span a wide range of volatilities (Donahue et al., 2011a) and, with increasing particle size, more and more low-volatile species can contribute to the growth process.

In contrast to sulfuric acid in combination with ammonia or amines, where growth proceeds close to the kinetic limit (Lehtipalo et al., 2016), the characteristics of growth driven by organics are governed by the resulting volatilities of the wide variety of oxidation products. Therefore, temperature likely plays a decisive role as the saturation concentration has a steep exponential temperature-dependence as described by the Clausius-Clapeyron relation. Additionally, a recent study has shown that temperature crucially influences the chemical composition of the initially formed molecular clusters in α-pinene ozonolysis (Frege et al., 2018). Therefore, the contribution of biogenic organics to new particle formation might be strongly sensitive to temperature. This, in turn, may significantly influence the importance of new particle formation at high altitudes (Bianchi et al., 2016) and in outflow regions of deep-convective clouds, e.g. over the Amazon Basin (Murphy et al., 2015; Wang et al., 2016; Andreae et al., 2018).

Here we investigate in the CLOUD chamber (Kirkby et al., 2011) the effect of temperature on the production of oxygenated molecules and subsequent particle growth from dark α-pinene ozonolysis at three different temperatures (-25°C, +5°C, and +25°C) for various precursor concentrations. The resulting volatility distributions are inferred by combining two types of

chemical-ionisation high resolution mass spectrometers (Jokinen et al., 2012; Breitenlechner et al., 2017) using different ionization techniques in order to obtain a detailed representation of the gaseous oxidation products. Together with the precision measurement of particle growth rates (Stolzenburg et al., 2017) this allows identification of the underlying processes and their temperature dependence responsible for initial growth in biogenic ozonolysis systems (See Methods for details about the experimental setup, measurement procedures and used instrumentation).

5.2 Results

5.2.1 Observed gas phase mass spectrum

Fig. 1 shows mass defect plots from the Nitrate-CI-APi-ToF (Nitrate-CI) (Jokinen et al., 2012) and the PTR3-ToF (PTR3) (Breitenlechner et al., 2017) during three representative experiments at three different temperatures. For all three cases, we averaged the observed gas-phase concentrations C^v over a period where comparable particle growth rates are measured with a DMA-train (Stolzenburg et al., 2017) and the α-pinene ozonolysis rate is similar with

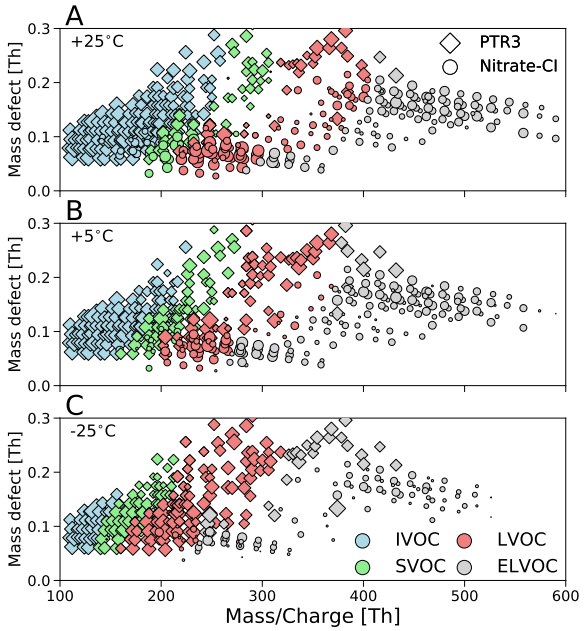

Figure 1: Mass defect of all measured neutral oxidized organic compounds versus the nominal mass to charge ratio of three representative experiments, at +25°C (A), at +5°C (B) and at -25°C (C), all with a similar α-pinene ozonolysis reaction rate. Diamonds represent molecular ions measured by the PTR3 and circles compounds measured by the Nitrate-CI, both taking the different reagent ions into account. The size of the symbols is proportional to the logarithm of the measured concentration and the color is related to the volatility class as defined in Fig. **??**.

$[\mathrm{k}(T) \cdot \mathrm{ap} \cdot \mathrm{O_3}] \sim 1.4 - 2.0 \cdot 10^6 \mathrm{cm^{-3}s^{-1}}$.

The mass defect plots for all temperatures show the typical pattern of HOMs (Tröstl et al., 2016). Two bands can be identified, one representing monomers (n_C=6-10, 100-400 Th) and one representing dimers (n_C=16-20, 400-600 Th); molecules with increasing oxidation state are found towards the lower right of the panels. Apparently, the PTR3 introduces more than 200 previously undetected molecular ion signals, not only HOMs, which are usually specified by their high O:C ratio (>0.7 for monomers), but mostly compounds towards lower oxidation states.

As temperature decreases, the intensity of the majority of the peaks drops, especially for compounds with a high oxidation state and with a high detection efficiency in the Nitrate-CI. This is similar to the observations by (Frege et al., 2018), where a significant decrease in O:C ratio of the nucleating charged clusters was observed during the same set of experiments.

In Fig. 1, the symbol color for peaks with an identified composition corresponds to a broad temperature-dependent classification of their volatility, based on the carbon and oxygen numbers of the individual compounds (see Supporting Information for detailed information on the volatility classification and its temperature dependence). We place them in four general groups, according to their saturation mass concentration C^*: extremely low volatility compounds (ELVOC, $\log_{10} C^*$ $\leq$-4.5), low volatility compounds (LVOC, $\log_{10} C^*$=(-4.5,-0.5]), semi-volatile compounds (SVOC, $\log_{10} C^*$=(-0.5,2.5]) and intermediate volatility compounds (IVOC, $\log_{10} C^*$ >2.5) (Donahue et al., 2011a). Compounds in the ELVOC and LVOC ranges have been shown to contribute to nanoparticle growth (Tröstl et al., 2016). Comparing this classification for the three different temperatures clearly indicates the importance of the compounds observed by the PTR3. At -25°C, large quantities of LVOC compounds can be observed by the usage of this additional ionization technique.

5.2.2 Observed volatility distribution within a volatility basis set (VBS)

As volatilities of organic compounds observed in the atmosphere vary by more than 10 orders of magnitude, it is convenient to simplify considerations of gas-to-particle partitioning by grouping compounds together within a volatility basis set (Donahue et al., 2006, 2011a). Within this framework, the volatility bins are separated by one decade in C^* at 300 K, and for other temperatures the binned distribution is shifted towards lower saturation mass concentrations. The saturation mass concentration of oxidized organics should follow the Clausius-Clapeyron relation at a constant evaporation enthalpy ΔH_{vap}, which in turn is linked to C^* at 300 K (Donahue et al., 2011a) (see Supporting Information for details).

Fig. **??** shows the resulting binned volatility distribution of all observed organic gas-phase compounds for the three representative experiments of Fig. 1. Due to the observed comparable growth rates of the three examples, the gas-particle partitioning is expected to be comparable, which is confirmed by the similarity of the observed total volatility distribution over the

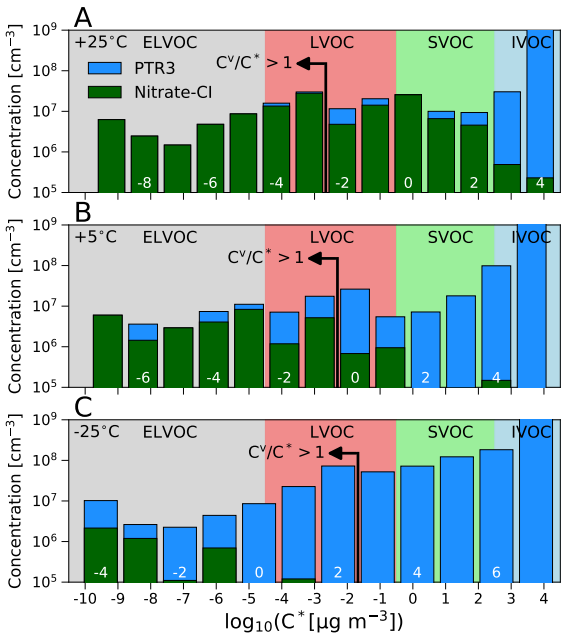

Figure 2: Volatility distributions for representative experiments with similar α-pinene ozonolysis rate, (A) +25°C, (B) +5°C and (C) -25°C. The green and blue bars show summed molecular ions observed in the Nitrate-CI and PTR3, respectively. The highest and lowest bin are overflow bins. Volatility bins are defined at 300 K, shifted and widened according to their corresponding temperature. The resulting saturation mass concentration is defined on the x-axis, while $\log_{10} C^*_{300K}$ is specified by white numbers. Additionally, the bins in supersaturation with $C^v/C^* > 1$ are found left of the indicating arrow.

ELVOC and LVOC ranges. However, it is important that this is only the case due to the additional observed compounds by the PTR3, which, in agreement with Fig. 1, mainly detects less oxygenated molecules with $n_O \leq 7$. Earlier work on growth of nucleated particles from α-pinene oxidation at +5°C employing only a Nitrate-CI found that the measured HOMs could only explain a fraction of the growth and speculated that the nitrate detection efficiency was progressively lower for less polar (and hence more volatile) species (Tröstl et al., 2016). We confirm the missing fraction and find that the PTR3 detects many new compounds not measured by the Nitrate-CI, independent of temperature. At low temperature, fewer polar functional groups are required for a compound to have a low volatility, and thus at +5 °C and even more significantly at -25°C (Panel (B) and (C) respectively) these species observed by the PTR3 contribute substantially in the LVOC and even ELVOC range.

5.2.3 Particle growth measurements

We measured growth rates during the experiments with a DMA-train over two different size-intervals, $1.8 - 3.2$ nm and $3.2 - 8$ nm (see Methods for details). Fig. 2 shows the measured growth rates versus several gas-phase variables. Panel (A) and (B) show the correlation with the estimated reaction rate of the α-pinene ozonolysis during the growth rate measurement.

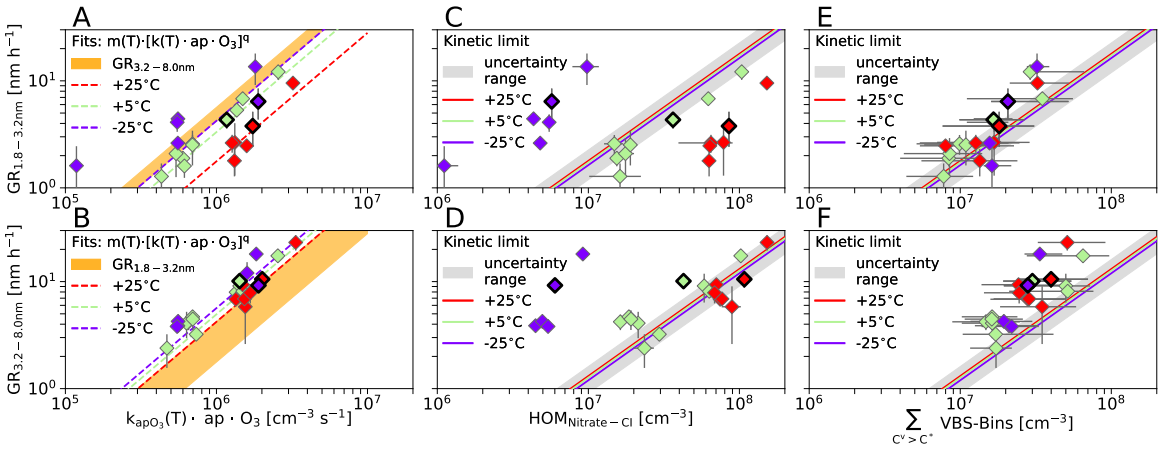

Figure 3: Growth rates measured by the DMA-train in two size intervals (1.8-3.2 nm, panels (A),(C),(E) and 3.2-8 nm, panels (B),(D),(F)) versus several gas phase variables. Representative experiments are highlighted. On the x-axis, panel (A) and (B) show the reacted α-pinene rate, panel (C) and (D) show the HOMs observed in the Nitrate-CI and panel (E) and (F) show the amount of condensable material determined by the temperature dependent volatility basis set. Colors in all plots indicate the run temperatures, purple corresponds to -25°C, green to +5°C and red to +25°C. In panel (A) and (B) the light yellow areas shows the range of growth rates of the other size-interval to demonstrate the observed lower growth rates at small diameters. In panels (C)-(F), the gray area illustrates the range of uncertainty on the kinetic condensation limits drawn as solid colored lines. In panel (E) and (F) the error on the sum over the VBS-distribution is determined from the 1 decade uncertainty in the volatility definition.

Higher reaction rates, and hence higher product concentrations, lead to higher growth rates, following an exponential relation $m(T, d_p) \cdot [\mathrm{k}(T) \cdot \mathrm{ap} \cdot \mathrm{O_3}]^q$ (see Supplementary Information for details). For a given α-pinene ozonolysis reaction rate we find lower growth rates at smaller sizes. The smaller size range also shows a more significant temperature dependency: the growth rates are higher at low temperatures at a given reaction rate. This indicates that the ozonolysis products at the three different temperatures have different properties influencing their ability to condense from molecular cluster sizes onward.

Fig. 2 panel (C) and (D) show the measured growth rates versus the total HOM signal observed in the Nitrate-CI only, along with a kinetic curve showing the growth rate if all measured HOMs condensed irreversibly (Nieminen et al., 2010). The growth rates of the three different temperatures are clearly separated, but condensation at the kinetic limit for HOMs would give almost identical values. Thus, the total HOM concentration observed in the Nitrate-CI cannot fully describe the observed growth at any temperature. At +25°C several HOMs measured by the Nitrate-CI are classified as SVOC and might not be able to condense, and at -25°C the Nitrate-CI measures only a small fraction of the less oxygenated α-pinene oxidation products responsible for particle growth (see Fig. **??**).

Therefore, panels (E) and (F) of Fig. 2 show the growth rates versus a sum, combining both

mass spectrometers, over all VBS bins in supersaturation for a given particle size, i.e. with $S = K(D_p) \cdot C^v_{\text{VBS bin}}/C^*_{\text{VBS bin}} > 1$. A Kelvin-term $K(D_p) = 10^{D_{K10}/D_p}$ accounts for the curvature of the particles, slowing growth of smaller particles. With this simple approach, it is possible to bring the growth measurements at these three different temperatures into reasonable agreement, aligning the data points roughly parallel to the kinetic line. This approach only accounts for bins in supersaturation, which should condense almost kinetically. Especially for the larger size-interval, the measured growth rates are slightly higher than the supersaturated kinetic limits for all temperatures. However, some VBS bins below supersaturation will contribute as well by gas-particle partitioning, which is not considered in this simple approach.

5.2.4 Comparison with an aerosol growth model

Aerosol growth is modeled with the same framework as used in (Tröstl et al., 2016). However, the model was adopted to take real time measured VBS-distributions from both mass spectrometers as input, without any adjustments of unknown charging efficiencies (see Supporting Information for details).

The most important remaining unknown in the condensation equations is the Kelvin-term and the Kelvin-diameter, describing the curvature effect for the condensation onto the smallest particles:

$$D_{K10} = \log_{10}(e) \cdot \frac{4\sigma M}{RT\rho} \tag{1}$$

However, the observed size-dependence and especially the growth measurements at diameters $< D_{K10}$ should provide a direct constraint on the curvature effect. For the three representative experiments, we find the best agreement with $D_{K10}(T) = (4.8 \pm 0.8) \cdot (300\,\text{K} \cdot T^{-1})$ nm, which could correspond to a surface tension of $\sigma = 0.03\,\text{N m}^{-1}$, a molecular mass of $M = 320\,\text{g mol}^{-1}$ and a density of $\rho = 1400\,\text{kg m}^{-3}$, values typical for a LVOC HOM. Fig. 3 shows the resulting predicted growth rates and their size-dependence in comparison with the measurements. The agreement between modeled and measured growth rate at the smallest sizes is within the uncertainties of the measurements. Other values for D_{K10}, e.g. $D_{K10}(300K) = 3.75$ nm, used previously, lead to a significant overestimation of the observed growth rates at the smallest diameters for all temperatures. Another reason for the higher D_{K10} could be an underestimation of the volatility of the most oxygenated compounds (Kurtén et al., 2016). Above 5 nm, the model agrees well with the observations at all temperatures. Considering the 1 decade uncertainty in saturation mass concentration (see Supporting Information for details), we achieve reasonable mass balance for growth of freshly nucleated particles between 2 and 30 nm over a wide range of conditions.

Although there is no disagreement of the model with the measurements, within the uncertainties, there are several contributions that we have not considered. First, some condensable

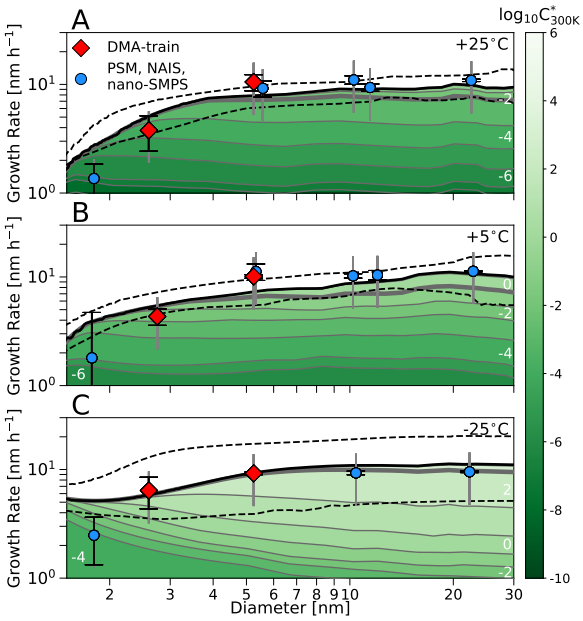

Figure 4: Modeled and measured growth rate versus particle diameter. (A) +25°C at increasing α-pinene ozonolysis reaction rates ($\sim$1.7-2.3·10^6 cm^{-3} s^{-1}) (B) +5°C at increasing reaction rates ($\sim$1.2-1.8·10^6 cm^{-3} s^{-1}) (C) -25°C at constant reaction rates ($\sim$1.9·10^6 cm^{-3} s^{-1}). The thick black lines indicates the modeled total growth rate inferred from real-time oxidized organics measurements and the dashed black lines indicate the associated uncertainty resulting from a ±one bin shift of the VBS-distribution. The contribution of the different bins of the VBS-distribution is illustrated by the colored areas, where white numbers and the color code represent the saturation mass concentration at 300 K for all three cases. The contribution below the thick gray line is from bins with $C^v > C^*$. For the measured growth rates, red diamonds show the DMA-train (shown as well in Fig. 2) and blue circles other instruments (see Supporting Information for details). The capped black errorbar shows the statistical uncertainty of the single measurements, while the gray errorbar gives the 50 % systematic uncertainty of the appearance time method.

compounds might still be undetected by the two used ionization-chemistries. Additionally, fragmentation of molecules within the instruments might disturb the volatility estimate. Second, as well the temperature dependence of organic volatilities is subject to uncertainties (Donahue et al., 2011b). Third, we do not model any particle phase reactions, such as oligomerisation. Reactive uptake is thought to be more important at larger particle sizes (Apsokardu and Johnston, 2018), again in part because of the Kelvin effect (Chuang and Donahue, 2017).

5.3 Conclusion

Organics play a leading role in atmospheric new particle formation and growth and thus govern the global budget of CCN. VOC oxidation products in the atmosphere make up a substantial portion of condensing vapors causing growth of existing particles. Because oxidized organics

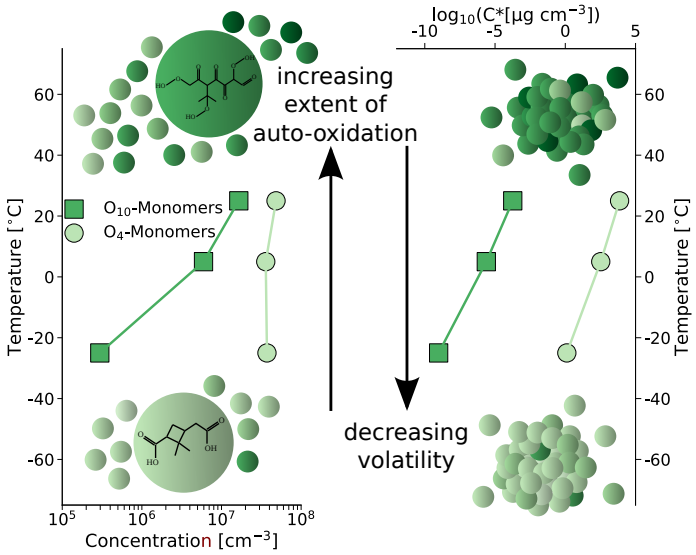

Figure 5: Overview over the competing processes and their temperature dependence. The left panel shows the summed measured concentration of the O_4 and O_{10} monomer (C_{6-10}) compounds. The right panel shows the averaged saturation mass concentration of the same groups of compounds. Data are taken from three experiments with comparable α-pinene ozonolysis reaction rate. The sketch on the left panel illustrates the higher measured concentrations at higher temperatures, especially of highly oxygenated products. The sketch on the right panel shows that growth at cold temperature can proceed already with the condensation of lower oxygenated products due to the decrease in volatility.

span a wide range of volatilities, temperature is a crucial parameter. We have shown that the combination of two mass spectrometers, both using different ionization techniques, and consideration of the volatility distribution of the measured compounds, here with a volatility basis set, gives a sufficient constraint of the gas-phase products, to comprehensively describe growth over a wide temperature range. The measurements are in good agreement with an aerosol growth model and for the first time a direct estimate of the Kelvin diameter for organics of 4.8 nm could be inferred.

Temperature influences the growth by organics from dark α-pinene ozonolysis in several ways via competing processes. This is illustrated in Fig. **??**, where the oxidation products containing 4 oxygen atoms are compared to the oxidation products containing 10 oxygen atoms with respect to their average saturation mass concentration and the measured concentration for three experiments with a comparable α-pinene ozonolysis reaction rate. While for both groups of compounds the volatility decreases with decreasing temperature, the measured concentrations increase with increasing temperature for the O_{10} monomers at similar α-pinene ozonolysis reaction rates. This is due to the temperature dependence of the unimolecular auto-oxidation reactions. It is highly likely that the intramolecular H-atom transfer reactions have significantly higher activation energies than radical-radical termination reactions, and so it is reasonable that the extent of auto-oxidation will increase with increasing tempera-

ture (Praske et al., 2018). As these intramolecular reactions have to occur several times in order to form higher oxygenated molecules, measured concentrations of O_{10} compounds drop significantly as temperature decreases.

Our precision measurement of particle growth rates across the critical size range from 2 - 30 nm reveal that organic condensation drives particle growth at a similar rate over a wide temperature range, when the precursor oxidation rate is held constant. This is due to counterbalancing temperature-dependent effects: lower volatility but also less extensive oxygenation at lower temperature. The competing processes described in Fig. **??** are thus of the same order of magnitude. This suggests a crucial role for organics in aerosol growth across the wide temperature range of the troposphere. Not only due to higher emission and ozonolysis reaction rates, but also due to rapid auto-oxidation to highly oxygenated states, organics can influence aerosol growth dramatically in warm regions. However, due to the strong drop in volatility of even modestly oxygenated organic products at low temperature, organics can drive aerosol growth also in cold regions, e.g. at high altitudes and the sub-arctic. Global aerosol models therefore need to implement robust descriptions of these processes, not only considering the first order rate constants of ozonolysis and OH reactivity, but rather a more detailed description of organic chemistry and its temperature dependence. Precision measurements with a complementary set of mass spectrometers and particle-size-distribution measurements in the crucial region below 10 nm provide important constraints for model predictions of the contribution of gas-to-particle conversion to the global budget of cloud condensation nuclei.

5.4 Materials and Methods

5.4.1 The CLOUD chamber

The CERN CLOUD chamber is a 26.1 m^3 electro-polished stainless steel vessel, surrounded by a thermal housing capable of stabilizing temperature in a range from -65 °C to +100 °C with ±0.1 K precision (Dias et al., 2017). The chamber is equipped with a gas control system achieving extremely high purities by mixing boil-off nitrogen and boil-off oxygen at the atmospheric ratio of 79:21. Highly pure trace gases can be precisely added at the ppt level. Before the start of the experiments the chamber was heated to 100 °C and rinsed with ultra-pure water for cleaning. This assured operation at contaminant levels of less than $5 \cdot 10^4$ cm^{-3} H_2SO_4 and total organics below 150 pptv (Kirkby et al., 2011; Frege et al., 2018).

A high-voltage field of ±30 kV can be applied between two electrode grids, located at the top and bottom of the chamber. The electric field sweeps out all ions from the chamber allowing for ion-free experiments. If the field is switched off, ions are created by the impact of galactic cosmic rays and decay products from ambient radioactivity.

Experiments were conducted as follows: At 38 % relative humidity, with no SO_2 and no NO_x

present in the chamber, stable ozone concentrations of 30-40 ppb were established. Under dark conditions, i.e.without any additional OH radical production mechanism except from the ozonolysis itself, the high-voltage field was switched on, to perform experiments under neutral conditions first. Injection of α-pinene initiated the ozonolysis reaction and the subsequent formation of particles. After steady-state α-pinene concentrations were reached and particle growth was measured up to at least 10 nm, the high-voltage field is switched off. Ions now present in the chamber lead to a significant increase in nucleation rate (Kirkby et al., 2016). Therefore two growth rate measurements can eventually be performed as the size-distribution will show two growing particle populations. Moreover, the second measurement is almost independent of changing gas concentrations as the steady-state is already reached during the neutral experiments. As no significant effect on growth due to the different ionization conditions was found all measurements are treated equally in this study.

5.4.2 Measurement of particle growth

Apparent particle growth rates are inferred from particle-size-distribution measurements with the appearance time method (Kulmala et al., 2013), as it was done in previous comparable studies (Lehtipalo et al., 2016; Tröstl et al., 2016). Particle-size-distributions are measured by several sizing instruments optimized for a certain size range. Each instrument was thereby treated separately but we found comparable results in the overlapping regions for all presented experiments (See Supporting Information for details).
Key part of this study is the precision measurement of particle-size-distributions in the size range between 1.8-8 nm by a newly developed instrument, a DMA-train (Stolzenburg et al., 2017). It uses six differential mobility analyzers in parallel with the classified size fixed for every device. Subsequent detection of the size-selected aerosol is done by the usage of six condensation particle counters. As no scanning is involved, high counting statistics at a single size is achieved, providing unprecedented high sensitivity to low number concentrations in the crucial sub 10-nm range.

5.4.3 Gas-phase measurements

Gas phase compounds were measured by high-resolution mass spectrometry. For this study two different instruments with two different chemical ionisation techniques were combined in order to obtain a more detailed overview of the neutral gas phase species present during the α-pinene ozonolysis experiments.
Using an atmospheric-pressure-interface, the rather selective ionization technique of a chemical-ionisation mass spectrometer using nitrate $(HNO_3)_n(NO_3^-)$ as the reagent ion (Jokinen et al., 2012) was used to obtain a very clean spectrum of HOMs (Ehn et al., 2014). The broad ionization efficiency of H_3O^+-water clusters was deployed in a novel proton-transfer-reaction time-of-flight mass spectrometer to ionize VOCs as well as semi-volatile organic compounds

(SVOCs) and HOMs (Breitenlechner et al., 2017). While the Nitrate-CI is calibrated to the response of H_2SO_4, the response of the PTR3 to HOMs is assumed to behave comparably to Butanon (Breitenlechner et al., 2017). Inlet loss corrections for HOMs have to be applied to both instruments and are adjusted for the PTR3 to give good overlap for peaks observed in both instruments (see Supporting Information for details).
When combining the two mass spectrometers, for molecular ion signals observed in both instruments the higher signal is used. Both spectra are background subtracted and therefore a weaker signal in either of the mass spectrometers could point towards a lower ionisation efficiency.

Author Contributions

D. S., L. F., M. H., M. Schervish, M. Simon, A. C. W., R. W., L. W., L. D. analyzed the main data sets; **D. S.**, L. F., M. H., M. Schervish, M. Simon, L. D., H. G., A. H., J. Kirkby, M. K., K. L., M. P. R., P. M. W. were involved in the scientific discussion and interpretation of the results; **D. S.**, L. F., J. Kirkby, N. M. D., P. M. W. wrote the manuscript; all other authors contributed to the design of the facility, preparation of the instruments or data collection and analysis, and commented on the manuscript.

Acknowledgements

We thank T.Kurten and N.Hyttinen for providing helpful COSMOtherm volatility estimates. We thank the European Organization for Nuclear Research (CERN) for supporting CLOUD with important technical and financial resources and for providing a particle beam from the CERN Proton Synchrotron. This research has received funding from the EC Seventh Framework Programme (Marie Curie Initial Training Networks 'CLOUD-TRAIN' (no. 316662), German Federal Ministry of Education and Research (no. 01LK1222A, no. 01LK1601A), the Swiss National Science Foundation (projects no. 20FI20_159851 , 200020_172602 , 20FI20_172622), the Austrian Research Funding Association FFG (Project Number 846050), the Austrian Science Fund (FWF; project no. J3951-N36), ERC-Consolidator Grant NANODYNAMITE 616075, ERC-Advanced Grant DAMOCLES 692891, ERC-Starting Grant COALA 638703, Horizon 2020 Marie Sklodowska-Curie Grant 656994 ("Nano-CAVa"), ERC Advanced grant 742206 ATM-GP, Academy of Finland Center of Excellence programme (grant no 307331), US Department of Energy DE-SC0014469, the Presidium of the Russian Academy of Sciences, the Program "High energy physics and neutrino astrophysics" 2015. We also thank K.Ivanova, P. Carrie, L.-P. De Menezes, J. Dumollard, F. Josa, I. Krasin, R. Kristic, A. Laassiri, O. S. Maksumov, B. Marichy, H. Martinati, S. V. Mizin, R. Sitals, A. Wasem and M. Wilhelmsson for their contributions to the experiment.

5.5 Supporting Information

5.5.1 Appearance time method for growth rate determination

Particle growth rate measurements were performed with the appearance time method, which can be used especially in chamber experiments, where a clear front of a growing particle population can be identified during most nucleation experiments.

The particle-size distribution was measured by a comprehensive set of four different instruments. Below 2.5 nm, a particle size magnifier in scanning mode was used (Vanhanen et al., 2011). The size range between 1.8-8 nm was covered by a DMA-train (Stolzenburg et al., 2017). Above 8 nm a scanning mobility particle sizer system, TSI nano-SMPS model 3982, measured up to 65 nm (Tröstl et al., 2015). Additionally, a neutral cluster and air ion spectrometer (NAIS) measured between 3-42 nm (Manninen et al., 2009).

Considering the evolution of particle size-distribution binned into different size-channels, the signal in each size-channel is fitted individually with a four parameter sigmoid function using a least-square algorithm:

$$S_{\mathrm{d_p}}(t) = \frac{a-b}{1+(t/t_{\mathrm{app}})^d} + b, \tag{2}$$

where a and b represent the background and plateau value of the sigmoid function respectively, d is a parameter for the steepness of the rising signal and t_{app} is the time at which the 50 % value between plateau and background is reached.

A representative fit for a 3.2 nm size channel of the DMA-train is shown in Fig. 4 (A). All size-channels are cross-checked manually after the automated fitting and a statistical error of t_{app} is estimated from the covariance of the fit-result. The values obtained for t_{app} can be plotted against the corresponding diameter as shown in Fig. 4 (B). A linear fit with an orthogonal distance regression is used to take into account both the uncertainties of t_{app} and of the diameter of the size-channels. The resulting value of the slope and its associated error can be interpreted as an apparent particle growth rate and its statistical uncertainty. However, this growth rate does not necessarily represent the growth caused by pure condensation, as it omits coagulation and, in chamber experiments, wall losses, which both alter the particle size-distribution (Pichelstorfer et al., 2018). Therefore, a systematic uncertainty of the method is estimated to be 50 % (Lehtipalo et al., 2014).

For the DMA-train two size-intervals for the growth rate measurement were defined: One between 1.8-3.2 nm and one between 3.2-8 nm. The choice of the size-intervals is arbitrary but proofed to be representative to show differences between early and later growth. In (Tröstl et al., 2016) it was shown that growth driven by biogenic organics shows only a minor size-dependence above 5 nm, i.e. the upper growth rate size-interval of the DMA-train is representative for growth >5 nm.

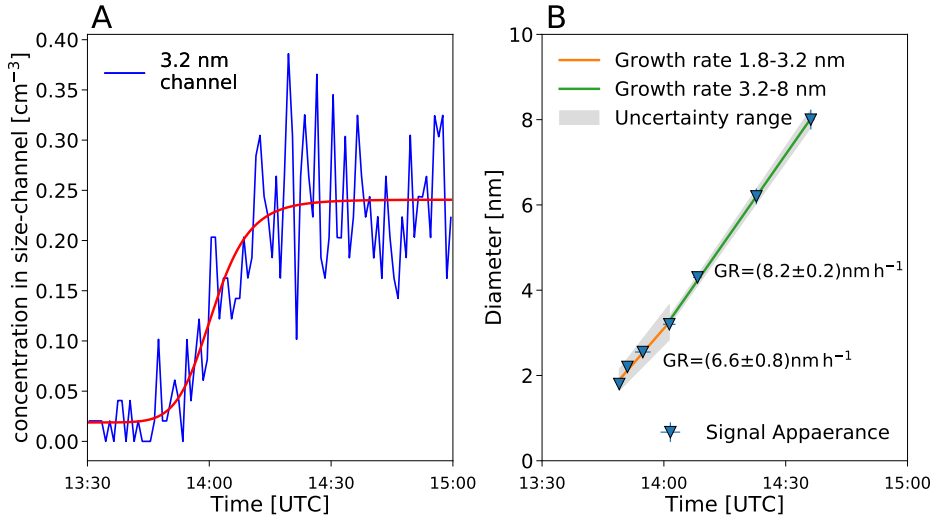

Figure 6: Example for a representative determination of the particle growth rate with the appearance time method for data obtained by the DMA-train. Panel (A) shows the sigmoid function fit to the measured concentration within the 3.2 nm channel. Panel (B) shows the orthogonal distance regression for the growth rate determination in two intervals.

5.5.2 Absolute HOM concentration measurements using Nitrate-CI-APi-ToF

The Nitrate-CI-APi-ToF (Nitrate-CI) uses negative nitrate, $(HNO_3)_n(NO_3^-)$, as reagent ion (Kürten et al., 2011), which shows high charging efficiencies towards H_2SO_4 and HOMs. The concentration of a HOM species is estimated via

$$[\mathrm{HOM}_i] = C \cdot T_i \cdot \mathrm{SL}_{\mathrm{HOM}_i} \cdot \ln\left(1 + \frac{[\mathrm{HOM}_i \cdot \mathrm{NO}_3^-]}{\sum_{j=0}^{2}[\mathrm{NO}_3^- \cdot (\mathrm{HNO}_3)_j]}\right) \quad (3)$$

Here $[\mathrm{HOM}_i \cdot \mathrm{NO}_3^-]$ is the background corrected peak area which is normalized to the intensity of the main reagent ions. To obtain a quantitative concentration, three factors are applied: First, a calibration factor C, which is inferred from a calibration using sulfuric acid (Kürten et al., 2012) and assuming that all detected HOMs have the same ionization efficiency (Ehn et al., 2014). Second, a mass dependent transmission efficiency T_i of the APi-ToF can be inferred in a seperate experiment by depleting the reagent ions with several perfluorinated acids (Heinritzi et al., 2016). Third, sampling line losses $\mathrm{SL}_{\mathrm{HOM}_i}$ are estimated assuming laminar flow diffusional losses in the sampling lines (Gormley and Kennedy, 1948) with a diffusion coefficient of HOMs scaling with the molecular mass M_i of the compound via $D[\mathrm{cm^2 s^{-1}}] = 0.31 \cdot M_i^{-1/3}$ at 278 K, determined from wall loss measurements in the CLOUD chamber. As the sampling lines of the Nitrate-CI are thermally insulated, for other experiment temperatures $D \propto (T/278K)^{1.75}$ is assumed. As the compounds detected by the Nitrate-CI are mostly classified ELVOC or LVOC in the temperature range of this study, we can assume that they all get lost irreversibly to sampling line walls due to diffusion.

5.5.3 Absolute concentration measurements of oxidized organics using PTR3-ToF

The PTR3-ToF (PTR3) uses $(H_3O^+)(H_2O)_n$ clusters as reagent ions, ionizing α-pinene as well as first and higher order oxidation products by proton transfer or ligand switch reactions (Breitenlechner et al., 2017). A contact minimized laminar flow inlet system with core sampling is used to transfer the sample air into the tripole reaction chamber operated at 80 mbar and reduces transmission losses. The $(H_3O^+)(H_2O)_n$ cluster ion distribution can be regulated by a radio-frequency-amplitude applied to the tripole rods without influencing the reaction time. Increased pressure in the reaction region and longer reaction times compared to traditional PTR instruments yield a 500 fold increased sensitivity to a broad range of organics. At the operating conditions of the PTR3, secondary reactions of ionized species with the most abundant neutral VOCs in the sample gas are limited to less then one percent at the highest measurable concentrations. The new instrument bridges the gap between precursor measurements at ppbv level to HOM measurements at sub ppt level, complementing atmospheric pressure CIMS techniques.

A quadrupole interfaced Long-ToF mass spectrometer (TOFWERK AG, Thun, Switzerland) is providing the high mass resolving power needed to separate isobaric compounds. We obtained more than 1500 individual mass peaks, excluding isotopes, during α-pinene ozonolysis experiments. A multi-peak fitting algorithm is applied to separate the major compounds and assign chemical sum formulas. Extracting the relevant signals is done omitting all masses rising less than 3σ above chemical background noise during ozonolysis measurements and removing peaks with possible uncertainties caused by interference of higher neighboring peaks. $(H_3O^+)(H_2O)_n$ clusters are known to be soft ionization reagent ions. Nevertheless we cannot exclude completely fragmentation of some ionized HOMs loosing most likely H_2O especially when containing an (-OOH) group.

The PTR3 was calibrated with a gas standard containing 1 ppm of 3-hexanone, heptanone and α-pinene in nitrogen, which was dynamically diluted by a factor of 1000 in VOC-free air to contain 1 ppbv of each compound. Duty cycle corrected counts per second *dcps* are used in order to compensate for the mass-dependent transmission of the TOF mass spectrometer ($dcps(i) = cps(i) \cdot (101/m_i)^{1/2}$) (Breitenlechner et al., 2017). For 3-hexanone and heptanone we obtained a sensitivity which is in agreement with the calculated sensitivity taking into account the duty cycle corrected $(H_3O^+)(H_2O)_n$ regent ion count rates, the pressure and the reaction time in the reaction chamber (80 mbar; 3 ms) and using $2 - 3 \cdot 10^{-9} \mathrm{cm^3 s^{-1}}$ as a fast reaction rate constant close to the collisional limit value. Consequently, only lower end product concentrations can be given.

In a previous α-pinene ozonolysis study PTR3 results showed quantitative agreement for several HOMs with the Nitrate-CI (Breitenlechner et al., 2017). The authors estimated 80 % inlet losses for low-volatile molecules with $n_O \geq 5$, bringing the two instruments into reasonable quantitative agreement for common molecular ion signals. However, the assumption

for the Nitrate-CI, that all detected molecules get lost on contact with sampling line walls, does not hold for all substances measured by the PTR3. In the transition from SVOC to LVOC the partitioning of substances between inlet line walls and sample gas is temperature dependent. We therefore extended the approach of (Breitenlechner et al., 2017) with our knowledge about an approximate volatility of the measured compounds. Assuming that all molecules in the LVOC and ELVOC range get lost by diffusion (the diffusion coefficient of a molecule is estimated similar to the Nitrate-CI) according to Gormley and Kennedy (1948), we can apply a temperature dependent loss-correction for the sampling line losses, which is split up into three sections:

$$\eta_{\text{tot}} = \eta_{\text{line,int}}(T) \cdot \eta_{\text{line,ext}}(298\text{K}) \cdot \eta_{\text{PTR3}}(310\text{K}) \tag{4}$$

We account for losses at the sampling line within the CLOUD chamber $\eta_{\text{line,int}}$ at chamber temperature T, as well as losses occurring at the sampling line outside the chamber at room temperature $\eta_{\text{line,ext}}$ (as it was not thermally insulated) and losses within the PTR3 instrument heated to 37°C η_{PTR3}. Therefore, for each sampling section other molecules might be subject to losses according to their temperature-dependent volatility classification.

5.5.4 Comparison of the used mass spectrometers

The considerations of the two previous sections result in the comparison for data obtained in three representative experiments at three different temperatures which is shown in Fig. **??**, where $\eta_{\text{line,int}}$ and $\eta_{\text{line,ext}}$ are calculated assuming diffusional losses similar to the Nitrate-CI and η_{PTR3} is estimated to correct for the 80% discrepancy found in (Breitenlechner et al., 2017). For higher oxygenated molecules the agreement between both mass spectrometers is in a reasonable range including the additional loss term η_{PTR3} for losses within the PTR3 ion source and inlet. This indicates that the loss in measured concentration from +25°C to -25°C for the three experiments at similar initial precursor oxidation rates is caused by the reduced reaction rates of the auto-oxidation process. For lower temperatures and lower oxidized states (n_O = 4/5/6) a discrepancy between the instruments gets significant. However, even at elevated temperatures, the Nitrate-CI is only detecting a small fraction of all oxidation products with n_O = 5/6 observed by the PTR3. Therefore it is concluded that the increasing discrepancy is likely due to a lowered sensitivity of the Nitrate-CI for such compounds. The ionization efficiency in the Nitrate-CI depends on the relative binding energy of a $(HNO_3)(NO_3^-)$ cluster compared to a $(\text{Analyte})(NO_3^-)$ cluster (Hyttinen et al., 2017). A relative shift in binding energies at lower temperatures that favors $(HNO_3)(NO_3^-)$ clustering instead of $(\text{Analyte})(NO_3^-)$ clustering, could explain the observed decrease of signal for the lower oxidation states for the Nitrate-CI. The higher oxidation states however are unaffected because the $(\text{HOM})(NO_3^-)$ clustering is generally very strong and will always dominate

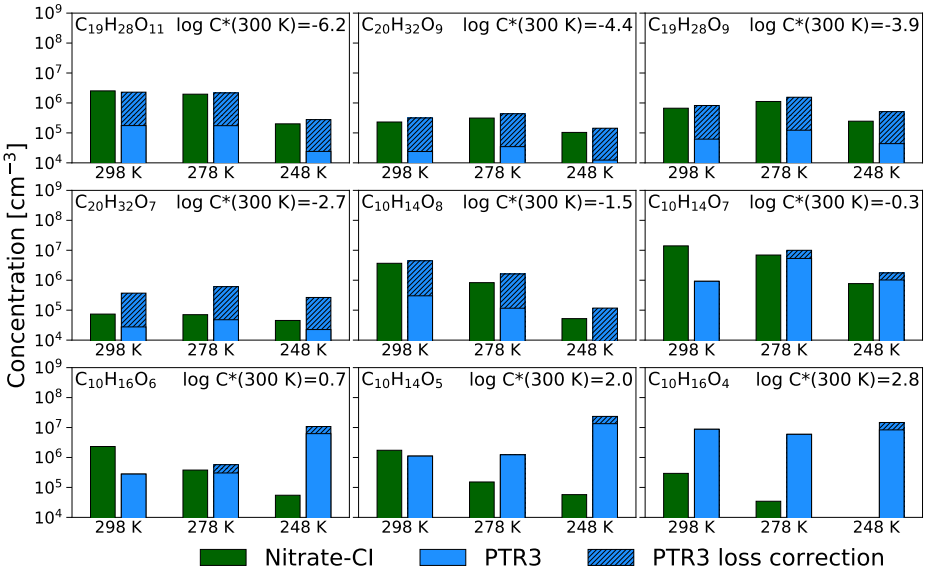

Figure 7: Quantitative comparison of selected peaks observed in both mass spectrometers and its temperature dependence for three representative runs with similar α-pinene ozonolysis rate. The correction for PTR3 compounds to account for sampling line losses and the additional 80 % wall loss inside the PTR3 ion source are displayed by the hatched area.

the $(HNO_3)(NO_3^-)$ clustering, which explains the good agreement of the two instruments for higher oxidized states.

5.5.5 Growth rate parametrization

Growth rates were parametrized in Fig. 2 (A) and (B) by the simple exponential relation GR=$m(T, d_p) \cdot [\mathrm{k}(T) \cdot \mathrm{ap} \cdot \mathrm{O_3}]^q$, to express the correlation between growth rate and α-pinene ozonolysis reaction rate. While the coeffcients $m(T, d_p)$ depend on temperature and size-range of the growth rate measurement, q is chosen to be independent of both. A minimum least-square regression yields the results presented in Table**??**.

Size-Range	m(+25°C)	m(+5°C)	m(-25°C)	q
1.8-3.2 nm	$1.12{\cdot}10^{-7}$	$2.09{\cdot}10^{-7}$	$2.67{\cdot}10^{-7}$	1.21
3.2-8.0 nm	$2.66{\cdot}10^{-7}$	$3.12{\cdot}10^{-7}$	$3.57{\cdot}10^{-7}$	1.21

Table 1: Resulting parameters from least-square regression for the growth rate parametrization of Fig. 2 (A) and (B) by the simple exponential relation $GR = m(T, d_p) \cdot [\mathrm{k}(T) \cdot \mathrm{ap} \cdot \mathrm{O_3}]^q$.

5.5.6 Volatility of HOMs

Direct measurements of volatilities of individual HOM are extremely challenging as they are difficult to synthesize and the vapour pressures are too low for current volatility measure-

ment techniques. To overcome this problem, vapour pressures can be inferred by several model calculations, like so-called group contribution methods (Pankow and Asher, 2008) or parametrizations according to the oxidation state (Donahue et al., 2011a). In this study a combined approach is applied.

We use a volatility parametrization according to the carbon n_{C}^{i} and oxygen n_{O}^{i} number of the specific molecule i. This is based on two general observed trends that increasing carbon and increasing oxygen number lower the volatility of oxidized organic molecules. Thus, these quantities are linked to volatility, expressed as the logarithm of the saturation mass concentration $\log_{10} C_i^*$ for compound i:

$$\log_{10} C_i^*(300K) = \left(n_{\mathrm{C}}^{0} - n_{\mathrm{C}}^{i}\right) \cdot b_{\mathrm{C}} - n_{\mathrm{O}}^{i} \cdot (b_{\mathrm{O}} - b_{\mathrm{add}}) - 2\frac{n_{\mathrm{C}}^{i} n_{\mathrm{O}}^{i}}{n_{\mathrm{C}}^{i} + n_{\mathrm{O}}^{i}} b_{\mathrm{CO}} \tag{5}$$

where the parameter n_{C}^{0}=25 is the baseline carbon backbone for a volatility of 1 μg m^{-3} without the addition of any functional groups. b_{C}=0.475 is the roughly half decade decrease in volatility per carbon atom and b_{O}=2.3 is the more than two decade decrease in volatility per oxygen atom assuming an average of (=O) and (-OH) groups. b_{CO} is a non-linearity term. More details can be found in (Donahue et al., 2011a).

However, other functionalities e.g. hydroperoxides (-OOH) and covalently bound dimers are not included in b_{O}, but are both abundant in HOMs from α-pinene ozonolysis. To account for these specific attributes, a representative set of proposed products (Tröstl et al., 2016; Kurtén et al., 2016) with known structure is analyzed with the group contribution method SIMPOL (Pankow and Asher, 2008). The results are fitted with Eq. 5 including a free parameter b_{add} altering the effect of oxygen b_{O}. Monomer and dimer products are fitted separately allowing this parameter to include the covalent binding. The resulting parametrisation at 300 K is shown in Fig. **??**. The free parameter yields $b_{\mathrm{add}} = 0.90$ for monomers and $b_{\mathrm{add}} = 1.13$ for dimers. Accordingly, for any α-pinene ozonolysis product with unambiguously identified composition, a volatility can be calculated.

However, computed volatilities from group-contribution methods generally tend to underestimate vapour pressures at low vapour pressures. A recent study investigating the volatility of α-pinene oxidation products with quantum-chemical based model calculations found large deviations due to intramolecular H-bonds (Kurtén et al., 2016). These deviations were significant especially for highly oxygenated monomers and dimers, while the agreement for the higher volatilities was much better.

This study focuses on the temperature dependence of the volatilities which is described by:

$$\log_{10} C^*(T) = \log_{10} C^*(300K) + \frac{\Delta H_{\mathrm{vap}}}{R \ln(10)} \left(\frac{1}{300} - \frac{1}{T}\right) \tag{6}$$

The evaporation enthalpy ΔH_{vap} can be linked to the saturation mass concentration at 300 K

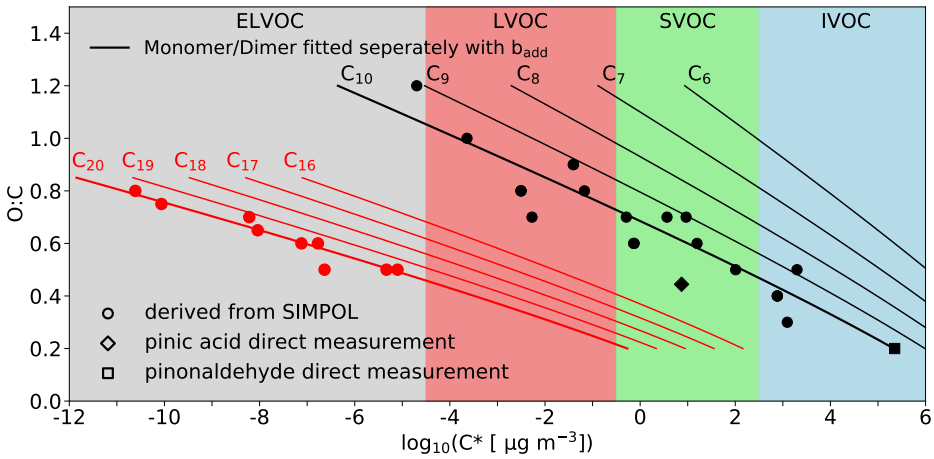

Figure 8: Volatility model used in this study. For a representative set of proposed products from α-pinene ozonolysis the known structure is used to calculate the volatility by the group-contribution method SIMPOL or are directly measured by (Hallquist et al., 1997; Bilde and Pandis, 2001). Results are fitted with the proposed relationship from (Donahue et al., 2011a) including a free parameter for the oxygen dependence.

$\log_{10} C^*(300K)$ according to Donahue et al. (2011a) and combined with Epstein et al. (2010):

$$\Delta H_{\text{vap}} \left[\text{kJ mol}^{-1}\right] = -5.7 \cdot \log_{10} C^*(300K) + 129 \tag{7}$$

The correlation between volatility at 300 K and the evaporation enthalpy ΔH_{vap} is very comparable for approaches like Epstein et al. (2010), Donahue et al. (2011a) and Kurtén et al. (2016). Moreover, the shift in volatility due to temperature in this study is most important for oxygenated compounds with volatilities around $\log_{10} C^*(300K) \approx 0$, at the transition between LVOC and SVOC. For those molecules also the predictions of the volatility between the different methods don't differ drastically (Kurtén et al., 2016). Therefore, we assume an overall uncertainty of the volatility description of ± 1 bin (i.e. 1 decade in $C^*(300K)$ for volatility distributions within a volatility basis set). This uncertainty is shown Fig. 2 panel (E) and (F) and gives the method uncertainties in Fig. 3.

5.5.7 Aerosol growth model

The measured VBS-distributions can be used to model aerosol growth. The modeling framework is based on the one used in (Tröstl et al., 2016) but simplified for the input of direct VBS-distribution measurements. Starting from a VBS-distribution at $t = 0$ the growth of a monodisperse population of nucleated particles at an initial size of 1.2 nm mobility diameter is modeled. Every VBS bin is treated like a single surrogate molecule having the properties of the averaged mass and concentration of the bin. It is assumed that the measured gas-phase concentrations are in steady-state with losses to particles and chamber walls. The

condensation flux $\phi_{i,p}$ of every VBS bin i should then follow:

$$\phi_{i,p} = N_p \cdot \sigma_{i,p}, \cdot k_{i,p} \cdot F_{i,p} \tag{8}$$

N_p gives the number concentration of particles of a given size. $\sigma_{i,p} = \pi/4(d_p + d_i)^2$ is the particle-vapor collision cross-section including the diameter of the monodisperse particle population d_p and mass-diameter of the VBS bin d_i. $k_{i,p} = \alpha_{i,p}\nu_{i,p}\beta_{i,p}$ is the deposition rate of vapor molecules at surface, with $\alpha_{i,p}$ the mass accommodation coefficient, $\nu_{i,p} = (8RT/(\pi\mu_{i,p}))^{1/2}$ the center of mass velocity for particle and vapor (with the reduced mass $\mu_{i,p} = (M_i M_p)/(M_i + M_p)$) and $\beta_{i,p}$ the correction factor for non-continuum dynamics (Fuchs and Sutugin, 1965). $F_{i,p}$ is the driving force of condensation, closely related to the saturation ratio S_i of the VBS bin by $F_{i,p} = C_i^0(S_i - X_{i,p}\gamma_{i,p}K_{i,p})$. This driving force of condensation for a VBS bin i gives the difference between gas phase activity S_i and particle phase activity $(X_{i,p}\gamma_{i,p}K_{i,p})$, which includes the Raoult term $X_{i,p}\gamma_{i,p}$ to account for the mixture effect of the particles and the Kelvin-term $K_{i,p} = \exp(4\sigma M/(RT\rho d_p))$ accounting for the curvature effect of the particle surface. The model assumes an ideal mass based solution, i.e. the condensed phase activity is the mass fraction $X_{i,p}$ and hence $\gamma_{i,p} = 1$. Therefore we use $C*$ as saturation mass concentration throughout this study, as $C^* = \gamma_{i,p}C^0$.
Solving the above condensation equations for the measured evolution of the VBS-distribution assuming this distribution always reflects a steady-state between production from α-pinene ozonolysis and wall losses and following the growing monodisperse aerosol population, yields a diameter versus time evolution which can be connected to a growth rate.
Besides from the different input VBS-distributions at different temperature, only the Kelvin-term and the collision-frequency include a temperature dependence.

5.6 References

Andreae, M. O., Afchine, A., Albrecht, R., Holanda, B. A., Artaxo, P., Barbosa, H. M. J., Borrmann, S., Cecchini, M. A., Costa, A., Dollner, M., Fütterer, D., Järvinen, E., Jurkat, T., Klimach, T., Konemann, T., Knote, C., Krämer, M., Krisna, T., Machado, L. A. T., Mertes, S., Minikin, A., Pöhlker, C., Pöhlker, M. L., Pöschl, U., Rosenfeld, D., Sauer, D., Schlager, H., Schnaiter, M., Schneider, J., Schulz, C., Spanu, A., Sperling, V. B., Voigt, C., Walser, A., Wang, J., Weinzierl, B., Wendisch, M., and Ziereis, H.: Aerosol characteristics and particle production in the upper troposphere over the Amazon Basin, Atmos. Chem. Phys., 18, 921–961, doi:10.5194/acp-18-921-2018, https://www.atmos-chem-phys.net/18/921/2018/, 2018.

Apsokardu, M. J. and Johnston, M. V.: Nanoparticle growth by particle-phase chemistry, Atmos. Chem. Phys., 18, 1895–1907, doi:10.5194/acp-18-1895-2018, https://www.atmos-chem-phys.net/18/1895/2018/, 2018.

Bianchi, F., Tröstl, J., Junninen, H., Frege, C., Henne, S., Hoyle, C. R., Molteni, U., Herrmann, E., Adamov, A., Bukowiecki, N., Chen, X., Duplissy, J., Gysel, M., Hutterli, M., Kangasluoma, J., Kontkanen, J., Kürten, A., Manninen, H. E., Münch, S., Peräkylä, O., Petäjä, T., Rondo, L., Williamson, C., Weingartner, E., Curtius, J., Worsnop, D. R., Kulmala, M., Dommen, J., and Baltensperger, U.: New particle formation in the free troposphere: A question of chemistry and timing, Science, 352, 1109–1112, doi:10.1126/science.aad5456, http://science.sciencemag.org/content/352/6289/1109, 2016.

Bilde, M. and Pandis, S. N.: Evaporation Rates and Vapor Pressures of Individual Aerosol Species Formed in the Atmospheric Oxidation of alpha- and beta-Pinene, Environ. Sci. Technol., 35, 3344–3349, doi:10.1021/es001946b, http://dx.doi.org/10.1021/es001946b, pMID: 11529575, 2001.

Breitenlechner, M., Fischer, L., Hainer, M., Heinritzi, M., Curtius, J., and Hansel, A.: PTR3: An Instrument for Studying the Lifecycle of Reactive Organic Carbon in the Atmosphere, Anal. Chem., 89, 5824–5831, doi:10.1021/acs.analchem.6b05110, http://dx.doi.org/10.1021/acs.analchem.6b05110, pMID: 28436218, 2017.

Chuang, W. K. and Donahue, N. M.: Dynamic consideration of smog chamber experiments, Atmos. Chem. Phys., 17, 10 019–10 036, doi:10.5194/acp-17-10019-2017, https://www.atmos-chem-phys.net/17/10019/2017/, 2017.

Dias, A., Ehrhart, S., Vogel, A., Williamson, C., Almeida, J., Kirkby, J., Mathot, S., Mumford, S., and Onnela, A.: Temperature uniformity in the CERN CLOUD chamber, Atmos. Meas. Tech., 10, 5075–5088, doi:10.5194/amt-10-5075-2017, https://www.atmos-meas-tech.net/10/5075/2017/, 2017.

Donahue, N. M., Robinson, A. L., Stanier, C. O., and Pandis, S. N.: Coupled Partitioning, Dilution, and Chemical Aging of Semivolatile Organics, Environ. Sci. Technol., 40, 2635–2643, doi:10.1021/es052297c, http://dx.doi.org/10.1021/es052297c, 2006.

Donahue, N. M., Epstein, S. A., Pandis, S. N., and Robinson, A. L.: A two-dimensional volatility basis set: 1. organic-aerosol mixing thermodynamics, Atmos. Chem. Phys., 11,

3303–3318, doi:10.5194/acp-11-3303-2011, http://www.atmos-chem-phys.net/11/3303/2011/, 2011a.

Donahue, N. M., Trump, E. R., Pierce, J. R., and Riipinen, I.: Theoretical constraints on pure vapor-pressure driven condensation of organics to ultrafine particles, Geophys. Res. Lett., 38, n/a–n/a, doi:10.1029/2011GL048115, http://dx.doi.org/10.1029/2011GL048115, l16801, 2011b.

Ehn, M., Thornton, J. A., Kleist, E., Sipila, M., Junninen, H., Pullinen, I., Springer, M., Rubach, F., Tillmann, R., Lee, B., Lopez-Hilfiker, F., Andres, S., Acir, I.-H., Rissanen, M., Jokinen, T., Schobesberger, S., Kangasluoma, J., Kontkanen, J., Nieminen, T., Kurten, T., Nielsen, L. B., Jorgensen, S., Kjaergaard, H. G., Canagaratna, M., Maso, M. D., Berndt, T., Petaja, T., Wahner, A., Kerminen, V.-M., Kulmala, M., Worsnop, D. R., Wildt, J., and Mentel, T. F.: A large source of low-volatility secondary organic aerosol, Nature, 506, 476–479, doi:10.1038/nature13032, http://dx.doi.org/10.1038/nature13032, 2014.

Epstein, S. A., Riipinen, I., and Donahue, N. M.: A Semiempirical Correlation between Enthalpy of Vaporization and Saturation Concentration for Organic Aerosol, Environ. Sci. Technol., 44, 743–748, doi:10.1021/es902497z, http://dx.doi.org/10.1021/es902497z, pMID: 20025284, 2010.

Frege, C., Ortega, I. K., Rissanen, M. P., Praplan, A. P., Steiner, G., Heinritzi, M., Ahonen, L., Amorim, A., Bernhammer, A.-K., Bianchi, F., Brilke, S., Breitenlechner, M., Dada, L., Dias, A., Duplissy, J., Ehrhart, S., El-Haddad, I., Fischer, L., Fuchs, C., Garmash, O., Gonin, M., Hansel, A., Hoyle, C. R., Jokinen, T., Junninen, H., Kirkby, J., Kürten, A., Lehtipalo, K., Leiminger, M., Mauldin, R. L., Molteni, U., Nichman, L., Petäjä, T., Sarnela, N., Schobesberger, S., Simon, M., Sipilä, M., Stolzenburg, D., Tomé, A., Vogel, A. L., Wagner, A. C., Wagner, R., Xiao, M., Yan, C., Ye, P., Curtius, J., Donahue, N. M., Flagan, R. C., Kulmala, M., Worsnop, D. R., Winkler, P. M., Dommen, J., and Baltensperger, U.: Influence of temperature on the molecular composition of ions and charged clusters during pure biogenic nucleation, Atmos. Chem. Phys., 18, 65–79, doi:10.5194/acp-18-65-2018, https://www.atmos-chem-phys.net/18/65/2018/, 2018.

Fuchs, N. and Sutugin, A.: Coagulation rate of highly dispersed aerosols, J. Colloid Sci., 20, 492 – 500, doi:https://doi.org/10.1016/0095-8522(65)90031-0, http://www.sciencedirect.com/science/article/pii/0095852265900310, 1965.

Gordon, H., Sengupta, K., Rap, A., Duplissy, J., Frege, C., Williamson, C., Heinritzi, M., Simon, M., Yan, C., Almeida, J., Tröstl, J., Nieminen, T., Ortega, I. K., Wagner, R., Dunne, E. M., Adamov, A., Amorim, A., Bernhammer, A.-K., Bianchi, F., Breitenlechner, M., Brilke, S., Chen, X., Craven, J. S., Dias, A., Ehrhart, S., Fischer, L., Flagan, R. C., Franchin, A., Fuchs, C., Guida, R., Hakala, J., Hoyle, C. R., Jokinen, T., Junninen, H., Kangasluoma, J., Kim, J., Kirkby, J., Krapf, M., Kürten, A., Laaksonen, A., Lehtipalo, K., Makhmutov, V., Mathot, S., Molteni, U., Monks, S. A., Onnela, A., Peräkylä, O., Piel, F., Petäjä, T., Praplan, A. P., Pringle, K. J., Richards, N. A. D., Rissanen, M. P., Rondo, L., Sarnela, N., Schobesberger, S., Scott, C. E., Seinfeld, J. H., Sharma, S., Sipilä, M., Steiner, G., Stozhkov, Y., Stratmann, F., Tomé, A., Virtanen, A., Vogel, A. L., Wagner, A. C., Wagner, P. E., Weingartner, E., Wimmer, D., Winkler, P. M., Ye, P., Zhang, X., Hansel, A., Dommen, J., Donahue, N. M., Worsnop, D. R., Baltensperger, U., Kulmala, M.,

Curtius, J., and Carslaw, K. S.: Reduced anthropogenic aerosol radiative forcing caused by biogenic new particle formation, P. Nat. Acad. Sci. USA, 113, 12 053–12 058, doi:10.1073/pnas.1602360113, http://www.pnas.org/content/113/43/12053.abstract, 2016.

Gordon, H., Kirkby, J., Baltensperger, U., Bianchi, F., Breitenlechner, M., Curtius, J., Dias, A., Dommen, J., Donahue, N. M., Dunne, E. M., Duplissy, J., Ehrhart, S., Flagan, R. C., Frege, C., Fuchs, C., Hansel, A., Hoyle, C. R., Kulmala, M., Kürten, A., Lehtipalo, K., Makhmutov, V., Molteni, U., Rissanen, M. P., Stozkhov, Y., Tröstl, J., Tsagkogeorgas, G., Wagner, R., Williamson, C., Wimmer, D., Winkler, P. M., Yan, C., and Carslaw, K. S.: Causes and importance of new particle formation in the present-day and preindustrial atmospheres, J. Geophys. Res.-Atmos., 122, doi:10.1002/2017JD026844, http://dx.doi.org/10.1002/2017JD026844, 2017JD026844, 2017.

Gormley, P. G. and Kennedy, M.: Diffusion from a Stream Flowing through a Cylindrical Tube, P. Roy. Irish Acad. A, 52, 163–169, 1948.

Guenther, A. B., Jiang, X., Heald, C. L., Sakulyanontvittaya, T., Duhl, T., Emmons, L. K., and Wang, X.: The Model of Emissions of Gases and Aerosols from Nature version 2.1 (MEGAN2.1): an extended and updated framework for modeling biogenic emissions, Geosci. Model Dev., 5, 1471–1492, doi:10.5194/gmd-5-1471-2012, https://www.geosci-model-dev.net/5/1471/2012/, 2012.

Hallquist, M., Wängberg, I., and Ljungström, E.: Atmospheric Fate of Carbonyl Oxidation Products Originating from Alpha-Pinene and Delta-3-Carene: Determination of Rate of Reaction with OH and NO3 Radicals, UV Absorption Cross Sections, and Vapor Pressures, Environ. Sci. Technol., 31, 3166–3172, doi:10.1021/es970151a, https://doi.org/10.1021/es970151a, 1997.

Heinritzi, M., Simon, M., Steiner, G., Wagner, A. C., Kürten, A., Hansel, A., and Curtius, J.: Characterization of the mass-dependent transmission efficiency of a CIMS, Atmos. Meas. Tech., 9, 1449–1460, doi:10.5194/amt-9-1449-2016, https://www.atmos-meas-tech.net/9/1449/2016/, 2016.

Hyttinen, N., Rissanen, M. P., and Kurtén, T.: Computational Comparison of Acetate and Nitrate Chemical Ionization of Highly Oxidized Cyclohexene Ozonolysis Intermediates and Products, J. Phys. Chem. A, 121, 2172–2179, doi:10.1021/acs.jpca.6b12654, https://doi.org/10.1021/acs.jpca.6b12654, pMID: 28234483, 2017.

Jokinen, T., Sipilä, M., Junninen, H., Ehn, M., Lönn, G., Hakala, J., Petäjä, T., Mauldin III, R. L., Kulmala, M., and Worsnop, D.: Atmospheric sulphuric acid and neutral cluster measurements using CI-APi-TOF, Atmos. Chem. Phys., 12, 4117–4125, doi:10.5194/acp-12-4117-2012, https://doi.org/10.5194/acp-12-4117-2012, 2012.

Kirkby, J., Curtius, J., Almeida, J., Dunne, E., Duplissy, J., Ehrhart, S., Franchin, A., Gagné, S., Ickes, L., Kürten, A., Kupc, A., Metzger, A., Riccobono, F., Rondo, L., Schobesberger, S., Tsagkogeorgas, G., Wimmer, D., Amorim, A., Bianchi, F., Breitenlechner, M., David, A., Dommen, J., Downard, A., Ehn, M., Flagan, R. C., Haider, S., Hansel, A., Hauser, D., Jud, W., Junninen, H., Kreissl, F., Kvashin, A., Laaksonen, A., Lehtipalo, K., Lima, J., Lovejoy, E. R., Makhmutov, V., Mathot, S., Mikkilä, J., Minginette, P., Mogo, S.,

Nieminen, T., Onnela, A., Pereira, P., Petäjä, T., Schnitzhofer, R., Seinfeld, J. H., Sipilä, M., Stozhkov, Y., Stratmann, F., Tomé, A., Vanhanen, J., Viisanen, Y., Vrtala, A., Wagner, P. E., Walther, H., Weingartner, E., Wex, H., Winkler, P. M., Carslaw, K. S., Worsnop, D. R., Baltensperger, U., and Kulmala, M.: Role of sulphuric acid, ammonia and galactic cosmic rays in atmospheric aerosol nucleation, Nature, 476, 429–433, doi:10.1038/nature10343, http://dx.doi.org/10.1038/nature10343, 2011.

Kirkby, J., Duplissy, J., Sengupta, K., Frege, C., Gordon, H., Williamson, C., Heinritzi, M., Simon, M., Yan, C., Almeida, J., Tröstl, J., Nieminen, T., Ortega, I. K., Wagner, R., Adamov, A., Amorim, A., Bernhammer, A.-K., Bianchi, F., Breitenlechner, M., Brilke, S., Chen, X., Craven, J., Dias, A., Ehrhart, S., Flagan, R. C., Franchin, A., Fuchs, C., Guida, R., Hakala, J., Hoyle, C. R., Jokinen, T., Junninen, H., Kangasluoma, J., Kim, J., Krapf, M., Kürten, A., Laaksonen, A., Lehtipalo, K., Makhmutov, V., Mathot, S., Molteni, U., Onnela, A., Peräkylä, O., Piel, F., Petäjä, T., Praplan, A. P., Pringle, K., Rap, A., Richards, N. A. D., Riipinen, I., Rissanen, M. P., Rondo, L., Sarnela, N., Schobesberger, S., Scott, C. E., Seinfeld, J. H., Sipilä, M., Steiner, G., Stozhkov, Y., Stratmann, F., Tomé, A., Virtanen, A., Vogel, A. L., Wagner, A. C., Wagner, P. E., Weingartner, E., Wimmer, D., Winkler, P. M., Ye, P., Zhang, X., Hansel, A., Dommen, J., Donahue, N. M., Worsnop, D. R., Baltensperger, U., Kulmala, M., Carslaw, K. S., and Curtius, J.: Ion-induced nucleation of pure biogenic particles, Nature, 533, 521–526, doi:10.1038/nature17953, http://dx.doi.org/10.1038/nature17953, 2016.

Kürten, A., Rondo, L., Ehrhart, S., and Curtius, J.: Calibration of a Chemical Ionization Mass Spectrometer for the Measurement of Gaseous Sulfuric Acid, J. Phys. Chem. A, 116, 6375–6386, doi:10.1021/jp212123n, https://doi.org/10.1021/jp212123n, pMID: 22364556, 2012.

Kulmala, M., Kerminen, V.-M., Anttila, T., Laaksonen, A., and O'Dowd, C. D.: Organic aerosol formation via sulphate cluster activation, J. Geophys. Res.-Atmos., 109, doi:10.1029/2003JD003961, http://dx.doi.org/10.1029/2003JD003961, d04205, 2004.

Kulmala, M., Kontkanen, J., Junninen, H., Lehtipalo, K., Manninen, H. E., Nieminen, T., Petäjä, T., Sipilä, M., M., Schobesberger, S., Rantala, P., Franchin, A., Jokinen, T., Järvinen, E., Äijälä, M., Kangasluoma, J., Hakala, J., Aalto, P. P., Paasonen, P., Mikkilä, J., Vanhanen, J., Aalto, J., Hakola, H., Makkonen, U., Ruuskanen, T., Mauldin, R. L., Duplissy, J., Vehkamäki, H., Bäck, J., Kortelainen, A., Riipinen, I., Kurtén, T., Johnston, M. V., Smith, J. N., Ehn, M., Mentel, T. F., Lehtinen, K. E. J., Laaksonen, A., Kerminen, V.-M., and Worsnop, D. R.: Direct Observations of Atmospheric Aerosol Nucleation, Science, 339, 943–946, doi:10.1126/science.1227385, http://science.sciencemag.org/content/339/6122/943, 2013.

Kürten, A., Rondo, L., Ehrhart, S., and Curtius, J.: Performance of a corona ion source for measurement of sulfuric acid by chemical ionization mass spectrometry, Atmos. Meas. Tech., 4, 437–443, doi:10.5194/amt-4-437-2011, https://www.atmos-meas-tech.net/4/437/2011/, 2011.

Kurtén, T., Tiusanen, K., Roldin, P., Rissanen, M., Luy, J.-N., Boy, M., Ehn, M., and Donahue, N.: Alpha-Pinene Autoxidation Products May Not Have Extremely Low Saturation Vapor Pressures Despite High O:C Ratios, J. Phys. Chem. A, 120, 2569–2582,

doi:10.1021/acs.jpca.6b02196, http://dx.doi.org/10.1021/acs.jpca.6b02196, pMID: 27049168, 2016.

Lehtinen, K. E., Maso, M. D., Kulmala, M., and Kerminen, V.-M.: Estimating nucleation rates from apparent particle formation rates and vice versa: Revised formulation of the Kerminen–Kulmala equation, J. Aerosol Sci., 38, 988 – 994, doi:http://dx.doi.org/10.1016/j.jaerosci.2007.06.009, http://www.sciencedirect.com/science/article/pii/S0021850207001024, 2007.

Lehtipalo, K., Leppä, J., Kontkanen, J., Kangasluoma, J., Franchin, A., Wimmer, D., Schobesberger, S., Junninen, H., Petäjä, T., Sipilä, M., Mikkilä, J., Vanhanen, J., Worsnop, D. R., and Kulmala, M.: Methods for determining particle size distribution and growth rates between 1 and 3 nm using the Particle Size Magnifier, Boreal Environ. Res., 19, 215–236, 2014.

Lehtipalo, K., Rondo, L., Kontkanen, J., Schobesberger, S., Jokinen, T., Sarnela, N., Kürten, A., Ehrhart, S., Franchin, A., Nieminen, T., Riccobono, F., Sipilä, M., Yli-Juuti, T., Duplissy, J., Adamov, A., Ahlm, L., Almeida, J., Amorim, A., Bianchi, F., Breitenlechner, M., Dommen, J., Downard, A. J., Dunne, E. M., Flagan, R. C., Guida, R., Hakala, J., Hansel, A., Jud, W., Kangasluoma, J., Kerminen, V.-M., Keskinen, H., Kim, J., Kirkby, J., Kupc, A., Kupiainen-Määttä, O., Laaksonen, A., Lawler, M. J., Leiminger, M., Mathot, S., Olenius, T., Ortega, I. K., Onnela, A., Petäjä, T., Praplan, A., Rissanen, M. P., Ruuskanen, T., Santos, F. D., Schallhart, S., Schnitzhofer, R., Simon, M., Smith, J. N., Tröstl, J., Tsagkogeorgas, G., Tomé, A., Vaattovaara, P., Vehkamäki, H., Vrtala, A. E., Wagner, P. E., Williamson, C., Wimmer, D., Winkler, P. M., Virtanen, A., Donahue, N. M., Carslaw, K. S., Baltensperger, U., Riipinen, I., Curtius, J., Worsnop, D. R., and Kulmala, M.: The effect of acid–base clustering and ions on the growth of atmospheric nano-particles, Nat. Commun., 7, 11 594, doi:10.1038/ncomms11594, http://dx.doi.org/10.1038/ncomms11594, 2016.

Manninen, H. E., Petäjä, T., Asmi, E., Riipinen, I., Nieminen, T., Mikkilä, J., Hõrrak, U., Mirme, A., Mirme, S., Laakso, L., Kerminen, V.-M., and Kulmala, M.: Long-term field measurements of charged and neutral clusters using Neutral cluster and Air Ion Spectrometer (NAIS), Boreal Environ. Res, 14, 591–605, 2009.

Murphy, B. N., Julin, J., Riipinen, I., and Ekman, A. M. L.: Organic aerosol processing in tropical deep convective clouds: Development of a new model (CRM-ORG) and implications for sources of particle number, J. Geophys. Res.-Atmos., 120, 10,441–10,464, doi:10.1002/2015JD023551, http://dx.doi.org/10.1002/2015JD023551, 2015JD023551, 2015.

Nieminen, T., Lehtinen, K. E. J., and Kulmala, M.: Sub-10 nm particle growth by vapor condensation – effects of vapor molecule size and particle thermal speed, Atmos. Chem. Phys., 10, 9773–9779, doi:10.5194/acp-10-9773-2010, http://www.atmos-chem-phys.net/10/9773/2010/, 2010.

Pankow, J. and Asher, W.: SIMPOL.1: a simple group contribution method for predicting vapor pressures and enthalpies of vaporization of multifunctional organic compounds, Atmos. Chem. Phys., 8, 2773–2796, doi:doi:10.5194/acp-8-2773-2008, www.atmos-chem-phys.net/8/2773/2008/, 2008.

Pichelstorfer, L., Stolzenburg, D., Ortega, J., Karl, T., Kokkola, H., Laakso, A., Lehtinen, K. E. J., Smith, J. N., McMurry, P. H., and Winkler, P. M.: Resolving nanoparticle growth mechanisms from size- and time-dependent growth rate analysis, Atmos. Chem. Phys., 18, 1307–1323, doi:10.5194/acp-18-1307-2018, https://www.atmos-chem-phys.net/18/1307/2018/, 2018.

Pierce, J. R. and Adams, P. J.: Efficiency of cloud condensation nuclei formation from ultrafine particles, Atmos. Chem. Phys., 7, 1367–1379, doi:10.5194/acp-7-1367-2007, https://www.atmos-chem-phys.net/7/1367/2007/, 2007.

Praske, E., Otkjær, R. V., Crounse, J. D., Hethcox, J. C., Stoltz, B. M., Kjaergaard, H. G., and Wennberg, P. O.: Atmospheric autoxidation is increasingly important in urban and suburban North America, P. Nat. Acad. Sci. USA, 115, 64–69, doi:10.1073/pnas.1715540115, http://www.pnas.org/content/115/1/64, 2018.

Riipinen, I., Yli-Juuti, T., Pierce, J. R., Petäjä, T., Worsnop, D. R., Kulmala, M., and Donahue, N. M.: The contribution of organics to atmospheric nanoparticle growth, Nat. Geosci., 5, 453–458, doi:10.1038/ngeo1499, http://dx.doi.org/10.1038/ngeo1499, 2012.

Stolzenburg, D., Steiner, G., and Winkler, P. M.: A DMA-train for precision measurement of sub-10 nm aerosol dynamics, Atmos. Meas. Tech., 10, 1639–1651, doi:10.5194/amt-10-1639-2017, http://www.atmos-meas-tech.net/10/1639/2017/, 2017.

Tröstl, J., Tritscher, T., Bischof, O. F., Horn, H.-G., Krinke, T., Baltensperger, U., and Gysel, M.: Fast and precise measurement in the sub-20 nm size range using a Scanning Mobility Particle Sizer, J. Aerosol Sci., 87, 75–87, doi:10.1016/j.jaerosci.2015.04.001, http://www.sciencedirect.com/science/article/pii/S0021850215000543, 2015.

Tröstl, J., Chuang, W. K., Gordon, H., Heinritzi, M., Yan, C., Molteni, U., Ahlm, L., Frege, C., Bianchi, F., Wagner, R., Simon, M., Lehtipalo, K., Williamson, C., Craven, J. S., Duplissy, J., Adamov, A., Almeida, J., Bernhammer, A.-K., Breitenlechner, M., Brilke, S., Dias, A., Ehrhart, S., Flagan, R. C., Franchin, A., Fuchs, C., Guida, R., Gysel, M., Hansel, A., Hoyle, C. R., Jokinen, T., Junninen, H., Kangasluoma, J., Keskinen, H., Kim, J., Krapf, M., Kürten, A., Laaksonen, A., Lawler, M., Leiminger, M., Mathot, S., Möhler, O., Nieminen, T., Onnela, A., Petäjä, T., Piel, F. M., Miettinen, P., Rissanen, M. P., Rondo, L., Sarnela, N., Schobesberger, S., Sengupta, K., Sipilä, M., Smith, J. N., Steiner, G., Tomè, A., Virtanen, A., Wagner, A. C., Weingartner, E., Wimmer, D., Winkler, P. M., Ye, P., Carslaw, K. S., Curtius, J., Dommen, J., Kirkby, J., Kulmala, M., Riipinen, I., Worsnop, D. R., Donahue, N. M., and Baltensperger, U.: The role of low-volatility organic compounds in initial particle growth in the atmosphere, Nature, 533, 527–531, doi:10.1038/nature18271, http://dx.doi.org/10.1038/nature18271, 2016.

Vanhanen, J., Mikkilä, J., Lehtipalo, K., Sipilä, M., Manninen, H. E., Siivola, E., Petäjä, T., and Kulmala, M.: Particle Size Magnifier for Nano-CN Detection, Aerosol Sci. Tech., 45, 533–542, doi:10.1080/02786826.2010.547889, http://www.tandfonline.com/doi/abs/10.1080/02786826.2010.547889, 2011.

Wang, J., Krejci, R., Giangrande, S., Kuang, C., Barbosa, H. M. J., Brito, J., Carbone, S., Chi, X., Comstock, J., Ditas, F., Lavric, J., Manninen, H. E., Mei, F., Moran-Zuloaga, D., Pöhlker, C., Pöhlker, M. L., Saturno, J., Schmid, B., Souza, R. A. F., Springston, S. R.,

Tomlinson, J. M., Toto, T., Walter, D., Wimmer, D., Smith, J. N., Kulmala, M., Machado, L. A. T., Artaxo, P., Andreae, M. O., Petäjä, T., and Martin, S. T.: Amazon boundary layer aerosol concentration sustained by vertical transport during rainfall, Nature, 539, 416–419, doi:10.1038/nature19819, `http://dx.doi.org/10.1038/nature19819`, 2016.

Chapter 6

Summary and Discussion

Nucleation and subsequent growth of nanoparticles is a process widely observed in the atmosphere and responsible for high uncertainities in climate change predictions (Kulmala et al., 2004; IPCC, 2013). This is due to the fact that the deep microphysical understanding is the only possibility to somehow access the influence of anthropogenic emissions on global cloud condensation nuclei concentrations and hence its impact on the earth's radiative balance. Especially nucleation and early growth of nanoparticles below 10 nm is difficult to investigate, in part because of missing instrumentation to observe for example particle dynamics at typical low atmospheric particle number concentrations. There are some outstanding research questions challenging the scientific community in the understanding of initial nanoparticle formation: Are nucleation and growth two processes which can be physically separated, what is the role of the Kelvin barrier in this process and how does this depend on the condensing or nucleating species? How do different organic compounds contribute and how can the atmospheric complexity be modeled best? These research questions were opened in Chapter 1 and connected to the missing information on aerosol dynamics in the crucial size range where molecular clusters grow to more stable and larger particles. The development of the DMA-train together with new particle formation experiments performed in atmospheric simulation chambers like the CERN CLOUD experiment is shown to be an excellent approach to investigate the microphysical dynamics of aerosol formation.

In this thesis, it was demonstrated in Chapter 2 that combining existing particle-sizing technology in a new parallel approach can solve the problem of low counting statistics by avoiding scanning procedures. This approach is called DMA-train. Chapter 2 Fig. **??** illustrates the different correction terms which are needed for the inversion of DMA-tain data acquired at a certain particle size. It shows that even with a minimization of inlet losses, the application of differential mobility analyzers optimized for the classification of ultrafine particles and the usage of condensation particle counters with the highest detection efficiencies at the smallest sizes, the overall detection efficiency of the newly developed DMA-train is below 1 % for particles smaller than 3 nm. Due to this strong reduction of detected particles, signal in the lowest size-channels is only significant above background noise due to the long integration time possible at a single size. This is mainly shown in Chapter 2 Fig. **??**, where the evolution of the particle concentration in every used channel can be followed during a nucleation and growth event in a chamber experiment. This is also supported by Chapter 4 Extended Data Fig. 2, where a combined particle size distribution of the DMA-train and a commercial fast-scanning TSI Model 3982 nano-SMPS is shown. Below 8 nm the DMA-train is used due to its clearly increased signal strength, resolving the size distribution evolution of the growing

aerosol down to 1.8 nm.

A decisive quantity to infer from such particle size distribution evolution measurements is the particle growth rate. Usually the appearance time method is used in this context, because it is a very reliable and robust method if experiments are started with particle-free chambers and nucleation experiments are performed leading to a clearly detectable front of the growing new particle population. The time when this front is reaching a certain size is determined and a growth rate is inferred by comparing these appearance times of different channels. This is in detail described e.g. in Chapter 5 Supporting Information and illustrated in Chapter 5 Fig. 4, where the method principle is demonstrated. Moreover, if the aerosol is rapidly growing, the time between the first appearance of signal and steady state conditions within the chamber might be established in the order of minutes. In that case the higher possible time-resolution of the DMA-train can help to more precisely estimate the signal appearance time and hence the particle growth rate inferred by the dynamics of the growing front. A somewhat similar example to this case is shown in Chapter 2 Fig. 7 demonstrating the time resolving power of the non-scanning DMA-train by the measurement of the fast evolving size-distribution of a tungsten oxide aerosol generator at warmup.

The appearance method omits other processes contributing to a changing particle size distribution like coagulation or loss terms, which was outlined by introducing the aerosol general dynamics equation (Chapter 1 Eq. 3 or repeated in Chapter 3 Eq. 1). However, if the particle size distribution is measured with high precision, aerosol dynamics can be simulated as the equations governing the coagulation and loss terms for the particle size distribution are, at least for chamber experiments, quite well known. This is demonstrated within Chapter 3, where two new analysis methods are presented. Both methods include the effects described by the aerosol general dynamics equation but use different approaches for the calculation of size- and time-dependent growth rates. This advantage of disentangling a possible size- and time-dependence within the growing aerosol is nicely illustrated in Chapter 3 Fig. 2, which shows the inferred growth rates from the two newly developed methods for an α-pinene ozonolysis chamber experiment. Especially in panel (c), where the methods are compared to the appearance time approach, it gets evident that the appearance time method is not able to conclude that the increase in growth rate towards larger particle sizes is due to an increase of the condensing vapors or an actual size effect.

This ambiguity of the appearance time or similar growth rate analysis methods led to a long debated observation of increasing particle growth rates with size and/or time in the atmosphere, especially for the sub-10 nm size-range. Generally the growth rate can be connected to the condensation of vapor molecules onto the newly formed clusters or larger particles. However, the rate of condensation depends on the properties of the condensing vapors, and the energy barrier which might be needed to overcome in this phase transformation process. Already McMurry and Wilson (1982) proposed that the diameter dependence of the observed

growth rate can be linked to the underlying process driving the growth. In the case of irreversible condensation of every vapor molecule, i.e. condensation which is only controlled by the kinetics of collisions, Nieminen et al. (2010) showed that the particle growth rate should actually be decreasing with increasing size in the sub 10 nm size range. In this case however, there is no energy barrier to overcome for the condensing molecules. Classical theory of nucleation and growth however suggests a Kelvin effect due to the additional surface energy needed as shown in Chapter 1 Eq. 2. This leads to an increased needed vapor pressure over a curved surface to achieve supersaturation and hence condensation. This effect might lead to a reduced ability of condensation of some vapors onto the smallest particles and which again would dominantly be influencing growth in the sub-10 nm size-range. If several condensable vapors are present simultaneously the reduced barrier at larger sizes would lead to more condensing vapors and hence a different size-dependence than the one proposed by Nieminen et al. (2010). Third, it should be mentioned that also chemistry in the condensed phase might play a role in binding volatile compounds to the particles, so-called reactive uptake. According to Apsokardu and Johnston (2018) this could as well lead to increased growth rates with increasing size.

Chapter 3 Fig. 2 indicates that there is indeed a strong size-dependency of the particle growth rates in the condensation of oxidation products from the ozonolysis of the most abundant monoterpene α-pinene. Increased growth rates with particle size are found throughout the complete experiment. After the initial build-up of condensable vapors, steady state between chemical production and loss mechanisms within the chamber is reached, and the observed size-dependency of growth rates can be identified as characteristic for the system. This clearly demonstrates again the power of the newly developed analysis methods and the high quality data set obtained by the DMA-train principle: It is speculated that the sharp increase in growth between 2 and 5 nm is indeed due to a multi-component Kelvin effect. The same effect was found by Tröstl et al. (2016), where it was shown that it is linked to the variety of oxidation products which emerge from the complex chemical reactions following the ozonolysis of monoterpenes. However, neither in Chapter 3 nor Tröstl et al. (2016) particle phase reactions could be ruled out of being responsible for the observed accelerating growth rates (Chuang and Donahue, 2017). In Chapter 5 quantitative mass balance between gas and particle phase is finally achieved for α-pinene ozonolysis experiments as novel instrumentation (Breitenlechner et al., 2017) is used for the observation of gas-phase compounds. Here similar to Tröstl et al. (2016) the observed gas-phase ozonolysis products are treated within a binned volatility framework, but as well less oxidized molecules are taken into account. Chapter 5 Fig. 3 shows the good agreement between the size-dependency predicted by a model including the Kelvin effect and the variety of saturation vapor pressures of the oxidation products and the measurements. The demonstrated mass-balance shows that particle phase reactions should at least not dominate the growth driven by organics in the size-range below 10 nm. Moreover,

the comparison of the modeled growth rates with the precision measurements from the DMA-train allow for an estimate of the Kelvin-diameter, i.e. the crucial size where the curvature effect dominates. The value of 4.8±0.8 nm found for this organic system indeed verifies that the curvature effect is dominant only for the smallest particles.

Apparently, the products from organic oxidation reactions span wide ranges of volatilities, leading to a multi-component Kelvin-effect governing the size-dependency of initial nanoparticle growth. This is also demonstrated in Chapter 5 Fig. 2 panel (A) and (B), where at similar α-pinene ozonolysis rates lower growth rates are observed for smaller sizes. The same observation is also made for the α-pinene ozonolysis system in the presence of isoprene as shown in Chapter 4 Extended Data Fig. 9 panel (a). Here at similar levels of C_{20} class oxidation products lower growth rates are found for the size-range of 1.3-3.2 nm compared to >3.2 nm, independent of isoprene addition. However, in Chapter 4 Fig. **??** the growth rates are plotted versus the total observed highly oxygenated molecules detected in the gas-phase and here a suppression of the initial growth rates becomes clearly visible. In fact, as soon as isoprene is present in the α-pinene ozonolysis system, the formation of α-pinene dimers and hence C_{20} class highly oxygenated molecules is reduced to the interference of isoprene termination reactions forming only C_{15} class products. However, they are characterized by generally lower saturation vapor pressures as e.g. shown in Chapter 5 Fig. **??**. The curvature effect therefore gets even more significant, as in total less products are formed which are able to condense from molecular cluster sizes onwards. This is confirmed by the clearly reduced initial growth rates in the presence of isoprene. Moreover, these experiments therefore showed also that the C_{20} class dimers are mainly responsible for initial growth, even in the pure α-pinene system. It therefore seems to be very important that the chemistry leading to the formation of molecules with extremely low saturation vapor pressures is included if the impact of organics on new particle formation is estimated.

These effects of chemistry and the wide range of product volatilities are also important if initial nanoparticle growth is investigated at different temperatures, which is discussed in Chapter 5. In Chapter 5 Fig. 2 panel (C) and (D) it is illustrated that growth is proceeding at similar speed at three different tropospheric temperatures despite completely different highly oxygenated molecule concentrations measured. If the temperature is reduced the ozonolysis of α-pinene and the subsequent reaction chains lead to less molecules having a high oxygen content simply because the auto-oxidation reactions get slower (Praske et al., 2018). But the reduction in temperature also leads to lower saturation vapor pressures of all compounds and therefore also less oxygenated molecules can already condense. These two competing processes, illustrated in Chapter 5 Fig. **??** are of similar magnitude and therefore initial growth driven by organic molecules can also proceed at very low temperatures. In this case it might not be only the C_{20} class dimers which drive the initial growth, but also less heavy and less oxygenated products. The correct estimation of the saturation vapor pressures and

the corresponding temperature dependencies are important to understand the contribution of oxygenated organics on initial growth. Therefore, as illustrated in Chapter 5 Fig. **??** it is the volatility distribution of the products from the specific organic oxidation process which controls the ability of the process to be important for condensation onto the smallest clusters. These findings might be highly important for new particle formation observed in cloud outflow regions, e.g. over the Amazon Basin. There, high amounts of organic molecules are emitted at ground level and transported to high altitudes and therefore low temperatures, where they then effectively can form molecular clusters and condense onto them.
This thesis clearly demonstrated the importance of organics in initial growth processes and the need for a very detailed treatment of atmospheric organic chemistry, physical properties like the saturation vapor pressures of a wide range of substances and the precision measurement of particle growth rates in the cluster-particle transition region. Chapter 4 Fig. **??** demonstrates the importance of the quantification of these initial growth processes at the example of the suppression due to the addition of isoprene to the α-pinene ozonolysis system. While the nucleation rate at 1.7 nm is suppressed by a factor of 5 at similar α-pinene ozonolysis reaction rates, it is the reduced initial growth rate which leads to a dramatic reduction of two orders of magnitude in formation rate at 3 nm for an atmospherically realistic condensation sink of $0.006\,\mathrm{s}^{-1}$. This is in agreement with the considerations presented in Chapter 1 Eq. 1 showing a very strong dependency of the formation rate on growth. Any process which influences the organic volatility distribution therefore might directly have severe impact on new particle formation and hence the global climate.

In summary, this thesis has underlined the speculations of e.g. Kulmala et al. (2013) that organics are, for a wide range of atmospheric conditions, especially important for the initial growth and therefore crucial for the survival of freshly nucleated particles. It might depend on the subtle differences in oxidation chemistry or external conditions if organic molecules are actually effective in the condensation onto molecular clusters. Under such favourable conditions, organics might take a dominant role in the importance of new particle formation for the global cloud condensation nuclei budget. As especially biogenic precursor molecules seem to be highly effective in producing volatility distributions with high contributions in the extremely low saturation vapor pressure range, they might have controlled global CCN number concentrations long before any anthropogenic influence. Gordon et al. (2016) speculated that this would clearly reduce the anthropogenic impact on new particle formation, reducing the radiative forcing of the indirect aerosol effect and hence leading to a stronger global warming than previously thought. In this context, the DMA-train has proven to be a decisive instrument for the precision determination of initial growth rates and the coupled aerosol dynamics and might yield many further insights into the role of biogenic and anthropogenic emissions in atmospheric new particle formation and their impact on the global climate.

6.1 References

Apsokardu, M. J. and Johnston, M. V.: Nanoparticle growth by particle-phase chemistry, Atmos. Chem. Phys., 18, 1895–1907, doi:10.5194/acp-18-1895-2018, https://www.atmos-chem-phys.net/18/1895/2018/, 2018.

Breitenlechner, M., Fischer, L., Hainer, M., Heinritzi, M., Curtius, J., and Hansel, A.: PTR3: An Instrument for Studying the Lifecycle of Reactive Organic Carbon in the Atmosphere, Anal. Chem., 89, 5824–5831, doi:10.1021/acs.analchem.6b05110, http://dx.doi.org/10.1021/acs.analchem.6b05110, pMID: 28436218, 2017.

Chuang, W. K. and Donahue, N. M.: Dynamic consideration of smog chamber experiments, Atmos. Chem. Phys., 17, 10 019–10 036, doi:10.5194/acp-17-10019-2017, https://www.atmos-chem-phys.net/17/10019/2017/, 2017.

Gordon, H., Sengupta, K., Rap, A., Duplissy, J., Frege, C., Williamson, C., Heinritzi, M., Simon, M., Yan, C., Almeida, J., Tröstl, J., Nieminen, T., Ortega, I. K., Wagner, R., Dunne, E. M., Adamov, A., Amorim, A., Bernhammer, A.-K., Bianchi, F., Breitenlechner, M., Brilke, S., Chen, X., Craven, J. S., Dias, A., Ehrhart, S., Fischer, L., Flagan, R. C., Franchin, A., Fuchs, C., Guida, R., Hakala, J., Hoyle, C. R., Jokinen, T., Junninen, H., Kangasluoma, J., Kim, J., Kirkby, J., Krapf, M., Kürten, A., Laaksonen, A., Lehtipalo, K., Makhmutov, V., Mathot, S., Molteni, U., Monks, S. A., Onnela, A., Peräkylä, O., Piel, F., Petäjä, T., Praplan, A. P., Pringle, K. J., Richards, N. A. D., Rissanen, M. P., Rondo, L., Sarnela, N., Schobesberger, S., Scott, C. E., Seinfeld, J. H., Sharma, S., Sipilä, M., Steiner, G., Stozhkov, Y., Stratmann, F., Tomé, A., Virtanen, A., Vogel, A. L., Wagner, A. C., Wagner, P. E., Weingartner, E., Wimmer, D., Winkler, P. M., Ye, P., Zhang, X., Hansel, A., Dommen, J., Donahue, N. M., Worsnop, D. R., Baltensperger, U., Kulmala, M., Curtius, J., and Carslaw, K. S.: Reduced anthropogenic aerosol radiative forcing caused by biogenic new particle formation, P. Nat. Acad. Sci. USA, 113, 12 053–12 058, doi:10.1073/pnas.1602360113, http://www.pnas.org/content/113/43/12053.abstract, 2016.

IPCC: Climate Change 2013: The Physical Science Basis. Contribution of Working Group I to the Fifth Assessment Report of the Intergovernmental Panel on Climate Change, Cambridge University Press, Cambridge, United Kingdom and New York, NY, USA, 2013.

Kulmala, M., Vehkamäki, H., Petäjä, T., Dal Maso, M., Lauri, A., Kerminen, V.-M., Birmili, W., and McMurry, P. H.: Formation and growth rates of ultrafine atmospheric particles: a review of observations, J. Aerosol Sci., 35, 143–176, doi:10.1016/j.jaerosci.2003.10.003, http://www.sciencedirect.com/science/article/pii/S0021850203004373, 2004.

Kulmala, M., Kontkanen, J., Junninen, H., Lehtipalo, K., Manninen, H. E., Nieminen, T., Petäjä, T., Sipilä, M., M., Schobesberger, S., Rantala, P., Franchin, A., Jokinen, T., Järvinen, E., Äijälä, M., Kangasluoma, J., Hakala, J., Aalto, P. P., Paasonen, P., Mikkilä, J., Vanhanen, J., Aalto, J., Hakola, H., Makkonen, U., Ruuskanen, T., Mauldin, R. L., Duplissy, J., Vehkamäki, H., Bäck, J., Kortelainen, A., Riipinen, I., Kurtén, T., Johnston, M. V., Smith, J. N., Ehn, M., Mentel, T. F., Lehtinen, K. E. J., Laaksonen, A., Kerminen, V.-M., and Worsnop, D. R.: Direct Observations of Atmospheric Aerosol Nucleation, Science, 339, 943–946, doi:10.1126/science.1227385, http://science.sciencemag.org/content/339/6122/943, 2013.

McMurry, P. and Wilson, J.: Growth laws for the formation of secondary ambient aerosols: Implications for chemical conversion mechanisms, Atmos. Environ., 16, 121 – 134, doi:10.1016/0004-6981(82)90319-5, http://www.sciencedirect.com/science/article/pii/0004698182903195, 1982.

Nieminen, T., Lehtinen, K. E. J., and Kulmala, M.: Sub-10 nm particle growth by vapor condensation – effects of vapor molecule size and particle thermal speed, Atmos. Chem. Phys., 10, 9773–9779, doi:10.5194/acp-10-9773-2010, http://www.atmos-chem-phys.net/10/9773/2010/, 2010.

Praske, E., Otkjær, R. V., Crounse, J. D., Hethcox, J. C., Stoltz, B. M., Kjaergaard, H. G., and Wennberg, P. O.: Atmospheric autoxidation is increasingly important in urban and suburban North America, P. Nat. Acad. Sci. USA, 115, 64–69, doi:10.1073/pnas.1715540115, http://www.pnas.org/content/115/1/64, 2018.

Tröstl, J., Chuang, W. K., Gordon, H., Heinritzi, M., Yan, C., Molteni, U., Ahlm, L., Frege, C., Bianchi, F., Wagner, R., Simon, M., Lehtipalo, K., Williamson, C., Craven, J. S., Duplissy, J., Adamov, A., Almeida, J., Bernhammer, A.-K., Breitenlechner, M., Brilke, S., Dias, A., Ehrhart, S., Flagan, R. C., Franchin, A., Fuchs, C., Guida, R., Gysel, M., Hansel, A., Hoyle, C. R., Jokinen, T., Junninen, H., Kangasluoma, J., Keskinen, H., Kim, J., Krapf, M., Kürten, A., Laaksonen, A., Lawler, M., Leiminger, M., Mathot, S., Möhler, O., Nieminen, T., Onnela, A., Petäjä, T., Piel, F. M., Miettinen, P., Rissanen, M. P., Rondo, L., Sarnela, N., Schobesberger, S., Sengupta, K., Sipilä, M., Smith, J. N., Steiner, G., Tomè, A., Virtanen, A., Wagner, A. C., Weingartner, E., Wimmer, D., Winkler, P. M., Ye, P., Carslaw, K. S., Curtius, J., Dommen, J., Kirkby, J., Kulmala, M., Riipinen, I., Worsnop, D. R., Donahue, N. M., and Baltensperger, U.: The role of low-volatility organic compounds in initial particle growth in the atmosphere, Nature, 533, 527–531, doi:10.1038/nature18271, http://dx.doi.org/10.1038/nature18271, 2016.

Acknowledgements

This thesis would have been very hard to finish if I had not the overwhelming support of so many people. In fact, I guess it is actually much more the work of many as the work of a single person. First, I want to thank Paul Winkler for his amazingly relaxed support with supervision whenever supervision was needed. I am really grateful to him for introducing me into the field of nucleation and aerosols, for giving me the opportunity to work at CERN on an amazing project, for motivating me to join international conferences and for taking me to an exciting Rapid Wien match. Additionally, I have to thank the European Research Council for funding my work within the project NANODYAMITE 616075.

Second, I'd like to thank the whole Vienna aerosol group for providing a very nice atmosphere to work and spend some Falafel lunch breaks in front of the Votiv Church. I'd like to thank Gerhard Steiner as the best tutor you can have in mobility analysis and his incredible responsiveness to every phone call, providing help for any possible problem, including finding a grill for my rooftop-terrace. I thank Paulus Bauer for being the most helpful person I have ever met, Sophia Brilke for having fun and support during four (!) CLOUD campaigns and Tamara Pinterich, Christian Tauber, Miguel Vazquez and all the others in our group for always being helpful and incredibly friendly. Additionally, I'd like to thank Lukas Pichelstorfer for introducing me to FORTRAN code and for solving all problems you can face with aerosol dynamics simulations.

Good research is nothing without international contacts and therefore I'd like to thank all my fellows from CERN which have made the time there incredible. The endless night and day shifts, all the 3 pm meetings, the nights in the cafeteria, all the cheese fondue we ate and the exciting tunnel tours would have not been the same without you. Especially, I'd like to thank Lubna Dada for emotional support during every campaign and all the chat we had on WhatsApp, scientific or not, and Lukas Fischer, Mario Simon and Martin Heinritzi for pitchers and fancy dinners and incredible support for my papers.

However, life is not only work and a big part of this successful thesis is due to the support from my family and friends. I'd like to thank my parents for being responsible for my way into physics as they taught me curiosity, for supporting me with all means since I can remember and for always paying the good wine and the nice restaurants when you came visiting me in Vienna. I am grateful to all my friends in Vienna, which really have made it easy to feel at home here, my handball team, my former flatmates and my Columbian connection. But most importantly, I'd like to thank Chrissi for coming with me to Vienna, for exploring the city together, for all the pasta you ate with me, for all the social sciences texts I had to read and for all the journeys we did and will do together. I guess without you, this thesis would be empty.